Engineering the structural and functional properties of transition metal oxide interfaces by cluster assembling

Settore Scientifico Disciplinare FIS/03

PhD candidate:
Francesca Borghi
Matr. R09595
XXVII ciclo

Supervisor: Professor Alessandro Podestà
Co-tutor: Professor Paolo Milani

Università degli Studi di Milano
Scuola di dottorato in Fisica, Astrofisica e Fisica Applicata
Academic Year 2014/2015

Commission of the final examination:

External Referee:

Peter Lievens, University of Leuven, Belgium

External Member:

Carlo Bottani, Politecnico di Milano, Italy

External Member:

Luca Gavioli, Università Cattolica del Sacro Cuore, Brescia, Italy

Final examination:

9 June 2015

Università degli Studi di Milano, Dipartimento di Fisica, Milano, Italy

To my sons

"Vi sono uomini che vogliono sapere per il solo gusto di sapere:
è bassa curiosità.
Altri cercano di conoscere per essere conosciuti:
è pura vanità.
Altri vogliono possedere la scienza per poterla rivendere e guadagnare
denaro ed onori: il loro movente è meschino.
Ma alcuni desiderano conoscere per edificare:
e questo è carità;
altri per essere edificati:
e questo è saggezza"

San Bernardo

MIUR subjects:

FIS/03

PACS:

68.37.Ps

68.55.A

68.55.J

68.47.-b

Contents

Introduction

Nanostructured materials are defined as systems composed of single or multiple phases such that at least one of them has characteristic dimensions in the nanometer range (1-100 nm)[1]. The strategic importance of nanostructured materials rely on the fact that their structural, electronic, magnetic, catalytic, and optical properties can be tuned and controlled by a careful choice and assembling of their nanoscale elemental building blocks[2-4].

Clusters, aggregations of a few atoms to a few thousands of atoms, are the building blocks used to synthetize nanostructured materials. The deposition of preformed clusters on a substrate offers the possibility to carefully control building blocks dimensions and hence to tune the structural and functional properties of the resulting systems. For this reason, one of the main goal for researches in cluster science is the production and deposition of clusters of any kind of materials in a wide controlled range of sizes and conditions.

Low-Energy Cluster Beam Deposition (LECBD) [2,5-8] is a technique of choice for the fabrication of nanostructured systems, since it allows the deposition on a substrate of neutral particles produced in the gas phase and maintaining their properties even after deposition. This has been proven to be a powerful bottom-up approach for the engineering of nanostructured thin films with tailored properties, since it allows in principle the control of the physical and chemical characteristics of the building blocks[2,9,10]. The survival of the nanoscale building blocks during the assembly process is at the basis of the so-called 'memory effect'[2].

Among different approaches to LECBD, supersonic cluster beam deposition (SCBD)[6,9,11] present several advantages in terms of deposition rate, lateral resolution compatible with planar microfabrication technologies and neutral particle mass selection by exploiting aerodynamic focusing effects. All these features make SCBD a superior tool to synthesize nanostructured films and their integration on microfabricated platforms.

One of the most relevant property of cluster-assembled materials is the surface morphology. The morphology of cluster-assembled materials is characterized by a hierarchical arrangements of small units in larger and larger features up to a certain critical length-scale, in general determined by the duration of the deposition process[12]. The cluster-

assembled film morphology is characterized by high specific area and porosity at the nano and sub-nanometer scale, extending in the bulk of the film. Surface pores and surface specific area, as well as rms roughness, depend on film thickness[13-15] , and increase with it. All these morphological properties is of great relevance for the use of cluster-assembled film in devices as gas sensor[16,17], (photo) catalysis[18-24], solar energy conversion [25,26] and as biocompatible substrates[27-29].

Recently it has been recognized that nanoscale surface morphology and nanopores play an important role in processes involving the interaction of biological entities (protein, viruses, enzymes) with nanostructured surfaces, via the modulation of electric interfacial properties. In particular, when the nanostructured material is used to produce electrodes and substrates for operation in liquid electrolytes, with given pH and ionic strength, double layer phenomena take place[27,30,31]. An important parameter to describe these electrostatic phenomena is the IsoElectric Point (IEP), which corresponds to the pH value at which the net charge of the compact layer is zero[32]. When two interacting surfaces approach to a distance comparable or smaller than the typical screening length of the electrolytic solution (the Debye length, determined by the ionic strength of the solution), the overlap of the charged layers determines complex regulation phenomena[33] that are difficult to describe theoretically. While significant insights have been obtained on the properties of the electric double layers formed between flat smooth surfaces[34-36], the case of rough surfaces still represents a severe challenge, hampering analytical, yet approximate, solutions of the double layer equations to be reliably obtained. Anyway, these phenomena have been recently shown to be strongly influenced by the morphological properties of the surface[37-41].

The quantitative characterization of all these interfacial properties requires imaging and force spectroscopy techniques with a resolution in and beyond the nanometer-scale. Atomic Force Spectroscopy (AFM) is an excellent candidate, since it couples the possibility of scanning with a z-resolution lower than fraction of nanometer and x-y resolution of 1 nm and also of performing very accurate force spectroscopy measurements[42].

The first aim of my PhD work is to characterize by AFM the evolution of morphological properties of transition-metal oxides cluster-assembled materials (in particular nanostructured Titania (ns-TiO_x) and nanostructured Zirconia (ns-ZrO_x), starting from sub-monolayer regime to thin film, and especially to describe the influence of the building-blocks dimensions on the growth mechanisms and on the final surface morphology and topography. With this information, I have explored the influence of

nanoscale morphology on double layer interactions which takes place on these nanostructured interfaces and on the wettability behaviour. The results have been used to highlight the role of morphological and structural surface properties as biophysical signal mediators for protein adsorption processes and cellular adhesion.

Thesis outline

This PhD thesis is divided into four parts. The first introductory part is dedicated to describing the main features of the techniques for the production and manipulation of clusters in gas phase (Chapter1) and to providing a theoretical framework for thin film growth description, from sub-monolayer to thin film regime (Chapter 2). The differences between atomic and preformed-cluster depositions are shown and the scaling laws, which characterize the morphological properties of thin film growth, are pointed out.

In the second part (Chapter 3) I present an overview of the experimental results, traceable in literature, of thin film growth by LECBD. This Chapter offers the possibility to face the main strategies on how to analyse experimental data and extract the relevant parameters for describing the elementary processes.

In the third part I present the methods for the deposition and characterization of the cluster-assembled film properties (Chapter 4), which is the Supersonic Cluster Beam Deposition (SCBD) and Atomic Force Microscopy (AFM) principally. In Chapter 5 I also present the transition-metal oxides I have studied, and in particular the structural properties of these nanostructured materials which have just been studied and presented in literature. In Chapter 6 an overview of the functional properties of nanostructured cluster-assembled oxide film is presented as useful theoretical models for the analysis of the experimental data.

In the last part I show the results regarding the morphological and structural properties of films obtained by SCBD in different deposition regimes and with different post-deposition treatments (Chapter 7). In Chapter 8 the interfacial functional properties affected by surface morphology are shown, while in Chapter 9 the response of biological entities to biophysical signals promoted by the nanostructured interface are illustrated. In Chapter 10 I resume the main conclusions and present future perspectives.

The Au-Polydimethylsiloxane (PDMS) nanocomposites morphological and nano-mechanical properties are discussed as appendix in Chapter 11.

References

1. *Handbook of nanostructured materials and nanotechnology*. (Academic Press, 2000).
2. Perez, A. *et al.* Cluster assembled materials: a novel class of nanostructured solids with original structures and properties. *J. Phys. Appl. Phys.* **30,** 709–721 (1997).
3. Melinon, P. *et al.* From free clusters to cluster-assembled materials. *Int. J. Mod. Phys. B* **9,** 339–397 (1995).
4. Binns, C. Nanoclusters deposited on surfaces. *Surf. Sci. Rep.* **44,** 1–49 (2001).
5. Melinon, P. *et al.* Low-energy cluster beam deposition : do you need it ? *J. Phys. I* **3,** 1585–1603 (1993).
6. Fuchs, G. *et al.* Films of controlled nano size grains deposited by low-energy cluster beam. *Z. Für Phys. At. Mol. Clust.* **26,** 249–251 (1993).
7. Jensen, P. *et al.* Continuous amorphous antimony thin films obtained by low-energy cluster beam deposition. *Appl. Phys. Lett.* **59,** 1421–1423 (1991).
8. Bouwen, W. *et al.* Characterization of granular Ag films grown by low-energy cluster beam deposition. *Thin Solid Films* **354,** 87–92 (1999).
9. Wegner, K., Piseri, P., Tafreshi, H. V. & Milani, P. Cluster beam deposition: a tool for nanoscale science and technology. *J. Phys. Appl. Phys.* **39,** R439–R459 (2006).
10. Milani, P. & Iannotta, S. *Cluster Beam Synthesis of Nanostructured Materials*. (Springer Berlin Heidelberg, 1999). at <http://dx.doi.org/10.1007/978-3-642-59899-9>
11. Piseri, P., Podestà, A., Barborini, E. & Milani, P. Production and characterization of highly intense and collimated cluster beams by inertial focusing in supersonic expansions. *Rev. Sci. Instrum.* **72,** 2261 (2001).
12. Podestà, A. Development of protocols for a quantitative characterization of morphological and tribological properties of nanostructured films via the atomic force microscopy. (Università degli Studi di Milano, 2001).
13. Scopelliti, P. E. *et al.* The Effect of Surface Nanometre-Scale Morphology on Protein Adsorption. *PLoS ONE* **5,** e11862 (2010).
14. Podestà, A. *et al.* Cluster-Assembled Nanostructured Titanium Oxide Films with Tailored Wettability. *J. Phys. Chem. C* **113,** 18264–18269 (2009).
15. Kholmanov, I. N. *et al.* The influence of the precursor clusters on the structural and morphological evolution of nanostructured TiO_2 under thermal annealing. *Nanotechnology* **14,** 1168–1173 (2003).
16. Göpel, W. New materials and transducers for chemical sensors. *Sens. Actuators B Chem.* **18,** 1–21 (1994).

17. Jiménez-Cadena, G., Riu, J. & Rius, F. X. Gas sensors based on nanostructured materials. *The Analyst* **132,** 1083 (2007).
18. Tong, H. *et al.* Nano-photocatalytic Materials: Possibilities and Challenges. *Adv. Mater.* **24,** 229–251 (2012).
19. Zhou, Z.-Y., Tian, N., Li, J.-T., Broadwell, I. & Sun, S.-G. Nanomaterials of high surface energy with exceptional properties in catalysis and energy storage. *Chem. Soc. Rev.* **40,** 4167 (2011).
20. Wan, K. T., Khouw, C. B. & Davis, M. E. Studies on the Catalytic Activity of Zirconia Promoted with Sulfate, Iron, and Manganese. *J. Catal.* **158,** 311–326 (1996).
21. Audry, F. *et al.* Infrared Study and Quantum Calculations of the Conversion of Methylbutynol into Hydroxymethylbutanone on Zirconia. *J. Catal.* **168,** 471–481 (1997).
22. Trovarelli, A. *et al.* Nanophase Fluorite-Structured CeO2–ZrO2Catalysts Prepared by High-Energy Mechanical Milling. *J. Catal.* **169,** 490–502 (1997).
23. Stichert, W. & Schüth, F. Synthesis of Catalytically Active High Surface Area Monoclinic Sulfated Zirconia. *J. Catal.* **174,** 242–245 (1998).
24. Davies, L. E., Bonini, N. A., Locatelli, S. & Gonzo, E. E. Characterization and catalytic activity of zirconium dioxide prepared by sol-gel. *Lat. Am. Appl. Res.* **35,** 23–28 (2005).
25. Grätzel, M. Photoelectrochemical cells. *Nature* **414,** 338–344 (2001).
26. Kamat, P. V. Meeting the Clean Energy Demand: Nanostructure Architectures for Solar Energy Conversion. *J. Phys. Chem. C* **111,** 2834–2860 (2007).
27. Williams, D. F. On the nature of biomaterials. *Biomaterials* **30,** 5897–5909 (2009).
28. Chevalier, J. What future for zirconia as a biomaterial? *Biomaterials* **27,** 535–543 (2006).
29. Carinci, F. *et al.* Zirconium oxide: analysis of MG63 osteoblast-like cell response by means of a microarray technology. *Biomaterials* **25,** 215–228 (2004).
30. Oldham, K. B. A Gouy–Chapman–Stern model of the double layer at a (metal)/(ionic liquid) interface. *J. Electroanal. Chem.* **613,** 131–138 (2008).
31. Grahame, D. C. The Electrical Double Layer and the Theory of Electrocapillarity. *Chem. Rev.* **41,** 441–501 (1947).
32. Kallay, N., Preočanin, T., Kovačević, D., Lützenkirchen, J. & Villalobos, M. Thermodynamics of the Reactions at Solid/Liquid Interfaces. *Croat. Chem. Acta* 1–10 (2011). doi:10.5562/cca1864
33. Lyklema, J. & Duval, J. F. L. Hetero-interaction between Gouy–Stern double layers: Charge and potential regulation. *Adv. Colloid Interface Sci.* **114–115,** 27–45 (2005).
34. Duval, J., Lyklema, J., Kleijn, J. M. & van Leeuwen, H. P. Amphifunctionally Electrified Interfaces: Coupling of Electronic and Ionic Surface-Charging Processes. *Langmuir* **17,** 7573–7581 (2001).

35. Duval, J., Kleijn, J. M., Lyklema, J. & van Leeuwen, H. P. Double layers at amphifunctionally electrified interfaces in the presence of electrolytes containing specifically adsorbing ions. *J. Electroanal. Chem.* **532,** 337–352 (2002).
36. Parsegian, V. A. & Gingell, D. On the Electrostatic Interaction across a Salt Solution between Two Bodies Bearing Unequal Charges. *Biophys. J.* **12,** 1192–1204 (1972).
37. Borghi, F., Vyas, V., Podestà, A. & Milani, P. Nanoscale Roughness and Morphology Affect the IsoElectric Point of Titania Surfaces. *PLoS ONE* **8,** e68655 (2013).
38. Daikhin, L. I., Kornyshev, A. A. & Urbakh, M. Double layer capacitance on a rough metal surface: Surface roughness measured by 'Debye ruler'. *Electrochimica Acta* **42,** 2853–2860 (1997).
39. Daikhin, L. I., Kornyshev, A. A. & Urbakh, M. Double-layer capacitance on a rough metal surface. *Phys. Rev. E* **53,** 6192–6199 (1996).
40. Daikhin, L. I., Kornyshev, A. A. & Urbakh, M. Nonlinear Poisson–Boltzmann theory of a double layer at a rough metal/electrolyte interface: A new look at the capacitance data on solid electrodes. *J. Chem. Phys.* **108,** 1715 (1998).
41. Duval, J. F. L., Leermakers, F. A. M. & van Leeuwen, H. P. Electrostatic Interactions between Double Layers: Influence of Surface Roughness, Regulation, and Chemical Heterogeneities. *Langmuir* **20,** 5052–5065 (2004).
42. Butt, H.-J., Cappella, B. & Kappl, M. Force measurements with the atomic force microscope: Technique, interpretation and applications. *Surf. Sci. Rep.* **59,** 1–152 (2005).

Part I

Theoretical framework

1. Clusters in the gas phase: production and manipulation

1.1. Cluster Sources

Gas-phase synthesis is an established and well-developed process able to produce large scale quantities of nanoparticles with a high level of control on particle physico-chemical properties such as phase and composition[1]. The formation and growth processes of objects relevant for cluster beam deposition follow the same physical and chemical mechanisms as any gas-phase particle synthesis process. These mechanisms have been extensively studied in aerosol synthesis, the gas-phase manufacture of nanoparticles at atmospheric pressure[2], and can also be applied to the cluster sources used in cluster beam deposition processes.

In gas phase synthesis, nanoparticles are made by "building" them from individual atoms or molecules up to the desired size. Cluster embryos are formed either by physical means such as condensation of a supersaturated vapor or by chemical reaction of gaseous precursors. Examples include inert gas condensation[3,4], plasma[5] and flame processes[6]. Formation of particles in the gas phase takes place either by homogeneous nucleation or by coagulation (collision) processes. The starting material can be vaporized from a hot source into a low density inert gas employing Joule heating, thermal plasma, or laser ablation. Cooling of the vapor rapidly leads to super-saturation followed by homogeneous nucleation and the formation of first product clusters[7].

Gas-phase cluster formation processes are characterized by critical parameters such as the number of collisions between aggregating species, collisions between aggregating species and the thermalizing gas and by the method to produce, in a defined volume, the cluster precursors[8].

Cluster formation can take place in a buffer gas acting as a thermal bath and at the same time as a carrier of the nanoparticles. These two aspects are intimately related so that the pressure inside the particle generation source determines the condensation efficiency, whereas the pressure gradient affects the cluster extraction and manipulation.

Cluster sources can be catalogued in terms of the regimes governing gas introduction and extraction: continuous or pulsed, effusive or supersonic. At a first glance, continuous production methods coupled to continuous gas flow regimes seem to guarantee an easier and a more efficient production and control on cluster parameters. Actually this

can be the case only when very huge gas loads can be handled for ambient pressure aerosol techniques (i.e. flame pyrolysis)[6]. For cluster beam deposition under vacuum conditions a continuous gas flow must be compatible with stringent vacuum requirements and hence only effusive regimes are of practical interest. Vacuum requirements also affect the pressure attainable in the cluster source that usually should not exceed a few Torr[8], this is a critical parameter to control the number of collisions then is the cluster source dimension and geometry.

The realization and operation of pulsed cluster sources appears to be more complicated compared to continuous ones, moreover, they are characterized by a low duty cycle[9]. On the other hand, the reduced gas load has the advantage to allow the use of a supersonic expansion regime and the compatibility with HV and UHV standards. Moreover, it is possible to control the gas pressure in the source region, where cluster formation takes place, over a very wide range. These aspects are of fundamental importance for applications and in particular for the compatibility of cluster beam deposition processes with micro-fabrication and planar technologies[10].

The structure and operation of cluster sources is also determined by the methods used for precursor production, here we will consider cluster sources as possible working tools for the fabrication of nanostructured systems.

1.1.1. Joule heating

Cluster sources based on joule heating are conceptually simple: they are based on a reservoir with well-defined exit opening in which a certain vapor pressure of the precursor material must be sustained. The control on the vapor pressure and temperature necessary to induce nucleation is usually realized by mixing the precursors with an inert gas.

Vaporization of the precursors is obtained by joule heating of high-temperature crucibles as in the case of molecular beam epitaxy (MBE)[11,12]. However, high intensity sources for the production of cluster beams have more stringent requirements. In particular, the vapor pressures are typically about two orders of magnitude higher than those used in MBE which are roughly 10^{-3} - 10^{-4} mbar. Hence they operate at significantly higher temperatures.

1.1.2. Sputtering

Plasma discharges are of particular relevance for cluster formation. Schematically, a discharge consists of a voltage supply that drives current through a low pressure gas between two conducting plates or electrodes[13]. The gas breaks down to form a weakly ionized plasma. Charged particles in the plasma acquire high kinetic energies and collide with the neutrals in the gas, causing the formation of very reactive species. Material sputtering from the plates or electrodes takes place: in this way the electrode material acts as a feedstock of particles injected in the plasma[14].

Plasma sputtering offers a method for vaporizing refractory materials without involving the complications of the target heating process. The combination of plasma sputtering with gas condensation was reported in 1986 and then developed by Haberland and co-workers through the use of magnetron sputtering[15]. This source is relatively easy to operate and, in principle, it allows the production of intense clusters beams, however, to date, applications to nano- and micro-fabrication are scarce. The gas pressure inside the sputtering chamber influences the discharge while gas inlet and extraction are critical to determine the nucleation and condensation processes. In order to control the cluster mass distribution, the distance between the sputtering region and the extraction nozzle can be varied. To favor condensation, the source region can be cooled by liquid nitrogen, which however imposes constraints on the source dimensions and geometry[16].

During cluster production, a typical gas pressure in the condensation chamber is 1 mbar, with a gas flow rate of a few hundreds of a standard cm^3 per minute. In order to achieve a high vacuum level of 10^{-7} mbar in the deposition chamber, a high throughput pump is installed in each section of the apparatus.

1.1.3. Laser vaporization

Laser vaporization can generate a high density vapor of virtually any material in a short time interval and in a well localized volume. By rapid quenching of the plasma, clusters and nanoparticles can be produced[17,18]. This technique was originally applied to the production of clusters in molecular beams by Smalley and co-workers[19]. Since this pioneering work, laser vaporization has become one of the most common techniques for generating cluster beams especially of refractory materials[8].

The kinetics of aggregation of the plasma produced by laser ablation and the characteristics of the resulting aggregates (density, size distribution, structure, etc.) as well

as the intensity and stability of the laser vaporization cluster source (LVCS) are influenced by the quantity and type of ablated material, the plasma – buffer gas interaction, the plasma – source wall interaction, and the cluster residence time prior to expansion. High power pulsed solid state or excimer lasers are used for the vaporization, the pulsed nature of the precursor production makes this approach particularly suited for pulsed gas regimes.

The light of a high intensity pulsed laser (usually with a pulse length in the order of tens of nanoseconds) is focused onto a target vaporizing a small amount of material into a flow of an inert carrier gas. The inert gas quenches the plasma and cluster condensation is promoted. The mixture is then expanded into vacuum and forms a cluster beam. When a pulsed vaporization takes place it is convenient to operate the LVCS with a pulsed valve for carrier gas introduction. Different geometries have been developed for target mounting and to favor cluster formation and growth prior to the extraction.

The characteristics of the cluster population are controlled by the local gas pressure during plasma production and the residence time of the particles in the source body. The plasma gas interaction affects not only the final cluster distribution but also the subsequent expansion and beam formation. By monitoring the pressure evolution in a LVCS, it has been shown that vaporization in a low pressure environment produces a large amount of monomers. Increasing the pressure during the ablation results in a shift of the cluster distribution towards larger masses[20].

LVCS are very flexible and allow the production of metallic, oxide and alloy clusters with a large variety of structures and stoichiometric combinations[21]. The low gas load allows to couple LVCS to UHV deposition equipment[21]. On the other hand, the deposition rates are rather low and typically only small areas are covered. This is a serious bottleneck for the use of LVCS for the synthesis of nanostructured materials in view of applications.

1.2. Effusive vs supersonic

The production of particle beams is based on the expansion of a particle-gas mixture through a nozzle, generating a sonic or supersonic gas stream[8]. The expansion of a high-pressure gas from a reservoir into vacuum can occur via two physically distinct limiting cases, depending on the relationship between the mean free path of the gas molecules in the reservoir, λ_0, and the diameter, D, of the expansion orifice. As these characteristic dimensions approach the limit $\lambda_0 >> D$, the number of collisions suffered by a molecule as

it leaves the reservoir approaches zero, and an effusive beam is generated. In the limit of $D >> \lambda_0$, molecules escaping from the reservoir suffer many collisions during the expansion process. The theory in its most basic form was first worked out in 1951[22], and experimental proof of the fundamental principles was provided shortly thereafter[23]. At high source pressures, the effects of gas viscosity and heat transfer may be neglected, and the gas flow may be treated as an adiabatic and isentropic expansion.

The basic concept of an effusive beam source is very simple: it is an orifice in a very thin wall of a reservoir where the gas or vapor is in thermal equilibrium. The opening is small enough so that the outgoing flow will not affect the equilibrium in the reservoir. If the pressure in the reservoir is low enough, the outgoing flow will be molecular so that the effusion rate and both the angular and velocity distributions of the formed beam can be calculated on the basis of the gas kinetic theory without any assumption.

A supersonic expansion can be obtained by imposing a pressure ratio less than $P_b/P_0=0.478$ across a convergent nozzle driving an isentropic flow expansion where P_0 and P_b are the stagnation and the background pressures, respectively. The expansion through a convergent nozzle will always take place in a subsonic regime regardless of the amount of the applied pressure ratio. Outside the converging nozzle, depending on the pressure ratio, the flow will supersonically expand to pressures even much lower than the background. A normal shock, known as Mach disk, matches the pressure inside the jet to the background and closes an area called zone of silence. The location of the Mach disk has been empirically determined as being only a function of the pressure ratio and independent of the fluid nature and nozzle geometry[3].

Separation effects in front of the skimmer should enrich the periphery of the beam of small clusters, leaving large clusters in the beam center[24]. The sudden free expansion of the flow at the immediate vicinity of the nozzle outlet produces a high outward radial velocity at the beginning of the free jet. Consequently, if the jet is seeded by clusters, the resulting outward radial drag on the particles causes a pronounced mass separation in terms of cluster masses. Light clusters can follow the expanding carrier gas, while large particles persist on their original trajectories, increasing their relative concentration in the jet core. Furthermore, the aforementioned radial drag changes with the radial position at the nozzle outlet: it is weak at the center and very strong close to the nozzle wall. Hence, in contrast to the particles located in the central regions, those far from the axis are exposed to a strong radial drag and they will be spatially separated according to their different masses. If the particles can be concentrated in the nozzle centerline, no significant divergence should

occur in the subsequent evolution of the expansion and the obtained beam will have a high intensity and collimation. Since the angular distribution of the clusters in the jet is a function of their mass and of their initial spatial distribution inside the nozzle, focusing the clusters on the beam center will directly improve the beam intensity and collimation[25].

In view of the use of clusters as building blocks of nanostructured thin films, intense and stable beams must be used and a good control on cluster mass and kinetic energies distribution must be achieved. These characteristics can be obtained with the use of beams produced by supersonic expansions. Compared to effusive beams used in Molecular Beam Epitaxy, supersonic beams provide higher intensity and directionality, allowing the deposition of films with very high growth rates. The use of supersonic expansions may improve the deposition rate and favor a better control on cluster mass distribution[8].

1.3. Manipulation and Handling in the Gas Phase

Cluster synthesis in the gas phase usually does not produce monodisperse particles but a size distribution, the width of which mainly depends on the synthesis conditions in the particle source. The ability to sort nanoparticles in the gas phase directly after their synthesis in terms of a size or geometry thus is of major importance. For device fabrication involving controlled particle deposition on substrates, a second requisite is of importance: the ability to deposit nanoparticles with very high lateral resolution. This can be obtained by controlling the shape of the particle beam and the particle velocities.

P.A.M. Dirac suggested during II world war that inertial effects in gas flow can be used for mass separation[26]. One decade later, the experimental evidence of such an effect was obtained by E.W. Becker and co-workers[27]. Although the first observations were done in the jet expansion of a supersonic molecular beam source, the subsequent work by Becker was aimed at uranium enrichment in a cascade of aerodynamic separation stages (the "separation nozzle") the product of which was not a beam of the selected specie.

In aerosol science, particle separation effects have long been exploited for particulate sampling with impactors. Significant advances in this field have been made pushing the limits of application to nanometre-sized particles and heavy molecules[28]. Regarding an exploitation of these effects for the production of high intensity molecular beams, only very little work was performed in the early times, even though J. Fenn already

recognized in 1963 that the gas mixture in a seeded supersonic beam source is nothing but an aerosol[29].

The first attempts to focus particles through supersonic expansions were made by Murphy and Sears[30] and Israel and Friedlander[31]. Dahneke and Flachsbart[32] increased the particle concentration in the core of an aerosol free jet by using an extra stream, sheath air, that confines the boundaries of the core jet downstream of the nozzle. In the recent literature, the major development in particle focusing dates back to the work of Liu et al.[33,34]. They were the first to produce an enriched stream of particles using only aerodynamics effects induced by nozzles. This was achieved with a system of so-called aerodynamic lenses consisting of successive axisymmetric contractions-enlargements of the aerosol flow passage. The work of Liu et al.[33,34] was inspired by the pioneering research carried out by Fernandez de la Mora[35,36] and co-workers who revealed the possibility of particle focusing and the existence of a common focal point for the near-axis particles when expanding an aerosol through a thin-plate orifice. Unfortunately, particle beams may diverge after a sharp focal point downstream of the nozzle because the gas streamlines diverge due to the sudden gas expansion. The over-exposing images reported by Fuerstenau et al.[37] visualize the above divergence in aerosol jets expanded through thin-plate orifices. The novelty of the work of Liu et al.[33,34] is that they employed thin plate orifices in a confined passage to manipulate the spatial distribution of particles prior to the nozzle and the subsequent expansion in the free jet.

In 1999, Mallina et al.[38] demonstrated that the beams produced by expansion through capillaries have lower angular spread than those formed by expansion through conical nozzles. This is due to the focalization of particle beams in a point downstream of the conical nozzle and beam divergence afterwards, similar to thin-plate orifices. In capillaries, however, particles asymptotically converge to the focal point, which appears to be inside the capillary, and do not significantly diverge afterwards as the capillary walls confine the gas streamlines.

Goo[39] simulated the aerosol concentration at atmospheric pressure in a cascade of aerodynamic slit lenses followed by a virtual impactor. Soon afterwards, Lee et al.[40] reported on experiments and numerical simulation of particle focusing at atmospheric pressure. Zhang et al.[41] repeated the simulations of Liu et al.[33] with less restrictive assumptions, allowing them to study a wider range of particle sizes. Specifically, they considered the compressibility of the continuous phase as well as particle loss due to wall

impaction. Zhang et al.[41] observed that the maximum particle displacement, as well as particle loss, occurs at a particle Stokes number near unity.

Piseri et al.[42] developed a new type of aerodynamic lens system. By placing an obstacle (a flat plate hereon called focuser) upstream a capillary nozzle, they forced the flow to undergo two 90-degree turns to reach the nozzle inlet. The spacing between the focuser and the nozzle inlet is the controlling parameter for selecting particles of desired size. In comparison to the aerodynamic lens system of Liu et al.[33,34], particles approach the orifice with a more uniform velocity and direction and experience a more uniform and higher acceleration. Furthermore, this new design is less sensitive to the upstream position of the particles (for instance in the cluster source or synthesis chamber). Thus, a broader size range of particles originating from distances farther from the centerline can be focused. The device is very compact, has few components that are easy to machine, and is not subject to critical alignment requirements. The main drawback of this design is the high rate of particle deposition to the wall. Vahedi Tafreshi et al[25] have simulated the performance of the above aerodynamic nozzle in its full three-dimensional geometry. They also considered an axisymmetric model and studied the effects of different operating conditions, spacing and the initial position of particles[43]. They reported that the Brownian diffusion cannot drastically affect the aerodynamic focusing effect of their lens but can broaden the focused beam to some degree[44]. Middha and Wexler[45] recently proposed an aerodynamic focuser with so-called capped-cone geometry that has revealed a certain improvement over the previous designs[25,43].

Since the invention of aerodynamic lenses by Liu et al.[33,34], this system has been used in a variety of applications. One example is single particle mass spectrometry for aerosol sampling. The ability of aerodynamic lenses to concentrate the beam on a very narrow near-axis region is of crucial importance for the performance of these instruments where a pulsed laser for particle ionization/vaporization is triggered by the single particle itself.

Mallina et al.[46] have reported on the capability of variable pressure inlets at the entrance of the lens system for producing beams of selected size ranges. By changing the nozzle source pressure, their design obviates the need for sizing the components in order to aerodynamically focus a special range of particles. Fernandez de la Mora[47] used aerodynamic lenses in a variable-pressure impactor to improve the resolution of an aerosol size spectrometer. Recently, McMurry and co-workers have proposed an aerodynamic lens system to focus nanoparticles smaller than 30 nm[48].

References

1. Wegner, K., Piseri, P., Tafreshi, H. V. & Milani, P. Cluster beam deposition: a tool for nanoscale science and technology. *J. Phys. Appl. Phys.* **39,** R439–R459 (2006).
2. Friedlander, S. K. *Smoke, dust, and haze: fundamentals of aerosol dynamics*. (Oxford University Press, 2000).
3. Hagena, O. F. & Obert, W. Cluster Formation in Expanding Supersonic Jets: Effect of Pressure, Temperature, Nozzle Size, and Test Gas. *J. Chem. Phys.* **56,** 1793–1802 (1972).
4. Siegel, R. W. Cluster-Assembled Nanophase Materials. *Annu. Rev. Mater. Sci.* **21,** 559–578 (1991).
5. Girshick, S. L. *et al.* Thermal plasma synthesis of ultrafine iron particles. *J. Aerosol Sci.* **24,** 367–382 (1993).
6. Pratsinis, S. E. Flame aerosol synthesis of ceramic powders. *Prog. Energy Combust. Sci.* **24,** 197–219 (1998).
7. Granqvist, C. G. & Buhrman, R. A. Ultrafine metal particles. *J. Appl. Phys.* **47,** 2200–2219 (1976).
8. Milani, P. & Iannotta, S. *Cluster Beam Synthesis of Nanostructured Materials*. (Springer Berlin Heidelberg, 1999). at <http://dx.doi.org/10.1007/978-3-642-59899-9>
9. *Atomic and molecular beam methods*. (Oxford University Press, 1988).
10. Mazza, T. *et al.* Libraries of cluster-assembled titania films for chemical sensing. *Appl. Phys. Lett.* **87,** 103108 (2005).
11. Ross, K. J. & Sonntag, B. High temperature metal atom beam sources. *Rev. Sci. Instrum.* **66,** 4409–4433 (1995).
12. Sattler, K., Mühlbach, J. & Recknagel, E. Generation of Metal Clusters Containing from 2 to 500 Atoms. *Phys. Rev. Lett.* **45,** 821–824 (1980).
13. Raĭzer, I. P. *Gas discharge physics*. (Springer, 1997).
14. Wiley: Principles of Plasma Discharges and Materials Processing, 2nd Edition - Michael A. Lieberman, Alan J. Lichtenberg.
15. Haberland, H., Karrais, M., Mall, M. & Thurner, Y. Thin films from energetic cluster impact: A feasibility study. *J. Vac. Sci. Technol. A* **10,** 3266–3271 (1992).
16. Sumiyama, K., Hihara, T., Liang Peng, D. & Katoh, R. Structure and magnetic properties of Co/CoO and Co/Si core–shell cluster assemblies prepared via gas-phase. *Sci. Technol. Adv. Mater.* **6,** 18–26 (2005).
17. Maruyama, S., Anderson, L. R. & Smalley, R. E. Direct injection supersonic cluster beam source for FT-ICR studies of clusters. *Rev. Sci. Instrum.* **61,** 3686–3693 (1990).

18. Milani, P. & deHeer, W. A. Improved pulsed laser vaporization source for production of intense beams of neutral and ionized clusters. *Rev. Sci. Instrum.* **61,** 1835–1838 (1990).
19. Dietz, T. G., Duncan, M. A., Powers, D. E. & Smalley, R. E. Laser production of supersonic metal cluster beams. *J. Chem. Phys.* **74,** 6511–6512 (1981).
20. Woenckhaus, J. & Becker, J. A. A fast pressure monitor for pulsed laser vaporization cluster sources. *Rev. Sci. Instrum.* **65,** 2019–2022 (1994).
21. Bansmann, J. *et al.* Magnetic and structural properties of isolated and assembled clusters. *Surf. Sci. Rep.* **56,** 189–275 (2005).
22. Kantrowitz, A. & Grey, J. A High Intensity Source for the Molecular Beam. Part I. Theoretical. *Rev. Sci. Instrum.* **22,** 328–332 (1951).
23. Kistiakowsky, G. B. & Slichter, W. P. A High Intensity Source for the Molecular Beam. Part II. Experimental. *Rev. Sci. Instrum.* **22,** 333–337 (1951).
24. Barborini, E., Piseri, P. & Milani, P. A pulsed microplasma source of high intensity supersonic carbon cluster beams. *J. Phys. Appl. Phys.* **32,** L105 (1999).
25. Vahedi Tafreshi *et al.* Aerodynamic focusing of clusters into a high intensity and low divergence supersonic beam. *Eur. Phys. J. - Appl. Phys.* **16,** 8 (2001).
26. Dirac, P. A. M. *Oxford Report*. 694 (UKAEA, 1946).
27. Becker, E. W. & Bier, K. Die Erzeugung eines intensiven, teilweise monochromatisierten Wasserstoff-Molekularstrahles mit einer Laval-Düse. *Zeitschrift für Naturforschung A* **9a,** 975–86 (1954).
28. Ude, S. & de la Mora, J. F. Hypersonic impaction with molecular mass standards. *J. Aerosol Sci.* **34,** 1245–1266 (2003).
29. Reis, V. H. & Fenn, J. B. Separation of Gas Mixtures in Supersonic Jets. *J. Chem. Phys.* **39,** 3240–3250 (1963).
30. Murphy, W. K. & Sears, G. W. Production of Particulate Beams. *J. Appl. Phys.* **35,** 1986–1987 (1964).
31. Israel, G. W. & Friedlander, S. K. High-speed beams of small particles. *J. Colloid Interface Sci.* **24,** 330–337 (1967).
32. Dahneke, B. & Flachsbart, H. An aerosol beam spectrometer. *J. Aerosol Sci.* **3,** 345–349 (1972).
33. Liu, P., Ziemann, P. J., Kittelson, D. B. & McMurry, P. H. Generating Particle Beams of Controlled Dimensions and Divergence: I. Theory of Particle Motion in Aerodynamic Lenses and Nozzle Expansions. *Aerosol Sci. Technol.* **22,** 293–313 (1995).
34. Liu, P., Ziemann, P. J., Kittelson, D. B. & McMurry, P. H. Generating Particle Beams of Controlled Dimensions and Divergence: II. Experimental Evaluation of Particle Motion in Aerodynamic Lenses and Nozzle Expansions. *Aerosol Sci. Technol.* **22,** 314–324 (1995).
35. De La Mora, J. F. & Riesco-Chueca, P. Aerodynamic focusing of particles in a carrier gas. *J. Fluid Mech.* **195,** 1–21 (1988).

36. Mora, J. F. de la & Rosell-Llompart, J. Aerodynamic focusing of heavy molecules in seeded supersonic jets. *J. Chem. Phys.* **91,** 2603–2615 (1989).
37. Fuerstenau, S., Gomez, A. & Fernández de la Mora, J. Visualization of aerodynamically focused subsonic aerosol jets. *J. Aerosol Sci.* **25,** 165–173 (1994).
38. Mallina, R. V., Wexler, A. S. & Johnston, M. V. High-Speed Particle Beam Generation: Simple Focusing Mechanisms. *J. Aerosol Sci.* **30,** 719–738 (1999).
39. Goo, J. Numerical simulation of aerosol concentration at atmospheric pressure by a cascade of aerodynamic slit lenses. *J. Aerosol Sci.* **33,** 1493–1507 (2002).
40. Lee, J.-W., Yi, M.-Y. & Lee, S.-M. Inertial focusing of particles with an aerodynamic lens in the atmospheric pressure range. *J. Aerosol Sci.* **34,** 211–224 (2003).
41. Zhang, X. *et al.* A Numerical Characterization of Particle Beam Collimation by an Aerodynamic Lens-Nozzle System: Part I. An Individual Lens or Nozzle. *Aerosol Sci. Technol.* **36,** 617–631 (2002).
42. Piseri, P., Podestà, A., Barborini, E. & Milani, P. Production and characterization of highly intense and collimated cluster beams by inertial focusing in supersonic expansions. *Rev. Sci. Instrum.* **72,** 2261 (2001).
43. Tafreshi, H. V. *et al.* A Simple Nozzle Configuration for the Production of Low Divergence Supersonic Cluster Beam by Aerodynamic Focusing. *Aerosol Sci. Technol.* **36,** 593–606 (2002).
44. Tafreshi, H. V., Piseri, P., Barborini, E., Benedek, G. & Milani, P. Simulation on the Effect of Brownian Motion on Nanoparticle Trajectories in a Pulsed Microplasma Cluster Source. *J. Nanoparticle Res.* **4,** 511–524 (2002).
45. Middha, P. & Wexler, A. S. Particle Focusing Characteristics of Sonic Jets. *Aerosol Sci. Technol.* **37,** 907–915 (2003).
46. Mallina, R. V., Wexler, A. S., Rhoads, K. P. & Johnston, M. V. High Speed Particle Beam Generation: A Dynamic Focusing Mechanism for Selecting Ultrafine Particles. *Aerosol Sci. Technol.* **33,** 87–104 (2000).
47. Moraa, J. F. de la. Drastic improvement of the resolution of aerosol size spectrometers via aerodynamic focusing: The case of variable-pressure impactors. *Chem. Eng. Commun.* **151,** 101–124 (1996).
48. Wang, X., Kruis, F. E. & McMurry, P. H. Aerodynamic Focusing of Nanoparticles: I. Guidelines for Designing Aerodynamic Lenses for Nanoparticles. *Aerosol Sci. Technol.* **39,** 611–623 (2005).

2. Thin film growth by cluster assembling

2.1. The atomistic ansatz

2.1.1. Sub-monolayer regime

The growth of thin films usually proceeds through nucleation and different stages such as adsorption, surface diffusion, chemical binding and other atomic processes at surfaces. The purpose of this section is to remind the basic physical mechanisms involved in the nucleation and growth of thin films of materials by atoms or molecules on solid surfaces.

The individual atomic processes responsible for adsorption and crystal growth on surfaces are illustrated in Fig. 1.

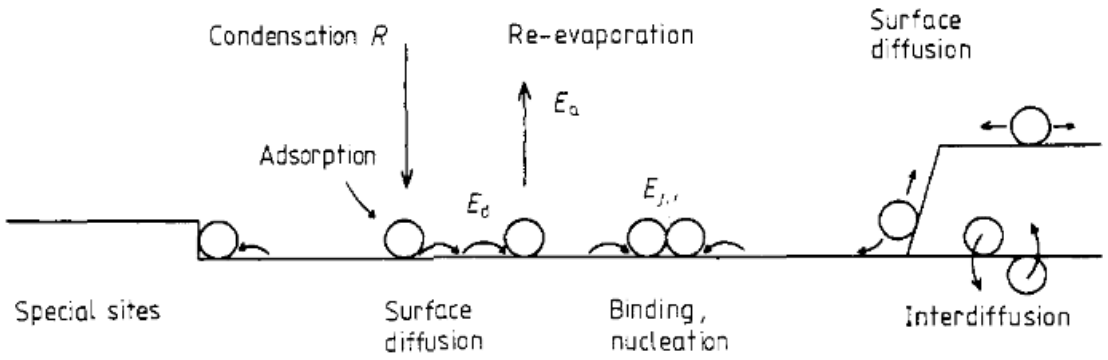

Fig. 1: Schematic diagram of processes and characteristic energies in nucleation and growth on surfaces[1].

For vapour deposition from an ideal gas at pressure *p*, the rate of arrival R at the substrate is given by $p(2\pi mkT)^{-1/2}$ where *m* if the molecular weight, *k* is the Boltzmann's constant and *T* is the source temperature; alternatively, the rate R ($m^{-2}s^{-1}$) may be assured by a molecular beam or evaporation source. This creates single atoms on the substrate (number density $n_1(t)$), on a substrate with N_0 sites per unit area, so that the single-atom concentration is (n_1/N_0). These single atoms may then diffuse over the surface until they are lost by one of several processes. These processes include re-evaporation or re-solution, nucleation of 2D or 3D clusters, capture by existing clusters, possibly dissolution into the substrate, and capture at special (defect) sites such as steps[2]. On an ideally flat, 'inert' substrate, these last two processes would be excluded, though they may often be present in practice. In fact, real surfaces contains a distribution of edges, kinks, dislocations and point

defects, in addition to the perfect terraces. These imperfections can influence the binding of single atoms and small clusters to the substrate and via such binding changes can strongly influence adsorption, diffusion and nucleation behaviour.

In thermodynamicequilibrium all processes proceed in opposite directions at equal rates, as requires by consideration of 'detailed balance'. Thus, for example, in equilibrium adsorption, surface processes such as condensation and re-evaporation, decay and binding of 2D clusters must be in detailed balance. There is no net growth and the system can be described by unchanging macroscopic variables, while microscopically the system is continually changing via these various surface processes. Equilibrium statistical mechanics can be used to describe models of such situations. By contrast, crystal growth is a non-equilibrium kinetic process and the final macroscopic state of the system depends on the route taken through various reactions paths. The state which is obtained is not necessarily the most stable, but it is kinetically determined[1].

2.1.2. Thin film regime

There are three principal modes of crystal growth on surfaces, formed by atoms (or molecules) deposition. I will shortly discuss them in order to individualize the most important parameters determining different growth dynamics in the sub-monolayer regime and beyond it:

- In the island, or Volmer-Weber mode (Fig. 2(a)), small clusters are nucleated directly on the substrate surface and then grow into islands of the condensed phase. This happens when the atoms of the deposit are more strongly bound to each other than to the substrate. This mode is displayed by many systems of metal growing on insulators, including many metals on alkali halides, graphite and other layer compounds such as mica[1].

- In the layer, or Frank-van der Merwe (Fig. 2(b)) mode, the atoms are more strongly bound to the substrate than to each other. The first atoms form a complete monolayer on the surface, which becomes covered with a somewhat less tightly bound second layer. This growth mode is observed in the case of adsorbed gases, such as several rare gases on graphite and on several metals, in some metal-metal systems, and in semiconductor growth on semiconductors[1].

- The layer-plus-island, or Stranski-Krastanov (Fig. 2(c)) growth mode, is an interesting intermediate case. After forming the first monolayer (ML), or a few ML, subsequent layer growth is unfavourable and islands are formed on the top of this intermediate layer. There are many examples of its occurrence on metal-metal, metal-semiconductor, gas-metal and gas-layer compound systems[1].

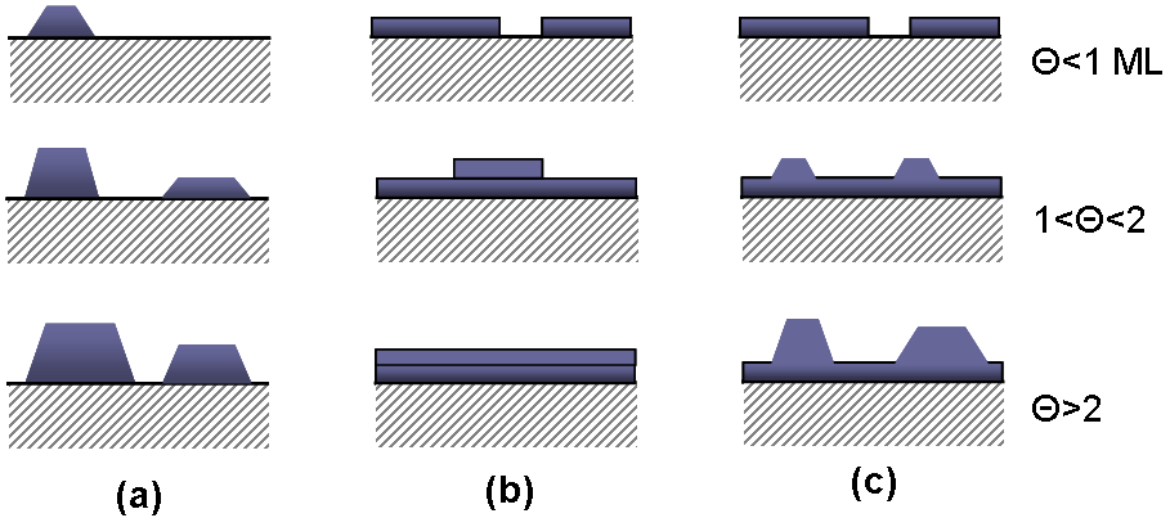

Fig. 2: Schematic representations of the main three different modes of crystal growth on surface: (a) island or Volmer-Weber mode, (b) layer or Frank-van der Merwe mode, (c) layer-plus-layer or Stranski-Krastanov mode.

The simplest energetic interpretation of Frank-Van der Merwe is that the atom attaching to the growth layer edge makes two or more bonds while on connecting the top surface makes only one, and hence reduces the interfacial energy by much more. In a kinetic interpretation the atom attached to the top of the surface will diffuse quickly until it encounters a new layer edge, and, now having two bonds, thereafter will have a much lower probability of moving back to the surface. In Volmer-Weber mode nucleation of islands is favoured over extended growth at layer edges. This can occurs if the new deposited species have a tendency to cluster. The new atoms bond more strongly with one another than to the surface, or diffusive processes slow layer growth until new surface nucleation far exceeds it. The net effect is that layers are filled in as islands are nucleated and merge[3].

2.2. Cluster assembling

It should be noted that for cluster deposition the situation is somewhat simpler than for atomic deposition since many elementary processes are very slow. For example, diffusion of clusters on the top of an already formed island is very low[4,5], cluster detachment from the islands is insignificant, and edge diffusion[6] is not an elementary process at all since the cluster cannot move as an entity over the island edge.

The first ingredient of the growth, *deposition*, is quantified by the flux F (i.e., the number of clusters that are deposited on the surface per unit area and unit time). The flux is usually uniform in time, but in some experimental situations it can be pulsed, (i.e., changed from a constant value to 0 over a given period). Chopping the flux can affect the growth of the film significantly[7], and we will take this into account when needed.

The second ingredient is the *diffusion* of the clusters which have reached the substrate. We assume that the diffusion is Brownian (i.e., the particle undergoes a random walk on the substrate). To quantify the diffusion, one can use both the usual diffusion coefficient D or the diffusion time (i.e. the time needed by a cluster to move by one diameter). These two quantities are connected by $D=d^2/(4\tau)$ where d is the diameter of the cluster. Experiments show that the diffusion coefficient of a cluster can be surprisingly large, comparable to the atomic diffusion coefficients (see Section 3.2.). The diffusion is here supposed to occur on a perfect substrate. Real surfaces always present some defects such as steps, vacancies, or adsorbed chemical impurities. The presence of these defects on the surface could significantly alter the diffusion of the particles and therefore the growth of the film.

A third process which could be present in growth is *re-evaporation* of the clusters from the substrate after a time τ_e. It is useful to define $X_S=\sqrt{D\tau_e}$, the mean diffusion length on the substrate before desorption.

The last simple process I will consider is the *interaction* between the clusters. The simplest case is when aggregation is irreversible and particles simply remain juxtaposed upon contact. This occurs at low temperatures. At higher temperatures, cluster–cluster coalescence will be active. Thermodynamics teaches us that coalescence should always happen but without specifying the kinetics. Since many clusters are deposited on the surface per unit time, kinetics is here crucial to determine the shape of the islands formed on the substrate. A total comprehension of the kinetics is still lacking. We note that the shape of the clusters and the islands on the surface need not be perfectly spherical, even in the case

of total coalescence. Their interaction with the substrate can lead to half spheres or even flatter shapes depending on the contact angle. Contrary to what happens for atomic deposition, a cluster touching an island forms a huge number of atom–atom bonds and will not detach from it. Thus, models including reversible particle–particle aggregation[8-10] are not useful for cluster deposition.

There is a hierarchy of growth phenomena time scales (Fig. 3), and the relevant ones are those lower than $t_{ML} \approx 1/F$, where t_{ML} is the time needed to fill a monolayer and F is the particle flux (ML/s)[11].

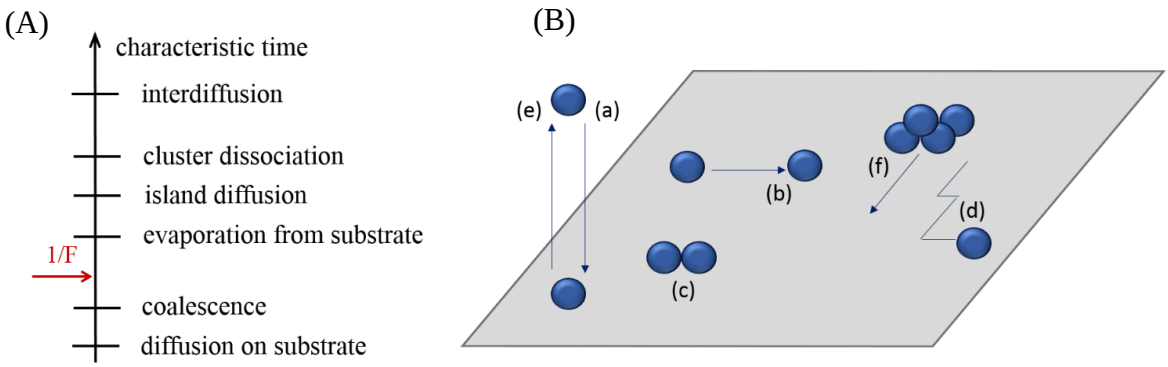

Fig. 3: (A) Time scales of some elementary processes considered for the growth of films by cluster deposition. In this example, of 1/F particular value, models including only cluster diffusion on the substrate and cluster–cluster coalescence are appropriate. (B) Main elementary processes considered for the growth of films by cluster deposition. (a) Adsorption of a cluster by deposition; (b) and (d) diffusion of the isolated clusters on the substrate; (c) formation of an island of two monomers by juxtaposition of two monomers (nucleation); (d) growth of a supported island by incorporation of a diffusing cluster; (e) evaporation of an adsorbed cluster. We also briefly consider the influence of island diffusion (f)[11].

In order to offer theoretical models to describe sub-monolayer stages of cluster assembled film growth, our choice is to extrapolate theoretical studies developed for atomic deposition and consider each cluster as a 'super atom'[5].

One may consider the use of the percolation model[12,13] to describe experiments of surface deposition. However, percolation assumes that particle do not diffuse after being deposited, and it accordingly forbids the aggregation of the diffusing particle. There exist models of diffusing particles that aggregate, as Cluster-Cluster Aggregation (CCA) model[14], but they do not allow the continual injection of new particles via deposition. Both

percolation and CCA model cannot be taken into consideration, because they are in contrast with the phenomenological evidences shown in Section 3.2.

For this reason, we are going to use a model that incorporates the three main physical ingredients of thin film growth: Deposition, Diffusion and Aggregation (DDA), which introduces the possibility of cluster diffusion.

2.2.1. DDA model for atomic deposition

The DDA model[15] is defined by:

1) Deposition of particles at randomly chosen position of the surface with a flux F per lattice site per unit time. It is useful to introduce the normalized flux ϕ defined as the number of particles deposited per unit site per diffusion time τ, where τ is the mean time needed by a monomer to jump by a lattice site;
2) Diffusion of particles and clusters (set of connected particles), with a probability which is assumed to be given by $D_s = D_1 s^{-\gamma}$, where s is the number of particle in the cluster, D_1 is the diffusion coefficient for a monomer (s=1) and the parameter γ characterizes the dependence of D_s on cluster size;
3) Aggregation: when two particles occupy neighboring sites they stick irreversibly.

We call *particles* the isolated atoms (or monomers) that are deposited on the surface, *clusters* any set of connected particles (including the monomers), and *islands* the clusters containing more than one particle. Physically, two competing mechanisms are introduced in the model, each one with its own time scale: deposition and diffusion.

It is possible to identify three characteristic regimes, delimited by two crossover length scale L_1 (related to the characteristic diffusion length of a single particle on the surface) and L_2 (related to the competition between deposition and cluster diffusion)[15]:

I. *Particle diffusion regime* ($L<L_1$). - Only one cluster is present in the system ($\phi=10^{-9}$, $L_1\approx500$ and $L=200$). Since the characteristic diffusion length of a single particle L_1 is larger than the system size L, every deposited particle attaches to the already existing cluster before the next particle is deposited (Fig. 4). At early time, the cluster is small, and virtually all the particles are deposited outside the cluster and reach it by brownian diffusion, so we can expect that cluster should have features in common with DLA model;

(a) 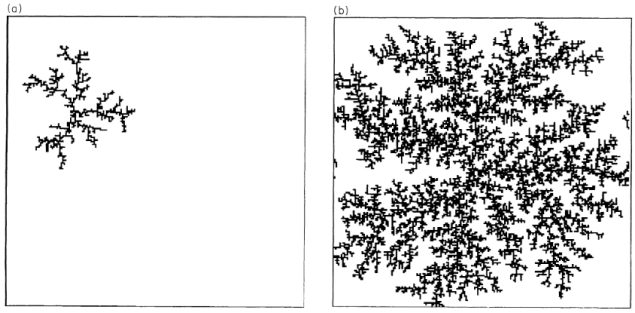 (b)

Fig. 4: System morphologies in regime I, at two stages of growth, with γ=1. (a) total coverage=0.02 (b) spanning point: total coverage=0.27[15].

II. *Cluster diffusion regime* ($L_1<L<L_2$). - Now several clusters are present in the system ($\phi=10^{-6}$, $L_1\approx90$, $L_2\approx10^4$ and L=300). The diffusion length is now smaller than the system size, so that several clusters nucleate on the surface (Fig. 5);

(c) 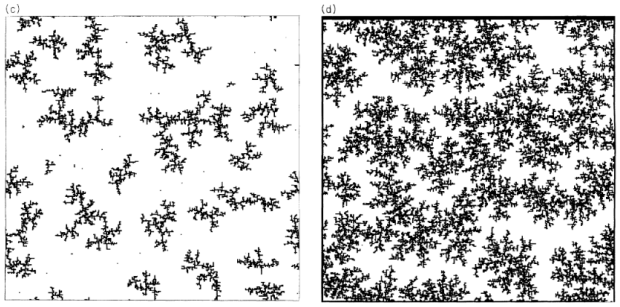 (d)

Fig. 5: System morphologies in regime II, at two stages of growth, with γ=1. (c) total coverage=0.1 (d) spanning point: total coverage=0.31[15].

III. *Percolation regime* ($L>L_2$). - At early time, many clusters are present in the system ($\phi=10^{-3}$, $L_1\approx17$, $L_2\approx36$ and L=300), and, as the system is bigger, their number is higher than in Regime II. As the time increases, larger clusters are formed both by the connection of clusters that diffuse and by the addition of single deposited particles (Fig. 6). At the spanning time, the system resembles a percolation network.

(e) 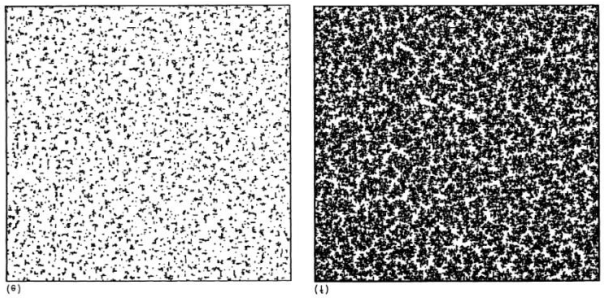 (f)

Fig. 6: System morphologies in regime III, at two stages of growth, with γ=1. (e) total coverage=0.1 (f) spanning point: total coverage=0.49[15].

The introduction of cluster diffusion leads to an exponential increase in the mean cluster size as a function of time, whereas in the other growth models this dependence is a power law[15]. In order to keep the DDA model as close as possible to experiments and as general as possible, it is included a tunable parameter γ that characterizes the dependence of a cluster diffusivity on its size. For a non-epitaxial system also large cluster can move on the substrate[16-18]. In a system where large cluster do diffuse, the diffusion is not rigid: clusters may change their internal structure to be able to move. At low temperature edge diffusion[6] is probably not relevant, due to the higher activation energy for the edge diffusion in comparison to the simple surface diffusion. The last assumption of this model is about the second layer: when a particle falls on a top of another particle it is assumed that the particle deposited on the second layer has no effect on the system. There's a barrier at the edge of the first layer clusters, which prevents single particles from falling on the substrate. Because of the existence of this "Schwoebel barrier"[19], particle diffusion on the second layer is much smaller than diffusion on the substrate. An important consideration is that it is not taken into account island coalescence[5,20].

2.2.2. Cluster-cluster interactions: juxtaposition and coalescence

Compared to the atomic case, a fundamental difference, due to the inner structure of the clusters, appears in preformed cluster deposition: two clusters can merge to form a larger cluster. In particular, DDA model only allows, for two touching clusters, to remain juxtaposed as two separated entities. There exist another possibility of interaction, and it is the possibility to merge into a new single one larger cluster. The choice between the two types of interactions depends on the substrate and deposited materials, substrate temperature, defects or contamination and incident cluster size[21,22,4,5].

The physical reason behind the merging of two clusters is the minimization of the free energy of the system, in particular the minimization of the surface energy. There is a competition between interfacial energy minimization and intrinsic stress energy, which tends to preserve the initial cluster morphology. Stress energy dominates in the case of large clusters, which thus undergo smaller deformations[23].

The motor of the coalescence is the diffusion of atoms on the cluster surface from the region of high curvature (where they have less neighbors and therefore are less bound) toward the regions of lower curvature. The equation for atom flux is[24]:

$$\vec{J_s} = - \frac{D_S \gamma \Omega \nu}{K_B T} \overrightarrow{\nabla_S K} \quad (1)$$

where D_s is the surface diffusion constant (supposed to be isotropic), γ is the surface energy (supposed to be isotropic too), Ω is the atomic volume, ν is the number of atoms per unit surface area, K_B is the Boltzmann's constant, T is the temperature, and K is the surface curvature ($K = 1/R_1 + 1/R_2$) where R_1 and R_2 are the principal radii of curvature.

Clusters size is a crucial parameter for coalescence, since there exists an energy barrier for coalescence proportional to the interface area between the clusters[25]. It is possible to introduce an arbitrary critical size N_c defined as follows: if both clusters are larger than N_c no merging is assumed; if at least one of the clusters is smaller than N_c then they merge into a single one. In fact, the ratio between the size of the incident cluster N_i and the cluster pre-deposited N_c ($\eta = N_i / N_c$) is an important parameter. If $\eta \ll 1$, the growth of the film is comparable to the three-dimensional (3D) growth of a classical atomic film. In the case of $\eta \approx 1$ the fusion of the cluster can be neglected and the film growth can be described using the two-dimensional (2D) mathematical formalism[25].

The process of island growth can also be studied as governed by characteristic times: the arrival time Δt, defined as the interval time between successive arrivals of clusters to an island, and a coalescence time τ(R,n) for a n-atom cluster of radius $r=r_0 n^{1/3}$ to entirely coalesce with a spherical island of radius R[26]. When Δt is longer than τ, the island reaches a compact spheroid shape before another cluster arrives. In the opposite case, the island does not have time to reach a compact shape before the arrival of the next cluster and evolves towards a non-compact or ramified shape. The reason is that now the atoms on the formerly outer surface of the first cluster do not feel curvature since they have neighbors on the second cluster. The mobile atoms are now those of the second cluster and the coalescence takes a longer time to proceed[11]. As time is going the number *p* of clusters forming an *np*-atom island increases linearly with time, and the island size increases as $R = r_0 (np)^{1/3}$. For given deposition conditions the arrival time is almost constant with R, at least for a certain range of R, whereas the coalescence time increases with R. For two spheres with different radius we can write τ(R,r) proportional to R^{α} [27]. From the relative variation of τ/Δt as a function of R, there's exist a critical island radius R_c and consequently a critical number p_c of clusters for which the cross-over occurs when τ=Δt. Compact islands are obtained for p smaller than p_c. Fig. 7 shows the competition between compact and ramified shape relaxation resulting from preformed cluster deposited on surface.

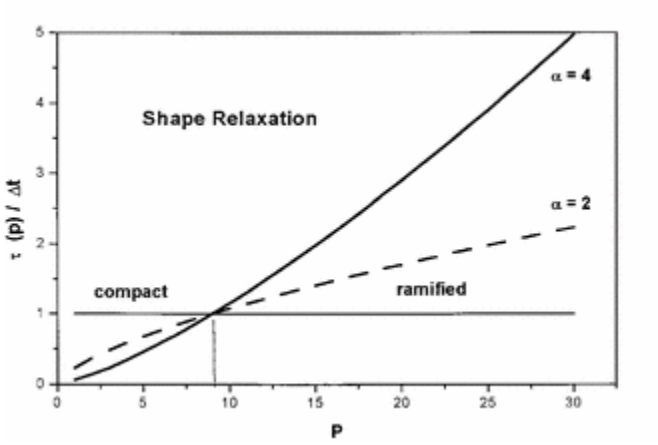

Fig. 7: Variation of the ratio between coalescence τ and diffusion Δt time versus the number p of clusters involved in island formation. The cross-over which occurs for $\tau/\Delta t=1$ separates the island morphologies into two different regimes: the compact island shapes for $\tau/\Delta t<1$ and the ramified shapes for $\tau/\Delta t>1$ [26].

Furthermore, the coalescence time between an incident cluster and a growing island depends on both island and incident cluster size. It increases as cluster size increases. Assuming that the arrival time Δt(n) of a n-atom cluster on substrate varies less rapidly than the coalescence time, the critical island radius $R_c(n)$ for the cross-over transition between compact and ramified shape increases as n decreases, as reported in Fig. 8 [21].

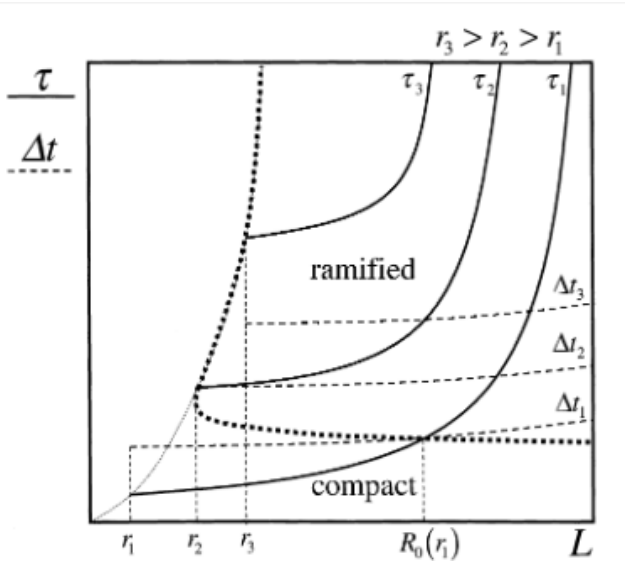

Fig. 8: Evolution of the critical size R_0 with the incident cluster size r. For small incident cluster ($r=r_1$), Δt is longer than τ in the beginning of islands growth and critical island size R_0 exists for a size larger than r_1. R_0 than decreases until $r=r_2$, where $\Delta t=\tau$ at $R=r_2$. When $r>r_2$, Δt is always smaller

than τ, R_0 is equal to r and increases with r. The thick dotted curve mimics the evolution of the branch width with respect to the incident cluster size[21].

2.3. Scaling laws

The dynamic scaling approach is an effective tool for understanding the temporal evolution of fluctuating interfaces. There is no a systematic formalism for treating non-equilibrium processes. This implies that standard approaches of statistical mechanics are not suitable for describing the interface growth problem. The realization that stochastically growing surfaces exhibit non-trivial scaling behavior and naturally evolves to a steady state, having no characteristic time or spatial scale, has led to the development of a general scaling approach for describing growing interfaces[28]. This formalism, which is based on the general concepts of scale-invariance and fractals, has become a standard tool in the study of growing surfaces. In particular the dynamic scaling approach has been applied to the study of a variety of theoretical models of growing interfaces[29,30]. To describe the growth qualitatively, we introduce shortly some definitions. The mean height of the surface, $\bar{h}$, is defined by:

$$\bar{h} \equiv \frac{1}{L}\sum_{I=1}^{L} h(i,t) \qquad (2)$$

where h(i, t) is the height of column i at time t and L is the system size. If the deposition rate (number of particles arriving on a site) is constant, the mean height increases linearly with time.

The interface width, which characterizes the roughness of the interface, is defined by the rms fluctuation in the height:

$$w\,(L, t) \equiv \sqrt{\frac{1}{L}\sum_{i=1}^{L}[h(i,t) - \bar{h}(t)]^2} \qquad (3)$$

A typical plot of the time evolution of the surface width has two regions separated by a crossover time t_x. Initially, the width increases as a power of time:

$$w\,(L, t) \sim t^{\beta} \qquad [t<<t_x] \qquad (4)$$

where the exponent β is the *growth exponent* and it characterizes the time-dependent dynamics of the roughening process. The power-law increase is followed by a saturation regime, during which the width reaches a saturation value, w_{sat}. As L increases, the saturation width increases as well, and the dependence also follows a power law:

$$w_{sat}\,(L) \sim L^{\alpha} \qquad [t>>t_x] \qquad (5)$$

where the exponent α is the *roughness exponent* and it characterizes the roughness of the saturated interface. The crossover time t_x at which the interface crosses over from the behavior of Eq. (4) to that of Eq. (5) depends on the system size,

$$t_x \sim L^z \tag{6}$$

where *z* is called the *dynamic exponent*.

The scaling exponents α, β, and z are not independent but they are related by the relation:

$$z = \frac{\alpha}{\beta} \tag{7}$$

There exists a simple scaling law (Family-Vicsek scaling law) into which the previous equations collapse:

$$w(L, t) \sim L^{\alpha} f\left(\frac{t}{L^z}\right) \tag{8}$$

where f(x) is called scaling function and is defined by:

$$f(x) = \begin{cases} x^{\alpha} & x \ll 1 \\ const & x \gg 1 \end{cases} \tag{9}$$

The extent of the correlations parallel to the surface can be measured by the length $\xi_{\parallel}$, which is the distance over which surface fluctuations spread during time t [29]. According to the dynamic scaling form (8), the correlation length $\xi_{\parallel}$ must vary as:

$$\xi_{\parallel} \sim t^{\beta/\alpha} = t^{1/z} \qquad [t << t_x] \tag{10}$$

$$\xi_{\parallel} \sim L \qquad [t >> t_x] \tag{11}$$

Application of dynamic scaling to a number of surface growth models can be now discussed.

Because of the close relationship between the scaling exponents and the fundamental mechanisms leading to scale invariance, universality classes can be defined[30,31,32,33].

2.3.1. Random deposition

Random Deposition (RD) is a very simple growth model and can be described by a sketch reported in Fig. 9.

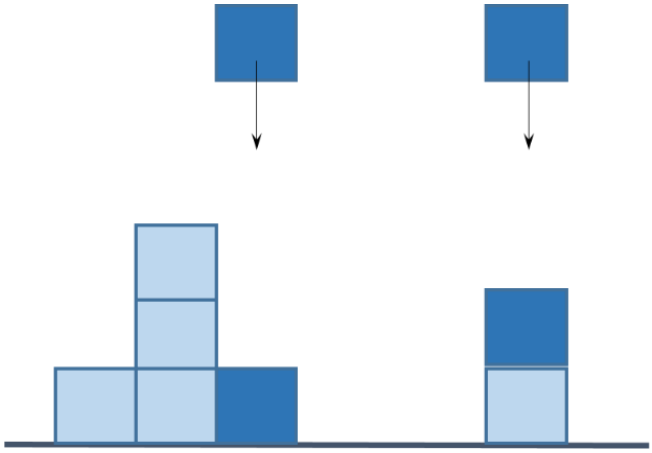

Fig. 9: Schematic representation of Random Deposition model.

From a random site over the surface, a particle falls vertically until it reaches the top of the column under it, whereupon it is deposited. Random deposition interface is uncorrelated. In fact, the columns grow independently as there is no mechanism that can generate correlations along the interface. For d=2, the growth exponent β is ½, while α is not defined (or $\alpha=\infty$), because the interface does not saturate and grows indefinitely with time[29,30].

2.3.2. Random deposition with surface relaxation

To include relaxation in RD model, it is allowed the deposited particles to diffuse along the surface up to a finite distance, stopping when it finds the position with the lowest height (Fig. 10).

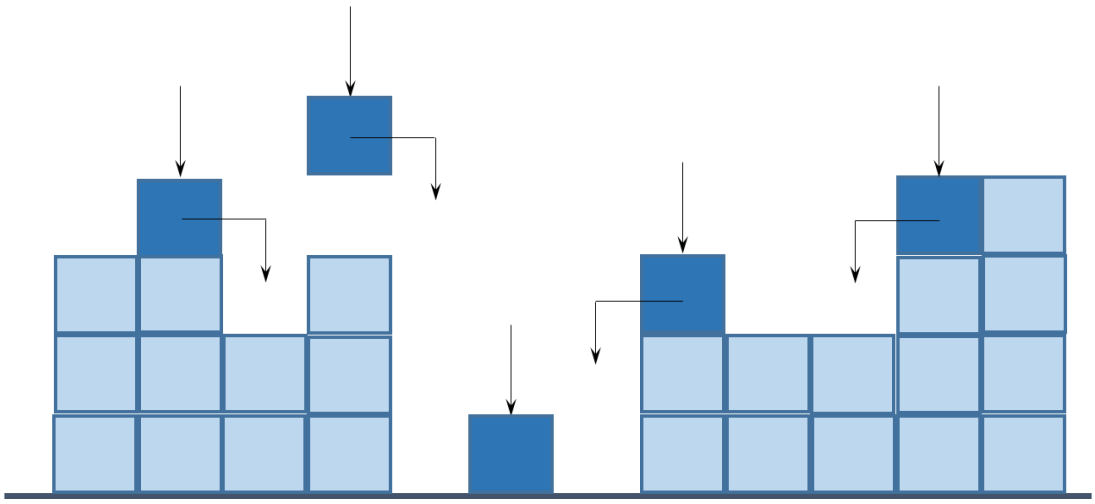

Fig. 10: Schematic representation of Random Deposition model with surface relaxation.

As a result of the relaxation process, the final interface will be smooth, compared to that without relaxation. Thus the newly-arriving particle compares the heights of nearby

columns before 'deciding' where to stick. This process generates correlations among the neighboring heights, which lead to the entire interface being correlated. Simulation in one dimension result in the scaling exponents β=0.24 ± 0.01 and α=0.48 ± 0.02 [34]. Otherwise, the scaling exponent of the Edwards-Wilkinson equation[30] are:

$$\alpha = \frac{2-d}{2}, \qquad \beta = \frac{2-d}{4}, \qquad z = 2 \qquad (12)$$

We note that the scaling exponent in Eqs. (12) for d=1, give β=1/4 and α=1/2, very close to the results that have been found to describe the random deposition model with surface relaxation. This similarity lead us to conclude that the model and the EW equation belong to the same universality class.

2.3.3. Ballistic deposition

In this growth model a particle is released from a randomly chosen position above the surface, located at a distance larger than the maximum height of the interface. The particle follows a straight vertical trajectory until it reaches the surface, whereupon it sticks. In the simplest version of the model, particles are deposited onto a surface oriented perpendicular to the particle trajectories. In Fig. 11 (a) it is reported a scheme of the nearest-neighbor (NN) model, where falling particles stick to the first nearest neighbour on the aggregate. If it is allowed particles to stick to a diagonal neighbour as well, we have the next-nearest neighbour (NNN) model (Fig. 11 (b))[30].

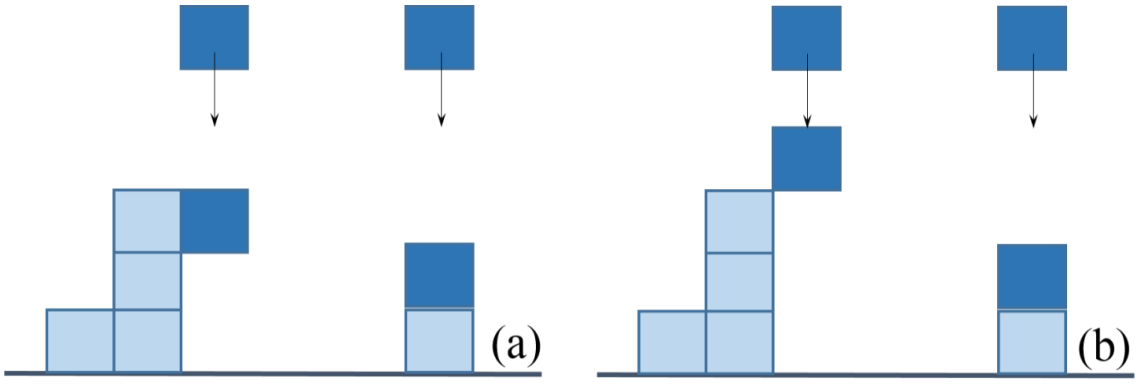

Fig. 11: Schematic representation of Ballistic Deposition model, (a) in nearest neighbor (NN) and (b) next- nearest neighbor (NNN) approximations.

The scaling properties for both the models are described by the non-linear theory. These two models belong to the same universality class (Kardar-Parisi-Zhang[35]), since they share

the same set of scaling exponent, α, β, and z. Their non-universal parameters however are different. In 2 dimensions the growth and the roughness exponents spans from 0.3 to 0.33 (for the NN and NNN models) and from 0.44 to 0.47 respectively[36]. In 2+1 dimensions, the growth exponent β value spans from 0.21 to 0.24[36-38,] while the roughness exponent α from 0.3 to 0.35. In contrast to random deposition and random deposition with surface diffusion, which lead to completely compact structures, there are vacancies and holes in the bulk of the ballistic deposition. Furthermore, in BD the fact that particles are able to sticking to the edge of the neighboring columns leads to lateral growth, allowing the spread of correlations along the surface.

2.3.3.1. Tanget rule

A peculiar characteristic of ballistic deposition is the columnar microstructure of the film. In fact, the existence of a region on each deposited particle where sticking is prevented causes the development of oriented voids, perpendicular to the incident direction. This morphology is observed in both two-dimensional and 3D computer simulations[39] and experiments[40]. It becomes more distinctive when particles are added via ballistic deposition trajectories from the same direction with a large angle of incidence (α). As the angle of incidence increases, the interaction of the self-shadowing effect[41] with the collision dynamics gives rise to rather densely packed columnar structures that grow apart as the angle of incidence is further increased[42]. By experiments and computer simulations it is found that the angle (β) between the growth direction of the columns and the normal to the surface is smaller than the incident angle. From measurements of Nieuwenheuzen and Hannstra[43] it has been found that the angle of growth β is empirically related to the angle of incidence α by the 'tangent rule'[36,44]:

$$\tan(\beta) = \frac{1}{2}\tan(\alpha) \qquad (13)$$

In Fig. 12 representative morphologies of BD with different incident angle are shown.

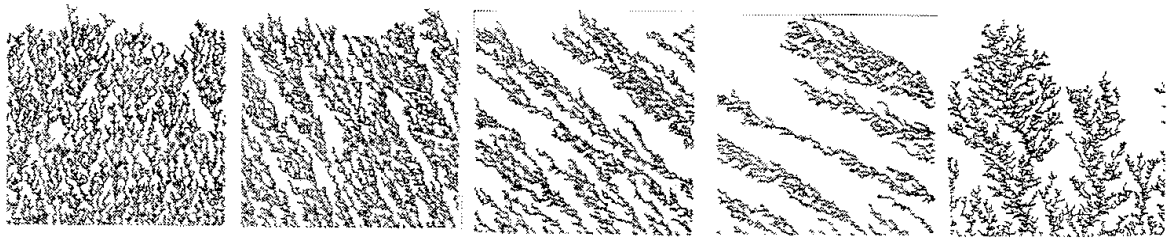

α=0° α=45° α=70° α=80° α=Ran(0,90°)

Fig. 12: Representative deposit morphologies generated at low impact velocity with various angle of incidence[42].

It is of interest to consider a quantitative measurement of the deposit surface morphology, such as the deposit surface roughness. Representative results for the evolution of the surface roughness of frozen deposits are shown in Fig. 13 for various angles of incidence[42].

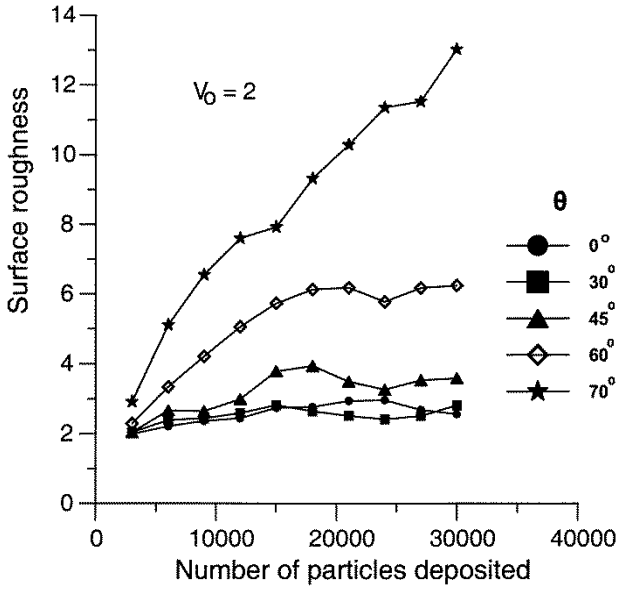

Fig. 13: Angular dependence of deposit roughness evolution for low impact velocity[42].

Increasing α beyond 45° causes a significant increase of the deposit roughness due to the emergence of the previously mentioned columnar structures.

2.3.3.2. Sticking probability

Once an incident particle reaches the collecting surface its fate is determined by its specific interaction upon collision with the collector and/or with other pre-deposited particles. In case of perfect capture, the particle arrival rate also determines the final deposition rate. The possibility of post-collisional motion of the particle and therefor the possibility of re-entrainment causes the actual deposition rate to be less than the particle arrival rate, a fact that has been traditionally described through the use of an empirically determined "sticking probability". A computational simulation work[42], based on dynamical models, suggests that after an initial stage of growth (which depends on the impact velocity) the deposit morphology forgets the influence of the substrate and the particle sticking fraction reaches a stationary state (Fig. 14(a)).

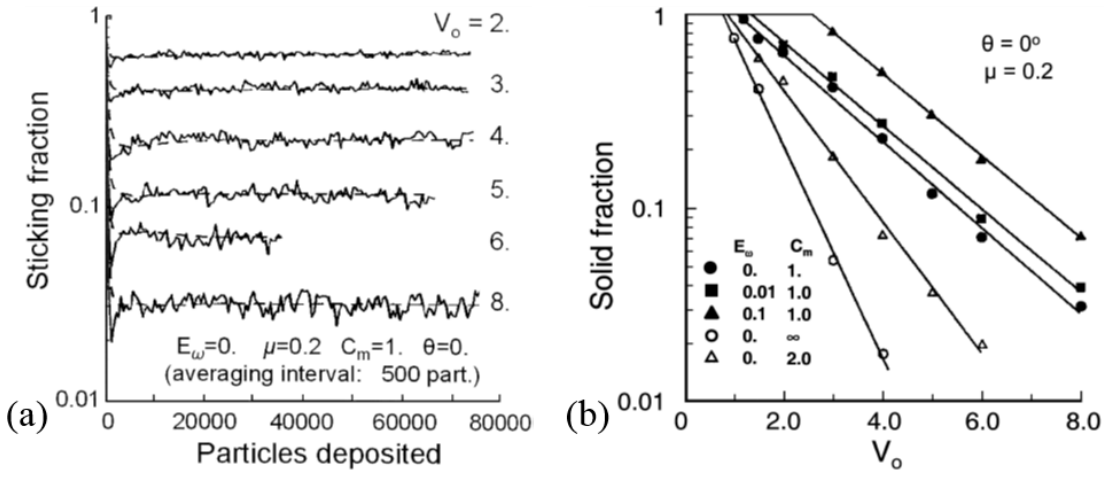

Fig. 14: (a) Sticking fraction evolution for different impact velocities at normal incidence. (b) Stationary sticking fraction as a function of impact velocity and model parameters[42].

The dependence of this steady-state sticking coefficient on impact velocity is shown in Fig. 14 (b) for various values of E_w (dimensionless number that expresses the rotational energy barrier in terms of the normal adhesion barrier) and C_w (deposit rigidity parameter). The results of these numerical experiments indicate the existence of a critical velocity V_{cr} below which all particles stick and above which sticking coefficients decay exponentially. This critical velocity is not the usual critical velocity[45,46] for particle sticking on a flat surface. Like the latter, it is a material parameter depending on particle size, mechanical moduli and surface energies of incident particle and target particle, as well as on the microstructural and rigidity characteristics of the growing deposit. Varying the angle of incidence in the range 0°-70° was found to produce only a slight decrease in sticking fraction.

2.3.4. Slippery Ballistic Deposition

In the regular ballistic deposition model the sticking probability p_s, which can be defined as probability under which the interception/sticking occurs, is considered to be unity. It is possible to generalize the rules for random deposition, by varying the sticking probability to be less than unity[47-49]. When p_s equals to 0, a fully random deposition occurs, as shown in Fig. 15.

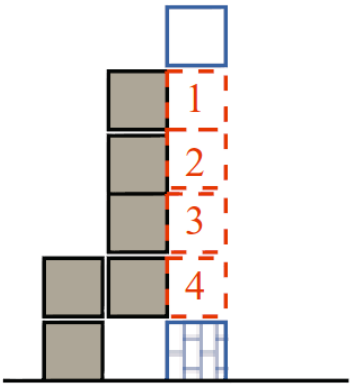

Fig. 15: Rendition of the slippery ballistic model. The approaching particle (empty blue square) missed the opportunity to stick at sites 1, 2, 3, and 4 and finally lands at an unoccupied position (hashed blue square)[47].

In Fig. 16 it is also possible to appreciate the growth pattern from a single seed as a function of different sticking probability p_s for a single simulation.

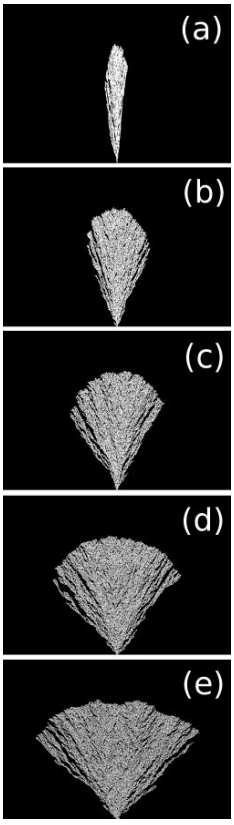

Fig. 16: 1D ballistic growth from a single seed for various sticking probabilities: (a) p_s = 0.01, (b) p_s = 0.1, (c) p_s = 0.25, (d) p_s = 0.5, (e) p_s = 1 [47].

The corresponding scaling parameters are reported in table I [48,49]:

Model	α	β	z	Ref.
Random	---	1/2	---	[30]
KPZ	1/2	1/3	3/2	[35]
Ballistic	0.42	0.3		[28]
Ballistic	0.46 ± 10^{-3}	0.28 ± 10^{-4}	1.65 ± 10^{-3}	[48]
p_s= 0%	0.49 ± 10^{-2}	0.29 ± 10^{-3}	1.69 ± 10^{-2}	[48]
p_s= 30%	0.47 ± 10^{-2}	0.28 ± 10^{-3}	1.69 ± 10^{-2}	[48]
p_s= 60%	0.48 ± 10^{-2}	0.29 ± 10^{-3}	1.66 ± 10^{-2}	[48]

Table I: Scaling parameters α, β and z for different models in d=2.

The simulated result of surface roughness for ballistic deposition at different interface width shows a variation of the slope of roughening[48]. In fact, interface starts with uncorrelated growth (1/2 slope) and later turns to correlated growth (ca. 0.3 slope). Anyway in the competition between random deposition and ballistic deposition processes, BD is the dominant, even at very small values of sticking probability[48].

2.4. Film porosity

Film porosity, defined as the ratio of empty to total volume, is a key morphological parameter for many different applications. In fact, high porous film are desirable because the film porosity governs mass transfer rates in catalytic devices[50], electron diffusion pathway in dye-sensitize solar cells[51] and performance of gas sensor films[52]. The film porosity is related to the particle dynamical behaviour near the surface. In general, deposits formed by particles arriving to an initially flat wall become structured in three level: a denser near-wall (NW) region, a uniform region with constant mean density, and an open and lighter active-growth (AG) region[53,49]. The NW region comes from the early deposition stages of the particle attaching on the initial clean surface which is not shadowed by any formed deposit structure, rendering a high-density layer. The uniform region corresponds

to the steady growth of the deposit with constant mean density. The Ag region is the topmost layer of the deposit where particles are still becoming attached. Here, the density is smaller and vanishes with increasing height.

2.4.1 Evolution with Pe number

Concerning the growth models we have explained previously, the diffusion-limited deposition (DLD) model is valid for particles moving in a stochastic manner due to thermal fluctuations, BD model applies to particles moving in a deterministic way. However, the particle motion is neither purely stochastic nor completely deterministic. The particle motion can be split into two contributions: a mean velocity V and a Brownian motion with a diffusion coefficient D. The particle convective-diffusion motion is characterized by the relative intensity of the convective (deterministic) contribution to the diffusive (stochastic) part, which is the particle Péclet number Pe= V*a*/D, where *a* stands for the characteristic length[53]. Péclet number tends to 0 for diffusion-limit model, while it tends to ∞ in ballistic deposition limit. In Fig. 17 is reported the simulated normalized density as a function of the Péclet number.

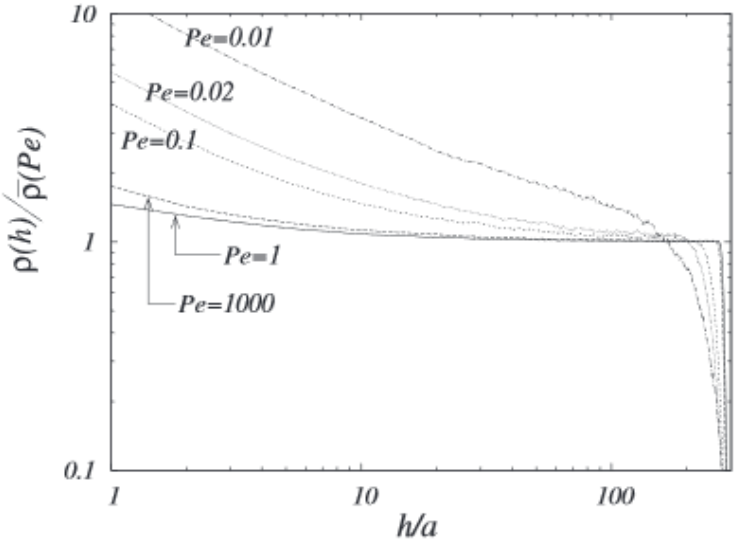

3.

Fig. 17: Log-log density profiles (with hmax= 300a) normalized to the uniform region density ρ̄(Pe) versus the deposit height[53].

For all the Pe values, density is higher in the near-wall region and becomes lower in topmost layer of the film. For the diffusion-limit deposition, the more packed is the NW region, the more porous is the region in the AG region compared to BD regime. Another relevant work[54] highlights the difference in porosity, for the two limiting models, due to the different

cluster shape (spherical or agglomerate), number and size of primary particles and their fractal dimensions.

2.4.2. From RD to BD

The variation in the sticking probability alters the matrix and surface properties formed. Fig. 18 shows that different porous structures are formed when the sticking probability increases from 10 to 60% [48]. It is visually clear that layers are less porous at lower sticking probabilities: the pores grow more in the vertical direction, generating channel type void spaces toward top layers, while at higher sticking probabilities pores grow both in horizontal and lateral direction.

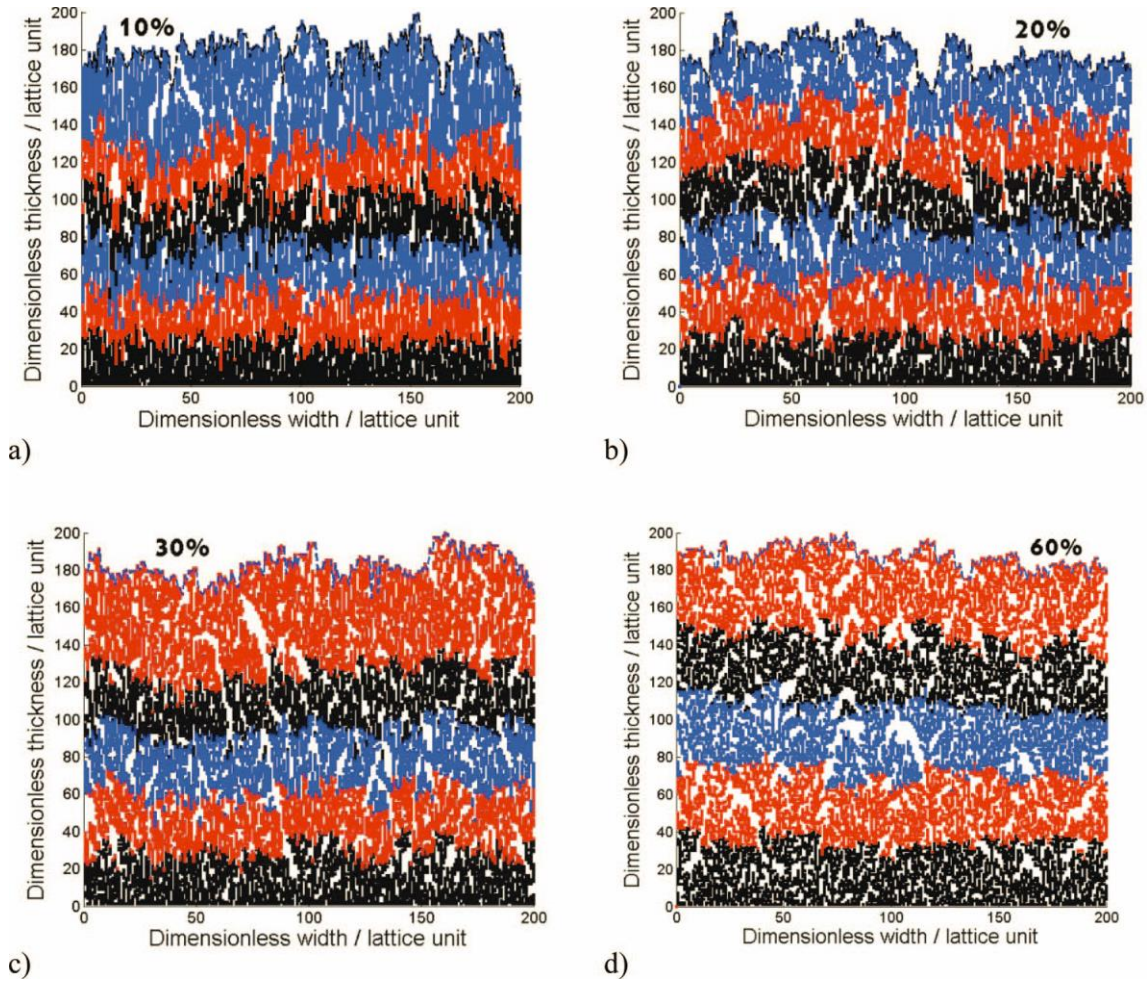

Fig. 18: The effect of sticking probability on the layer structure. a) 10%, b) 20%, c) 30%, d) 60%. The different colors correspond to the deposition of 1000 particles[48].

From low sticking surface to ballistic deposition limit, the density of the particles decreases and saturates after reaching saturation loading (Fig. 19), which is proportional to the film thickness. The most pronounced difference between the growth processes is the saturation particle density, which increases from 46% to 72% of the closely packed layers, when the sticking probability decreases from 100% to 10%.

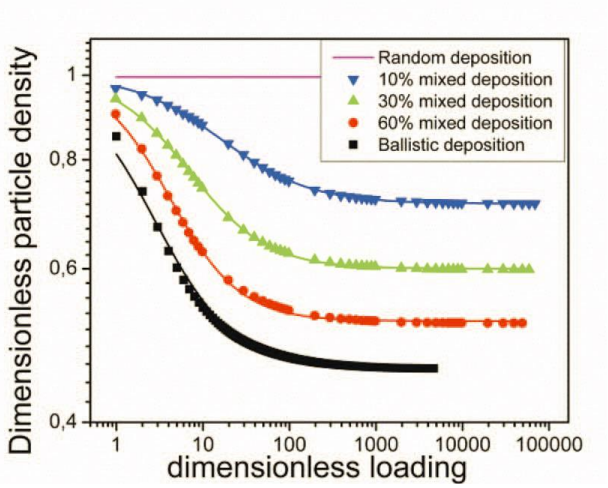

Fig. 19: Comparison of the volumetric particle's density with loading[48].

Average height is in linear relationship with loading[48]. Similar trends with height are also shown in ref [49] for slippery ballistic deposition in the presence of Coulomb type or Van der Waals interactions between particles (Fig. 20).

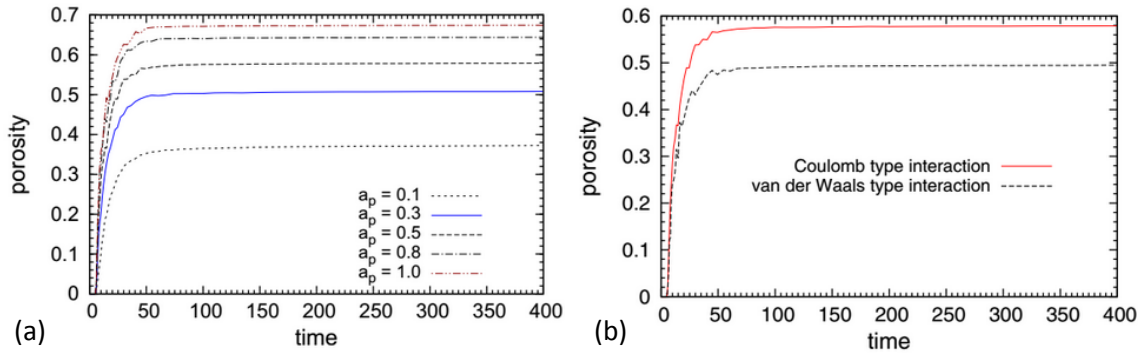

Fig. 20: (a) Growth of porosity at different sticking probability (a_p) for Coulomb-type interactions. (b) Growth of porosity for Coulomb- and van der Waals-type interaction[49].

Increasing the angle of incidence of clusters further increase the porosity of the matrix, as can be visualized by the Fig. 13 presented in the previous Section, from Ref.[42].

References

1. Venables, J. A., Spiller, G. D. T. & Hanbucken, M. Nucleation and growth of thin films. *Rep. Prog. Phys.* **47,** 399 (1984).
2. Zhang, Z. & Lagally, M. G. Atomistic Processes in the Early Stages of Thin-Film Growth. *Science* **276,** 377–383 (1997).
3. Benning, L. G. & Waychunas, G. A. in *Kinetics of Water-Rock Interaction* (eds. Brantley, S. L., Kubicki, J. D. & White, A. F.) 259–333 (Springer New York, 2008). at <http://link.springer.com/chapter/10.1007/978-0-387-73563-4_7>
4. Bardotti, L., Jensen, P., Hoareau, A., Treilleux, M. & Cabaud, B. Experimental Observation of Fast Diffusion of Large Antimony Clusters on Graphite Surfaces. *Phys. Rev. Lett.* **74,** 4694–4697 (1995).
5. Bardotti, L. *et al.* Diffusion and aggregation of large antimony and gold clusters deposited on graphite. *Surf. Sci.* **367,** 276–292 (1996).
6. Jensen, P. Growth of nanostructures by cluster deposition: Experiments and simple models. *Rev. Mod. Phys.* **71,** 1695–1735 (1999).
7. Jensen, P. & Niemeyer, B. The effect of a modulated flux on the growth of thin films. *Surf. Sci.* **384,** L823–L827 (1997).
8. Zhdanov, V. P. & Norton, P. R. Nucleation during molecular beam epitaxy. *Appl. Surf. Sci.* **81,** 109–117 (1994).
9. Bartelt, M. C., Perkins, L. S. & Evans, J. W. Transitions in critical size for metal (100) homoepitaxy. *Surf. Sci.* **344,** L1193–L1199 (1995).
10. Ratsch, C., Šmilauer, P., Zangwill, A. & Vvedensky, D. D. Submonolayer epitaxy without a critical nucleus. *Surf. Sci.* **329,** L599–L604 (1995).
11. *Nanoclusters and nanocrystals*. (American Scientific Publishers, 2003).
12. Melinon, P. *et al.* Comparison of molecular and cluster deposition: Evidence of different percolation processes. *Phys. Rev. B* **44,** 12562–12564 (1991).
13. Stauffer, D. & Aharony, A. *Introduction To Percolation Theory*. (CRC Press, 1994).
14. Meakin, P. Formation of Fractal Clusters and Networks by Irreversible Diffusion-Limited Aggregation. *Phys. Rev. Lett.* **51,** 1119–1122 (1983).
15. Jensen, P., Barabási, A.-L., Larralde, H., Havlin, S. & Stanley, H. E. Deposition, diffusion, and aggregation of atoms on surfaces: A model for nanostructure growth. *Phys. Rev. B* **50,** 15316–15329 (1994).
16. Chapon, C. & Henry, C. R. Mobility effects of submicroscopical particles during the deposition of ultrathin gold films on alkali halide. *Surf. Sci.* **106,** 152–156 (1981).
17. Kashchiev, D. Recent progress in the theory of thin film growth. *Surf. Sci.* **86,** 14–27 (1979).

18. Henry, C. R., Chapon, C. & Mutaftschiev, B. The coalescence of very small gold clusters (of diameter less than 15 Å) on a rock-salt substrate at room temperature. *Thin Solid Films* **46,** 157–165 (1977).
19. Schwoebel, R. L. Step Motion on Crystal Surfaces. II. *J. Appl. Phys.* **40,** 614–618 (1969).
20. Binns, C. Nanoclusters deposited on surfaces. *Surf. Sci. Rep.* **44,** 1–49 (2001).
21. Yoon, B. *et al.* Morphology control of the supported islands grown from soft-landed clusters. *Surf. Sci.* **443,** 76–88 (1999).
22. Fuchs, G. *et al.* Cluster-beam deposition of thin metallic antimony films: Cluster-size and deposition-rate effects. *Phys. Rev. B* **44,** 3926–3933 (1991).
23. Bardotti, L., Prével, B., Treilleux, M., Mélinon, P. & Perez, A. Deposition of preformed gold clusters on HOPG and gold substrates: influence of the substrate on the thin film morphology. *Appl. Surf. Sci.* **164,** 52–59 (2000).
24. Nichols, F. A. & Mullins, W. W. Morphological Changes of a Surface of Revolution due to Capillarity-Induced Surface Diffusion. *J. Appl. Phys.* **36,** 1826–1835 (1965).
25. Melinon, P. *et al.* From free clusters to cluster-assembled materials. *Int. J. Mod. Phys. B* **9,** 339–397 (1995).
26. Bréchignac, C. *et al.* Control of island morphology by dynamic coalescence of soft-landed clusters. *Eur. Phys. J. - At. Mol. Opt. Plasma Phys.* **16,** 265–269 (2001).
27. Rosenfeld, G., Morgenstern, K., Esser, M. & Comsa, G. Dynamics and stability of nanostructures on metal surfaces. *Appl. Phys. A* **69,** 489–496 (1999).
28. Family, F. & Vicsek, T. Scaling of the active zone in the Eden process on percolation networks and the ballistic deposition model. *J. Phys. Math. Gen.* **18,** L75 (1985).
29. Family, F. & Vicsek, T. *Dynamics of Fractal Surfaces*. (World Scientific, 1991).
30. Barabási, A.-L. & Stanley, H. E. *Fractal Concepts in Surface Growth*. (Cambridge University Press, 1995).
31. Vicsek, T. *Fractal growth phenomena*. (World Scientific, 1992).
32. Family, F. & Landau, D. P. *Kinetics of Aggregation and Gelation*. (Elsevier, 2012).
33. Meakin, P. *Fractals, Scaling and Growth Far from Equilibrium*. (Cambridge University Press, 1998).
34. Family, F. Scaling of rough surfaces: effects of surface diffusion. *J. Phys. Math. Gen.* **19,** L441 (1986).
35. Kardar, M., Parisi, G. & Zhang, Y.-C. Dynamic Scaling of Growing Interfaces. *Phys. Rev. Lett.* **56,** 889–892 (1986).
36. Meakin, P., Ramanlal, P., Sander, L. M. & Ball, R. C. Ballistic deposition on surfaces. *Phys. Rev. A* **34,** 5091–5103 (1986).
37. Baiod, R., Kessler, D., Ramanlal, P., Sander, L. & Savit, R. Dynamical scaling of the surface of finite-density ballistic aggregation. *Phys. Rev. A* **38,** 3672–3679 (1988).

38. Family, F. Dynamic scaling and phase transitions in interface growth. *Phys. Stat. Mech. Its Appl.* **168,** 561–580 (1990).
39. Henderson, D. Simulation of structural anisotropy and void formation in amorphous thin films. *Appl. Phys. Lett.* **25,** 641 (1974).
40. Dalla Torre, J. *et al.* Microstructure of thin tantalum films sputtered onto inclined substrates: Experiments and atomistic simulations. *J. Appl. Phys.* **94,** 263 (2003).
41. Dirks, A. G. & Leamy, H. J. Columnar microstructure in vapor-deposited thin films. *Thin Solid Films* **47,** 219–233 (1977).
42. Konstandopoulos, A. G. Deposit growth dynamics: particle sticking and scattering phenomena. *Powder Technol.* **109,** 262–277 (2000).
43. Nieuwenhuizen, J. M. & Haanstra, H. B. Microfractography of thin films. *Philips Tech. Rev.* **27,** 87–91 (1966).
44. Ramanlal, P. & Sander, L. M. Theory of Ballistic Aggregation. *Phys. Rev. Lett.* **54,** 1828–1831 (1985).
45. Thornton, C. & Yin, K. K. Impact of elastic spheres with and without adhesion. *Powder Technol.* **65,** 153–166 (1991).
46. Dahneke, B. The capture of aerosol particles by surfaces. *J. Colloid Interface Sci.* **37,** 342–353 (1971).
47. Robledo, A. *et al.* Morphologies from slippery ballistic deposition model: A bottom-up approach for nanofabrication. *Phys. Rev. E* **83,** 051604 (2011).
48. Kriston, A., Pfrang, A., Popov, B. N. & Boon-Brett, L. Development of a Full Layer Pore-Scale Model for the Simulation of Electro-Active Material Used in Power Sources. *J. Electrochem. Soc.* **161,** E3235–E3247 (2014).
49. Banerjee, K., Shamanna, J. & Ray, S. Surface morphology of a modified ballistic deposition model. *Phys. Rev. E* **90,** 022111 (2014).
50. Thybo, S. *et al.* Flame spray deposition of porous catalysts on surfaces and in microsystems. *J. Catal.* **223,** 271–277 (2004).
51. Grätzel, M. Photoelectrochemical cells. *Nature* **414,** 338–344 (2001).
52. Dimitrov, D. T., Luchinin, V. V., Moshnikov, V. A. & Panov, M. V. Ellipsometry as a rapid method of establishing a correlation between the porosity and the gas sensitivity of tin dioxide layers. *Tech. Phys.* **44,** 468–469 (1999).
53. Rodríguez-Pérez, D., Castillo, J. L. & Antoranz, J. C. Density scaling laws for the structure of granular deposits. *Phys. Rev. E* **76,** 011407 (2007).
54. Mädler, L., Lall, A. A. & Friedlander, S. K. One-step aerosol synthesis of nanoparticle agglomerate films: simulation of film porosity and thickness. *Nanotechnology* **17,** 4783 (2006).

Part II

Experimental background

3. Low-energy cluster beam deposition

In this chapter, I will focus on an alternative approach to form nanometer islands on substrates: instead of growing them by atom–atom aggregation on the substrate, a process which dramatically depends on the properties of the substrate and its interaction with the deposited atoms, one can prepare the islands (as free clusters) before deposition and then deposit them. It should be noted that the cluster structure can be extensively characterized prior to deposition by several in-flight techniques such as time-of-flight mass spectrometry, photoionization, or fragmentation[1]. Moreover, the properties of these building blocks can be adjusted by changing their size, which also affects the growth mechanisms and therefore the film morphology[2-4]. There are several additional interests for depositing clusters. First, they can be grown in extreme non-equilibrium conditions, especially with the laser vaporization technique, which allows one to obtain metastable structures or alloys. It is true that no islands grown on a substrate are generally in equilibrium, but the quenching rate is very high in a beam, and the method is more flexible since one avoids the effects of nucleation and growth on a specific substrate. For example, PdPt alloy clusters - which are known to have interesting catalytic properties - can be prepared with a precise composition (corresponding to the composition of the target rod used in the cluster source) and variable size and then deposited on a surface[5,6]. This allows the tuning within a certain range the properties of the films by choosing the preparation conditions of the preformed clusters. It might also be mentioned that cluster nucleation is less sensitive to impurities than atomic nucleation.

3.1. Thin film grown from preformed clusters

3.1.1. Low-Energy Cluster Beam Deposition

Nanostructured materials are systems characterized, at least in one dimension, by a nanometer dimension[7]. Among various type of nanostructured materials, cluster assembled materials represent an original class with specific structures and properties[8-11]. They can be classified in between amorphous and crystalline materials for their structure, while their properties are strongly influenced by the size of their constituents and diverge significantly

from those of the bulk and of molecules by the emergence of new phenomena, not seen in system built by building-blocks of smaller or larger scales. The typical cluster size ranges from few tens to a few thousands of atoms.

The different techniques used to deposit cluster-assembled materials can be divided into two groups, according to the growth process of cluster: clusters nucleated on a substrate by atomic deposition technique or clusters preformed in a cluster source[12,13]. The control of the thin film properties and the efficiency of deposition are generally incompatible with the former technique, while it is possible to carefully control specific properties of cluster assembled film depending only on the material and on the morphology of the preformed clusters and the interaction between clusters and the surface.

An important method to prepare cluster assembled materials is the Low-Energy Cluster Beam Deposition (LECBD), which consists in depositing neutral clusters with low kinetic energy (E_{kin} <1eV/atom), which prevents them from a post deposition fragmentation on the substrate[2, 8,11,14-17] (schematically shown in Fig. 21). In fact, the binding energy per atom inside the cluster is higher that the energy per atom at the impact[18,19].

Fig. 21: Molecular-dynamics simulations of the morphology of films obtained by Mo_{1043} cluster deposition on a Mo(001) surface as a function of the cluster incident kinetic energy: (a) 0.1 eV/atom; (b,) 1 eV/atom; (c) 10 eV/atom[20].

LECBD has introduced the possibility to produce nanostructured samples with unique morphological and chemico-physical properties. These samples are generally composed by a highly porous matrix of interconnected clusters. Due to the high surface/volume fraction of the single component of the nanostructures[21] (as shown in Fig. 22), the whole interface gain a huge increase of the available surface for chemical reactions (like catalytic processes[22]) and for physical interactions between clusters or interfaces[23-26].

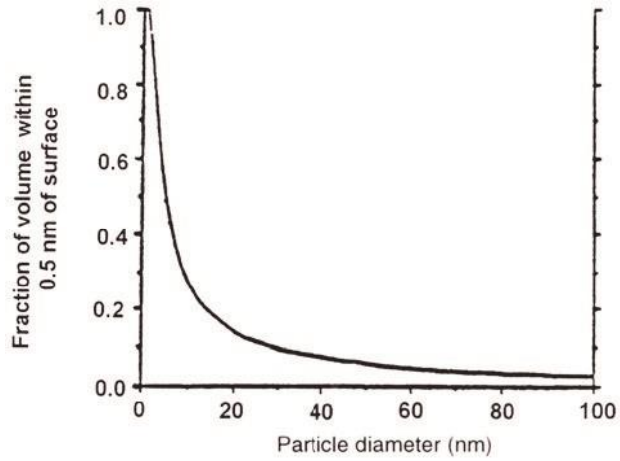

Fig. 22: Fraction of atoms within 0.5 nm of the surface of a nanoparticle as a function of its diameter[21].

The deposition techniques which produce thin films by depositions of atom or molecules usually present asymmetric and broad cluster size distributions, with an important residual concentration of atomic or molecular species, while depositions of preformed clusters present a more symmetric and narrow grain size distribution[15,16,27,28]. For this reason LECBD offers a perfect choice for the study of the influence of incident cluster (building-bocks) size on thin film growth and on its properties at the nano and meso-scale. In fact, a possible 'memory effect' of the original free cluster structure is at the origin of its specific properties.

3.1.2. Memory effect

"Memory effect" refers to the possibility of depositing clusters exhibiting quantum-size-effects and managing to survive on the substrate without shape and internal structural changes in order to print into the continuous porous matrix of cluster assembled film structural and morphological properties which are not destroyed by the multilayers deposition[9].

In a general way, the quantum properties are governed by the surface atoms. As <N> increases, the surface/bulk atom ratio N_{surf}/N_{bulk} decreases and the probability to preserve the molecular character becomes lower. The energy per atom E/<N> in the cluster increases as the cluster size decreases and so the comparison of E/<N> with ε (ε is the cluster binding energy) is helpful to determine when clusters are expected to survive in the initial state. The ideal solution is to deposit cold clusters without kinetic energy. In the best cluster

source (high super-saturation ratio with cold carrier gas), the vibrational cluster temperature is about a few hundreds K with a kinetic energy corresponding to a velocity roughly equal to that of the carrier gas. Two conditions have to be satisfied to synthesize new structural properties of cluster films:

- Cluster size small enough to observe quantum size effects;
- Cluster size big enough to preserve the memory of the free cluster (low surface diffusion regime).

LECBD techniques reach a regime of soft landing ($E/\langle N\rangle \ll \varepsilon$) in a large range of cluster sizes and these two conditions seem to be satisfied in the LECBD technique according to the experimental results presented below:

1. *Structural properties*. - The main result obtained is that LECBD allows the preparation of continuous and amorphous antimony films stable at room temperature, whereas such films have never been obtained by MBD at room temperature[29]. Continuous amorphous Sb films obtained by other conventional methods are unstable at RT. For these films the amorphous-crystal transformation occurs at about T_c = 250 K. LECBD films are amorphous and crystallize at 323 K. TEM observations show that each amorphous domain crystallizes individually in the normal rhomboedral Sb structure without any shape or grain size modification[29]. In addition, this LECBD amorphous antimony phase presents a particular electronic structure as shown by electron transport studies. A size effect can also be involved for other metallic material structural properties, as Cobalt and Samarium[9]. For covalent bond, as carbon clusters, is easily observable the memory effect: the comparison between the intensities of the first-order Raman scattering spectra of C_{20}, C_{60} and C_{900} films indicates clearly that the sp3-hybridization strongly present in the C_{20}-films is lost as the mean free incident cluster size increases from 20 to 900 atoms per clusters. The main conclusion is the direct correlation between the structure (diamond-like or amorphous) of the films and the incident-free clusters properties[9].

2. *Morphological properties*. - In addition to the first asset of the LECBD technique, which is the direct control and the low value of grain size of metallic films, the high roughness of LECBD will play a crucial role in the improvement of chemical

reactivity of surfaces. A typical use of the roughness profile properties and the small grain size of the LECBD films is the giant surface/volume ratio. This "nano-sponge" behaviour is clearly observed by electrical measurements for Bi LECBD films. To compare the LECBD and MBD film reactivity with oxygen, they have measured ,after deposition, the resistance evolution of these samples under 600 Pa of O_2. Notwithstanding the higher resistance of the LECBD Bi deposits, LECBD films are much more sensitive to air exposure than MBD ones: after introduction of oxygen in the deposition chamber, the oxidation of the LECBD film causes a large increase of the electrical resistance. In comparison, the electrical resistance of MBD films remains unchanged. The morphology of deposits and especially the higher roughness and the low grain size of LECBD Bi films explain such a behaviour[14].

Reference[16] it has also highlighted the difference between film properties of Ag_n clusters produced by laser vaporization cluster source or by molecular beam deposition and deposited onto SiO_2 substrates. In particular, it has been shown that after annealing processes, the grain size of the 180nm thick cluster film has increased by 70%, while for the MBD film the rise is 440%. It is an illustrative evidence that with LECBD we can consider a great 'preservation of the nanostructure', for example after thermal annealing processes[30,31]. A clear example of the possibility to change the film morphology by varying only the mean cluster size was given a few years ago by Fuchs et al.[2] and this study has been extended by Bréchignac's group for larger cluster sizes[4].

3. *Electronic properties.* – The LECBD technique allows the synthesis of thin films for which the exploration of the whole scale of electron localization effects can be possible. Experimental results for antimony show that these cases can now be studied:

    a. Before crystallization (deposition at room temperature), the deposits are amorphous and strong localization effects are evidenced;
    b. After crystallization, the deposits are formed with small crystalline aggregates presenting similar effects than weak localization ones.

While size of supported aggregates obtained by MBD is larger than the electron elastic mean free path, the LECBD technique allows to study these localization effects[15].

4. *Magnetic properties.* – Despite the conventional crystallographic structure of the granular films obtained by transition metal clusters depositions, direct relation between the nanostructure and the magnetic properties is interesting. In this case, the magnetic behaviour of these films is strongly influenced by the grain size and the interactions between grains leading to a magnetic state intermediate between amorphous materials and crystals. This state comparable to a correlated spin glass can be treated in the frame of the random anisotropy model to simulate the magnetic behaviour of the films in an external applied magnetic field [9].

5. *Optical properties.* – A promising application of the LECBD technique is the preparation of optical nanostructures formed by clusters embedded in a transparent dielectric matrix. In the particular case of metallic nanoparticles, the film exhibit normal adsorption bands in the near-UV, visible or near-IR regions[32-38], due to the collective excitation of conduction electrons (surface plasmon resonance). The positions and shapes of such absorption bands strongly depend on the size distribution, shape and volume fraction of the metallic inclusions.

3.2. Sub-monolayer regime

In this section I review the experimental results obtained for Low Energy Cluster Beam Deposition in the sub-monolayer regime, in order to give some examples on how to analyse experiments and to deduce the important physical quantities characterizing the interaction of a cluster with a surface and with other clusters.

3.2.1. Sb_{2300}, Sb_{250} and Au_{250} clusters on Highly Oriented Pyrolitic Graphite (HOPG)

Different works[3,17,39-41] have been performed to study the sub-monolayer growth of Sb_{2300}, Sb_{250} and Au_{250} clusters on Highly Oriented Pyrolitic Graphite (HOPG). The main experimental results are shown below.

For films grown on highly oriented (0001) pyrolitic graphite, before deposition at room temperature, freshly cleaved graphite samples are annealed at 500 °C for 5 hours in the deposition chamber (where the pressure is 10^{-7} Torr) in order to clean the surface. The main advantage of HOPG conveniently annealed is that its surface consists mainly of defect-free large terraces (1μm) between steps. The Sb_n cluster beam is generated by the gas aggregation technique in a thermal source similar to that developed by Sattler[27]. The metallic vapor obtained from a heated crucible is condensed in an inert gas (Ar or He) and cooled at liquid nitrogen temperature. This leads to the formation of the beam of incident clusters, which are neutral and have low kinetic energy (less than 10 eV/cluster[42]). The free Au_n clusters are produced in a laser vaporization source similar to the one described by Smalley et al.[43] and Milani et al.[44], as described in Section 1.1.3. A plasma created by the impact of an Nd:YAG laser beam (wavelength 532 nm) focused on a rod is thermalized by injection of a high-pressure He pulse (3-5 bar for 150-300 μs), which permits cluster growth. The mean cluster size is governed by several parameters, such as the helium flow, the laser power, and the delay time between the laser shot and the helium pulse. After transfer in air, the films are observed by transmission electron microscopy (TEM) and by scanning electron microscopy (SEM). A detailed analysis of this kind of micrograph shows that the ramified islands are formed by the juxtaposition of particles for both the metals, which have the same size distribution as the free clusters of the beam. From this consideration, we can infer two important results. First, in the low energy deposition regime, clusters do not fragment upon landing on the substrate. Second, antimony and gold clusters remain juxtaposed upon contact and do not coalesce to form larger particles (Fig. 23).

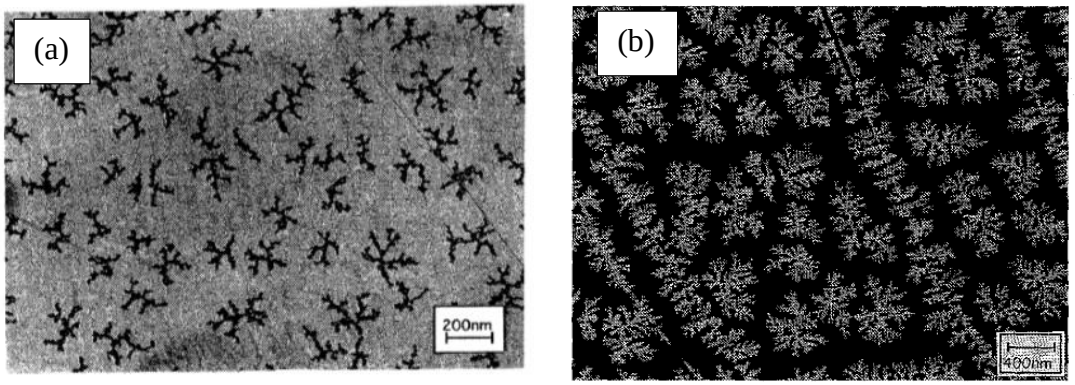

Fig. 23: Typical island morphologies of Sb_{2300} islands obtained experimentally by transmission electron microscopy. T_s = 298 K and F = $2.1x10^9$ clusters $cm^{-2}s^{-1}$, N_{isl} = $3.7x10^{-4}$ per site[39] (a); typical Au island morphologies obtained experimentally by scanning electron microscopy (SEM)

for a 0.5 nm thick films produced by deposition of Au_{250} clusters on a substrate annealed at 353 K. The incident flux is $f=10^{-2}$ nms^{-1} [40].

From a qualitative point of view, Fig. 23 also shows that the clusters are able to move on the surface. Indeed, since the free clusters are deposited at random positions on the substrate, it is clear that, in order to explain the aggregation of the clusters in those ramified islands, one has to admit that the clusters move on the surface. Fig. 24 shows the evolution of the island density as a function of the surface coverage.

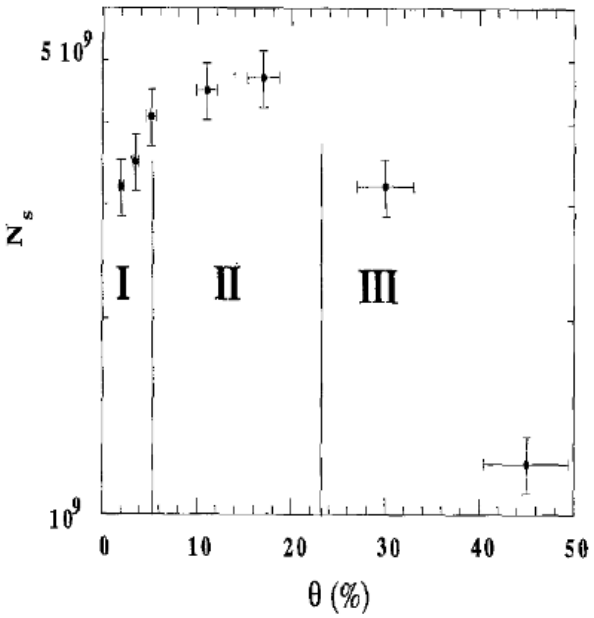

Fig. 24: Evolution of the island density N_S as a function of the surface coverage θ [40].

We see that the saturation island density N_{sat} is reached for $\theta \approx 15$ML. This indicates that evaporation or island diffusion is not important in this case. Therefore, we guess that the growth should be described by a simple combination of deposition, diffusion of the incident clusters, and juxtaposition. When a cluster arrives on the substrate it can meet another cluster diffusing on the surface and form an island (nucleation event) or be captured by an already existing island (growth process). For very low coverage the primeval incident cluster density rapidly grow leading to a rapid increase of island density N_s for nucleation events by cluster-cluster encounter on the surface. This goes on until the islands occupy a small fraction of the surface, roughly 0.1% [19]. For larger coverages, a competition appears between nucleation events and island growth processes, leading to a slower increase of island density. N_s saturates for coverage around 10-15% [19,40,45], when all the incident

clusters are eaten by previously formed islands, before they can meet another cluster and form a new island: nucleation becomes negligible. When the coverage is about 30-40%, the linear dimension of the island becomes of the order of their separation distance and coalescence between islands (static coalescence) starts, which leads to a decrease of the island density.

Fig. 25 presents the morphology of the Sb_{2300} films for different incident fluxes (f).

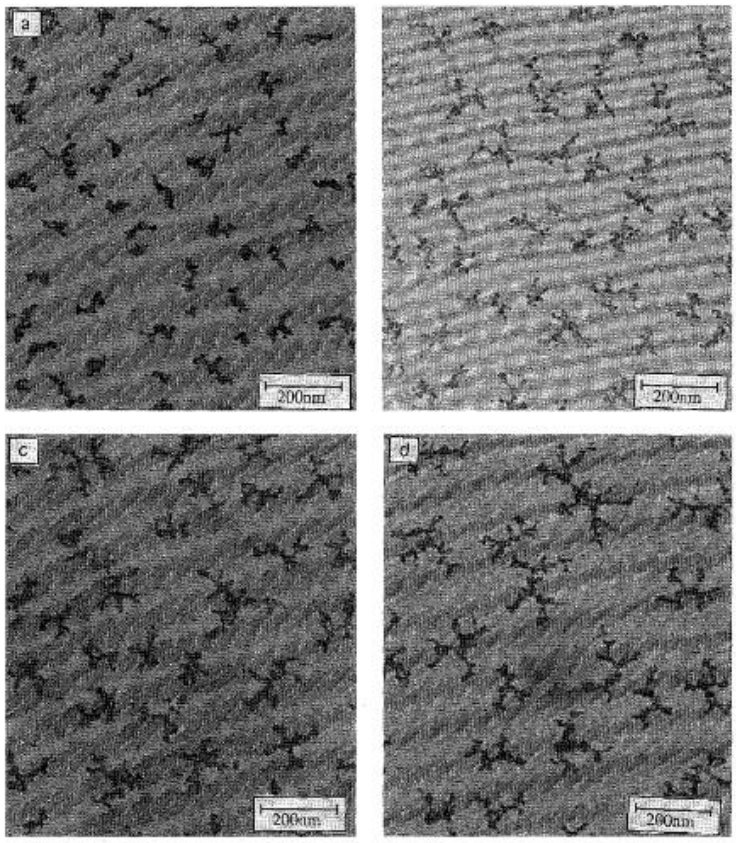

Fig. 25: TEM micrographs of 0.5 nm Sb_{2300} thick films preformed at room temperature for several incident fluxes, (a) f = 3.2 x 10^{-2} nms^{-1}, (b) f = 2 x 10^{-2} nms^{-1}, (c) f = 3 x 10^{-3} nms^{-1}, (d) f = 1.5 x 10^{-3} nms^{-1} [40].

When the flux decreases, the island density decreases whereas the island ramifications increase. This means that:

1. The deposition, the diffusion and the aggregation of antimony clusters are simultaneous on the graphite. Before this study, we could imagine that the diffusion starts only when all the clusters are deposited on the graphite. Nevertheless, this hypothesis cannot explain the changes in the island density when the incident flux is changed;

2. The participation of the nucleation centers of the graphite surface on the film growth is negligible. This is not the case, for example, when the antimony clusters are deposited on amorphous surfaces[28] (like amorphous carbon or glass), where nucleation centers acts as traps for the incident particles, restricting their diffusion. We conclude that surface contamination - which could not be ruled out given the vacuum conditions - does not affect significantly our results.

Knowing the experimental fluxes, one can derive the diffusion times and coefficients. The result is a surprisingly high mobility of Sb_{2300} on graphite, with diffusion coefficients of the same order of magnitude as the atomic ones, that is, 10^{-8} cm^2s^{-1} (Fig. 26).

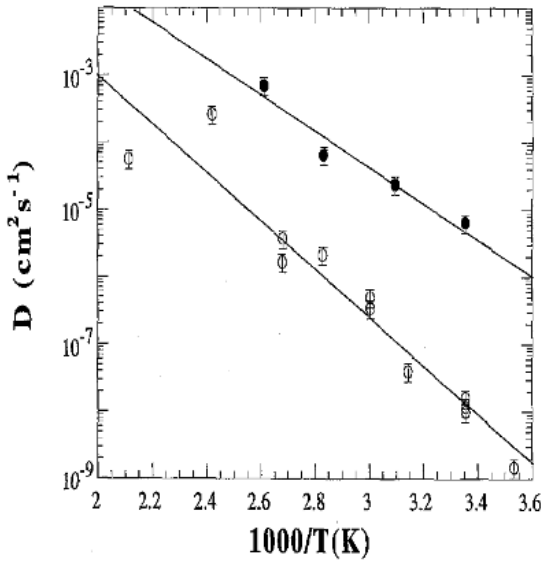

Fig. 26: Dependence of the diffusion coefficient of Sb_{2300} clusters (●) and Au_{250} clusters (○) on the temperature. The solid lines are fits to the experimental data. We find $D = D_0 \exp(-E_a/kT)$, with $E_a = 0.7 \pm 0.1$ eV and $D_0 = 10^4$ cm^2 s^{-1} for Sb_{2300} clusters, and with $E_a = 0.5 \pm 0.1$ eV and $D_0 = 10^3$ cm^2 s^{-1} for Au_{250} clusters [40].

A similar study has been carried out for Sb_{250} on graphite, showing the same order of magnitude for the mobility of the clusters[40].

3.2.2. Sb_n ($n \leq 100$) clusters on a-C

Antimony clusters deposited on amorphous carbon substrate have been studied by different groups[2-4,46]. Here the main results are shown.

Neutral antimony clusters are produced by a gas-aggregation cluster source[44] and are deposited at low-kinetic energy on surfaces maintained at room temperature. The cluster

size is controlled by the oven temperature, pressure of the carrier gas, and nozzle diameter. Small antimony clusters are able to move on amorphous carbon, as demonstrated by Fig. 27.

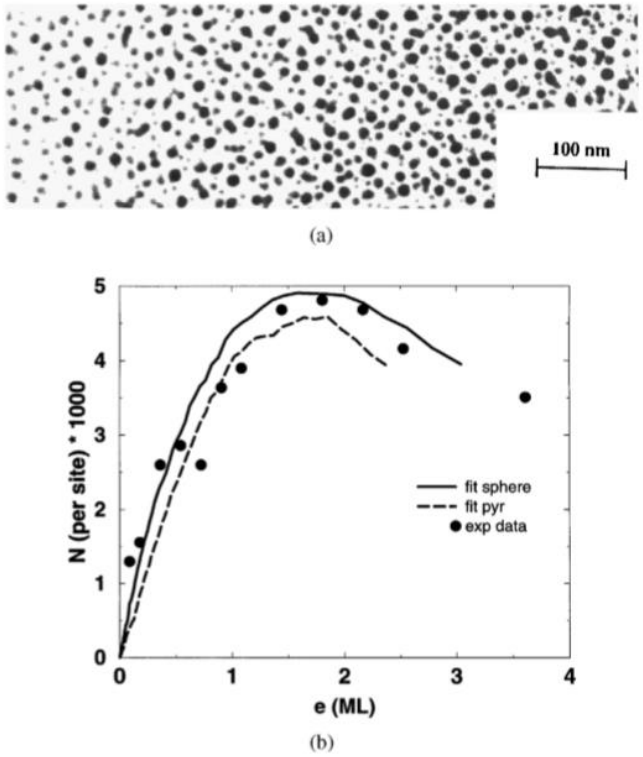

Fig. 27: (a) Morphology of Sb_{36} film at e =1.8ML; (b) Evolution of the island density (per site) as a function of thickness (ML). The dashed line represents a fit of the data with $F\tau = 10^{-5}$ assuming a pyramidal (half-sphere) shape for the supported islands, while the solid line assumes that islands are spherical and $F\tau = 3\times10^{-6}$ [47].

Small clusters gather in large islands and coalesce upon contact. The maximum of island density (Fig. 27) is reached for very high thickness (e ≈ 1.8 ML), which can only be explained by supposing that there is significant re-evaporation of Sb_{36} clusters from the surface.

Furthermore, as shown in Fig. 28, the average island diameter decreases as the cluster size increases until $\langle n \rangle \approx 350$ and then increases as the cluster size increases to converge towards the diameter of incident clusters[2,46].

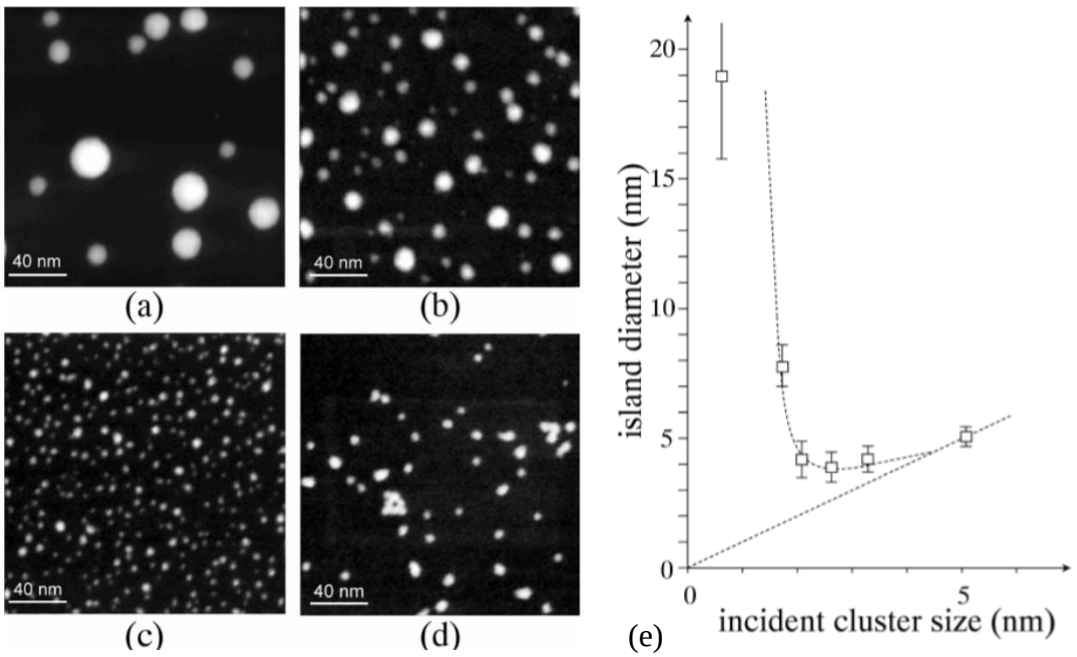

Fig. 28: STEM images of antimony islands grown on amorphous carbon surfaces for different sizes of the incident clusters: the mean cluster size over the distribution of the incident cluster size is determined by time-of-flight mass spectroscopy. (a) n =4, (b) n =90, (c) n =150, and (d) n =2200 [46]. Evolution of antimony island size on amorphous carbon surfaces as a function of the mean diameter of incident clusters for a given coverage of 0.5 ML (e) [46].

3.2.3. Au_n clusters on Au(111) and Ag(111)

Gold clusters are produced, by the group of Ref [17], in a laser vaporization source and are characterized prior to deposition by mass spectrometry.

Au_n clusters on Au(111)

Preformed clusters are then deposited onto Au(111) surfaces without noticeable energy (E< 1eV/atom). In this experiment the whole size distribution is deposited without size selection. This size distribution is centered on 2.9 nm (i.e. <N>= 750 atoms) for experiment performed on Au(111). After deposition at room temperature, the films have been observed in situ with a UHV scanning tunneling microscope (STM) and by atomic force microscopy (AFM) with the same omicron microscope. In addition, TEM and Scanning Electron Microscopy (SEM) analysis has been carried out for comparison with near-field microscopies. In this last case, the samples are transferred to air prior to observation. Fig. 29 presents STM images of Au_{750} cluster thin films on Au(111) substrate, for various thicknesses from 0.01 up to 3.4 nm.

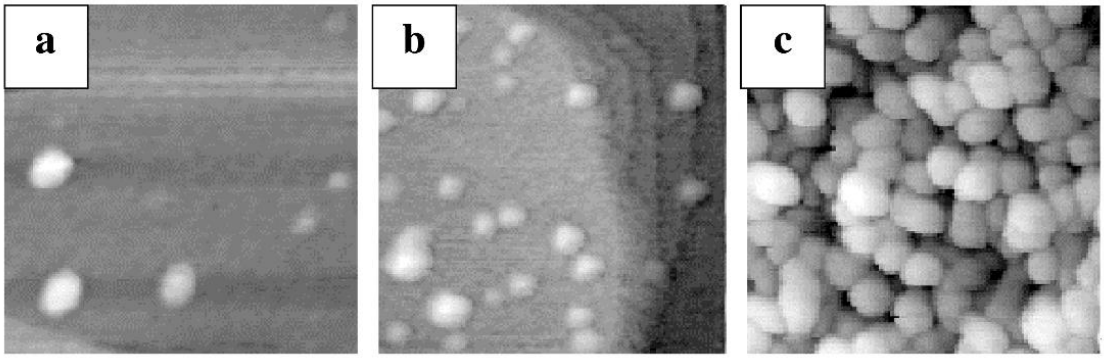

Fig. 29: STM images 100x100nm^2 of the morphologies of Au_{750} cluster films on Au(111) vs. the equivalent thickness (E_q). (a) E_q = 0.01 nm; (b) E_q = 0.03 nm; (c) E_q = 3.4 nm [17].

One can see, in contrast to previous observations on HOPG, that here, the film is composed by a random distribution of isolated particles. It is important to figure out if one isolated particle is corresponding to one incident cluster, or if it results from the aggregation and the merging of several incident particles into a larger compact one. For this purpose, they have compared in Fig. 30 the evolution of the density of the supported particles with the equivalent deposited thickness, to the prediction of a simple ballistic model (without diffusion and coalescence), assuming that each incident cluster becomes, after deposition, one supported particle[48].

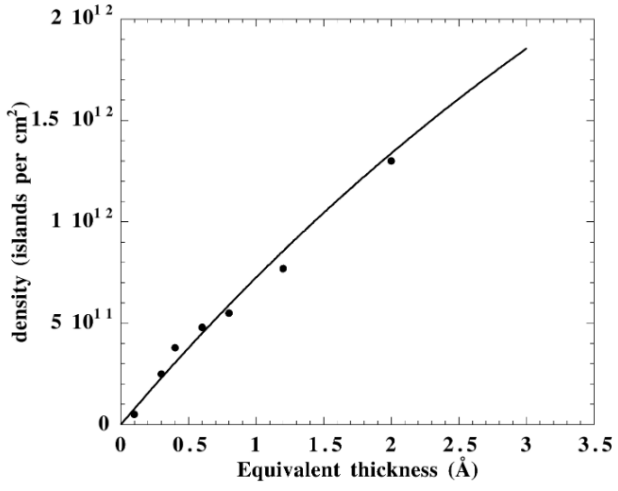

Fig. 30: Supported clusters density vs. the equivalent thickness. The continuous line shows the prediction of a simple ballistic deposition model without diffusion and coalescence taking into account the overlapping of the incident clusters after deposition [17].

The good agreement between experimental results and predicted ones reveals that there is no aggregation of the incident clusters on the surface, suggesting that the clusters do not diffuse on the surface to form islands. Moreover, additional successive STM observations of the same surface area point out that two neighboring clusters do not coalesce to form a larger particle, contrary to the previous case, and that the position of the mass center of the supported particles do not change with time (i.e. no cluster diffusion). Thus, finally, one supported particle corresponds to one incident cluster, in other words, each supported particle is roughly composed by 750 atoms. As a consequence, the cluster shape is provided by the simultaneous analysis of the height profile given by STM and the "free" cluster size distribution. This is consistent with the fact that (111) facets in the gold cluster (assuming a cuboctahedron shape) have a lattice parameter close to the (111) surface. This favors strongly the epitaxy between the cluster and the substrate[49].

Au_n clusters on Ag(111)

In Fig. 31 three STM images of gold clusters deposited on a Ag(111) substrate are shown[41].

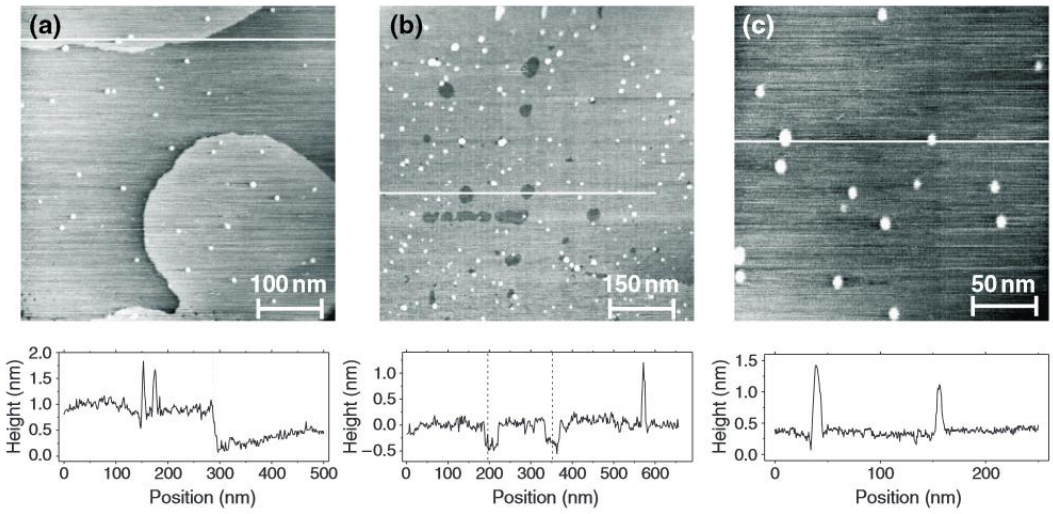

Fig. 31: STM images (1 nA, 100 mV) of Au_n clusters deposited on a Ag(111) substrate. The scan ranges are (a) 200 x 200 nm^2 (z-range is 2nm), (b) 750 x 750 nm^2 (z-range is 2nm), and (c) 250 x 250 nm^2 (z-range is 1.5nm). Neither at the step edges in (a) (indicated by the dotted line in the height profile), nor at the defects in (b) (indicated by the dashed lines in the height profile) are higher cluster concentrations observed. (c) The particles measured on top of an atomically flat terrace correspond to single clusters or to aggregates of a few clusters[41].

Apart from the morphology of the silver film itself (which contains one-monolayer-deep hole-liked effects), the topography is very similar to that in the case of the Au(111) substrate. On the Ag(111) surface there is no preferential positioning of the particles at the surface steps (see Fig. 31(a)), nor at the defects in the silver film (Fig. 31(b)). The main difference between cluster deposition on a gold and on a silver substrate appears when studying the cluster stability over longer periods of time. On a gold surface the cluster configuration remains unaltered during repeated scanning and as a function of time (even after a few months). On the other hand, on the silver substrate the clusters tend to diffuse.

3.2.4. TiO_x on Au(111)

Ref [50] reports on Ti clusters, produced by a laser vaporization source and deposited with low kinetic energy (≈0.13 eV/atom) onto cleaned Au(111) substrates at room temperature[51]. Epitaxially grown 140-nm thick Au(111) films on freshly cleaved mica were prepared ex situ by Molecular Beam Epitaxy (MBE) at elevated temperatures[41]. After exposure to ambient conditions, the Au(111) surfaces are cleaned in the UHV preparation chamber (with a typical base pressure in the low 10^{-10} mbar range) of the low-temperature UHV STM by repeated cycles of Ar ion sputtering (at about 4 KeV, 10^{-6} mbar of Ar pressure and with the beam current density typically around 50 μA/cm^2) and annealing at about 720 K [52]. The maximum in the cluster-size distribution was tuned to around 750 atoms (≈3.1nm cluster diameter). TiO_x clusters films have been investigated by means of Scanning Tunneling Microscopy and Scanning Tunneling Spectroscopy, after oxidation process and thermal annealing up to high temperatures (970 K).

Fig. 32 presents a typical STM image of TiO_X clusters on an atomically flat Au(111) surface before annealing.

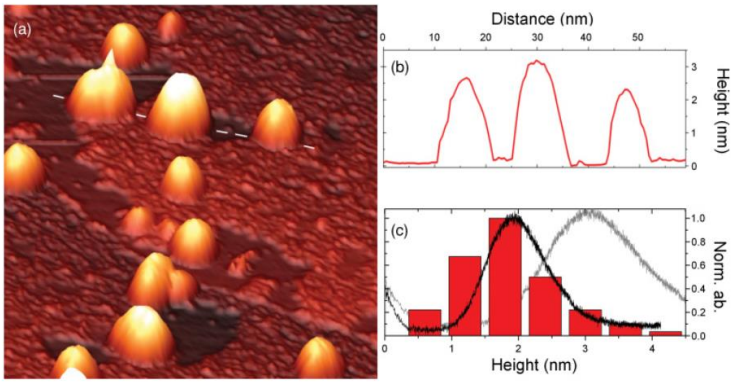

Fig. 32: (a) 100 × 100 nm^2 STM image of deposited TiO_x clusters on a Au(111) surface (V=1.0

V, I=1.0 nA). The clusters show negligible mobility after deposition. (b) Height profile taken along the dashed white line in (a) comprising three TiO_x clusters. (c) Normalized height histogram of the deposited TiO_x clusters and complementary abundance spectra of free cationic TiO_x clusters as a function of cluster diameter in the spherical approximation (gray) and as a function of cluster radius in the hemispherical approximation (black) [50].

The TiO_x nanoparticles are distributed randomly across the Au(111) surface and do not show any preferential positioning at, e.g., Au(111) step edges, nor do they show any clear alignment at elbows of the Au(111) reconstruction as was the case for self-organized Co islands in a previous study[53]. These findings imply that the TiO_x nanoparticles do not exhibit significant diffusion on Au(111) at room temperature. The height distribution of the particles after deposition is presented in Fig. 32(c).

Fig. 33(a) presents a topographic STM image after annealing of the TiO_x nanoparticles up to a temperature of 970 K. Comparison with Fig. 32(a) shows that the substrate is now atomically flat and the Au(111) herringbone reconstruction is observed, indicating a clean surface.

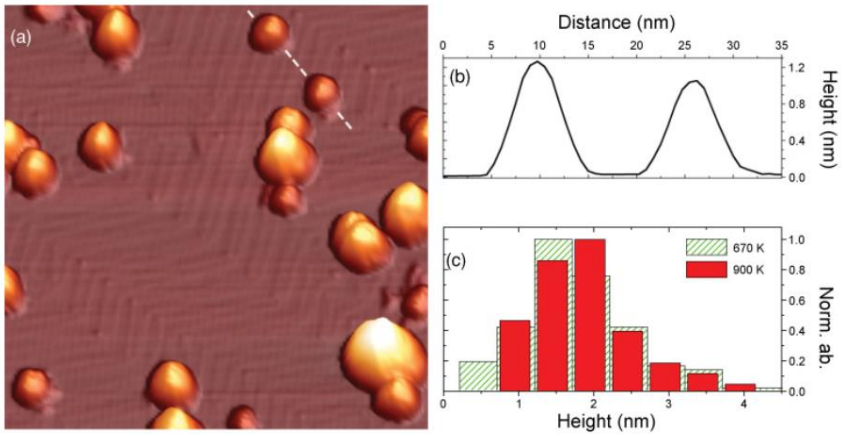

Fig. 33: (a) 100×100nm^2 STM image of TiO_x nanoparticles on a Au(111) surface after annealing to 970 K (V=−1.0 V,I=0.1 nA). (b) Line profile taken along the dashed white line indicated in (a). (c) Normalized height histogram of the TiO_x nanoparticles after annealing to 670 K (dashed) and after annealing to 970 K (shaded) [50].

The contamination layer is evaporated, which happened already after annealing to 570 K (data not shown). The removal of this layer also eliminates the uncertainty for the height measurement. Still, no preferential cluster heights are observed when looking at an ensemble containing a lot of different clusters. Analysis of the STM images after annealing to 670 and 970 K does not reveal a significant difference in the distribution of particle heights (Fig. 33(c)) when compared to the substrate before annealing (Fig. 32(c)). This

indicates that TiO_x nanoparticles do not "sink" into the Au(111) surface as is the case for, e.g., Co nanoparticles[54]. Meanwhile, the density of particles on the surface also remains constant (around 20 per 100 nm^2). After annealing, the particles are still randomly distributed across the surface and they do not coalesce. From these results, it can be concluded that, even at high temperatures, the TiO_x nanoparticles do not diffuse and remain on the surface as single entities.

3.3. Thin films by LECBD

In this section I review the experimental results obtained for Low Energy Cluster Beam deposition beyond the sub-monolayer regime, in order to deduce the important physical properties characterizing the interaction between clusters, depending on the deposition technique and annealing processes.

3.3.1. Ag_n clusters on SiO_2

In Ref [16], free charged and neutral Ag_n clusters were produced by a laser vaporization cluster source (using a pulsed flow of He gas, with 125 μs pulse duration) and deposited onto SiO_2 substrates resulting in cluster films. To minimize the influence of the substrate morphology on the films, Si substrates with a 700 nm thick thermally grown SiO_2 top layer were chosen because of their low surface roughness and the amorphous character of the SiO_2. These films were characterized by Atomic Force Microscopy, X-ray diffraction and resistivity measurements to determine films topography, grain sizes, dimensions of the coherent scattering regions perpendicular to the films plane, and the mean free path length of the conduction electrons. A 100 nm thick Ag films grown by Molecular Beam Deposition (MBD) was investigated using the same characterization techniques. The cluster films were annealed in vacuum (10^{-6} hPa) for 1h at 493K and finally they were characterized again.

Fig. 34 gives the images of the 180 nm thick Ag cluster film (before and after annealing, Fig. 34 a, b) and of the Ag film deposited by MBD (before and after annealing, Fig. 34 c, d).

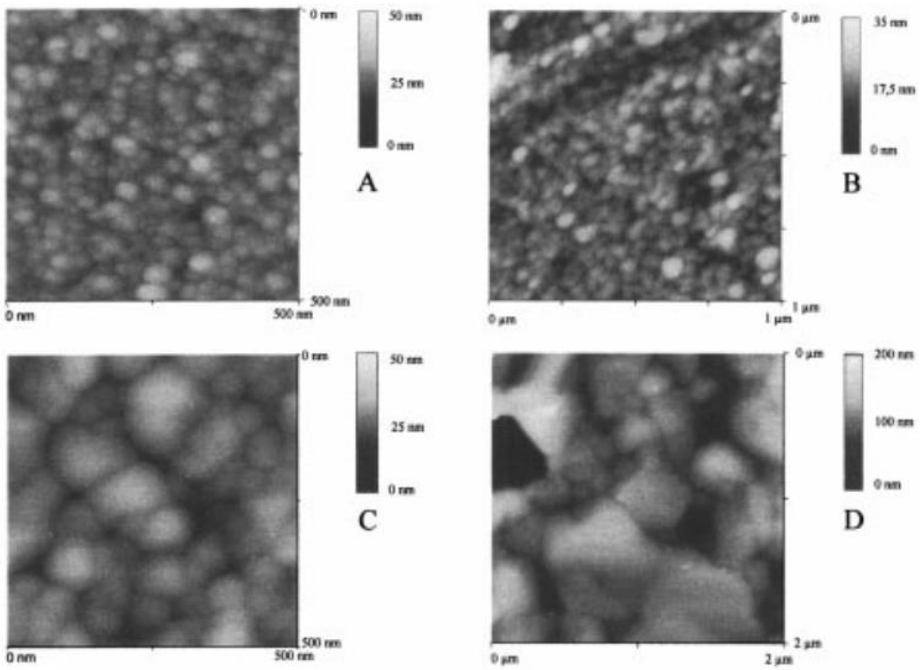

Fig. 34: AFM images of (a) Ag cluster film 180 nm as deposited and (b) annealed at 493K; AFM images of Ag film deposited with MBD film as deposited (c) and annealed at 493K (d) [16].

Fig. 34 shows a granular structure for each film. The mean grain diameters, determined from the AFM picture section analysis at half the grain height, of the cluster films (22 and 25 nm, for 60 and 180 nm thin film respectively) are clearly smaller than the one of the MBD film (75 nm) (see Table II).

	Cluster film		MBD film		
Thickness (nm)	60	180	180	100	100
Annealing	no	no	yes	no	yes
Mean grain diameter (nm)	22	25	42	75	330
Mean roughness (nm)	2.4	3.3	3.6	3.2	18

Table II: Experimental and calculated values for the cluster films and the MBD film deduced from the atomic force microscopy, X-ray diffraction and resistivity measurement [16].

Fig. 35 demonstrates that the grain size distribution for the cluster films is symmetric and narrow (FWHM: ~ 10 nm), whereas the distribution is asymmetric and clearly broader for the MBD film (FWHM: ~ 30 nm).

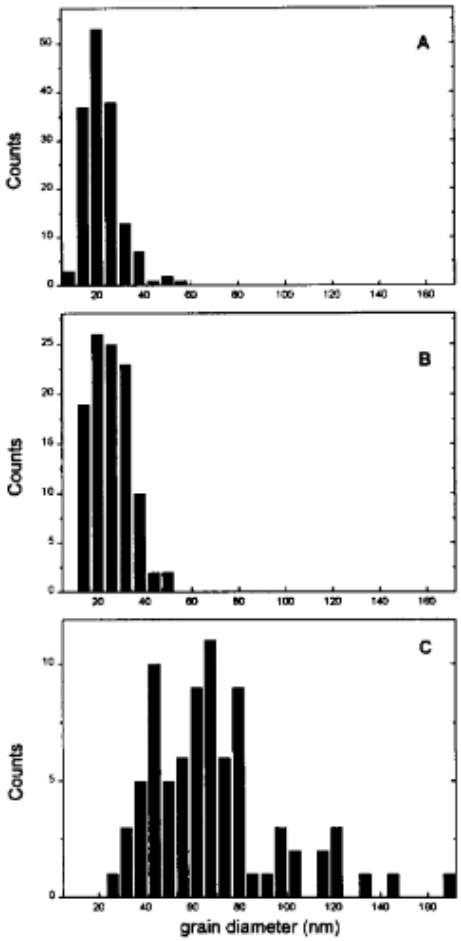

Fig. 35: Distribution of the grain diameters of (A) Ag cluster film 60 nm thin, (B) Ag cluster film 180 nm thin and (C) Ag-MBD film 100 nm thin. The histogram intervals are 6 nm [16].

Because of the dimensions of the grains in the cluster films it is clear that one grain must consist of many initial clusters, obviously indicating cluster aggregation. The cluster film thickness has only a weak influence on the topographic features. After annealing, the grain size of the 180 nm thick cluster film has increased by 70%, for the MBD film the rise is 440%. The root mean square (rms) roughness (measured on an area of 500 nm^2) increases slightly with film thickness for the cluster films and it is nearly the same before and after annealing. The significant rise of the rms roughness after annealing the MBD film, from 3.2 up to 18 nm, is due to the presence of holes down to the substrate of the MBD film.

3.3.2. Sb_n clusters on Si and a-C

In Ref.[14,19], metallic vapor obtained from an heated crucible is cooled in an inert gas (He or Ar) at liquid nitrogen temperature to obtain a Sb-cluster vapor. Fig. 36 shows the size distribution of incident clusters used: the mean size of Sb free clusters used for the growth of Sb LECBD film is centered on 4 nm diameter (which corresponds to n=1200 atoms). It

is important to note the sharpness of this distribution (FWHM = 0.2nm) and the total absence of molecular component (Sb_4).

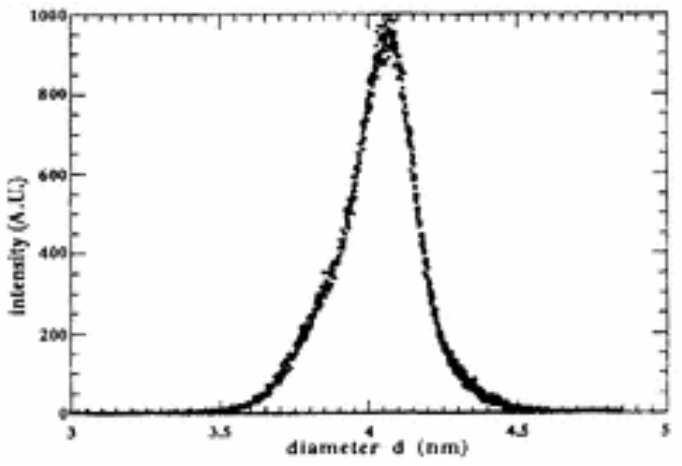

Fig. 36: size distribution of ionized antimony clusters. The diameter of free clusters is calculated assuming they have a spherical shape and the bulk density[14].

The cluster vapor condenses on a Si substrate or a-carbon microscopy grips maintained at room temperature. After transfer through air, the deposits have been characterized by TEM on a JEOL-200CX microscope.

Previous studies have shown that the different choice of the substrate does not change dramatically the characteristics of the film[29]. This allows to compare plan-view MET observations of Sb film deposited on a-C (Fig. 37) and cross section observation of Sb films deposited on Si substrate (Fig. 38).

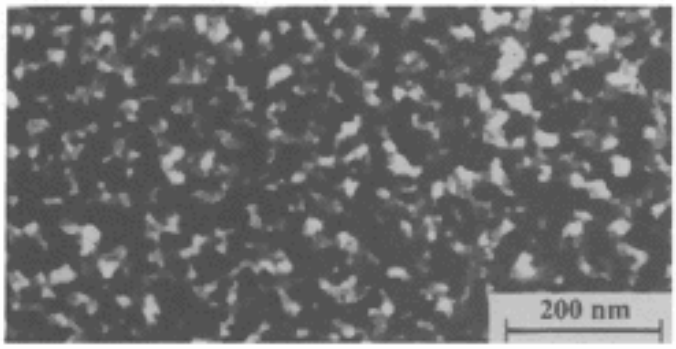

Fig. 37: TEM image of an amorphous 13.5nm thick Sb film prepared by LECBD at room temperature[29].

Fig. 37 presents a plan-view TEM micrograph of a 13.5 nm-thick film. After thermal annealing at 380 K, the film crystallization occurs and the electron diffraction shows rings characteristic of the antimony crystalline phase[29]. To investigate the morphology of the

crystallized film, 30 nm-thick LECBD Sb film have been deposited to prepare cross-section TEM. Fig. 38 shows a typical cross-section view.

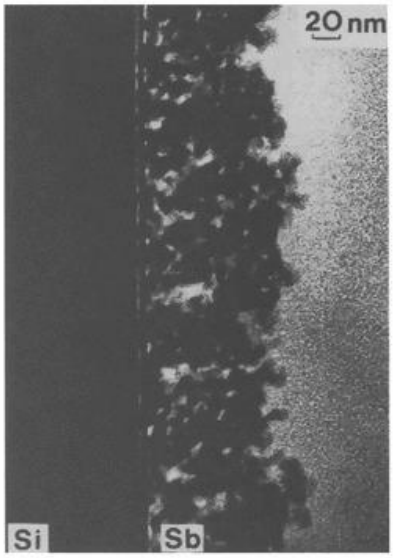

Fig. 38: TEM cross section of a LECBD Sb film. The grain mean size of the film is about 6 nm diameter which corresponds to the coalescence of 4 incident free clusters[14].

The mean grain size of the film measured from this micrograph is about 6 nm diameter. This size roughly corresponds to the size of incident clusters (centered on 4nm from Fig. 36). This result agrees with previous results obtained in the very first stages of Sb film growth[48] showing that the surface diffusion coefficient $D_{<n>}$ of clusters is low enough to have a supported cluster mean diameter centered in the size distribution of the free clusters. In addition, it appears clearly that the growth of the film is the result of a random packing of clusters. Moreover, this TEM micrograph shows the low compactness of the film: the thickness measured from TEM is about 100 nm while RBS and crystal quartz measurements give a 30 nm equivalent thickness.

References

1. Vialle, J. L. *et al.* A cylindrical reflectron time-of-flight mass spectrometer. *Rev. Sci. Instrum.* **68,** 2312 (1997).
2. Fuchs, G. *et al.* Cluster-beam deposition of thin metallic antimony films: Cluster-size and deposition-rate effects. *Phys. Rev. B* **44,** 3926–3933 (1991).
3. Bréchignac, C. *et al.* Mobility and aggregation of free clusters soft landed on amorphous and crystalline carbon substrates. *Z. Für Phys. At. Mol. Clust.* **40,** 516–519 (2014).
4. Bréchignac, C. *et al.* Size effects in nucleation and growth processes from preformed soft-landed clusters. *Phys. Rev. B* **57,** R2084–R2087 (1998).
5. Rousset, J. L. *et al.* Study of bimetallic Pd–Pt clusters in both free and supported phases. *J. Chem. Phys.* **102,** 8574–8585 (1995).
6. Rousset, J. L. *et al.* Investigations on supported bimetallic PdPt nanostructures. *Surf. Sci.* **352-354,** 583–587 (1996).
7. *Handbook of nanostructured materials and nanotechnology*. (Academic Press, 2000).
8. Rodríguez-Pérez, D., Castillo, J. L. & Antoranz, J. C. Density scaling laws for the structure of granular deposits. *Phys. Rev. E* **76,** 011407 (2007).
9. Melinon, P. *et al.* From free clusters to cluster-assembled materials. *Int. J. Mod. Phys. B* **9,** 339–397 (1995).
10. Sumiyama, K., Hihara, T., Liang Peng, D. & Katoh, R. Structure and magnetic properties of Co/CoO and Co/Si core–shell cluster assemblies prepared via gas-phase. *Sci. Technol. Adv. Mater.* **6,** 18–26 (2005).
11. Binns, C. Nanoclusters deposited on surfaces. *Surf. Sci. Rep.* **44,** 1–49 (2001).
12. Pauwels, B. *et al.* Low-energy-deposited Au clusters investigated by high-resolution electron microscopy and molecular dynamics simulations. *Phys. Rev. B* **62,** 10383–10393 (2000).
13. *Nanoclusters and nanocrystals*. (American Scientific Publishers, 2003).
14. Fuchs, G. *et al.* Films of controlled nano size grains deposited by low-energy cluster beam. *Z. Für Phys. At. Mol. Clust.* **26,** 249–251 (1993).
15. Melinon, P. *et al.* Low-energy cluster beam deposition : do you need it ? *J. Phys. I* **3,** 1585–1603 (1993).
16. Bouwen, W. *et al.* Characterization of granular Ag films grown by low-energy cluster beam deposition. *Thin Solid Films* **354,** 87–92 (1999).
17. Bardotti, L., Prével, B., Treilleux, M., Mélinon, P. & Perez, A. Deposition of preformed gold clusters on HOPG and gold substrates: influence of the substrate on the thin film morphology. *Appl. Surf. Sci.* **164,** 52–59 (2000).

18. Woodley, S. M., Hamad, S., Mej?as, J. A. & Catlow, C. R. A. Properties of small TiO2, ZrO2 and HfO2 nanoparticles. *J. Mater. Chem.* **16,** 1927 (2006).
19. Jensen, P. Growth of nanostructures by cluster deposition: Experiments and simple models. *Rev. Mod. Phys.* **71,** 1695–1735 (1999).
20. Haberland, H., Insepov, Z. & Moseler, M. Molecular-dynamics simulation of thin-film growth by energetic cluster impact. *Phys. Rev. B* **51,** 11061–11067 (1995).
21. Navrotsky, A. Thermochemistry of Nanomaterials. *Rev. Mineral. Geochem.* **44,** 73–103 (2001).
22. Steiner, S. A. *et al.* Nanoscale Zirconia as a Nonmetallic Catalyst for Graphitization of Carbon and Growth of Single- and Multiwall Carbon Nanotubes. *J. Am. Chem. Soc.* **131,** 12144–12154 (2009).
23. Ko, Y.-S. & Kwon, Y.-U. Mesoporous Zirconia Thin Films with Three-Dimensional Pore Structures and Their Application to Electrochemical Glucose Detection. *ACS Appl. Mater. Interfaces* **5,** 3599–3606 (2013).
24. Dolatshahi-Pirouz, A. *et al.* Fibronectin Adsorption, Cell Adhesion, and Proliferation on Nanostructured Tantalum Surfaces. *ACS Nano* **4,** 2874–2882 (2010).
25. Wang, G., Meng, F., Ding, C., Chu, P. K. & Liu, X. Microstructure, bioactivity and osteoblast behavior of monoclinic zirconia coating with nanostructured surface. *Acta Biomater.* **6,** 990–1000 (2010).
26. Chao, C.-C., Hsu, C.-M., Cui, Y. & Prinz, F. B. Improved Solid Oxide Fuel Cell Performance with Nanostructured Electrolytes. *ACS Nano* **5,** 5692–5696 (2011).
27. Sattler, K., Mühlbach, J. & Recknagel, E. Generation of Metal Clusters Containing from 2 to 500 Atoms. *Phys. Rev. Lett.* **45,** 821–824 (1980).
28. Bréchignac, C. *et al.* Control of island morphology by dynamic coalescence of soft-landed clusters. *Eur. Phys. J. - At. Mol. Opt. Plasma Phys.* **16,** 265–269 (2001).
29. Jensen, P. *et al.* Continuous amorphous antimony thin films obtained by low-energy cluster beam deposition. *Appl. Phys. Lett.* **59,** 1421–1423 (1991).
30. Kholmanov, I. N. *et al.* The influence of the precursor clusters on the structural and morphological evolution of nanostructured TiO_2 under thermal annealing. *Nanotechnology* **14,** 1168–1173 (2003).
31. Della Foglia, F., Losco, T., Piseri, P., Milani, P. & Selli, E. Photocatalytic activity of nanostructured TiO2 films produced by supersonic cluster beam deposition. *J. Nanoparticle Res.* **11,** 1339–1348 (2009).
32. Harbich, W., Fedrigo, S. & Buttet, J. The optical absorption spectra of small silver clusters (n=5–11) embedded in argon matrices. *Chem. Phys. Lett.* **195,** 613–617 (1992).
33. Harbich, W., Fedrigo, S., Buttet, J. & Lindsay, D. M. Deposition of mass selected gold clusters in solid krypton. *J. Chem. Phys.* **96,** 8104–8108 (1992).

34. Kreibig, U. & Vollmer, M. *Optical Properties of Metal Clusters*. **25,** (Springer Berlin Heidelberg, 1995).
35. Doremus, R., Kao, S.-C. & Garcia, R. Optical absorption of small copper particles and the optical properties of copper. *Appl. Opt.* **31,** 5773 (1992).
36. Berthier, S. & Lafait, J. Black chromium coatings : experimental and calculated optical properties using inhomogeneous medium theories. *J. Phys.* **40,** 1093–1103 (1979).
37. Sella, C. & Lafait, J. Adjustable selective profiles using cermet absorbing films. *Appl. Surf. Sci.* **33-34,** 942–951 (1988).
38. Fedrigo, S., Harbich, W. & Buttet, J. Optical response of Ag2, Ag3, Au2, and Au3 in argon matrices. *J. Chem. Phys.* **99,** 5712–5717 (1993).
39. Bardotti, L., Jensen, P., Hoareau, A., Treilleux, M. & Cabaud, B. Experimental Observation of Fast Diffusion of Large Antimony Clusters on Graphite Surfaces. *Phys. Rev. Lett.* **74,** 4694–4697 (1995).
40. Bardotti, L. *et al.* Diffusion and aggregation of large antimony and gold clusters deposited on graphite. *Surf. Sci.* **367,** 276–292 (1996).
41. Vandamme, N., Janssens, E., Vanhoutte, F., Lievens, P. & Haesendonck, C. V. Scanning probe microscopy investigation of gold clusters deposited on atomically flat substrates. *J. Phys. Condens. Matter* **15,** S2983 (2003).
42. Kellogg, G. L. Field ion microscope studies of single-atom surface diffusion and cluster nucleation on metal surfaces. *Surf. Sci. Rep.* **21,** 1–88 (1994).
43. Smalley, R. E. Laser Studies of Metal Cluster Beams. *Laser Chem.* **2,** 167–184 (1983).
44. Milani, P. & deHeer, W. A. Improved pulsed laser vaporization source for production of intense beams of neutral and ionized clusters. *Rev. Sci. Instrum.* **61,** 1835–1838 (1990).
45. Amar, null, Family, null & Lam, null. Dynamic scaling of the island-size distribution and percolation in a model of submonolayer molecular-beam epitaxy. *Phys. Rev. B Condens. Matter* **50,** 8781–8797 (1994).
46. Yoon, B. *et al.* Morphology control of the supported islands grown from soft-landed clusters. *Surf. Sci.* **443,** 76–88 (1999).
47. Dos Santos Aires, F. PhD thesis. (University of Lyon, 1990).
48. Melinon, P. *et al.* Comparison of molecular and cluster deposition: Evidence of different percolation processes. *Phys. Rev. B* **44,** 12562–12564 (1991).
49. Vandamme, N. *et al.* Deposition of gold clusters on atomically flat gold films. *Appl. Phys. A* **72,** S177–S180 (2001).
50. Bouwen, W. *et al.* Production of bimetallic clusters by a dual-target dual-laser vaporization source. *Rev. Sci. Instrum.* **71,** 54–58 (2000).

51. Lauwaet, K., Schouteden, K., Janssens, E., Van Haesendonck, C. & Lievens, P. Morphology and electronic properties of thermally stable TiOx nanoclusters on Au(111). *Phys. Rev. B* **83,** 155433 (2011).
52. Schouteden, K., Lievens, P. & Van Haesendonck, C. Fourier-transform scanning tunneling microscopy investigation of the energy versus wave vector dispersion of electrons at the Au(111) surface. *Phys. Rev. B* **79,** 195409 (2009).
53. Schouteden, K., Lando, A., Janssens, E., Van Haesendonck, C. & Lievens, P. Morphology and electron confinement properties of Co clusters deposited on Au(111). *New J. Phys.* **10,** 083005 (2008).
54. Padovani, S., Scheurer, F. & Bucher, J. P. Burrowing self-organized cobalt clusters into a gold substrate. *Europhys. Lett. EPL* **45,** 327–333 (1999).

Part III

Materials and Methods

4. Experimental methods

4.1. Supersonic Cluster Beam Deposition

4.1.1. SCBD apparatus

The apparatus consists of three differentially pumped vacuum chambers (Fig. 39): the first is an expansion chamber (18 dm^3 volume, pumped with a 2000 l/s turbo molecular pump and a 270 m^3/h Roots pump) where the supersonic molecular beam is formed. It is connected to a second chamber (11 dm^3 volume, pumped by a 550 l/s turbo molecular pump) by an electroformed skimmer.

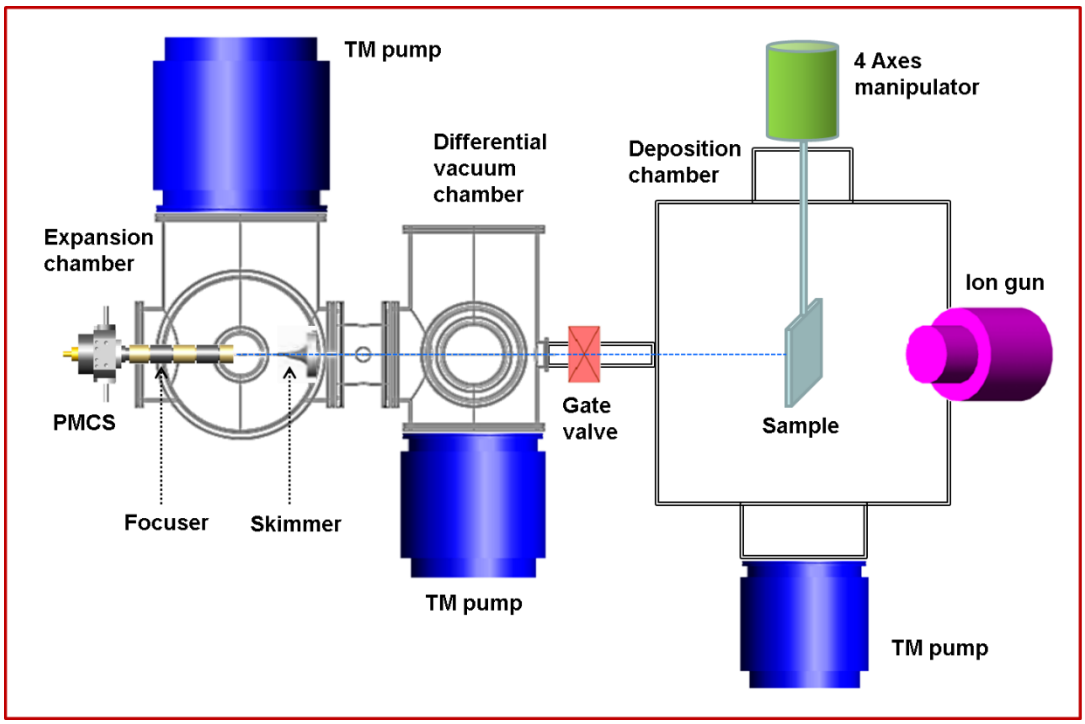

Fig. 39: Schematic representation (not to scale) of the SCBD deposition apparatus. Cluster source (PMCS) is mounted on the expansion chamber; a second source (not shown) can be mounted on the deposition chamber.

The coating deposition takes place in a third deposition chamber (200 dm^3 volume, pumped by a 1000 l/s turbo molecular pump) connected to the rest of the apparatus through a gate valve. A PMCS is mounted outside the expansion chamber on the axis of the apparatus (Fig. 39); an additional PMCS can be mounted off-axis directly on the deposition chamber. A remotely controlled 4-axes manipulator allows for rastering of the sample to guarantee a uniform deposition over a large area. A resistive cartridge heater system can be mounted on the sample holder to heat the substrates in the range room-temperature - 300°C. The deposition chamber also hosts a Kaufman ion gun (Cyberis 40-f) which can be used for either sample cleaning (etching) or co-deposition (sputtering).

4.1.2. Pulsed Microplasma Cluster Source

Pulsed Microplasma Cluster Sources (PMCS) represent a combination of different elements typical of sputtering sources and Laser Vaporization Cluster Source (LVCS)[1]. The working principle of PMCS is based on spatially confined pulsed plasma discharge ablation of a target placed in a condensation chamber. The vaporized species are quenched by a pulse of inert gas and condense to form clusters[2]. Schematically the source consists of a ceramic body with a channel drilled through to perpendicularly intersect a larger cylindrical cavity (see Fig. 40).

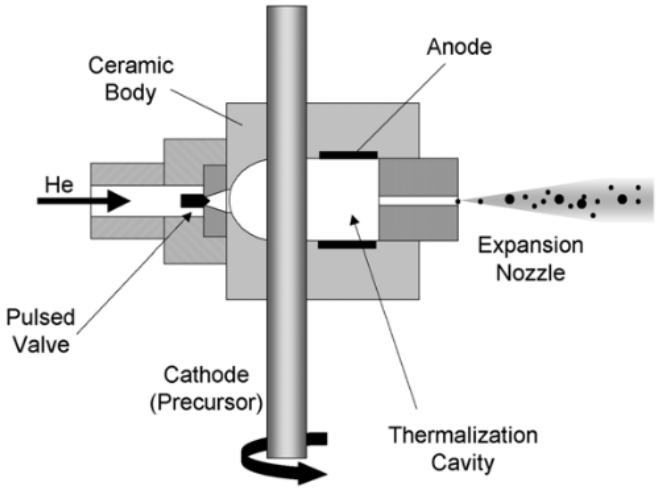

Fig. 40: Schematic representation of a PMCS according to Ref [1]. Inert gas is introduced through a pulsed valve into a cavity containing the rotating target cathode. When a high voltage is applied between anode and cathode, the material is sputtered from the cathode rod. The precursor vapour condenses into clusters which grow in the thermalization cavity before they are extracted from the source through an expansion nozzle.

The channel holds the target to be vaporized which typically is connected to the negative pole of a power source, thus acting as a cathode. The anode can be placed at some location inside the cavity or can also be introduced through the channel, opposing the cathode. A solenoid pulsed valve for introduction of inert carrier gas closes one side of the cavity while a nozzle is located in the opposite cavity wall. The valve, backed with a high gas pressure (typically up to 50 bars), delivers inert gas pulses to the source cavity with an opening time of a few hundreds of microseconds. If the pulsed valve is closed, the source cavity is at the same pressure as the first vacuum chamber. Once the valve opens, the large pressure difference causes the formation of a supersonic gas jet directed against the cathode. A pulsed voltage (typical duration: 50 μs) applied between the electrodes, ionizes the gas and generates a plasma. This is accelerated against the cathode and ablates the material that thermalizes and condenses to form clusters[1,2]. Due to the formation of a strong pressure gradient close to the cathode surface, as has been demonstrated by computational fluid dynamics, an aerodynamic confinement of the plasma is produced in the source cavity and the sputtering process is restricted to a cathode area of less than 1 mm^2 [2]. These simulations showed how a hypersonic helium jet develops inside the source at the time of the electric discharge, causing the confinement of the ablation plasma, improving the sputtering yield and favouring cluster seed condensation by creating a high pressure region that coincides with the one of ablation. This is crucial to assure a PMCS operation stability and reproducibility that is superior to other cluster sources[3,4]. Since the volume of the source cavity is very small (~2 cm^3), the source mean pressure rises rapidly after each pulse. The pressure difference across the nozzle drives the aerosol expansion into the adjacent expansion chamber in the form of a supersonic beam.

PMCS can be used for the production of refractory material clusters and in particular of transition metal-oxides and nitrides[4,5]. Using cathodes consisting of various chemical species, mixed clusters can be obtained in order to deposit nanocomposite films at high deposition rates over a large area. PMCS have been used for the production of devices such as supercapacitors[6], sensors arrays[7,8] or high-throughput screening arrays for biological applications[9].

4.1.3. Mass separation effects

In view of the use of clusters as building blocks of nanostructured thin films, intense and stable beams must be used and a good control on cluster mass and kinetic energies

distribution must be achieved. These characteristics can be obtained with the use of beams produced by supersonic expansions. Due to the long gas pulse exiting form the source (i.e. high duty cycle regime[10]), the source-skimmer distance D_{sk} and the background pressure strongly affect the expansion. Depending upon $D_{sk,}$ a shock wave can be produced in front of the skimmer (Fig. 41), causing mass separation effects and changing the final characteristics of the beam[10].

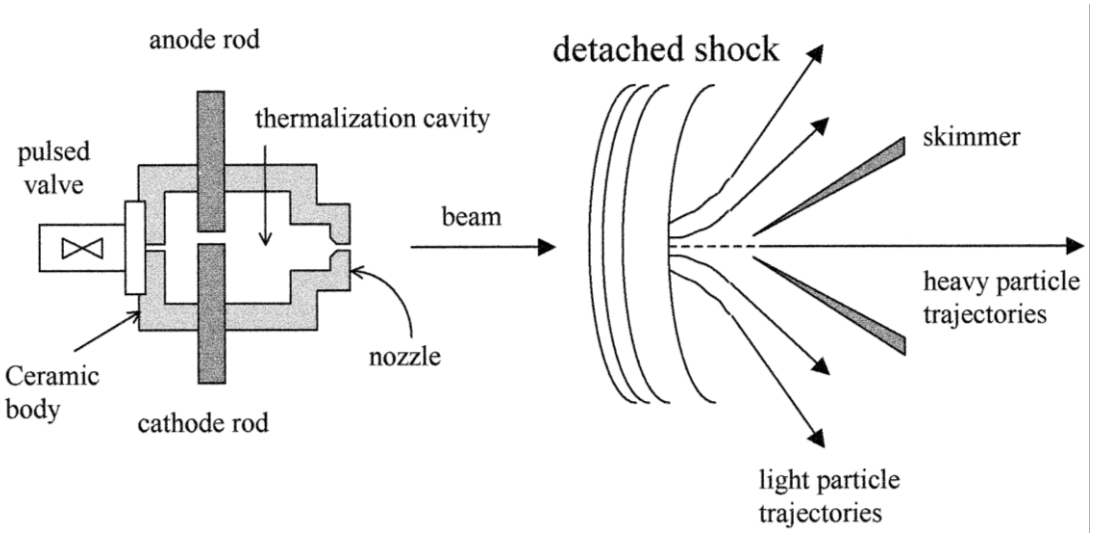

Fig. 41: Expanded view of the pulsed cluster source and of the region near the skimmer where a shock wave is formed. The trajectories of the heavy and light particles are schematically shown. Due to separation effects, films with different nanostructures can be deposited by placing a substrate to intercept different regions of the beam[1].

Separation effects in front of the skimmer should enrich the periphery of the beam of small clusters, leaving large clusters in the beam center[1].

The expansion through a convergent nozzle will always take place in a subsonic regime regardless of the amount of the applied pressure ratio[11]. Outside the converging nozzle, depending on the pressure ratio, the flow will supersonically expand to pressures even much lower than the background. The sudden free expansion of the flow at the immediate vicinity of the nozzle outlet produces a high outward radial velocity at the beginning of the free jet. Consequently, if the jet is seeded by clusters, the resulting outward radial drag on the particles causes a pronounced mass separation in terms of cluster masses. Light clusters can follow the expanding carrier gas, while large particles persist on their original trajectories, increasing their relative concentration in the jet core. Furthermore, the aforementioned radial drag changes with the radial position at the nozzle outlet: it is weak

at the center and very strong close to the nozzle wall. Hence, in contrast to the particles located in the central regions, those far from the axis are exposed to a strong radial drag and they will be spatially separated according to their different masses. If the particles can be concentrated in the nozzle centerline, no significant divergence should occur in the subsequent evolution of the expansion and the obtained beam will have a high intensity and collimation. Since the angular distribution of the clusters in the jet is a function of their mass and of their initial spatial distribution inside the nozzle, focusing the clusters on the beam center will directly improve the beam intensity and collimation[12].

4.2. Sub-monolayer sample deposition

In order to characterize the growth of the islands composed of transition metal oxide clusters in sub-monolayer regime as a function of the surface coverage, depending on the incident cluster dimension and on the carrier gas used inside the source (helium or argon), we have deposited clusters with SCBD onto small substrates which are fragments of polished Si wafers, at room temperature.

Silica substrates (1x0.5 cm^2 in dimensions) have been cleaned in acqua regia and ethanol subsequently. After been dried in a nitrogen flux, they have been adjusted onto a sample holder (shown in Fig. 42) with the peculiarity of intercepting the whole cluster beam, from the center to the periphery of the beam axis. The maximum distance between the sample in the middle of the holder and the most peripheral one is approximately 2.1 cm.

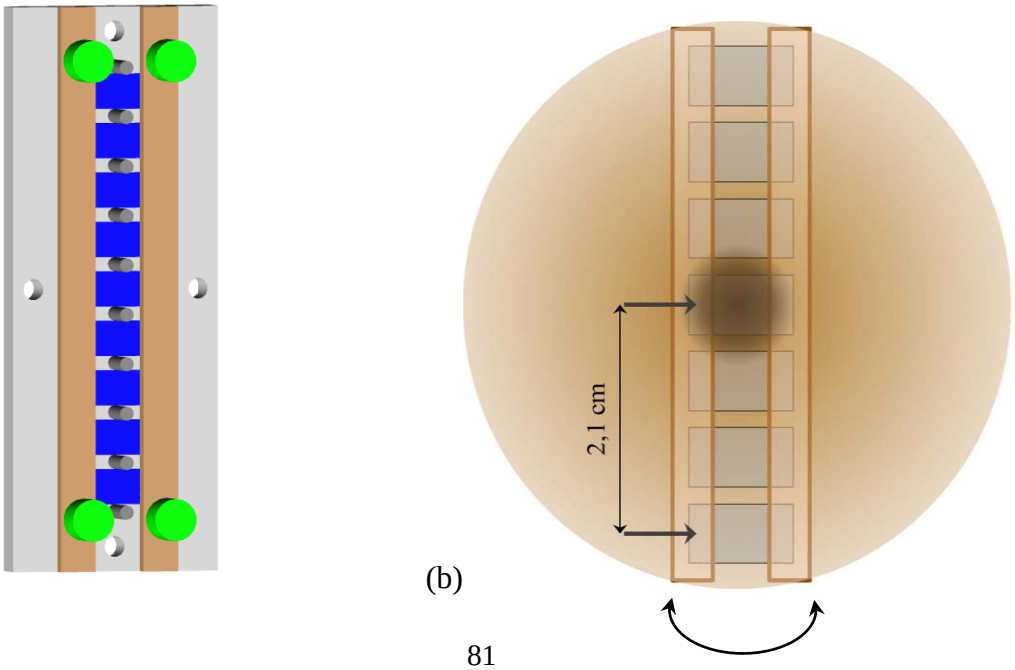

(a) (b)

Fig. 42: (a) Schematic representation (with AutoCAD software) of the sample holder; (b) sample holder representation with superimposition of the cluster beam.

The sample holder has been kept constantly in movement around its central axis in order to intercept the beam only for few seconds, for different time intervals. Each intercepting time has been called *single shot*, and it is 6 seconds long for Argon and 23 seconds long for He. The difference in time is due to the different deposition rate for the two carrier gases, because of their different sputtering yield[13,14].

In all the systems analyzed (ns-TiO_x or ns-ZrO_x, He or Ar), the chopping frequency is 4 Hz, the carrier gas is injected inside the source chamber for 250 μs with a pressure of 40 Torr, a tension of 850 V is applied to the electrodes for 80 μs after 650 μs from the gas valve opening. The pressure inside the expansion chamber is 7.5×10^{-4} Torr, while the one into the deposition chamber is 1.1×10^{-4} Torr.

4.3. Atomic Force Microscopy

Atomic Force Microscopy (AFM) belongs to the family of the Scanning Probe Microscopes (SPM), created in the 1980. The progenitor of this category is the Scanning Tunneling Microscope (STM)[15], which allows the imaging of conductive or semi-conductor material surfaces with atomic resolution.

With an AFM the imaging of insulator or biological samples is possible, also in UHV or fluid environment, with a lateral resolution of few nanometers on corrugated samples (limited by the tip dimension) and vertical resolution of less than 1 Å[16-18]. Fig. 43 is a schematic representation of operation principles of AFM: a tiny sharp probe at the top of an elastic cantilever, whose stiffness changes with its dimensions, scans an area of the surface of the sample. During the scanning of the surface the interaction between the tip and the surface is measured by recording the deflection of a laser[19,20] aligned onto the cantilever (*contact mode*) or the amplitude of the cantilever oscillation (*tapping mode*). The position of the reflected beam is monitored by a position sensitive detector (PSD). Often the backside of the cantilever is covered with a thin gold layer to enhance its reflectivity.

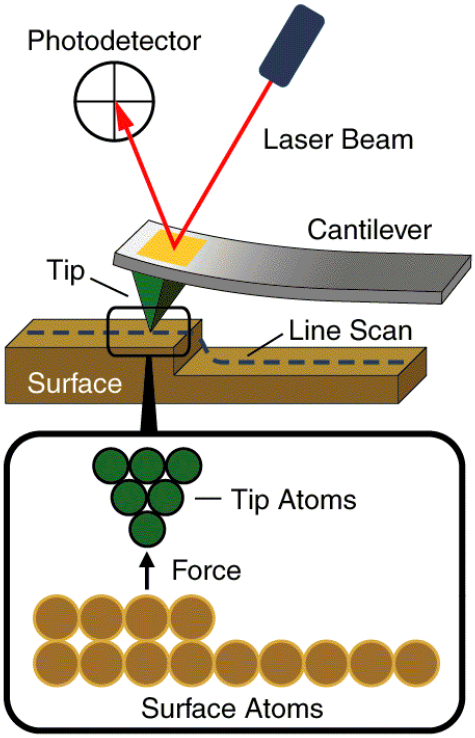

Fig. 43: Schematic representation of operation principles of AFM.

A feedback loop (Fig. 44) moves the sample vertically relative to the tip in order to keep constant a parameter (deflection or amplitude set-point, depending on the scanning mode) characterizing the tip-sample interactions.

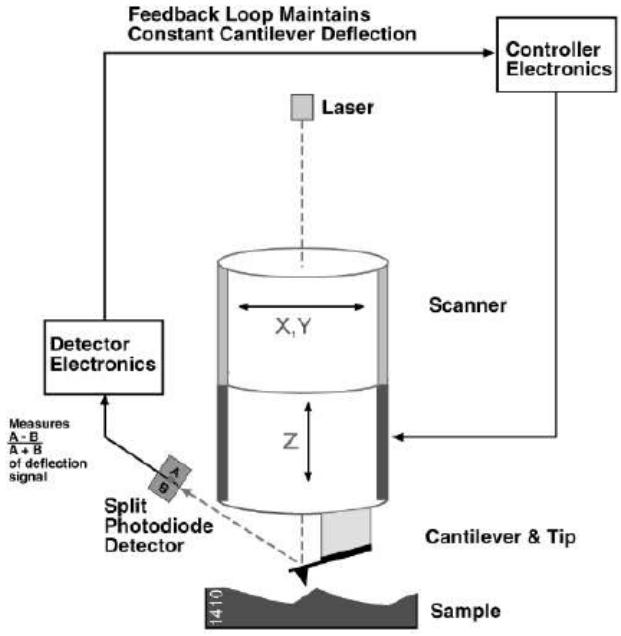

Fig. 44: schematic representation of the feedback system of an AFM.

The AFM output is a numerical matrix of the voltage values applied to the scanner to adjust its position in order to keep the feedback parameter constant at the set-point value, as a function of the x-y position on the surface.

The atomic force microscope is not only a tool to image the topography of solid surfaces at high resolution. It can also be used to measure force-versus-distance curves[16,21]. Such curves, briefly called force curves, provide valuable information on local material properties such as elasticity, hardness, Hamaker constant, adhesion and surface charge densities. To acquire force curves in liquid different types of liquid cells are employed. Typically liquid cells consist of a special cantilever holder and an O-ring sealing the cell.

Deeper details concerning AFM force spectroscopy measurements are reported in Section 4.3.4.

In my project I have used a Bioscope Catalyst AFM (Bruker instruments) and a Multimode AFM equipped with a Nanoscope IV controller (Bruker).

4.3.1. Characterization of sub-monolayer morphology

For each sample, different images (typically nine) with a scan area of 2x1 μm^2 have been acquired in tapping mode, with a sampling frequency of 1nm/pixel e 2 nm/pixel in x and y directions. The images have been acquired in air with a scan rate of 2 Hz and small target amplitude (approximately 10 nm).

After a smoothing and a flattening process of the AFM images (via subtraction of 2^{nd}-order polynomials, line by line), in order to individualize the objects of interest on the surface and to discard the residual dirty background it has been built a mask (Fig. 45), setting a z-threshold value at two standard deviations upon the mean value of the background ($2\sigma \sim 0.3$ nm).

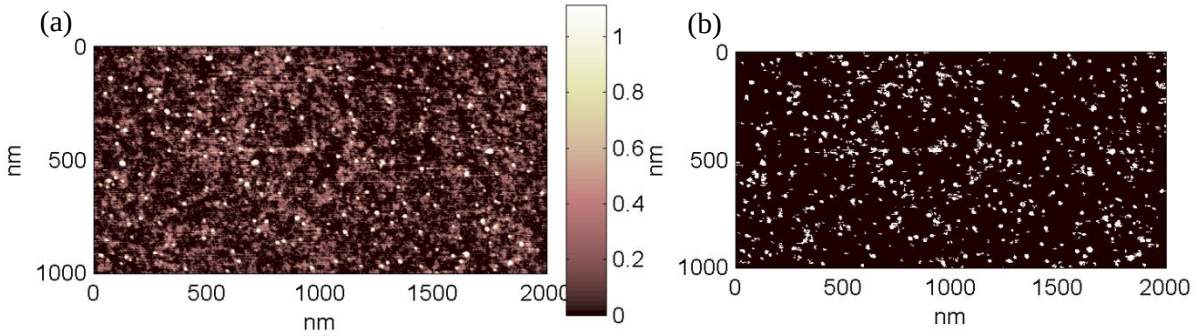

Fig. 45: AFM topographical map of ns-ZrO_x clusters and islands for low coverage (~ 5%), (b) with a mask at a z-threshold of ~ 2σ.

Objects with an area smaller than 20 pixels have been discarded.

Since an image contains multiple objects of interest we must assign a unique label at each object. Subsequently, we measure the following quantities for each labelled object (others can be measured if necessary):

- Area, i.e. the product between the number of pixels in the object and the pixel-area in nm^2 ;
- Equivalent Radius, i.e. the radius in nm of a circle with the same area as the region ($\sqrt{\frac{Area}{\pi}}$);
- Major Axis, i.e. the length (in nm) of the major axis of the ellipse that has the same normalized second central moments as the region;
- Orientation, i.e. the angle (in degrees) between the x-axis and the major axis;
- Minor Axis, i.e. the length (in nm) of the minor axis of the ellipse that has the same normalized second central moments as the region. In particular this parameter is calculated as $\frac{Area}{(MajorAxis)\pi}$;
- Eccentricity, i.e. a scalar parameter calculated as $\sqrt{1-\frac{MinorAxis}{MajorAxis}}$. This value is between 0 (for a circle) and 1 (for a line segment);
- Bounding Box, i.e. the smallest rectangle containing the object;
- Height, i.e. the difference between the highest point of the object and the mean value of the background in nm;
- Volume in nm^3 is obtained by integrating the height profile over the area occupied by the object, i.e. $V_k = \sum_{ij} h(i,j)x(pixel-area)$, where V_k is the volume of k-th object in the image, *(i,j)* are the spatial coordinates occupied by the object in the image.

In the sample with the lowest coverage (θ~1%) only globular objects have been selected, with the strong assumption that for this very low coverage the objects on the surface are the incident clusters (primeval incident clusters) as they arrived on the silica surface, without diffusion-induced juxtaposition or coalescence phenomena. For this reason additional selection rules have been applied: only objects with a linear relationship in semi-log scale between volume and height or between equivalent radius and height, with axes ratio in the range between 0.6 and 1 and with height lower than 20 nm have been chosen.

In the following shots, the objects with dimension (in z-direction) different from the dimension of primeval incident cluster (calculated from the histogram of the height in semi-log scale, as shown in Fig. 46) have been called islands.

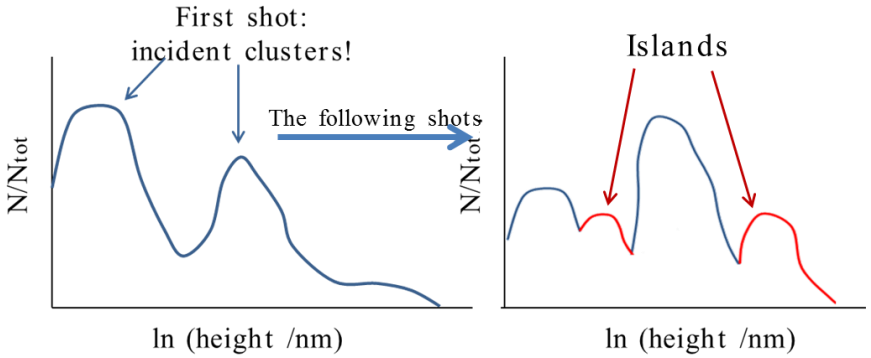

Fig. 46: Schematic representation of the histogram in semi-log scale of the height of the objects identified in the AFM maps.

For each sample the normalized height distribution in semi-log scale has been analyzed with a Gaussian fit (a log-normal distribution turns into a Gaussian one in this scale)[22]. It is supposed that the grain dimension distribution is log-normal because this is peculiar for systems which are the results of aggregation processes[23].

We have chosen to refer to the height value as diameter in z-direction because its value is not affected by the effect of convolution with the tip[24]. We could rescale the x-y apparent dimension of the objects with a simple relation (eq. 14) in order to compare lateral with vertical dimension:

$$r_c = 4\sqrt{Rr} \qquad (R \approx r) \qquad (14)$$

where r_c is the convolution-broadened radius, R is the radius of the tip and r is the radius of the spherical object[25]. If we assume that the scanned object is hemispherical, Eq. 14 becomes:

$$r_c = 2\sqrt{2Rr + r^2} \qquad (R \approx r) \qquad (15)$$

Anyway, because of the unknown real dimension of the nanometer tip and the possibility to increase in its dimension during scanning because of small contaminations, it is better to consider with higher attention the dimension in z and to add a systematic error to the x-y morphological parameters due to the effect of convolution with the tip.

The resolution in z direction (Δz) can be the minimum Z-coordinate change during scanning which can be detected at a given noise level. Resolution depends much on scan

parameters (speed, scan size, parameters of the feedback circuit) as well as on the sample elastic properties and interfacial adhesion[16,17]. Normally, the vertical resolution is a few angstroms.

4.3.2. Characterization of thin film morphology

AFM images were processed using custom routines written in a Matlab environment. The main morphological properties are shown schematically in Fig. 47 and they are defined below.

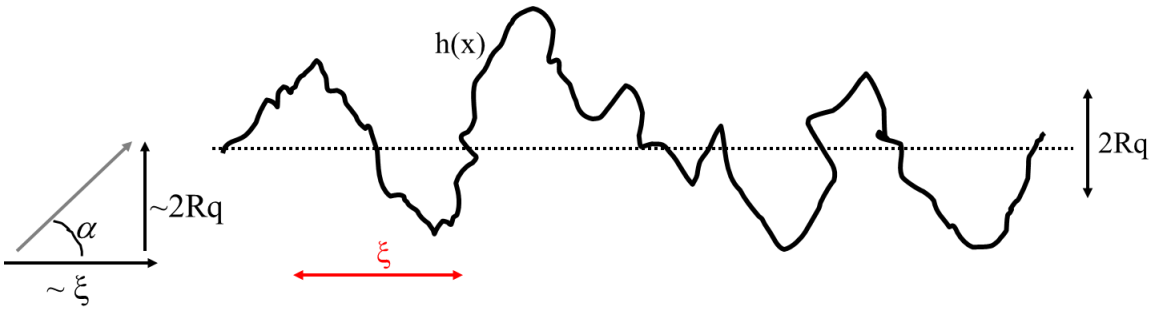

Fig. 47: Representative surface profile of a thin film with the main morphological parameters indicated.

The RMS roughness (Rq) is calculated as $Rq=\sqrt{\frac{1}{N}\sum_{i,j}(h_{ij}-\bar{h})^2}$, where h_{ij} are height values in the topographic map (i,j are the row and column indices) and N is the number of pixels in the map, $\bar{h}$ is the average height ($\bar{h}=\frac{1}{N}\sum_{i,j} h_{ij}$). The specific area A_{spec} is the ratio of the three-dimensional area calculated on the image to the projected area, i.e. to the AFM scanning area. It is calculated as $A_{spec}=\frac{1}{N}\sqrt{1+|\nabla h_{ij}|^2}$, where $|\nabla h_{ij}|$ is the modulus of the discretized surface gradient. The specific area calculated from AFM images is always underestimated because of the inability of the AFM tip to detect overhangs and because of its finite size (typical AFM A_{spec} values do not exceed 2). The in-plane correlations of self-affine surfaces (or profiles) are described by two parameters: the Hurst exponent *H* and the correlation length ξ, which is the characteristic length over which two randomly chosen points on the surface (or on the profile) have uncorrelated heights. The average quadratic difference between heights of two points separated by a distance Δx (also called the height-height correlation function) scales indeed as Δx^{2H} for $\Delta x < \xi$, then it saturates. The mesoscopic slope of the interface can be calculated as 2Rq/ξ (this result is strictly valid only for a Gaussian surface[26]). For a surface with gaussian distribution of surface heights,

the mesoscopic specific area can be calculated as $A_{spec} = 1+2(Rq/\xi)^2$ [26]. Being the determination of both Rq and ξ reliable, the estimation of the mesoscopic specific area is such, as well; it has to be noted that this mesoscopic value fails in reproducing the gain in available area due to sub-correlation length surface structures.

4.3.3 Surface granulometry

In order to correlate the evolution of the surface morphological properties with coalescence, juxtaposition, thermal growth and phase transition phenomena we have performed granulometry studies of the surface also in thin film regime. Quantitative granulometry study proceeds typically through the identification of the grain map and at a further step the statistical evaluation of geometrical parameters describing the granularity of the surface. In particular, we have defined grains as the connected domains in the topographic map having a well-defined local curvature[27]. Grains boundaries are characterized by sudden discontinuities of both the mean (H) and the Gaussian (K) local curvature, defined as:

$$H=\frac{1}{2}\left(\frac{1}{R_1}+\frac{1}{R_2}\right) \quad (16)$$

$$K=\frac{1}{R_1 R_2} \quad (17)$$

where R_1 and R_2 are the principal curvature radii and they have the properties of being the lower and the upper limit accordingly for all the curvature radii of curves obtained intersecting the local tangent plane with all the plane containing the local normal[28]. A logical condition of the form: H>0, K>0, H, K, k_1, k_2 finite, will thus define the grains map. Another important operation is also the removal of the high frequency noise, originated from electronic and thermal induced vibration of the cantilever, by a smoothing of the AFM images with a gaussian kernel[27] which has to be approximately one half of the grain size in dimension. It is also possible to impose different restrictions on the boundaries conditions, in order to have a relaxed mask (with a ratio between error associated to the local curvature and the local curvature lower than 1.5) or a tighter mask (the same ratio lower than 0.5). Fig. 48(a) shows a representative AFM topographic map of a rough ns-ZrO_x surface and the same image with two different masks obtained with relaxed (Fig. 48(b)) and tighter (Fig. 48(c)) conditions, while Fig. 48(d) shows the subtraction between the two, which permits to appreciate a little difference between the masks obtained with the two choices. The dimension of the Gaussian kernel of Fig. 48 is approximately one half of the grain size.

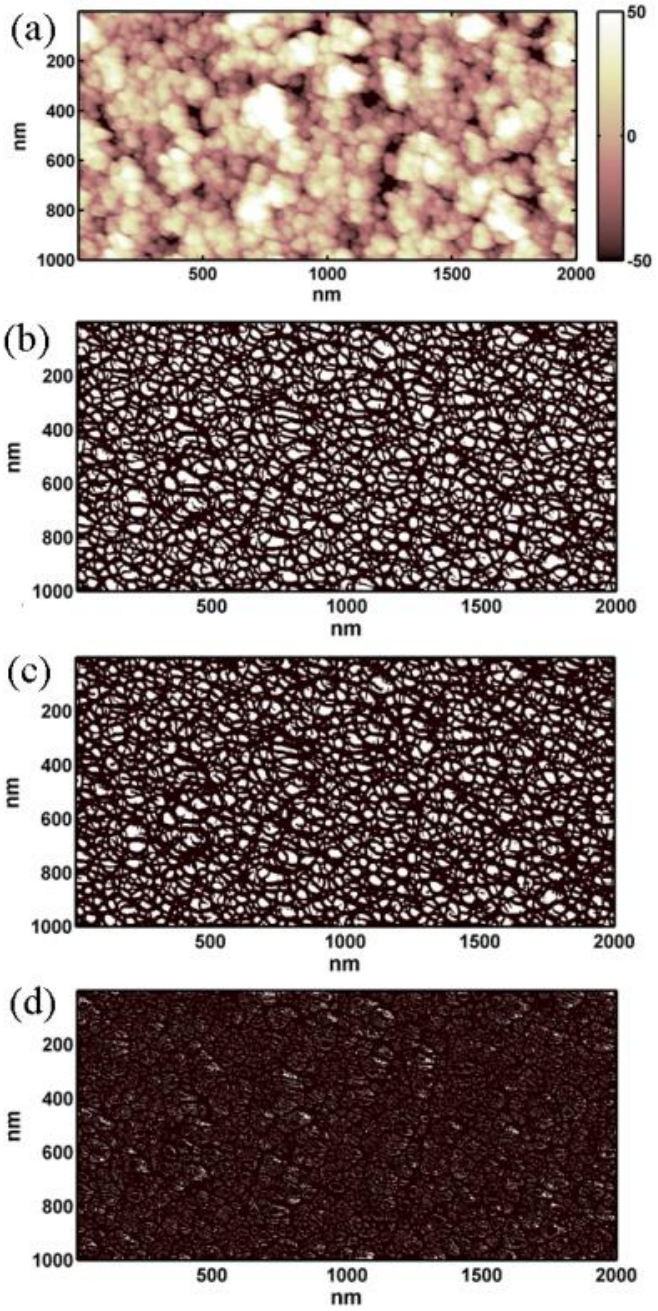

Fig. 48: (a) Representative AFM topographic map of a ns-ZrO_x 168 nm thick film; (b) the same topographic map with a mask obtained with a relaxed filter and a kernel size of 8.4 nm; (c) mask obtained with a tighter filter and a kernel size of 8.4 nm; (d) difference between mask (b) and mask (c). In (b-d) z scale ranges from 0 to 1 nm.

Fig. 49 show masks obtained using a kernel dimension of 2.8 nm (a) or of 17 nm (b). It is evident the difference in the grain size of the objects individualized. Noise may cause a severe fragmentation of the grain map (visible in Fig. 49 (a)), for this reason smoothing of the AFM images with a *n x n* gaussian kernel[27] is an important operation for

the removal of the high frequency noise. In particular, *n* has to be big enough to smooth out inter-grain features, and low enough to avoid that topographic features are gradually mixed together (Fig. 49 (b)) and the original image is transformed.

At the beginning of the analysis a median filter on the whole image has also been performed. This non-linear operation of filtering remove efficiently the salt-and-pepper impulsive noise from the images.

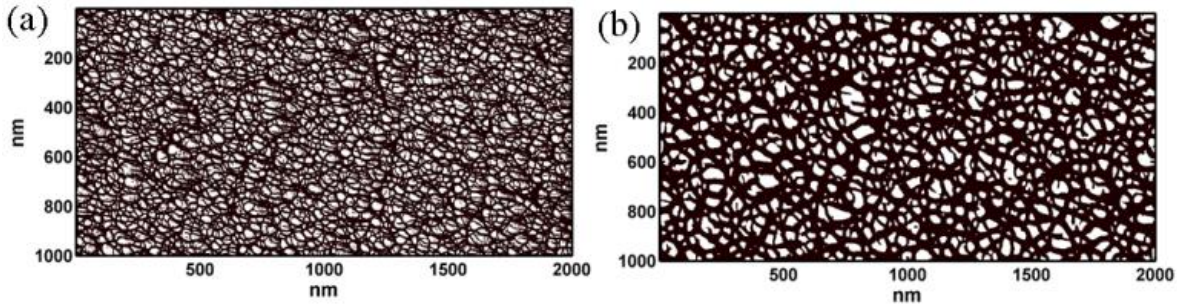

Fig. 49: (a) Mask of Fig. 48(a) obtained with a relaxed filter and a kernel size of 2.8 nm; (b) mask of Fig. 48(a) obtained with a relaxed filter and a kernel size of 17 nm. Z scale ranges from 0 to 1 nm.

Subsequently, the statistical evaluation of geometrical parameters describing the granularity of the surface is performed. The grain radius is calculated as the equivalent radius of each grain area defined by the binary mask, by supposing each grain with a spherical shape.

We have to notice that the determination of the radius is not an accurate quantitative characterization process; in fact AFM maps are affected by the effect of the convolution of the tip with the surface and radius values determination could be partially influenced by the analysis process, as it has been explained before. The level of criticality in the analysis explains also the big value of dispersion associated to the median of the radius distribution shown in Results Section 7.3.

4.3.4. Force Spectroscopy

In a force measurement, the sample is moved up and down below the AFM tip by applying a voltage to the piezoelectric translator, onto which the sample is mounted, while measuring the cantilever deflection (Fig. 50), as the tip-sample distance periodically changes.

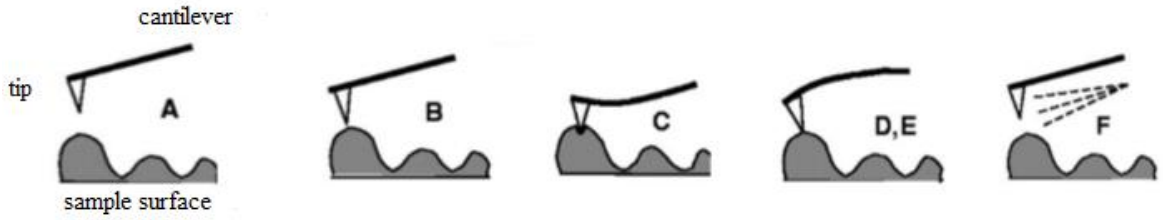

Fig. 50: Movements of the tip in force spectroscopy mode. The tip approaches the surface (A); the first contact point between the tip and the surface is mediated by the attractive Van der Waals forces which induce the attraction of the tip towards the surface (B); when the tip is in contact it applies a constant force on the surface which causes in turn the cantilever deflection (C); hereafter the tip begins to retract from the surface and finish the contact with it (D); different adhesion forces between the tip and th sample prevent the retracting movement of the tip (E); subsequently the tip disconnects from the surface by overcoming the adhesion force (F).

In some AFMs the chip to which the cantilever is attached is moved by the piezoelectric translator rather than the sample.

The first result of a force measurement is a measure of the cantilever deflection, Z_c, versus the relative position of the piezo, Z_p (Fig. 51).

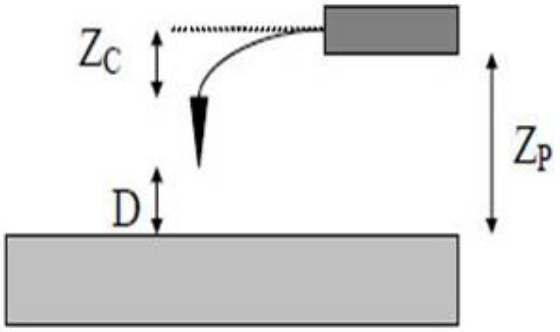

Fig. 51: Representative scheme of the tip-sample distance[16].

To obtain a force-versus-distance curve, Z_c and Z_p have to be converted into force and tip-sample distance. The force F is obtained by multiplying the deflection of the cantilever by its spring constant k_c, $F=k_cZ_c$, calculated by the thermal noise method[16]. The tip-sample separation D is calculated by adding the deflection to the position of the piezo: $D=Z_p+Z_c$, where Z_c is negative or positive, depending whether the cantilever is bent upward or downward. The raw deflection signal from the detector in Volts was converted into a displacement in nm units multiplying by the deflection sensitivity factor α (the inverse of the slope of the contact region of the force curve, acquired on a hard glass surface), $Z_c=\alpha\Delta V$ [16].

We call tip–sample separation D *distance*. In Fig. 52 a typical force-vs-Z_p curve is shown, representative of the steps reported in Fig. 50.

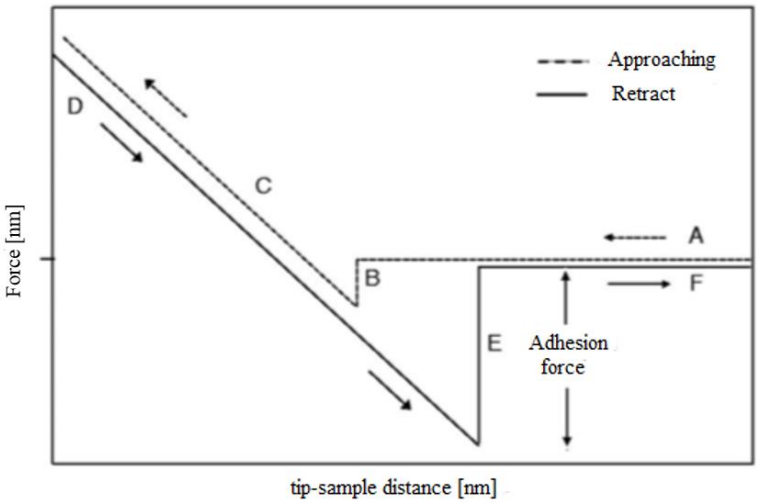

Fig. 52: force-versus- Z_p curve[16].

In this PhD thesis, force spectroscopy measurements have been performed for two main reasons:

1. The characterization of the electrostatic interactions between a colloidal probe and nanostructured surfaces. Deeper details concerning the analysis procedure are reported in Section 4.3.4.2 and 6.1.1.
2. The characterization of the mechanical properties of Au/PDMS nanocomposite, by nanoindentation experiments. In particular, from force-indentation curves the effective Young's modulus of the composite structure formed by the PDMS substrate and the thin nanocomposite Au/PDMS layer is extracted[29], depending solely on the amount of metal clusters implanted in the elastomeric matrix (see Chapter 11 for details).

4.3.4.1. Colloidal probes

The most widely used tips in an Atomic Force Microscopy set-up are the sharp micro-fabricated Si_3N_4 or Si tips. Despite these tips offer a very high spatial resolution, there are some drawbacks which are not negligible:

1. The exact dimension and geometry of the tip are unknown, and consequently it is not possible to utilize simple analytical models for tip-sample interaction in order to fit the data;
2. The contact area between the tip and the surface is very small because of the low radius of curvature. The pressure applied to the substrate is high enough to induce plastic deformation and partially destroy the sample interface;
3. A small contamination attached to the tip can create important changes in the overall tip-surface interaction.

In order to overcome these limitations it has been proposed to attach colloidal tip (Fig. 53) onto the AFM cantilever[30-35].

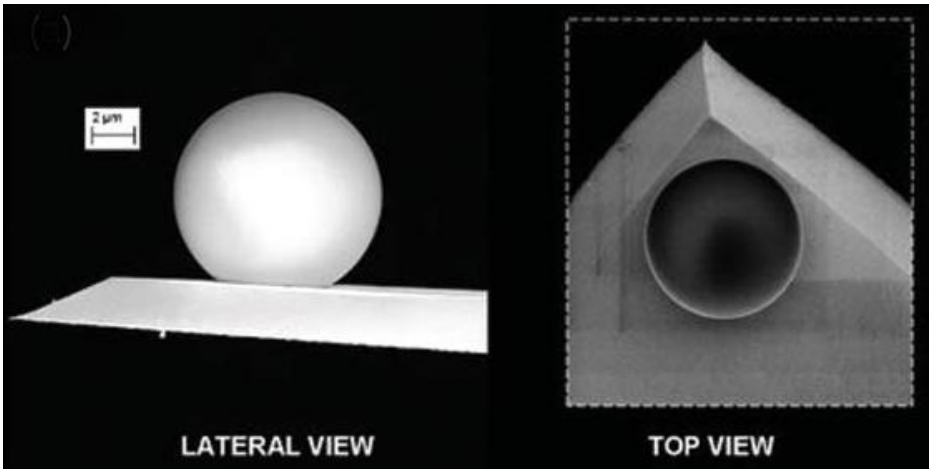

Fig. 53: SEM image of a micrometer spherical probe attached on the top of a cantilever.

These colloidal probes have different advantages:

1. The smooth spherical surface is an ideal interfacial system for the application of analytic models which describe the mechanic contact and electrostatic interactions in the system;
2. The signal/noise ratio is larger thanks to the higher interaction area;
3. It is simpler to functionalize this large spherical tip than sharp little one with chemical group or other functionalization;
4. The pressure applied to the surface is lower;
5. Large spherical probes provide an averaged and robust output, representative of the mesoscopic properties of the interface.

In Ref.[35] a detailed explanation of the production process and calibration of the colloidal tip used during this PhD work is described.

4.3.4.2. DLVO interactions at metal-oxide surfaces: fit procedure

Here below, part of the supporting method of "Nanoscale roughness and morphology affects the IsoElectric Point of titania surfaces" [36] is reported. In particular, details on force curves and curve fitting procedures have been reported. In Section 6.1 a detailed description of the double layer interaction has been proposed.

3. Details on force curves and curve fitting procedures

Typical average force curves, acquired using a borosilicate glass colloidal probe with radius R=2170±65 nm on a flat glass borosilicate surface with [NaCl] varying in the range 0.1-100 mM and fixed neutral pH (≈6.5), are shown in Fig. S4.

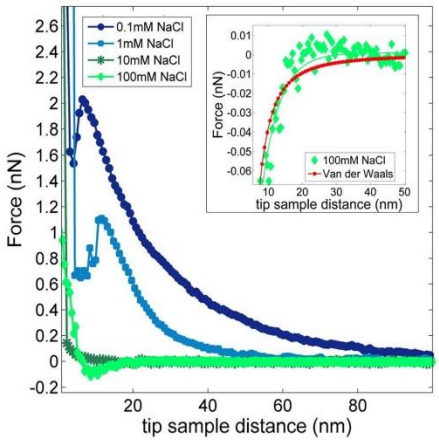

Figure S4. Average force curves between borosilicate glass colloidal probe and a flat borosilicate glass coverslip, acquired in solution with different ionic strength (0.1mM – 100mM NaCl). In the inset it is shown the overlapping between Van der Waals force curve (calculated using $A=0.8*10^{-20}$ J) and the experimental curves in 100mM NaCl solution.

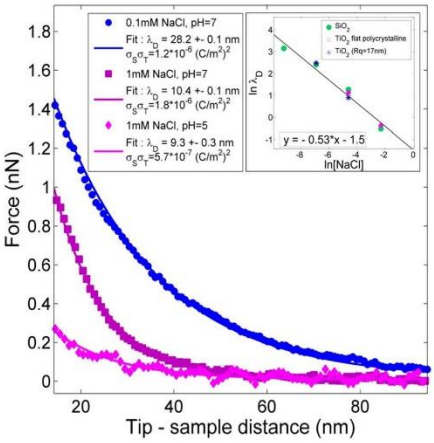

Figure S5. Best fit of average force curves between borosilicate glass colloidal probe and a flat borosilicate glass coverslip, acquired in solution with different ionic strength (0.1mM and 1mM NaCl, pH=7) or with the same ionic strength but different pH (1mM NaCl, pH_1=7 and pH_2=5). In the inset, log plot of the Debye length versus the inverse of the square root of NaCl concentration, calculated in experiments with different substrates.

Error bars on average force data (not shown here, see main text) are calculated summing in quadrature two errors: a statistical error, typically negligible, calculated as the standard deviation of the mean of force values that are averaged, and a systematic error due to the calibration of the AFM cantilever, which is determined considering a 2% error due to deflection sensitivity calibration (see Mats&Methods in the main text) and 5% error due to the force constant calibration. Interpretation of force curves is the following. The tip, approaching the surface, remains in its rest position (constant deflection signal) until at a certain distance from the surface, depending on the ionic strength of the solution, it feels first the long-range electrostatic interaction with the sample surface and subsequently the Van der Waals attraction force [4,5]. An increased salt concentration (or an

increased Ionic strength of the solution) determines a decrease of the electrostatic force, even if the repulsion grows steeper. At the same time, the jump-in due to the Van der Waals attraction, takes place at larger distance from the surface; by increasing the salt concentration it shifts from 7 to 18nm. The smearing of the force curves at short distances is an artifact caused by the averaging process, due to the fact that the jump-in distance fluctuates by several nm from curve to curve; DLVO fit is performed in the large-distance region, typically between 10 and 100 nm, well before the onset of the jump-in. At the highest salt concentration the electrostatic repulsion is completely overwhelmed by Van der Waals attraction; a minimum appears, due to van der Waals force, while only at the shortest distance electrostatic repulsion can be appreciated. An expanded view of this curve is shown in the inset of Fig. S4, together with the Van der Waals contribution evaluated by the second term of Eq. 6 (main text) using $A=0.8\ 10^{-20}$ J.

It is very important to control the pH of the solution before and after AFM measurements in order to check the stability of the system and guarantee the accuracy in the determination of the IEP. It is also important to wait more than fifteen minutes after the immersion of the thin film and tip in the solution and to rinse the surfaces, before and after measurements, with neutral distilled water, in order to reach the equilibrium stability and to restore surface charges. Experimental data confirm that different ionic strengths determine the value of the Debye length according to Eqs. 3,4 without affecting the $\sigma_S\sigma_T$ value, while for the same value of Ionic Strength, $\sigma_S\sigma_T$ decreases with the pH of the solution until the value equals the first IEP of the system. Representative force curves and their best fit (using Eq.6) are shown in Fig. S5. The inset of Fig. S5 shows experimental values of λ_D measured in different salt concentrations solution, with different surfaces (SiO_2, flat polycrystalline TiO_2 and rough ns-TiO_2). λ_D scales as the inverse of the square root of $[NaCl]^{-1/2}$, as predicted by Eq. 4. We have also verified the stability of the solutions characterized by different value of pH during a period of one month, in the pH range between 3 and 7. pH values were checked using a pH meter. We have chosen to fix the 1mM NaCl concentration because it allows us to analyze a large range of pH values without changing Ionic strength of the solution and also because, in a more concentrated solution, the 1:1 electrolyte is no more completely inert for SiO_2 and TiO_2, promoting a shift of the IEP. Furthermore, for 1mM NaCl solution, the Debye length ($\lambda_D \sim 9.6$ nm) is large enough to guarantee a wide interval of electrostatic interaction and a higher signal-to-noise ratio.

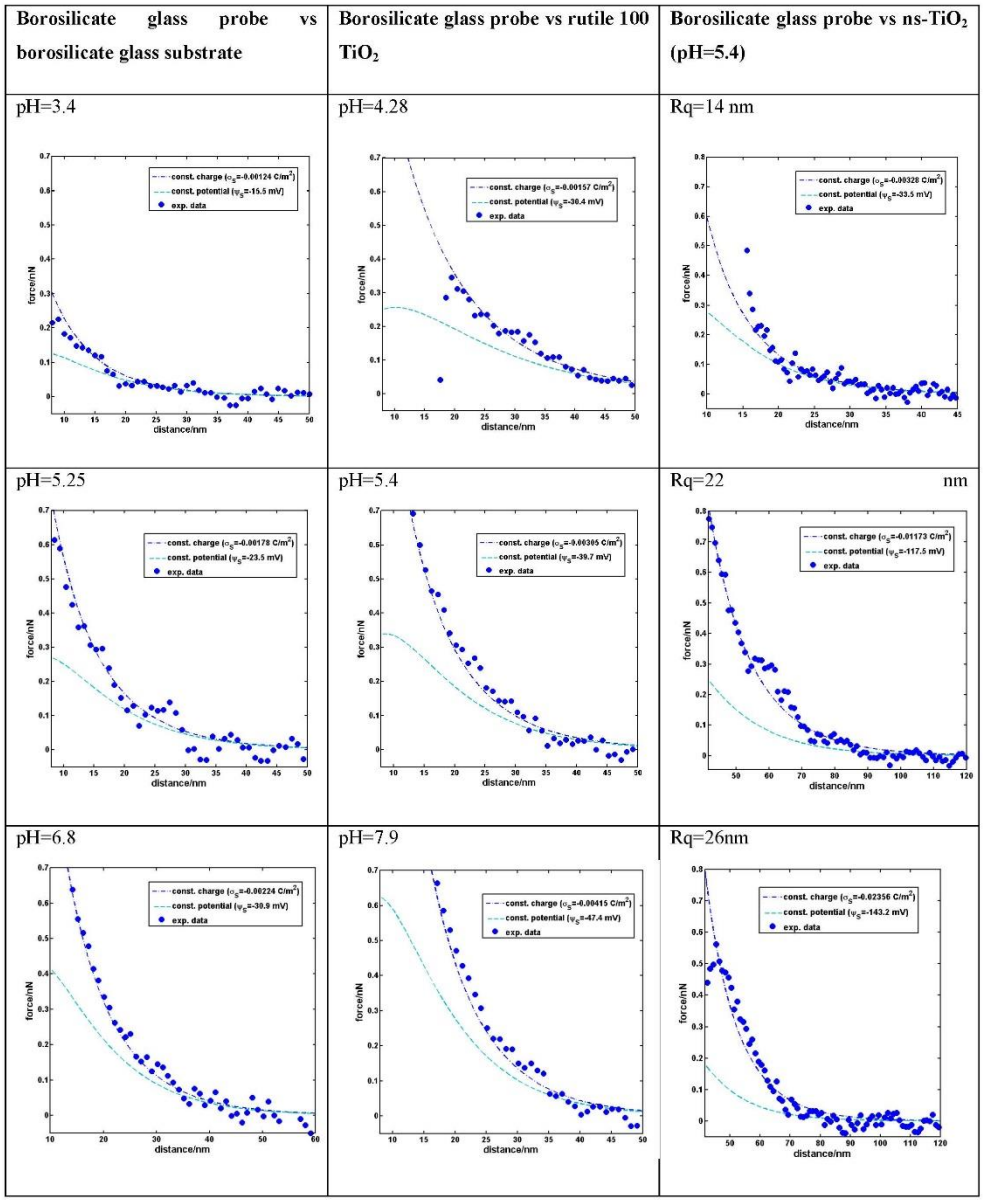

Figure S6. Comparison of force data acquired using a borosilicate glass colloidal probe on borosilicate glass substrate, rutile <100> and nanostructured TiO_2, with constant charge and constant potential curve obtained from nonlinear regression via Eq. 1 and from Eq. 2, using potentials calculated by Grahame equation (Eq. 5).

3.1. Applicability of the constant charge model for DLVO force

We have tested the applicability of the constant charge DLVO force model (Eq. 1 in the text, and its approximation for larger distances, Eq. 6), which is typically found to describe appropriately DLVO interactions between insulating oxide surfaces in aqueous electrolytes. Both constant charge and constant potential models (Eq. 1 and Eq. 2) overlap at distances sufficiently larger than λ_D, where Eqs. 1,2 reduce to a single exponential term whose prefactor contains the product of surface charges or surface potential, depending on the boundary conditions; charge densities and potentials are related by Grahame equation (Eq. 5). We have fitted the force curves by Eq. 1 across a distance range exceeding $1.5\lambda_D$, and used Grahame equation to calculate the diffuse layer potentials from the values of the diffuse charge densities σ_S and σ_T (the AFM probe-borosilicate glass substrate system was considered symmetric, which allowed to determine the absolute charge density of the probe; the latter parameter was kept fixed in fitting curves of other systems). It turned out that constant potential force curves systematically underestimate experimental data (Fig. S6), while the constant charge model could fit data across the complete range of distances (from jumpin to about 50 nm).

3.2. Fitting strategy

Eq. 1 and Eq. 6 overlap at sufficiently large distances; by fitting the force curves data with Eq.6 at distances larger than approximately $1.5\lambda_D$ it was possible to determine the Debye length and the product $\sigma_S\sigma_T$ of charge densities. If one knows the charge density of one of the two surfaces, the other can be determined. In particular, on symmetric systems $\sigma_S \approx \sigma_T$ and therefore $\sigma_T \approx \sqrt{\sigma_S\sigma_T}$. We could therefore characterized the net surface charge density of the colloidal probe from force measurements in aqueous electrolyte on a borosilicate glass substrate (see section 2.1 of file Supporting Text S1); we have then used the values of σ_T at different pH to calculate the absolute net charge density σ_S of crystalline and nanostructured TiO_2 surfaces.

For each sample 100 force curves were typically acquired in six different locations (separated by 100μm) in order to accurately characterize the Debye length and the charge densities of the surfaces. Charge densities and Debye lengths extracted from average force curves of different locations were averaged; their errors were estimated as the 68% confidence interval according to the optimized strategy discussed by Lybanon [6], consisting in repeating the fit on a set of artificial experimental data obtained by summing a Gaussian error to the original data based on errors on both force and distances, then looking at the dispersion of fit parameters obtained. For both Debye

lengths and charge densities, the error δ associated to the averages across different locations was calculated propagating the errors δ_i of the nonlinear regression through the arithmetic mean function, i.e. $\delta = {}^{1}/_{N}\sqrt{\sum_i^N \delta_i^2}$.

9

4. Bibliography

1. Daikhin L I, Kornyshev A A, Urbakh M (1996) Double-layer capacitance on a rough metal surface. Physical Review E 53: 6192-6199. DOI: 10.1103/PhysRevE.53.6192.
2. Indrieri M, Podestà A, Bongiorno G, Marchesi D, Milani P (2011) Adhesive-free colloidal probes for nanoscale force measurements: production and characterization. Rev. Sci. Instrum. 82: 023708-10. DOI: 10.1063/1.3553499.
3. Butt H, Jaschke M (1995) Calculation of thermal noise in atomic force microscopy. Nanotechnology 6: 1-7. DOI: 10.1088/0957-4484/6/1/001.
4. Butt H J, Cappella B, Kappl M (2005) Force measurements with the atomic force microscope: Technique, interpretation and applications. Surface Science Reports 59: 1–152. DOI: 10.1016/j.surfrep.2005.08.003.
5. Leckband D, Israelachvili J (2001) Intermolecular forces in biology. Quarterly Reviews of Biophysics 34: 105-267. DOI: 10.1017/S0033583501003687.
6. Lybanon M (1984) A better least-squares method when both variables have uncertainties. Am. J. Phys. 52: 22-26.

4.4. Protein Surface Interaction Microarray

Traditional techniques used to measure the amount of adsorbed proteins on surfaces, such as Quartz Crystal Microbalance (QCM) and ellipsometry, fail in giving reliable results on rough surfaces[37] making the exploration of the multi-parameter phase space that characterizes the adsorption process even more complicate. In order to overcome this difficulty, and to correlate adsorption data with morphological surface parameters, in Ref [38] they designed an innovative integrated experimental strategy to study protein adsorption.

They developed a novel high-throughput method for studying protein adsorption: Protein-Surface Interaction Microarray (PSIM). PSIM is based on protein array technology and it enables to study in one single experiment hundreds of different protein surface interactions.

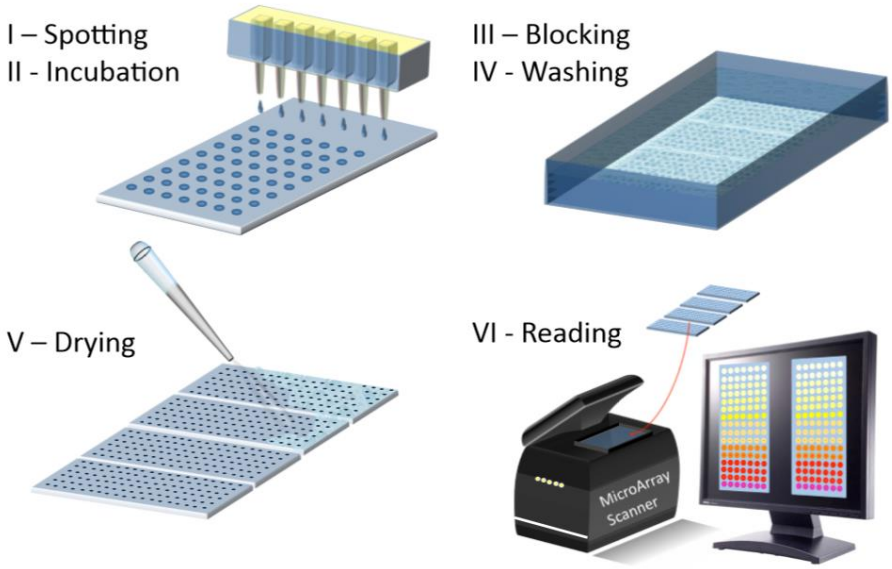

Fig. 54: PSIM protocol-Sketch of the 6 steps PSIM protocol. I)Fluorescent protein solutions, in a wide range of dilution are spotted on several biomaterials in parallel. II) Biomaterial slides are incubated for 1h in controlled atmosphere at 75% humidity. III) Slides are immersed in the blocking solution (BSA 4%) and next IV) rinsed 3 times in PBS and 3 times in MilliQ water. V) They are drayed using a gentle nitrogen flux and VI) the fluorescent signal is read with a commercial microarray scanner [38].

PSIM protocol (Fig. 54) consists in spotting small volume droplets (30 nL) of fluorescent labeled proteins on the sample surface under investigation. After incubation, blocking, washing and drying, the amount of adsorbed proteins is evaluated by reading the fluorescent signal with a commercial microarray scanner. Using PSIM it is possible to compare, on the

same biomaterial sample, the amount of adsorbed proteins for a panel of proteins under various conditions such as protein concentration and pH. Furthermore, since the experiment can be performed in parallel on several biomaterial samples, PSIM allows characterizing the role of surface synthesis parameters in protein immobilization. PSIM is a very flexible method, in each of the 300 drops that can be spotted on a glass slide (25 mm x 75 mm), it is possible to change protein concentration, protein pH, buffer, salt concentration or protein type. The spotter used in their experiments (BioDot 3000) can allocate 8 slides per experiment, giving the possibility to study 2.400 different protein surface interactions in a single experiment. This high number of spots can also be used to make replicates and to produce very good statistics for each interaction. Since the more established techniques allow performing just one measurement of the amount of adsorbed proteins for experiment, PSIM increases by three orders of magnitude the throughput of existing technology for studying protein adsorption.

4.4.1. Langmuir isotherms

Most of the dynamic adsorption models were developed in the field of gas adsorption, but they can be adapted to proteins in a straightforward manner. Here we will present a rather simple but very successful model (the Langmuir model[39]), which is the most used model for interpreting protein adsorption data. It was developed by Irving Langmuir in 1916 to describe the dependence of the surface coverage of an adsorbed gas on the pressure of the gas above the surface at a fixed temperature. The basic idea of this model is that proteins can adsorb only in a monolayer fashion, and that the rate of adsorption and desorption from the surface must coincide at equilibrium. Starting from kinetic considerations:

$$\frac{\partial b(t)}{\partial t} = K_{on}\, C(SU - b) - K_{off}\, b \qquad (18)$$

where b(t) is the fractional occupancy of the adsorption sites, K_{on} and K_{off} are the adsorption and desorption rate constants respectively, C is the bulk protein concentration and SU is the saturation uptake, the total number of available sites on the surface. Equation (18) can be easily solved:

$$\frac{b(t)}{SU} = \frac{K_{on}\, C}{K_{on}\, C + K_{off}} \left(1 - e^{-(K_{on} + K_{off})\, t}\right) \qquad (19)$$

Introducing the equilibrium dissociation constant $K_D = K_{on}/K_{off}$, equation (19) can be rewritten as:

$$\frac{b(t)}{SU} = \frac{K_D\, C}{K_D\, C + 1} \left(1 - e^{-(K_{on} + K_{off})\, t}\right) \qquad (20)$$

so that in equilibrium we find:

$$b_{eq} = \frac{SU}{1+\frac{Kd}{C}} \quad (21)$$

which is the Langmuir isotherm. Reproducing experimentally protein surface adsorption isotherm is quite challenging. In fact, there are technical problems related to sample production and measurement reproducibility, because of the high number of adsorption measurement needed to reproduce the isotherm trend. This requires the capability of synthesizing high number of identical samples and of measuring the amount of adsorbed proteins on each of them. Isotherms are very powerful for analyzing adsorption data, because from the isotherm shape several information can be extracted. The Langmuir isotherms is characterized by two parameters:

- the saturation uptake (SU) that corresponds to the maximum amount of proteins that the surface can load;
- K_D that is inversely proportional to the protein-surface binding affinity.

However it is worth saying that these parameters are independent from the chosen adsorption model. In fact SU and K_D have their own physical meaning also outside the Langmuir model. They represent respectively the level of adsorption saturation, and the concentration for which the isotherm reaches its half maximum.

There is an unsolved paradox in the interpretation of adsorption data[40]. On one hand, protein adsorption depends on protein concentration, increasing protein concentration the amount of adsorbed proteins is increased until reaching saturation, usually following a trend described by Langmuir isotherms. On the other, several works show that proteins are irreversibly adsorbed onto the surface, i.e. they are immobilized. Evidently an irreversible adsorption process can not be concentration dependent, having enough time to interact with the surface, proteins should cover all the surface regardless of the solution concentration. Some attempts of explaining the apparent antithesis between the observed dependence on concentration and irreversible adsorption have been made[37,40,41]:

- proteins may adsorb in two or more distinct orientations in space, with corresponding different surface coverage: for low concentrations, the probability of

the various arrangements are assumed comparable, while as the concentration increases the one which covers more densely the surface become somehow more probable;

- high concentrations may promote a more closely packed arrangement than the randomly deposited one occurring at low bulk concentration[41].

This paradox is accepted in the biomaterials community and different approaches are used to interpret different situations: adsorption isotherms, typical of a system in dynamic equilibrium, are used to analyze adsorption data as a function of protein concentrations and Random Sequential Adsorption (RSA) model, based on irreversible adsorption, is the standard model for describing the adsorption process and calculating protein surface coverage[42].

References

1. Barborini, E., Piseri, P. & Milani, P. A pulsed microplasma source of high intensity supersonic carbon cluster beams. *J. Phys. Appl. Phys.* **32,** L105 (1999).
2. Tafreshi, H. V., Piseri, P., Benedek, G. & Milani, P. The Role of Gas Dynamics in Operation Conditions of a Pulsed Microplasma Cluster Source for Nanostructured Thin Films Deposition. *J. Nanosci. Nanotechnol.* **6,** 1140–1149 (2006).
3. Piseri, P., Podestà, A., Barborini, E. & Milani, P. Production and characterization of highly intense and collimated cluster beams by inertial focusing in supersonic expansions. *Rev. Sci. Instrum.* **72,** 2261 (2001).
4. Bongiorno, G. *et al.* Nanocrystalline Metal/Carbon Composites Produced by Supersonic Cluster Beam Deposition. *J. Nanosci. Nanotechnol.* **5,** 1072–1080 (2005).
5. Bongiorno, G. *et al.* Nanostructured CNx ($0 < x < 0.2$) films grown by supersonic cluster beam deposition. *Carbon* **43,** 1460–1469 (2005).
6. Diederich, L. *et al.* Supercapacitors based on nanostructured carbon electrodes grown by cluster-beam deposition. *Appl. Phys. Lett.* **75,** 2662–2664 (1999).
7. Mazza, T. *et al.* Libraries of cluster-assembled titania films for chemical sensing. *Appl. Phys. Lett.* **87,** 103108 (2005).
8. Bruzzi, M. *et al.* First study of humidity sensors based on nanostructured carbon films produced by supersonic cluster beam deposition. *Sens. Actuators B Chem.* **100,** 173–176 (2004).
9. Carbone, R. *et al.* Biocompatibility of cluster-assembled nanostructured TiO2 with primary and cancer cells. *Biomaterials* **27,** 3221–3229 (2006).
10. *Atomic and molecular beam methods*. (Oxford University Press, 1988).
11. Tafreshi, H. V. *et al.* A Simple Nozzle Configuration for the Production of Low Divergence Supersonic Cluster Beam by Aerodynamic Focusing. *Aerosol Sci. Technol.* **36,** 593–606 (2002).
12. Vahedi Tafreshi *et al.* Aerodynamic focusing of clusters into a high intensity and low divergence supersonic beam. *Eur. Phys. J. - Appl. Phys.* **16,** 8 (2001).
13. Kubart, T., Nyberg, T. & Berg, S. Modelling of low energy ion sputtering from oxide surfaces. *J. Phys. Appl. Phys.* **43,** 205204 (2010).
14. Yamamura, Y. & Tawara, H. Energy dependence of ion-induced sputtering yields from monoatomic solids at normal incidence. *At. Data Nucl. Data Tables* **62,** 149–253 (1996).
15. Binnig, G., Rohrer, H., Gerber, C. & Weibel, E. Surface Studies by Scanning Tunneling Microscopy. *Phys. Rev. Lett.* **49,** 57–61 (1982).
16. Butt, H.-J., Cappella, B. & Kappl, M. Force measurements with the atomic force microscope: Technique, interpretation and applications. *Surf. Sci. Rep.* **59,** 1–152 (2005).

17. Binnig, G., Quate, C. F. & Gerber, C. Atomic Force Microscope. *Phys. Rev. Lett.* **56,** 930–933 (1986).
18. Wiesendanger, R. *Scanning probe microscopy and spectroscopy: methods and applications*. (Cambridge University Press, 1994).
19. Meyer, G. & Amer, N. M. Erratum: Novel optical approach to atomic force microscopy [Appl. Phys. Lett. 53, 1045 (1988)]. *Appl. Phys. Lett.* **53,** 2400–2402 (1988).
20. Alexander, S. *et al.* An atomic-resolution atomic-force microscope implemented using an optical lever. *J. Appl. Phys.* **65,** 164–167 (1989).
21. Cappella, B. & Dietler, G. Force-distance curves by atomic force microscopy. *Surf. Sci. Rep.* **34,** 1–104 (1999).
22. Limpert, E., Stahel, Werner A. & Abbt, M. Log-normal Distributions across the Sciences: Keys and Clues. *BioScience* **51,** 341–352 (2001).
23. Granqvist, C. G. & Buhrman, R. A. Statistical model for coalescence of islands in discontinuous films. *Appl. Phys. Lett.* **27,** 693 (1975).
24. Colombi, P., Alessandri, I., Bergese, P., Federici, S. & Depero, L. E. Self-assembled polystyrene nanospheres for the evaluation of atomic force microscopy tip curvature radius. *Meas. Sci. Technol.* **20,** 084015 (2009).
25. Shiramine, K. *et al.* Tip artifact in atomic force microscopy observations of InAs quantum dots grown in Stranski-Krastanow mode. *J. Appl. Phys.* **101,** 033527 (2007).
26. Daikhin, L. I., Kornyshev, A. A. & Urbakh, M. Double-layer capacitance on a rough metal surface. *Phys. Rev. E* **53,** 6192–6199 (1996).
27. Podestà, A. Development of protocols for a quantitative characterization of morphological and tribological properties of nanostructured films via the atomic force microscopy. (Università degli Studi di Milano, 2001).
28. Pagani, C. D. & Salsa, S. *Analisi matematica. Vol. 2*. (Masson, 1993).
29. Niklaus, M. & Shea, H. R. Electrical conductivity and Young's modulus of flexible nanocomposites made by metal-ion implantation of polydimethylsiloxane: The relationship between nanostructure and macroscopic properties. *Acta Mater.* **59,** 830–840 (2011).
30. Ducker, W. A., Senden, T. J. & Pashley, R. M. Direct measurement of colloidal forces using an atomic force microscope. *Nature* **353,** 239–241 (1991).
31. Pedersen, H. G. Aluminum Oxide Probes for AFM Force Measurements: Preparation, Characterization, and Measurements. *Langmuir* **15,** 3015–3017 (1999).
32. Hook, M. S., Hartley, P. G. & Thistlethwaite, P. J. Fabrication and Characterization of Spherical Zirconia Particles for Direct Force Measurement Using the Atomic Force Microscope. *Langmuir* **15,** 6220–6225 (1999).

33. Ralston, J., Larson, I., Rutland, M. W., Feiler, A. A. & Kleijn, M. Atomic force microscopy and direct surface force measurements (IUPAC Technical Report). *Pure Appl. Chem.* **77,** (2005).
34. Mak, L. H. *et al.* Reproducible attachment of micrometer sized particles to atomic force microscopy cantilevers. *Rev. Sci. Instrum.* **77,** 046104 (2006).
35. Indrieri, M., Podestà, A., Bongiorno, G., Marchesi, D. & Milani, P. Adhesive-free colloidal probes for nanoscale force measurements: production and characterization. *Rev. Sci. Instrum.* **82,** 023708 (2011).
36. Borghi, F., Vyas, V., Podestà, A. & Milani, P. Nanoscale Roughness and Morphology Affect the IsoElectric Point of Titania Surfaces. *PLoS ONE* **8,** e68655 (2013).
37. Rechendorff, K., Hovgaard, M. B., Foss, M., Zhdanov, V. P. & Besenbacher, F. Enhancement of Protein Adsorption Induced by Surface Roughness. *Langmuir* **22,** 10885–10888 (2006).
38. Scopelliti, E. Development and application to nanostructured surfaces of novel quantitative high-throughput methods for studying protein-surface interaction. (Università degli Studi di Milano, 2009).
39. Langmuir, I. The constitution and fundamental properties of solids and liquids. Part I. Solids. *J. Am. Chem. Soc.* **38,** 2221–2295 (1916).
40. Ramsden, J. J. Puzzles and paradoxes in protein adsorption. *Chem. Soc. Rev.* **24,** 73–78 (1995).
41. Nakanishi, K., Sakiyama, T. & Imamura, K. On the adsorption of proteins on solid surfaces, a common but very complicated phenomenon. *J. Biosci. Bioeng.* **91,** 233–244 (2001).
42. Talbot, J., Tarjus, G., Van Tassel, P. R. & Viot, P. From car parking to protein adsorption: an overview of sequential adsorption processes. *Colloids Surf. Physicochem. Eng. Asp.* **165,** 287–324 (2000).

5. Transition-metal oxides clusters and nanostructured films

The development of new technologies based on micro and nano components[1,2] in different interdisciplinary fields ask for a precise control and simple manipulation of the interface morphological properties at different length scale. Parameters such as surface roughness[4,5] and substrate topography[6,7] are important for cells to sense and adapt to a surface and to activate specific intracellular signals[8,9] or for create the best conditions for proteins adsorption and nucleation[10]; high surface area has significant advantage in catalysing gas reactions due to the increased adsorption capacity[11] and can often provide more active sites thus giving higher catalytic activity[12].

The nanostructured surface of biocompatible materials strongly influences the adhesion and proliferation of mammalian cells on solid substrates. The observation of these phenomena has led to an increased effort to develop new strategies to prevent bacterial adhesion and biofilm formation, primarily through nanoengineering the topology of the materials used in implantable devices. For example, in Ref[13] they have shown that the increase in surface pore aspect ratio and volume, related to the increase of surface roughness, improves protein adsorption, which in turn downplays bacterial adhesion and biofilm formation.

Protein adsorption on a solid artificial surface is a fundamental phenomenon that determines the biological response of a living organism entering any implant material[14,15]. The adsorbed proteins are the mediator in the interactions between cells and implants. Proteins adsorbed stimulate intracellular specific processes which determine cell adhesion and dispersion, its shape and growth and cellular differentiation[15]. Active studies during recent years in the field of biomolecular materials show that the non-covalent (long-range electrostatic and short-range van der Waals) interactions between the protein and the artificial surface are major factors in the protein adsorption. Calculations in Ref.[16] suggests that the nanostructured surface possesses area of high charge density, while the smooth areas have a lower variation of surface charge density. These nanostructured surfaces are expected to provide sufficiently strong binding of proteins to the surface and provide the necessary protein orientation[16]. In Ref[10] it is experimentally shown that the increase of nanoscale roughness (from 15 nm to 30 nm) induces a decrease of protein binding affinity

(≤90%) and a relevant increase in adsorbed proteins (≥500%) beyond the corresponding increase of specific area. They demonstrated that these effects are caused by protein nucleation on the surface, which is promoted by surface nanoscale pores. Furthermore, in Ref [17] they have shown that the films, resulting from a random stacking of nanoparticles, are characterized, at the nanoscale, by a granularity and porosity mimicking those of recently observed ECM structures.

5.1. Titanium dioxide

Titanium dioxide (TiO_2) exists in nature in three major crystalline structures: rutile, anatase, and brookite [18-20], only rutile and anatase have properties of interest for applications so that they have been extensively characterized[18-20]. Rutile is thermodynamically stable and it can be obtained by thermal annealing of amorphous titania which transforms into anatase at moderate temperatures; in the bulk, the transition to rutile takes place around 800–1000 °C [21].

As a well-known functional material, titanium dioxide has been widely used as a white pigment in paints, food colouring, cosmetics, and toothpastes. Since the first report of photocatalytic splitting of water on a TiO_2 electrode under ultraviolet (UV) light in 1972[22], TiO_2 has been extensively studied and remained one of the most important candidates used as photovoltaic cells, photocatalysis, photodegradation, electrochromic devices etc, [23-29] due to its excellent biocompatibility, low cost and low toxicity, and high chemical stability. Among all the applications, the medical applications of TiO_2 are undoubtedly promising, which may play an important role in the improvement of health care, especially cancer treatment[30]. Titanium dioxide, thanks to its properties, is currently widely employed as low-cost material also in several applications for sensors[31], coatings with controlled-wettability (superhydrophilic, amphiphilic, and antifogging surfaces; self-cleaning coatings)[32,33], optical coatings[34,35], antimicrobial coatings and biocompatible substrates for cell culture, prosthesis and implantations[36-38].

5.1.1. Ns-TiO_x

SCBD has been used to grow nanostructured TiO_2 films[17,39-43]. In this Section I report the main results of Ref.[44]. Titania clusters are generated by a pulsed microplasma cluster source (PMCS). Deposition occurs under high vacuum conditions. The as-deposited films, after exposition to air, are stoichiometric[39,40]. During the expansion of the cluster beam an

aerodynamic mass separation takes place causing the divergence of smaller clusters away from the beam axis, while larger clusters concentrate in the central part of the beam[45,46] (see Section 4.1.3). Typically the thickness in the central part of the deposited film is about 500 nm, whereas at the periphery the film has a thickness of about 200 nm. They have investigated the microstructure and surface morphology of the cluster-assembled films by atomic force microscopy. The crystalline phases and phase transformations were characterized by means of Xray diffraction (XRD). Annealings of the films deposited on a silicon substrate were performed inside a cylindrical furnace by holding the samples on a cylindrical quartz tube with open ends under ambient atmosphere. The samples were annealed for 4 h at temperatures of 400, 600, 800 °C.

The XRD spectra of the as-deposited and annealed nanostructured TiO_2 films are reported in Fig. 55. A broad diffraction peak at around $2\theta \approx 26.0°$ in the spectrum of the as-deposited films can be attributed to the diffraction from randomly oriented nanocrystallites. The high background intensity observed in this spectrum can be caused by defects, porous structure and the presence of an amorphous phase[47,48]. The very broad feature in the low angle scattering region suggests that the amorphous structure is the dominant factor for the high background intensity[47]. Annealing at 400 °C causes the crystallization and growth of nanoparticles and the amorphous-to-anatase transition (Fig. 55).

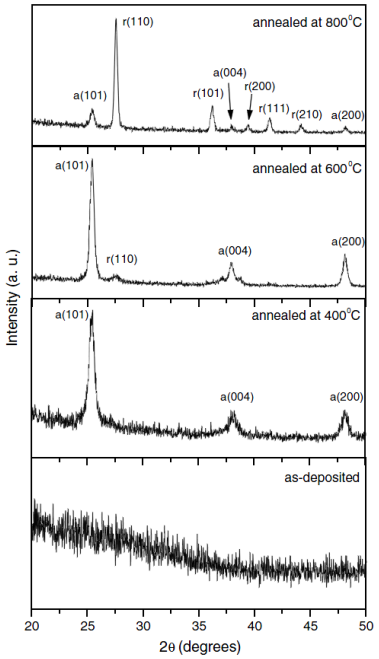

Fig. 55: X-ray diffraction spectra of the nanostructured TiO_2 films. The spectra demonstrate the

structural phase evolution from amorphous (as-deposited) to anatase (a) and rutile (r) phases under thermal annealing[44].

The low intensity amorphous peak is replaced by an intense and sharp peak at about $2\theta \approx 25.4°$ which can be attributed to the anatase phase[48]. The XRD spectrum of the sample annealed at 600 °C is characterized by the appearance of low intensity diffraction peaks typical of the rutile phase coexisting with anatase. This behavior indicates that the onset of the anatase-to-rutile phase transition occurs below T = 600 °C as observed for other nanostructured TiO_2. materials[49]. After annealing at 800 °C the sample is mainly rutile with a minor amount of anatase evidenced by the low intensity peak at $2\theta = 25.4°$. The weight fraction of the rutile phase changes from 5% at 600 °C to 90% at 800 °C. The size of the anatase nanocrystallites after annealing at 400, 600 and 800 °C is roughly 29, 39 and 42 nm, respectively, as determined by Scherrer's equation[50]. The growth of anatase nanograins can be considered as the result of conventional grain growth processes during thermal treatment[51]. During the annealing the anatase nanocrystals coarsen and when their size reaches a critical value they transform to stable rutile phase. This behavior has been described by the critical-nuclear-size model[52]. According to this model the rutile crystallites cannot grow until the nucleus size of this phase reaches a critical value; this requires the agglomeration of fine-grained anatase particles into larger ones. The growth of anatase nanocrystallites beyond the critical size is energetically not favourable since anatase has a higher total energy compared to rutile. Further growth of anatase grains during thermal annealing at 800 °C is unlikely and the transformation to rutile takes place. This is confirmed by the drastic decrease in the weight fraction of the anatase components after annealing at 800 °C. In contrast to the anatase, during the annealing at this temperature the rutile grains grow very fast. The mean size of rutile grains increases from 49 nm after annealing at 600 °C up to 164 nm after annealing at 800 °C. TEM analysis of the as-deposited nanostructured films confirms that cluster-assembled titania is formed by nanocrystals and an amorphous phase. The size of the nanocrystals ranges from several tens of nanometers to a few nanometers depending on the position in the film. The amorphous fraction is uniformly distributed and it becomes the dominant fraction at the film periphery. In Fig. 56(a) a TEM micrograph of the central region of a film is reported showing nanograins randomly assembled to constitute a porous structure typical of the ballistic deposition regime[53].

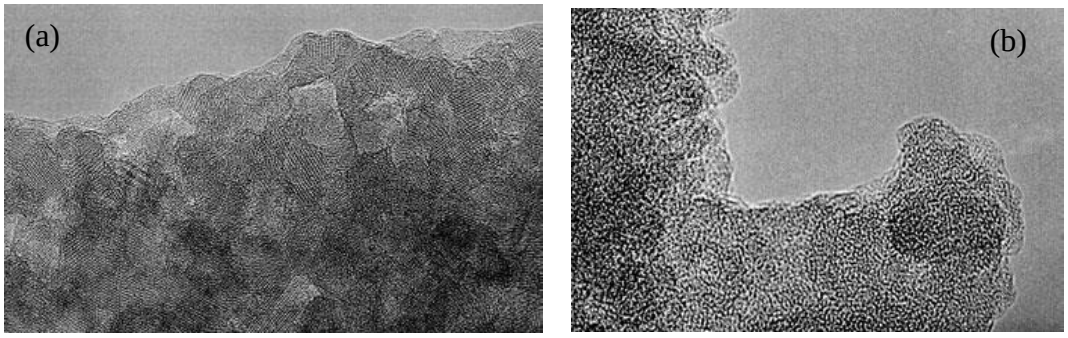

Fig. 56: TEM micrographs of an as-deposited film. (a) In the central part of the film the deposited clusters form randomly oriented nanocrystalline structures. (b) The peripheral regions are mainly amorphous[44].

The nanoparticle lattice spacings are consistent with nanocrystalline TiO_2. Moving from the film center to the periphery, the grain dimension decreases until the amorphous phase becomes predominant (Fig. 56(b)) since large precursor clusters remain confined in the central region of the seeded beam. Fig. 57 shows the film nanostructure after annealing at 800 °C.

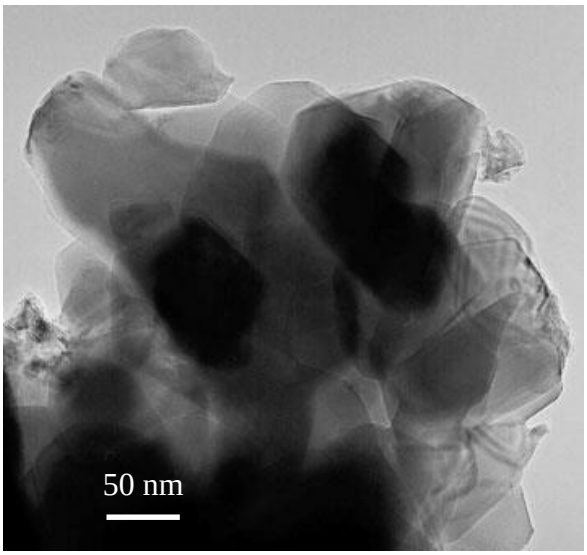

Fig. 57: TEM micrograph of the crystalline TiO_2 nanograins after annealing at 800 °C [44].

The film is composed of well-crystallized grains with dimensions of the order of 100 nm. The evolution of surface morphology, roughness and granularity has been characterized by AFM. Fig. 58 (a1) – (a2) shows the structure for two as-deposited film regions grown with different cluster size distributions. The evolution upon annealing is reported in Fig. 58 (b1)-(b2) where the same regions characterized in Fig. 58 (a1) – (a2) are shown.

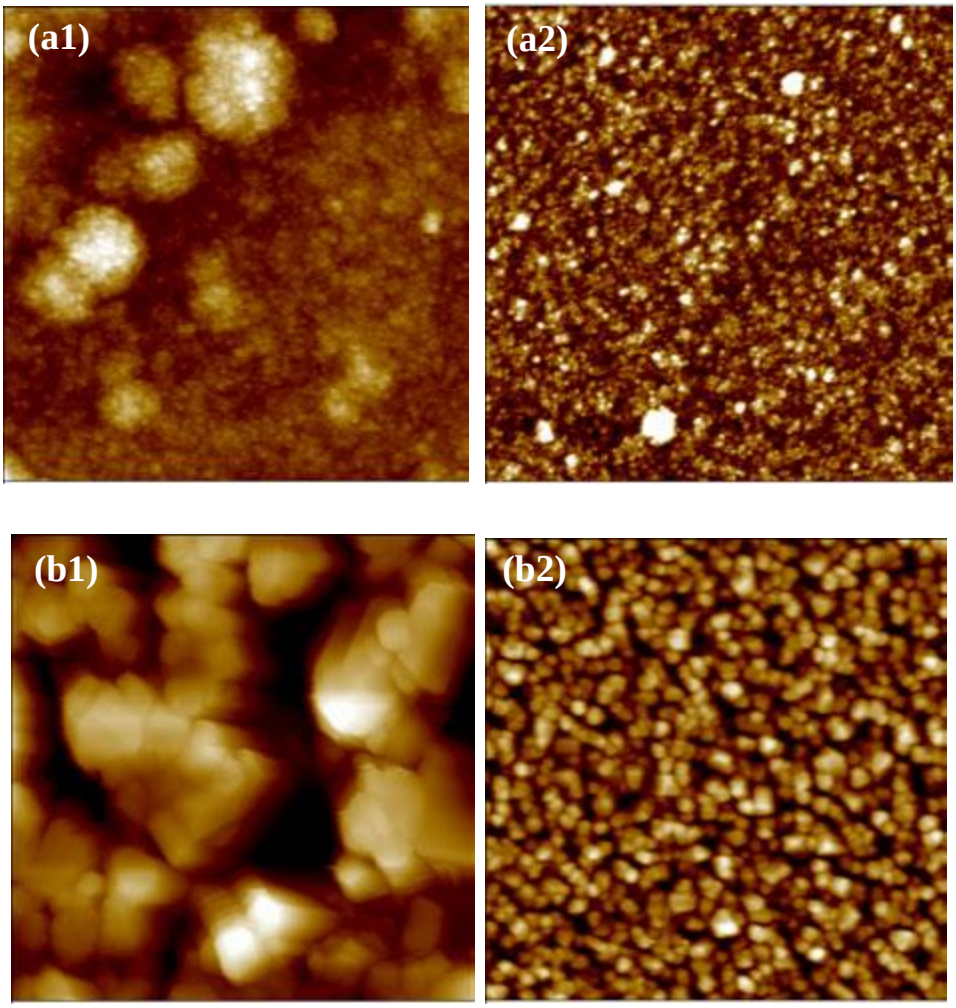

Fig. 58: AFM images of three as-deposited TiO_2 regions consisting of different cluster size distributions. We have imaged two different positions on the film starting from the center and going towards the periphery (from (a1) to (a2)). The regions are separated by roughly 1 cm. (a1)-(a2) are low magnification *(*$2 \times 2\ \mu m^2$*)* images; (b1)-(b2) AFM images of the same TiO_2 regions as reported on in Fig. (a1)-(a2) after annealing at 800 °C [44].

Regions grown from different precursor clusters evolve towards different morphologies both on the micrometer and on the nanometer scale (Fig.s 58(a1–2)). Although having the same granularity when deposited, the original nanograins transform into polyhedral particles with different dimensions, accounting for the crystallization of nanostructured TiO_2 into a polycrystalline material (Fig.s 58(b1–2)). Agglomeration of nanoparticles tends to form islands and well-oriented crystalline structures: the oriented agglomeration of anatase crystallites favors the growth of twin structures as observed in Fig. 58(a). Interfacial regions appearing as a result of such agglomeration of anatase nanocrystallites can serve as sites of nucleation of rutile[54]. Moreover, the decreased activation barrier for formation of

the rutile nucleus at such interfaces is a likely cause of the lowering in temperature of the anatase-to-rutile phase transformation, compared to that in coarse TiO_2 materials. The crystallite dimensions and packing are different and they appear to be related to the precursor dimensions. This correlation indicates that the evolution of the nanostructure and microstructure of the films is influenced by the structure of the precursor clusters even after a quite severe annealing.

5.2. Zirconium dioxide

Zirconium dioxide (ZrO_2), which is also known as zirconia, is a polymorphic material and occurs in three phases: monoclinic, tetragonal and cubic. The monoclinic phase is stable at room temperature up to 1170° C, the tetragonal at temperatures of 1170-2370° C and the cubic at over 2370° C [55,56]. Tetragonal and cubic zirconia possess superior mechanical properties but undergo low temperature degradation (LTD) in water or water vapor[57,58]. LTD can reduce the mechanical strength and service life of the zirconia-based materials[59,60]. The phase transformation, taking place while cooling, is associated with a volume expansion of approximately 3-4%. Stresses generated by the expansion originate cracks in pure zirconia ceramics, that after sintering in the range 1500-1700° C, break into pieces at room temperature[61]. LTD, which depends on the microstructure and the fabrication process, is accelerated by micro-cracks, high roughness and pores[57,58,59]. Monoclinic zirconia is more stable at room temperature than cubic and tetragonal zirconia: the calculated energy versus volume data at absolute zero temperature confirmed the higher stability of the monoclinic phase[62]. The thermal stability of monoclinic zirconia could however be improved significantly by addition of various oxides: CaO, Y_2O_3, La_2O_3, all led to an improvement in the thermal stability of the Partially Stabilized Zirconia (PSZ) up to 900°C, while MgO exhibited stabilizing properties only up to 700°C [63].

Zirconia is an important ceramic material with attractive mechanical properties, similar to those of stainless steel. In fact it's resistance to traction can be as high as 0.9 - 1.2 GPa and its compression resistance is about 2 GPa[61]. These mechanical properties and corrosion resistance in biological environments make zirconia a material of choice for orthopaedic prosthesis and dental restorative applications[64-66]. Chemical and dimensional stability[11,67], mechanical strength, toughness, and Young's modulus alloys make zirconia an excellent ceramic biomaterial for use as a femoral head[68]. Zirconium dioxide is an interesting material also for its electrical and optical properties[69], for thin-film coating[9,70]

and for catalytic applications[71-75] and of great relevance for its extensively evaluated biocompatibility[76].

The first paper concerning biomedical application of zirconia was published in 1969 by Helmer and Driskell[77], while the first paper concerning the use of zirconia to manufacture ball heads for Total Hip Replacements (THR), which is the current main application of this ceramic biomaterial, was introduced by Christel et al.[78]. Some studies have demonstrated that fewer bacteria accumulate around zirconia than titanium[79-81]. This could be possibly explained by different protein adsorption properties[82]. Zirconium oxide may be a suitable material for manufacturing implant abutments with a low bacterial colonization potential[81].

Zirconia is currently attracting considerable interest as support material in a variety of catalyst systems[83,84]. In most of the cases this interest can be ascribed to at least one of the following two properties: as a carrier, it gives rise to an unique kind of interaction between the active phase and support, and as support, it is more chemically inert than the classical supports (Al_2O_3 and SiO_2).

5.2.1. Ns-ZrO_x

Ns-ZrO_2 deposited by SCBD compose a highly porous matrix cluster-assembled film (see Fig. 59), whose structural properties can be changed by a thermal annealing treatments[85]. A fine quantitative characterization of the incident cluster dimensions is reported in the Chapter of Results of this Thesis.

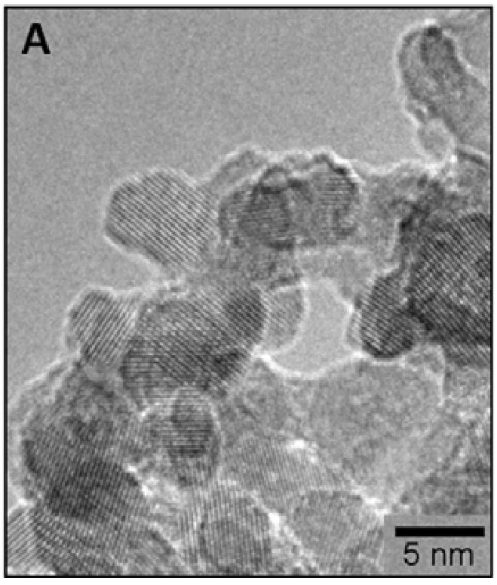

Fig. 59: TEM micrograph of a region of a cluster-assembled ZrO_2 film[8].

The works of Ref.s[8,85] demonstrated the fabrication of nanostructured cubic zirconia films by supersonic cluster beam deposition at room temperature. In particular, Ref.[85] shows that the transition from cubic to monoclinic phase, as well as the nanocrystals growth, are driven by the combined contribution of temperature and oxygen provision.

The annealing experiments were performed either in air and in low vacuum (~ 10^{-3} mbar), in order to assess the role of the oxygen abundance in the phase transformation and in the change of nanocrystal size. The increase of temperature is then expected to favor the transition from the metastable cubic phase to the stable monoclinic phase in the considered range of temperatures, but even the amount of the available molecular oxygen can foster the phase transition by promoting the fully oxidation of the sample. The mutual occurrence of thermal energy and oxidizing environment also leads to the coalescence of adjoining nanocrystallites. Fig. 60 reports the fractions of the cubic and monoclinic phases as a function of the annealing temperature. The top panel shows the behavior in vacuum, whereas the bottom one in air.

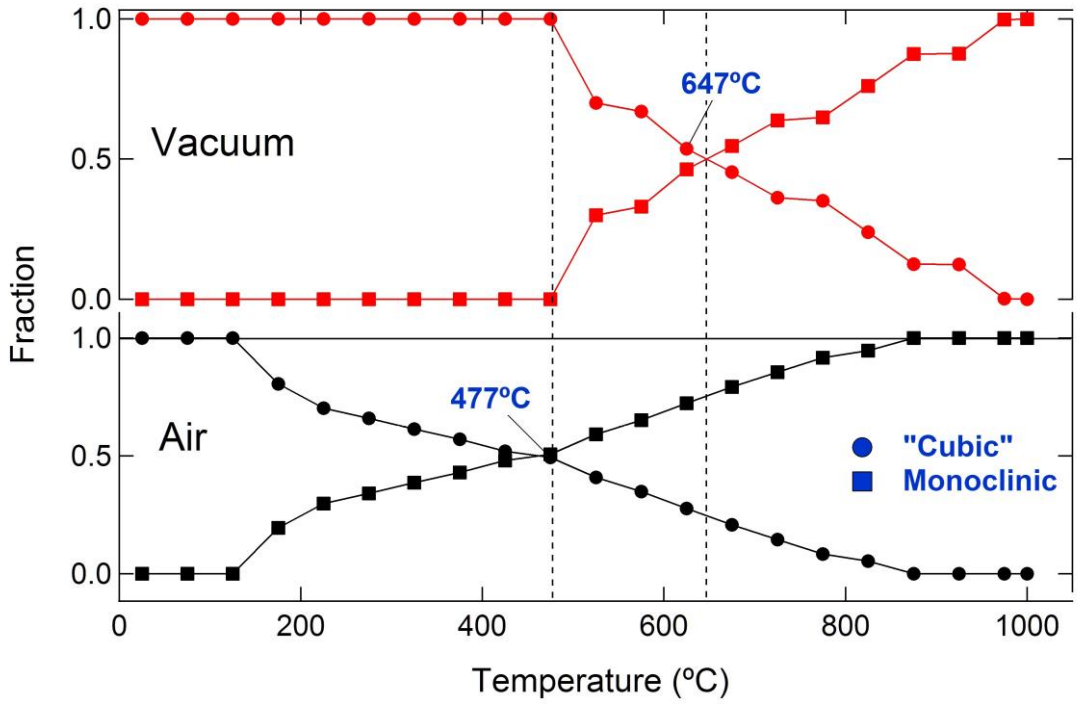

Fig. 60: Fractions of the cubic and monoclinic phases as a function of the annealing temperature [85].

As the temperature increases, the plots reveal the appearance of the monoclinic phase and the decreasing of the cubic phase. The arising of the stable phase takes place at 190 °C and 480 °C in air and in vacuum respectively. The transformation rate appears to be more high in the case of vacuum condition, in fact the presence of the 50% of each fraction happens

at 475 °C and 645 °C in air and in vacuum respectively, whereas the phase transformation is completed at 875 °C in air and at 975 °C in vacuum. The observed different rapidity indicates that once the transformation is primed the temperature is the main ruler of the process. However it is interesting to observe as the same thermal treatment is operated in air and in low vacuum the trigger of the phase transformation is not only due by the temperature but also by the abundance of oxygen. Thus, even if the data are related to the followed heating-up protocol, it can be argued that the oxygen has a fundamental role in the phase change as well as in the aggregation of the nanocrystals.

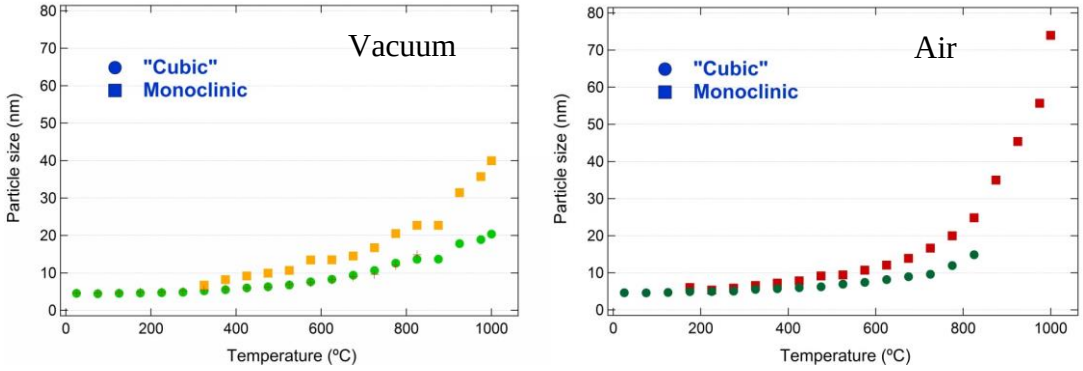

Fig. 61: ZrOx particle size depending on annealing temperature and oxidizing environment, by XRD analysis[85].

Figure 61 shows the nanocrystal dimension of the cubic and monoclinic phases as a function of the annealing temperature. In the pristine sample the dimension of the crystallites is around 5 ˚A, in good agreement with the mean value obtained with the analysis of the grain size distribution from TEM images (6.0±1.7 nm). The nanocrystals in cubic phase grow up to 18-20 nm in both cases whereas the nanonocrystals in monoclinic phase keep on growing.

From Figure 61 it can be also observed as the annealing in more oxidizing environment favors the nanocrystal growth, reaching at about 1000 °C a size double (~80 nm) with respect to the vacuum case (~40 nm). These results suggest that ns-ZrO_{2-x} in reducing environment can preserve the crystalline cubic structure even if operate at high temperature. This behavior is compliant for example with the application of these materials as supports for chemical reactions, i.e. catalysis, requiring high operational temperatures or as coating of device exhibiting high local thermal gradients.

References

1. Staples, M., Daniel, K., Cima, M. J. & Langer, R. Application of Micro- and Nano-Electromechanical Devices to Drug Delivery. *Pharm. Res.* **23,** 847–863 (2006).
2. Kautt, M., Walsh, S. T. & Bittner, K. Global distribution of micro–nano technology and fabrication centers: A portfolio analysis approach. *Technol. Forecast. Soc. Change* **74,** 1697–1717 (2007).
3. *Sensors: a comprehensive survey*. (VCH, 1989).
4. Zeng, H. C. Preparation and integration of nanostructured titanium dioxide. *Curr. Opin. Chem. Eng.* **1,** 11–17 (2011).
5. Truong, V. K. *et al.* The influence of nano-scale surface roughness on bacterial adhesion to ultrafine-grained titanium. *Biomaterials* **31,** 3674–3683 (2010).
6. Wegner, K., Piseri, P., Tafreshi, H. V. & Milani, P. Cluster beam deposition: a tool for nanoscale science and technology. *J. Phys. Appl. Phys.* **39,** R439–R459 (2006).
7. Piseri, P., Podestà, A., Barborini, E. & Milani, P. Production and characterization of highly intense and collimated cluster beams by inertial focusing in supersonic expansions. *Rev. Sci. Instrum.* **72,** 2261 (2001).
8. Singh, A. V. *et al.* Bottom-up engineering of the surface roughness of nanostructured cubic zirconia to control cell adhesion. *Nanotechnology* **23,** 475101 (2012).
9. Wang, G., Meng, F., Ding, C., Chu, P. K. & Liu, X. Microstructure, bioactivity and osteoblast behavior of monoclinic zirconia coating with nanostructured surface. *Acta Biomater.* **6,** 990–1000 (2010).
10. Scopelliti, P. E. *et al.* The Effect of Surface Nanometre-Scale Morphology on Protein Adsorption. *PLoS ONE* **5,** e11862 (2010).
11. Ge, Q. Synthesis and characterization of mesoporous zirconia nanocomposite using self-assembled block copolymer template. *Grad. Theses Diss.* (2012). at <http://lib.dr.iastate.edu/etd/12616>
12. Jaenicke, S., Chuah, G. K., Raju, V. & Nie, Y. T. Structural and Morphological Control in the Preparation of High Surface Area Zirconia. *Catal. Surv. Asia* **12,** 153–169 (2008).
13. Singh, A. V. *et al.* Quantitative Characterization of the Influence of the Nanoscale Morphology of Nanostructured Surfaces on Bacterial Adhesion and Biofilm Formation. *PLoS ONE* **6,** e25029 (2011).
14. Kasemo, B. Biological surface science. *Surf. Sci.* **500,** 656–677 (2002).
15. Wilson, C. J., Clegg, R. E., Leavesley, D. I. & Pearcy, M. J. Mediation of Biomaterial–Cell Interactions by Adsorbed Proteins: A Review. *Tissue Eng.* **11,** 1–18 (2005).

16. Sabirianov, R. F., Rubinstein, A. & Namavar, F. Enhanced initial protein adsorption on engineered nanostructured cubic zirconia. *Phys. Chem. Chem. Phys.* **13,** 6597–6609 (2011).
17. Carbone, R. *et al.* Biocompatibility of cluster-assembled nanostructured TiO2 with primary and cancer cells. *Biomaterials* **27,** 3221–3229 (2006).
18. Mo, S.-D. & Ching, W. Y. Electronic and optical properties of three phases of titanium dioxide: Rutile, anatase, and brookite. *Phys. Rev. B* **51,** 13023–13032 (1995).
19. Wang, Z., KSaxena, S., Pischedda, V., Liermann, H. P. & Zha, C. S. X-ray diffraction study on pressure-induced phase transformations in nanocrystalline anatase/rutile (TiO2). *J. Phys. Condens. Matter* **13,** 8317 (2001).
20. Diebold, U. The surface science of titanium dioxide. *Surf. Sci. Rep.* **48,** 53–229 (2003).
21. Mazza, T. *et al.* Raman spectroscopy characterization of TiO_2 rutile nanocrystals. *Phys. Rev. B* **75,** 045416 (2007).
22. Fujishima, A. & Honda, K. Electrochemical Photolysis of Water at a Semiconductor Electrode. *Nature* **238,** 37–38 (1972).
23. Chen, X. & Mao, S. S. Titanium dioxide nanomaterials: synthesis, properties, modifications, and applications. *Chem. Rev.* **107,** 2891–2959 (2007).
24. Hagfeldt, A. & Graetzel, M. Light-Induced Redox Reactions in Nanocrystalline Systems. *Chem. Rev.* **95,** 49–68 (1995).
25. Grätzel, M. Photoelectrochemical cells. *Nature* **414,** 338–344 (2001).
26. Fujishima, A., Zhang, X. & Tryk, D. TiO2 photocatalysis and related surface phenomena. *Surf. Sci. Rep.* **63,** 515–582 (2008).
27. Pang, C. L., Lindsay, R. & Thornton, G. Chemical reactions on rutile TiO2(110). *Chem. Soc. Rev.* **37,** 2328–2353 (2008).
28. Dohnálek, Z., Lyubinetsky, I. & Rousseau, R. Thermally-driven processes on rutile TiO_2(1 1 0)-(1 × 1): A direct view at the atomic scale. *Prog. Surf. Sci.* **85,** 161–205 (2010).
29. Feng, X., Zhu, K., Frank, A. J., Grimes, C. A. & Mallouk, T. E. Rapid Charge Transport in Dye-Sensitized Solar Cells Made from Vertically Aligned Single-Crystal Rutile TiO2 Nanowires. *Angew. Chem. Int. Ed.* **51,** 2727–2730 (2012).
30. Fei Yin, Z., Wu, L., Gui Yang, H. & Hua Su, Y. Recent progress in biomedical applications of titanium dioxide. *Phys. Chem. Chem. Phys.* **15,** 4844 (2013).
31. Garzella, C., Comini, E., Tempesti, E., Frigeri, C. & Sberveglieri, G. TiO2 thin films by a novel sol–gel processing for gas sensor applications. *Sens. Actuators B Chem.* **68,** 189–196 (2000).
32. Kamegawa, T., Shimizu, Y. & Yamashita, H. Superhydrophobic Surfaces with Photocatalytic Self-Cleaning Properties by Nanocomposite Coating of TiO_2 and Polytetrafluoroethylene. *Adv. Mater.* **24,** 3697–3700 (2012).
33. Lai, Y.-K. *et al.* Bioinspired TiO2 Nanostructure Films with Special Wettability and Adhesion for Droplets Manipulation and Patterning. *Sci. Rep.* **3,** (2013).

34. Parker, J. C. & Siegel, R. W. Raman microprobe study of nanophase TiO_2 and oxidation-induced spectral changes. *J. Mater. Res.* **5,** 1246–1252 (1990).
35. Parker, J. C. & Siegel, R. W. Calibration of the Raman spectrum to the oxygen stoichiometry of nanophase TiO2. *Appl. Phys. Lett.* **57,** 943 (1990).
36. Haenle, M. *et al.* An extended spectrum bactericidal titanium dioxide (TiO_2) coating for metallic implants: in vitro effectiveness against MRSA and mechanical properties. *J. Mater. Sci. Mater. Med.* **22,** 381–387 (2011).
37. Kubacka, A. *et al.* Understanding the antimicrobial mechanism of TiO_2-based nanocomposite films in a pathogenic bacterium. *Sci. Rep.* **4,** 4134 (2014).
38. Park, S. *et al.* Mesoporous TiO_2 as a nanostructured substrate for cell culture and cell patterning. *RSC Adv.* **3,** 23673 (2013).
39. Barborini, E. *et al.* Supersonic cluster beam deposition of nanostructured titania. *Eur. Phys. J. - At. Mol. Opt. Phys.* **24,** 277–282 (2003).
40. Barborini, E. *et al.* Engineering the nanocrystalline structure of TiO_2 films by aerodynamically filtered cluster deposition. *Appl. Phys. Lett.* **81,** 3052 (2002).
41. Barborini, E. *et al.* Nanostructured TiO2 Films with 2 eV Optical Gap. *Adv. Mater.* **17,** 1842–1846 (2005).
42. Della Foglia, F., Losco, T., Piseri, P., Milani, P. & Selli, E. Photocatalytic activity of nanostructured TiO2 films produced by supersonic cluster beam deposition. *J. Nanoparticle Res.* **11,** 1339–1348 (2009).
43. Mazza, T. *et al.* Libraries of cluster-assembled titania films for chemical sensing. *Appl. Phys. Lett.* **87,** 103108 (2005).
44. Kholmanov, I. N. *et al.* The influence of the precursor clusters on the structural and morphological evolution of nanostructured TiO_2 under thermal annealing. *Nanotechnology* **14,** 1168–1173 (2003).
45. Barborini, E., Piseri, P. & Milani, P. A pulsed microplasma source of high intensity supersonic carbon cluster beams. *J. Phys. Appl. Phys.* **32,** L105 (1999).
46. Tafreshi, H. V. *et al.* A Simple Nozzle Configuration for the Production of Low Divergence Supersonic Cluster Beam by Aerodynamic Focusing. *Aerosol Sci. Technol.* **36,** 593–606 (2002).
47. Eastman, J. A. Microstructural development in nanophase TiO_2 during annealing. *J. Appl. Phys.* **75,** 770–779 (1994).
48. DeLoach, J. D., Scarel, G. & Aita, C. R. Correlation between titania film structure and near ultraviolet optical absorption. *J. Appl. Phys.* **85,** 2377–2384 (1999).
49. Kumar, K.-N. P. *et al.* Densification of nanostructured titania assisted by a phase transformation. *Nature* **358,** 48–51 (1992).

50. Wiley: X-Ray Diffraction Procedures: For Polycrystalline and Amorphous Materials, 2nd Edition - Harold P. Klug, Leroy E. Alexander. at <http://eu.wiley.com/WileyCDA/WileyTitle/productCd-0471493694.html>
51. Kim, H. G. & Kim, K. T. Densification behavior of nanocrystalline titania powder compact under high temperature. *Acta Mater.* **47,** 3561–3570 (1999).
52. Kumar, K.-N. P. Growth of rutile crystallites during the initial stage of anatase-to-rutile transformation in pure titania and in titania-alumina nanocomposites. *Scr. Metall. Mater.* **32,** 873–877 (1995).
53. Barabási, A.-L. & Stanley, H. E. *Fractal Concepts in Surface Growth*. (Cambridge University Press, 1995).
54. Penn, R. L. & Banfield, J. F. Formation of rutile nuclei at anatase (112) twin interfaces and the phase transformation mechanism in nanocrystalline titania. *Am. Mineral.* **84,** 871–876 (1999).
55. Kelly, P. M. & Francis Rose, L. R. The martensitic transformation in ceramics — its role in transformation toughening. *Prog. Mater. Sci.* **47,** 463–557 (2002).
56. Chevalier, J., Gremillard, L., Virkar, A. V. & Clarke, D. R. The Tetragonal-Monoclinic Transformation in Zirconia: Lessons Learned and Future Trends. *J. Am. Ceram. Soc.* **92,** 1901–1920 (2009).
57. Kim, D.-J. Influence of aging environment on low-temperature degradation of tetragonal zirconia alloys. *J. Eur. Ceram. Soc.* **17,** 897–903 (1997).
58. Částková, K., Hadraba, H. & Cihlář, J. Ceramics-Silikáty. *HYDROTHERMAL AGEING OF TETRAGONAL ZIRCONIA CERAMICS* **48,** 85–92 (2004).
59. Swab, J. J. Low temperature degradation of Y-TZP materials. *J. Mater. Sci.* **26,** 6706–6714 (1991).
60. Kenner, G. H., Pasco, W. D., Frakes, J. T. & Brown, S. D. Mechanical properties of calcia stabilized zirconia following in vivo and in vitro aging. *J. Biomed. Mater. Res.* **9,** 63–66 (1975).
61. Piconi, C. & Maccauro, G. Zirconia as a ceramic biomaterial. *Biomaterials* **20,** 1–25 (1999).
62. Dewhurst, J. K. & Lowther, J. E. Relative stability, structure, and elastic properties of several phases of pure zirconia. *Phys. Rev. B* **57,** 741–747 (1998).
63. Mercera, P. D. L., van Ommen, J. G., Doesburg, E. B. M., Burggraaf, A. J. & Ross, J. R. H. Zirconia as a support for catalysts Influence of additives on the thermal stability of the porous texture of monoclinic zirconia. *Appl. Catal.* **71,** 363–391 (1991).
64. Kelly, J. R. & Denry, I. Stabilized zirconia as a structural ceramic: an overview. *Dent. Mater. Off. Publ. Acad. Dent. Mater.* **24,** 289–298 (2008).
65. Bocanegra-Bernal, M. H. & Torre, S. D. de la. Phase transitions in zirconium dioxide and related materials for high performance engineering ceramics. *J. Mater. Sci.* **37,** 4947–4971 (2002).

66. Natanzon, Y., Boniecki, M. & Łodziana, Z. Influence of elastic properties on superplasticity in doped yttria-stabilized zirconia. *J. Phys. Chem. Solids* **70,** 15–19 (2009).
67. Nawrocki, J., Rigney, M., McCormick, A. & Carr, P. W. Chemistry of zirconia and its use in chromatography. *J. Chromatogr. A* **657,** 229–282 (1993).
68. Chevalier, J. What future for zirconia as a biomaterial? *Biomaterials* **27,** 535–543 (2006).
69. Manicone, P. F., Rossi Iommetti, P. & Raffaelli, L. An overview of zirconia ceramics: basic properties and clinical applications. *J. Dent.* **35,** 819–826 (2007).
70. Sohn, Y. H., Biederman, R. R. & Sisson, R. D. Microstructural development in physical vapour-deposited partially stabilized zirconia thermal barrier coatings. *Thin Solid Films* **250,** 1–7 (1994).
71. Wan, K. T., Khouw, C. B. & Davis, M. E. Studies on the Catalytic Activity of Zirconia Promoted with Sulfate, Iron, and Manganese. *J. Catal.* **158,** 311–326 (1996).
72. Audry, F. *et al.* Infrared Study and Quantum Calculations of the Conversion of Methylbutynol into Hydroxymethylbutanone on Zirconia. *J. Catal.* **168,** 471–481 (1997).
73. Trovarelli, A. *et al.* Nanophase Fluorite-Structured CeO2–ZrO2Catalysts Prepared by High-Energy Mechanical Milling. *J. Catal.* **169,** 490–502 (1997).
74. Stichert, W. & Schüth, F. Synthesis of Catalytically Active High Surface Area Monoclinic Sulfated Zirconia. *J. Catal.* **174,** 242–245 (1998).
75. Davies, L. E., Bonini, N. A., Locatelli, S. & Gonzo, E. E. Characterization and catalytic activity of zirconium dioxide prepared by sol-gel. *Lat. Am. Appl. Res.* **35,** 23–28 (2005).
76. Carinci, F. *et al.* Zirconium oxide: analysis of MG63 osteoblast-like cell response by means of a microarray technology. *Biomaterials* **25,** 215–228 (2004).
77. Helmer, J. D. & Driskell, T. D. Research on bioceramics. in (1969).
78. Christel, P. *et al.* Biomechanical compatibility and design of ceramic implants for orthopedic surgery. *Ann. N. Y. Acad. Sci.* **523,** 234–256 (1988).
79. Rimondini, L., Cerroni, L., Carrassi, A. & Torricelli, P. Bacterial colonization of zirconia ceramic surfaces: an in vitro and in vivo study. *Int. J. Oral Maxillofac. Implants* **17,** 793–798 (2001).
80. Welander, M., Abrahamsson, I. & Berglundh, T. The mucosal barrier at implant abutments of different materials. *Clin. Oral Implants Res.* **19,** 635–641 (2008).
81. Scarano, A., Piattelli, M., Caputi, S., Favero, G. A. & Piattelli, A. Bacterial adhesion on commercially pure titanium and zirconium oxide disks: an in vivo human study. *J. Periodontol.* **75,** 292–296 (2004).
82. Milleding, P., Carlén, A., Wennerberg, A. & Karlsson, S. Protein characterisation of salivary and plasma biofilms formed in vitro on non-corroded and corroded dental ceramic materials. *Biomaterials* **22,** 2545–2555 (2001).
83. Tanabe, K. Surface and catalytic properties of ZrO2. *Mater. Chem. Phys.* **13,** 347–364 (1985).

84. Mercera, P. D. L., Van Ommen, J. G., Doesburg, E. B. M., Burggraaf, A. J. & Ross, J. R. H. Zirconia as a support for catalysts: Evolution of the texture and structure on calcination in air. *Appl. Catal*. **57,** 127–148 (1990).
85. Lenardi, C., Sogne, E., Borghi, F., Podestà, A. & Paolo, M. Effects of Temperature and Oxygen Vacancies on Nanocrystallite Phase and Size in Metastable Cluster Assembled ZrO_2 films. (to be published).

6. Nanoscale functional properties of nanostructured cluster-assembled oxides

6.1. Double layer interactions

Electrostatic interactions taking place at the interface of transition metal oxides (TMO) with water play a fundamental role in determining the behavior of systems and devices strategic for applications in biomedicine, catalysis, energy production/conversion, environmental remediation[1-3]. Biophysical phenomena such as the formation of bilayer membranes[4-6] or the adsorption and reorganization of proteins and cells at interfaces[7,8] depend upon the charging state of TMO surfaces in aqueous medium[8-12].

The charge of TMO surfaces in aqueous medium is mainly determined by two phenomena: protonation/de-protonation of surface hydroxyls[13-15], and adsorption of electrolyte ions onto the surface[16]. Two spatially defined regions of electric charge thus develop: a first compact layer of charge (Stern layer), closer to the solid surface and a few atomic sizes thick, including truly surface charges (originating in the amphoteric dissociation of surface groups) and surface-bound charges (adsorbed ions from the solution); a second diffuse layer of hydrated ions of both signs extends toward the bulk of the solution[17-19]. An electrostatic potential, solution of the Poisson-Boltzmann equation, exponentially decaying away from the surface, is associated to the overall charge distribution[19-21].

In this Chapter I will briefly show the DLVO theory used to characterize the double layer interaction, in the particular case of an interaction between a sphere and a flat surface, the main charging mechanisms of the metal oxide surfaces in aqueous electrolytes and the works of literature which consider the influence of local morphological as well as chemical heterogeneities of the nanostructured surfaces on DLVO interaction.

6.1.1. DLVO between sphere and flat surfaces

Electrostatic and van der Waals forces in aqueous solution usually occur together and are considered additive in the Derjaguin-Landau-Verwey-Overbeek (DLVO) theory. In

particular, the interaction between a sphere and a flat surface is approximated by the following equations, valid for $D>\lambda_D$ [21-26]:

$$F_{DLVO}^{cc} = \frac{2\pi R\lambda_D}{\varepsilon\varepsilon_0}\left[2\sigma_S\sigma_T e^{-\frac{D}{\lambda_D}} + (\sigma_S^2+\sigma_T^2)\, e^{-\frac{2D}{\lambda_D}}\right] - \frac{AR}{6D^2} \quad (22)$$

$$F_{DLVO}^{cp} = \frac{2\pi R\lambda_D}{\varepsilon\varepsilon_0}\left[2\psi_S\psi_T e^{-\frac{D}{\lambda_D}} - (\psi_S^2+\psi_T^2)\, e^{-\frac{2D}{\lambda_D}}\right] - \frac{AR}{6D^2} \quad (23)$$

Here the superscripts cc and cp indicate constant-charge and constant-potential boundary conditions for the electrostatic contributions (first terms in Eqs. 22, 23, while the second terms represent the van der Waals force); the constant charge and constant potential conditions are typically well satisfied on insulating and conductive (metallic) surfaces, accordingly. R and σ_T (ψ_T) are the radius and surface charge density (surface potential) of the sphere, and σ_S (ψ_S) is the surface charge density (surface potential) of the smooth (idealized) sample surface; e is the dielectric constant of the medium (the aqueous electrolyte, we assume e=78.54), e ε_0 is the vacuum permittivity, λ_D is the Debye length, i.e. the screening length of the electrolyte:

$$\lambda_D = \sqrt{\frac{\varepsilon\varepsilon_0 K_B T}{2e^2 I}} \quad (24)$$

where k_B is the Boltzmann constant, T is the absolute temperature, e is the electric charge of the electron and I the ionic strength of the solution: I= 1/2 $\sum_i z_i^2 c_i$, c_i and z_i being the concentration (number of particles per unit volume) and valence of the i-th ionic species. The higher is the ionic strength, the more effective is the screening of electric fields in the solution. For 1:1 electrolyte with bulk concentration c, Eq. 24 simplifies to:

$$\lambda_D = 0.3/\sqrt{c}\ \text{nm} \quad (25)$$

where the concentration of the salt is given in mol/l. The Van der Waals force in Eqs. 22,23 depends on the Hamaker constant A of the surface/medium/probe system[25]. Potentials and surface charge densities in Eqs. 22,23 are related by the Grahame equation, which for a 1:1 electrolyte is[19]:

$$\sigma = \sqrt{8\varepsilon\varepsilon_0 K_B T c}\,\sinh\frac{e\psi}{2K_B T} \quad (26)$$

The first terms of Eqs. 22, 23 represent upper and lower limits for the general case of double layer interactions when charge regulation phenomena occur. When regulation phenomena

occur, none of the following conditions, the constant surface charge or the constant surface potential, hold; these quantities become a function of the separation distance between the two interacting surfaces, or equivalently of the degree of overlap of the corresponding double layers. This brings the solution of the electrostatic problem far from the boundaries of the simplified linearized theory, which strictly holds only at low surface potential, large distances, and low ionic strength[19-21]. While the overlap of probe and sample double layers could not lead to important regulation mechanisms, it does not imply that regulation phenomena are absent also within the double layer of corrugated ns surfaces, as it is discussed later. For relatively large distances Eq. 22 simplifies to:

$$F_{DLVO}^{cc} = \frac{4\pi R\lambda_D}{\varepsilon\varepsilon_0}\sigma_S\sigma_T e^{-\frac{D}{\lambda_D}} - \frac{AR}{6D^2} \quad (27)$$

6.1.2. Charging of Metal Oxide Surfaces in Aqueous Electrolytes

The charge of TMO surfaces in aqueous medium is mainly determined by two phenomena: protonation/de-protonation of surface hydroxyls[13-15], and adsorption of electrolyte ions onto the surface[16]. Protonation/de-protonation phenomena can be formally regarded as a two-step protonation of surface M-O$^-$ groups:

$$M\text{-}O^- + H^+ \leftrightarrow M\text{-}OH;\ K_1 \quad (28)$$

$$M\text{-}OH + H^+ \leftrightarrow M\text{-}OH_2^+;\ K_2 \quad (29)$$

or to the interaction of surface hydroxyls M-OH with OH$^-$ and H$^+$ ions, in which case the first reaction must be replaced with:

$$M\text{-}OH + OH^- \leftrightarrow M\text{-}O^- + H_2O;\ K_1' \quad (30)$$

The equilibrium constants K_1 and K_2 are defined as: $K_1=[M\text{-}OH]/([M\text{-}O^-][H^+])$ and $K_2=[MOH_2^+]/([M\text{-}OH][H^+])$, [X] representing the molar concentration of the species X. It turns out that $1/K_1'=K_wK_1$, $K_w=10^{-14}$ being the equilibrium constant of the dissociation reaction of water into H$^+$ and OH$^-$ ions (due to its very small value, pK_1 and pK_1' are almost equal, being $pK=-\log_{10}(K)$).

In addition to association/dissociation of surface hydroxyls described by Eqs. 28, 29, also adsorption of anions A$^-$ and cations C$^+$ from solution to charged surface sites may take place, according to reactions:

$$M\text{-}O^- + C^+ \leftrightarrow M\text{-}O^-\cdot C^+ \quad (31)$$

$$M\text{-}OH_2^+ + A^- \leftrightarrow M\text{-}OH_2^+\cdot A^- \quad (32)$$

where $K_+=[M\text{-}O^-\cdot C^+]/[M\text{-}O^-][C^+]$ and $K_-=[M\text{-}OH_2^+\cdot A^-]/[M\text{-}OH_2^+][A^-]$.

Two spatially defined regions of electric charge thus develop: a first compact layer of charge (Stern layer), closer to the solid surface and a few atomic sizes thick, including truly surface charges (originating in the amphoteric dissociation of surface groups) and surface-bound charges (adsorbed ions from the solution); a second diffuse layer of hydrated ions of both signs extends toward the bulk of the solution[17-19]. An electrostatic potential, solution of the Poisson-Boltzmann equation, exponentially decaying away from the surface, is associated to the overall charge distribution[19-21]. It should be noted that AFM tip senses the diffuse part of the electrostatic double layer[27,28], therefore surface charge densities σ_S and σ_T in Eqs. 22,23 must be identified with the surface charge density σ_d of the diffuse layer, i.e. with the charge in the diffused layer projected on the outer Helmholtz plane; this charge density is equal in magnitude to the total charge density of the Stern layer: $\sigma_d = -(\sigma_0 + \sigma_i)$, where σ_0 is the density of truly surface charges and σ_i is the density of charges by ions from the electrolyte adsorbed (complexated) at the inner Helmholtz plane[17]. On amphifunctional surfaces, i.e. on surfaces where an electronic surface charging mechanism is present (as for example on bare, or partially oxidized, metallic surfaces), the previous equation must be changed in: $\sigma_d = -(\sigma_0+\sigma_i+\sigma_e)$, where σ_e is the electronic surface charge density of the solid surface[11,16]. Our nanostructures however have a marked insulating character[29] and we will neglect in the following the σ_e term. Under the assumption that the ions bind only to oppositely charged sites (energetically the most favourable option) it turns out that σ_d represents a net surface charge density, being determined by the density of naked surface charges $M\text{-}O_2$ and $M\text{-}OH_2^+$ only, i.e. by those charges that are not neutralized by specifically absorbed electrolyte ions[28,30,31]. The surface charge density σ_0, the charge density at the inner Helmholtz plane σ_i, and the charge density of the diffuse layer at the outer Helmholtz plane σ_d are equal to[30]:

$$\sigma_0 = F([M\text{-}OH_2^+] + [M\text{-}OH_2^+\cdot A^-] - [M\text{-}O^-] - [M\text{-}O^-\cdot C^+]) \quad (33)$$

$$\sigma_i = F([M\text{-}O^-\cdot C^+] - [M\text{-}OH_2^+\cdot A^-]) \quad (34)$$

$$\sigma_d = -(\sigma_0+\sigma_i) = -F([M\text{-}OH_2^+] - [M\text{-}O^-]) \quad (35)$$

where F is the Faraday constant, i.e. the number of coulombs per mole of electrons.

At IEP σ_d=0 while at PZC σ_0=0. AFM measurements can be used therefore to characterize IEP, not directly PZC, unless ion adsorption is negligible or symmetrical (indifferent electrolyte), in which case PZC=IEP.

6.1.3. Electrostatic interactions at nanostructured interfaces

While significant insights have been obtained on the properties of the electric double layers formed between flat smooth surfaces[11,16,17,21], the case of rough surfaces still represents a severe challenge, hampering analytical, yet approximate, solutions of the double layer equations to be reliably obtained. Several authors have speculated that surface roughness may be responsible for discrepancies observed between experimental data and the predictions of the linearized DLVO theory; for example, a geometrical implication of surface corrugation is that the "average plane of charges", which produces the electrostatic double layer interaction, is shifted backwards with respect to the point of first contact between the surface and an incoming probe[27,32-36]. Despite the paramount importance of the explicit consideration of surface corrugation for the description of double layer electrostatic phenomena in real systems, and the significant theoretical efforts made to model electrostatic interactions at rough interfaces, the practical implementation of such models is still a land of pioneering studies, relying on approximated representations of rough morphology and/or on suitable approximation of the Poisson-Boltzmann equations. The interaction energy between mildly corrugated planes exhibiting periodic undulations (in the weak roughness regime, i.e. amplitude small compared to wavelength) has been calculated by means of Derjaguin approximation[37] by Tsao[38] and by Suresh et al.[39]. The surface element integration (SEI) technique allowed overcoming the limitations of the Derjaguin approximation when calculating the interaction energy between curves surfaces, modeled as a collection of convex and concave regions (spherical or sinusoidal bumps or depressions) with arbitrarily large curvatures (yet within the limits of the linearized PB equations)[40-44].

Duval et al. have explicitly included in their calculation of interfacial electrostatic interactions the charging mechanisms of the surfaces, developing a theoretical/numerical framework to account for local morphological (though calculations are implemented only for LEGO-like corrugated interfaces) as well as chemical heterogeneities of the surfaces. Their model takes into account the fine structure of the electrostatic double layer and boundary conditions beyond the limits of the linearized PB equations, allowing therefore

to account for spatially-resolved charge regulation mechanisms and surface roughness effects[45]. Daikhin et al. have considered a statistical representation of surface morphology (in terms of height distributions) rather than on simplified geometrical constructions[46-48]; yet, their focus is limited to the calculation of some measurable electrochemical observables, typically the double layer capacitance. None of the works discussed so far present explicit calculations of the interaction force between rough surfaces in electrolyte solutions, and for this reason a direct application of theories for the analysis of experimental data acquired at complex rough interfaces is not straightforward. Since most of the relevant biophysical phenomena cited above take place at the nanoscale, the characterization of charging mechanisms of nanostructured surfaces in electrolytic solutions and of the influence of the surface nanostructure is a necessary step towards the fundamental understanding and the effective exploitation of the role of nanostructured surfaces in tailoring and determining the functionality of the TMO interface with bio-objects[7-9]. A major problem hampering to reach a systematic and theoretically well-established description at the nanoscopic scale of interface charging is the lack of systematic experimental studies on double layer interactions at nanorough interfaces: in particular this is a consequence of the difficulty of preparing and characterizing, at the nanoscale, interfaces with controlled morphology, roughness, average slope, specific area, etc. Electrokinetic and electrophoretic measurements, potentiometric and calorimetric titration methods have been employed to characterize IEP and PZC of oxide particles in suspension[9,31,49-51], unfortunately these methods cannot provide quantitative local (i.e. at sub-micrometer scale) information of surface properties, and the application of these standard macroscopic techniques to surfaces in the form of thin films supported on solid substrates is problematic.

6.2. Wettability

In the year 1805, Thomas Young and Pierre Simon de Laplace proposed that an interface between two materials has specific energy, interfacial energy, which is proportional to the interfacial surface area[52,53]. This concept is the basis for the field of wetting, which describes the contact between a fluid and a solid surface. Liquid with high surface tension, or liquid on low-energy solid surfaces, usually form nearly completed spherical droplets, whereas liquids with low surface tension, or liquids on high-energy surfaces, usually spread out on the surfaces. This phenomenon is a result of the minimization of interfacial energy.

The contact angle of a drop on a solid is ideally (on a flat homogeneous solid) given by the classical Young's equation:

$$\cos\vartheta = \frac{\gamma_{sv}-\gamma_{sl}}{\gamma_{lv}} \quad (36)$$

where γ_{sv}, γ_{sl}, and γ_{lv} are the different surface tensions (solid/vapour, solid7liquid and liquid/vapour) involved in the system. The wettability of an ideal surface (perfectly smooth, rigid and with chemical homogeneity) is determined by the outermost chemical groups of the solid. But in real surfaces, it is well accepted that the wettability of a surface is a function of its roughness (or better specific area, defined as the ratio between the 3D area and the projected one). It is an amazing phenomenon which occurs for example on some leaves, which exhibit super-hydrophobic behavior even if they do not express particularly low-energy surface compounds [Herminghaus2000, Yang2008]. Two classical models describe approximately this rough dependence: Wenzel[54] and Cassie[55] models.

In the Wenzel model it is assumed that complete contact occurs at the liquid-solid interface. The increase of surface specific area enhances the intrinsic wetting character of the surface. The contact angle ϑ on the rough surface in terms of the contact angle ϑ_0 on the microscopically flat surface of the same material is:

$$\cos\vartheta = r\cos\vartheta_0 \quad (37)$$

where r (called roughness or specific area in this PhD work) is the ratio between the surface area of the rough surface and the projected surface area. In the Cassie model it is assumed that some air (or vapour) remains trapped between the drop and the cavities of the rough surfaces. This heterogeneous surface is explained using the Cassie–Baxter equation (Cassie's law):

$$\cos\vartheta = r\cos\vartheta_0 - (1-\phi)(1 + r\cos\vartheta_0) \quad (38)$$

where ϕ is the fraction of the projected area where the liquid is in contact with the solid and $(1-\phi)$ is the fraction of the air pockets[55,56]. Of the two states the stable one, that is the one with lower free energy, is the one with larger $\cos\vartheta$. For hydrophobic surfaces with large enough roughness the Cassie state is the thermodynamically stable state, while in hydrophilic regime Wenzel is the stable one.

6.2.1 Wettability of ns-TiO_x

The main results about ns-TiO_x wettability depending on roughness and anneling treatments are reported below as in Ref [57].

Contact Angle Measurements

Contact angles of water have been measured with a homemade apparatus consisting of a syringe pump, a video camera, and motorized sample and camera stages, all of them controlled via a PC. Small drops (volume ~0.5 mL) of Milli-Q water were produced with the syringe pump and gently deposited on the surface. For each image, the overall drop profile was fitted with an elliptic curve and the error related to the fitting procedure was typically less than ±1° [58]. To obtain statistically sound results, at least five drops for each sample were typically analysed. The representative contact angle θ was then taken as the mean of these different determinations and the corresponding standard deviation was around ±2°, unless otherwise stated.

Contact Angles vs. Morphology

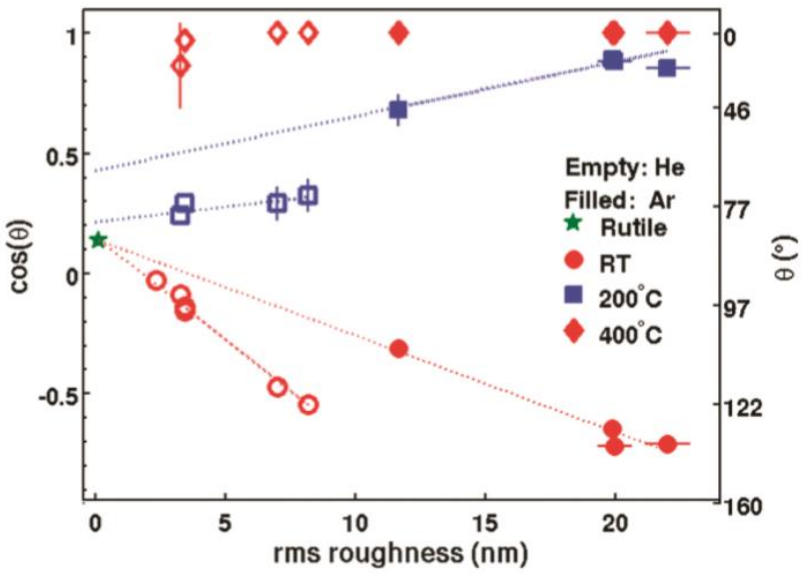

Fig. 62: Contact angles and corresponding cos(θ) values measured on ns-TiO_x films produced in different deposition and postdeposition conditions as a function of root-mean-square roughness. The contact angle measured on a single-crystal rutile TiO_2 sample at room temperature is also shown as reference. The dotted lines are a linear fit of data. Error bars, when not visible, are smaller than the data markers[57].

Fig. 62 shows the contact angle θ and cos(θ) values measured on films with different root-mean-square roughness, which underwent different thermal treatments. The polished ⟨100⟩ surface of a single-crystal rutile TiO_2 sample has also been characterized and the corresponding morphological and wetting parameters have been included in Fig. 62 as a reference. The surface morphology of the rutile sample is fairly ideal, with a roughness of only a few angstroms and a specific area of ∼1, values typical of nearly atomically smooth surfaces. Our data show that post-deposition thermal annealing changes the overall wetting character of ns-TiOx films: while as-deposited films are hydrophobic, annealing at 200 °C makes them mildly hydrophilic, and annealing at 400 °C turns them into superhydrophilic films.

The improved wettability of ns-TiOx films upon annealing at moderate temperatures can be explained in terms of removal of physisorbed hydrophobic organic contaminants and of the recovering of OH groups bonded to undercoordinated Ti atoms[59].

Morphology has an important impact on the wetting behavior of ns-TiOx. Controlling surface roughness in the range 3-30 nm allows tuning the contact angle from 140° to 90° in the hydrophobic regime, from 70° to 25° in the hydrophilic regime. Remarkably, in the superhydrophilic regime it is still possible to avoid complete wetting by keeping the roughness parameter below 5 nm, i.e., by depositing films with thickness below 20 nm. Combining morphological and chemical surface properties of ns-TiOx it is therefore possible to tune the wetting properties of these films with high elasticity, spanning almost the whole range of contact angles, from 0° (complete wetting) to 140° (almost superhydrophobic). The measured cos(θ) values for the samples as-deposited and annealed at 200 °C scale linearly to a good approximation with the surface roughness. The dotted lines in Fig. 62 represent linear fits to the data. The trend observed for the samples annealed at 200 °C is compatible with the Wenzel equation (Eq. 37), predicting a positive slope for the cos(θ) vs. specific area curve, i.e., the enhancement of the intrinsic hydrophilic character of the surface. The same trend in our case is expected for the cos(θ) vs. roughness curve, because the two quantities are linearly correlated. In the case of as-deposited films, we observe that the poor hydrophilicity of the flat sample ($\theta_{Rutile} = 82°$) is reverted, and the surface becomes more and more hydrophobic as the roughness increases. In other words, the surface wettability obeys an effective Wenzel rule, but with a critical angle that is smaller than 90°; in the case of as-deposited ns-TiOx samples the critical angle is actually smaller than $\theta_{Rutile} = 82°$. Such effective Wenzel behavior has been recently observed for

cluster-assembled nanostructured carbon films deposited by SCBD and wetted by water[60], and for functionalized porous silicon surfaces[61,62]. This effective Wenzel regime, according to some authors, is a consequence of the effect of a complex random surface morphology, which can be regarded as a random composition of grooves, with radial and circular symmetry[63-65]. Another factor that can provide an enhancement of hydrophobicity of rough surface is the formation of air pockets[55,56], which is possible also in intrinsically hydrophilic surfaces provided some overhang is present, at least at the smallest scales[66]. This condition is certainly satisfied in nanoporous ns-C and ns-TiOx films. Moreover, theoretical works have recently predicted that the multiscale (self-affine) character of a surface, like that of our nanostructured surfaces, promotes transition toward superhydrophobicity, irrespective to the intrinsic wettability of the surface[56,66]. Remarkably, both ns-C and ns-TiOx films possess a self-affine morphology[67]. Moreover, we observe in Fig. 62 that for all films the slope of the linear trends depends on the carrier gas used during deposition, despite the fact that the statistical morphological properties of films deposited with different carrier gases evolves similarly with thickness, and that the surface chemistry is expected to be rather independent of the carrier gas. One possible explanation for the observed difference in contact angles is the different porosity (different granularity) of the films deposited with different carrier gases, which can account for different evolution of air pockets, and therefore for the observed different contact angles.

References

1. Lyklema, J. & Lyklema, J. *Solid-liquid interfaces*. (Academic Press, 2001).
2. Leonard, K. C., Suyama, W. E. & Anderson, M. A. Evaluating the Electrochemical Capacitance of Surface-Charged Nanoparticle Oxide Coatings. *Langmuir* **28,** 6476–6484 (2012).
3. Khin, M. M., Nair, A. S., Babu, V. J., Murugan, R. & Ramakrishna, S. A review on nanomaterials for environmental remediation. *Energy Environ. Sci.* **5,** 8075 (2012).
4. Cremer, P. S. & Boxer, S. G. Formation and Spreading of Lipid Bilayers on Planar Glass Supports. *J. Phys. Chem. B* **103,** 2554–2559 (1999).
5. Oleson, T. A. & Sahai, N. Oxide-Dependent Adsorption of a Model Membrane Phospholipid, Dipalmitoylphosphatidylcholine: Bulk Adsorption Isotherms. *Langmuir* **24,** 4865–4873 (2008).
6. Oleson, T. A. *et al.* Neutron reflectivity study of substrate surface chemistry effects on supported phospholipid bilayer formation on sapphire. *J. Colloid Interface Sci.* **370,** 192–200 (2012).
7. Vogler, E. A. Structure and reactivity of water at biomaterial surfaces. *Adv. Colloid Interface Sci.* **74,** 69–117 (1998).
8. Wilson, C. J., Clegg, R. E., Leavesley, D. I. & Pearcy, M. J. Mediation of Biomaterial–Cell Interactions by Adsorbed Proteins: A Review. *Tissue Eng.* **11,** 1–18 (2005).
9. Parks, G. A. The Isoelectric Points of Solid Oxides, Solid Hydroxides, and Aqueous Hydroxo Complex Systems. *Chem. Rev.* **65,** 177–198 (1965).
10. Brown, G. E. *et al.* Metal Oxide Surfaces and Their Interactions with Aqueous Solutions and Microbial Organisms. *Chem. Rev.* **99,** 77–174 (1999).
11. Duval, J., Lyklema, J., Kleijn, J. M. & van Leeuwen, H. P. Amphifunctionally Electrified Interfaces: Coupling of Electronic and Ionic Surface-Charging Processes. *Langmuir* **17,** 7573–7581 (2001).
12. Bonnell, D. A. & Garra, J. Scanning probe microscopy of oxide surfaces: atomic structure and properties. *Rep. Prog. Phys.* **71,** 044501 (2008).
13. Morimoto, T., Nagao, M. & Tokuda, F. Relation between the amounts of chemisorbed and physisorbed water on metal oxides. *J. Phys. Chem.* **73,** 243–248 (1969).
14. Schaub, R. *et al.* Oxygen Vacancies as Active Sites for Water Dissociation on Rutile TiO_2 (110). *Phys. Rev. Lett.* **87,** 266104 (2001).
15. Brookes, I. M., Muryn, C. A. & Thornton, G. Imaging Water Dissociation on TiO_2 (110). *Phys. Rev. Lett.* **87,** 266103 (2001).

16. Duval, J., Kleijn, J. M., Lyklema, J. & van Leeuwen, H. P. Double layers at amphifunctionally electrified interfaces in the presence of electrolytes containing specifically adsorbing ions. *J. Electroanal. Chem.* **532,** 337–352 (2002).
17. Lyklema, J. & Duval, J. F. L. Hetero-interaction between Gouy–Stern double layers: Charge and potential regulation. *Adv. Colloid Interface Sci.* **114–115,** 27–45 (2005).
18. Oldham, K. B. A Gouy–Chapman–Stern model of the double layer at a (metal)/(ionic liquid) interface. *J. Electroanal. Chem.* **613,** 131–138 (2008).
19. Grahame, D. C. The Electrical Double Layer and the Theory of Electrocapillarity. *Chem. Rev.* **41,** 441–501 (1947).
20. Debye, P. & Hückel, E. Physikalische Zeitschrift. *On the theory of electrolytes* **24,** 185–206 (1923).
21. Parsegian, V. A. & Gingell, D. On the Electrostatic Interaction across a Salt Solution between Two Bodies Bearing Unequal Charges. *Biophys. J.* **12,** 1192–1204 (1972).
22. Butt, H.-J. Electrostatic interaction in atomic force microscopy. *Biophys. J.* **60,** 777–785 (1991).
23. Cappella, B. & Dietler, G. Force-distance curves by atomic force microscopy. *Surf. Sci. Rep.* **34,** 1–104 (1999).
24. Butt, H.-J., Cappella, B. & Kappl, M. Force measurements with the atomic force microscope: Technique, interpretation and applications. *Surf. Sci. Rep.* **59,** 1–152 (2005).
25. Leckband, D. & Israelachvili, J. Intermolecular forces in biology. *Q. Rev. Biophys.* **34,** 105–267 (2001).
26. Butt, H.-J. Electrostatic interaction in scanning probe microscopy when imaging in electrolyte solutions. *Nanotechnology* **3,** 60 (1992).
27. Barten, D., Kleijn, J. M., Duval, J., Lyklema, J. & Cohen Stuart, M. A. Double Layer of a Gold Electrode Probed by AFM Force Measurements. *Langmuir* **19,** 1133–1139 (2003).
28. Raiteri, R., Martinoia, S. & Grattarola, M. pH-dependent charge density at the insulator-electrolyte interface probed by a scanning force microscope. *Biosens. Bioelectron.* **11,** 1009–1017 (1996).
29. Chiappini, C. Electrical transport measurements on nanostructured Titanium Dioxide thin films. (Università degli Studi di Milano, 2006).
30. Kallay, N., Preočanin, T., Kovačević, D., Lützenkirchen, J. & Chibowski, E. Electrostatic Potentials at Solid/Liquid Interfaces. *Croat. Chem. Acta* **83,** 357–370 (2010).
31. Preočanin, T. & Kallay, N. Point of Zero Charge and Surface Charge Density of TiO2 in Aqueous Electrolyte Solution as Obtained by Potentiometric Mass Titration. *Croat. Chem. Acta* **79,** 95–106 (2006).

32. Johnson, S. B., Drummond, C. J., Scales, P. J. & Nishimura, S. Electrical double layer properties of hexadecyltrimethylammonium chloride surfaces in aqueous solution. *Colloids Surf. Physicochem. Eng. Asp.* **103,** 195–206 (1995).
33. Johnson, S. B., Drummond, C. J., Scales, P. J. & Nishimura, S. Comparison of Techniques for Measuring the Electrical Double Layer Properties of Surfaces in Aqueous Solution: Hexadecyltrimethylammonium Bromide Self-Assembly Structures as a Model System. *Langmuir* **11,** 2367–2375 (1995).
34. Ducker, W. A., Senden, T. J. & Pashley, R. M. Measurement of forces in liquids using a force microscope. *Langmuir* **8,** 1831–1836 (1992).
35. Drummond, C. J. & Senden, T. J. Examination of the geometry of long-range tip—sample interaction in atomic force microscopy. *Colloids Surf. Physicochem. Eng. Asp.* **87,** 217–234 (1994).
36. Considine, R. F. & Drummond, C. J. Surface Roughness and Surface Force Measurement: A Comparison of Electrostatic Potentials Derived from Atomic Force Microscopy and Electrophoretic Mobility Measurements. *Langmuir* **17,** 7777–7783 (2001).
37. White, L. R. On the deryaguin approximation for the interaction of macrobodies. *J. Colloid Interface Sci.* **95,** 286–288 (1983).
38. Tsao, H.-K. The Electrostatic Interactions between Two Corrugated Charged Planes. *J. Colloid Interface Sci.* **216,** 370–378 (1999).
39. Suresh, L. & Walz, J. Y. Effect of Surface Roughness on the Interaction Energy between a Colloidal Sphere and a Flat Plate. *J. Colloid Interface Sci.* **183,** 199–213 (1996).
40. Bhattacharjee, S., Ko, C.-H. & Elimelech, M. DLVO Interaction between Rough Surfaces. *Langmuir* **14,** 3365–3375 (1998).
41. Hoek, E. M., Bhattacharjee, S. & Elimelech, M. Effect of membrane surface roughness on colloid-membrane DLVO interactions. *Langmuir* **19,** 4836–4847 (2003).
42. Hoek, E. M. V. & Agarwal, G. K. Extended DLVO interactions between spherical particles and rough surfaces. *J. Colloid Interface Sci.* **298,** 50–58 (2006).
43. Huang, X., Bhattacharjee, S. & Hoek, E. M. V. Is Surface Roughness a 'Scapegoat' or a Primary Factor When Defining Particle−Substrate Interactions? *Langmuir* **26,** 2528–2537 (2010).
44. Martines, E., Csaderova, L., Morgan, H., Curtis, A. S. G. & Riehle, M. O. DLVO interaction energy between a sphere and a nano-patterned plate. *Colloids Surf. Physicochem. Eng. Asp.* **318,** 45–52 (2008).
45. Duval, J. F. L., Leermakers, F. A. M. & van Leeuwen, H. P. Electrostatic Interactions between Double Layers: Influence of Surface Roughness, Regulation, and Chemical Heterogeneities. *Langmuir* **20,** 5052–5065 (2004).

46. Daikhin, L. I., Kornyshev, A. A. & Urbakh, M. Double-layer capacitance on a rough metal surface. *Phys. Rev. E* **53,** 6192–6199 (1996).
47. Daikhin, L. I., Kornyshev, A. A. & Urbakh, M. Double layer capacitance on a rough metal surface: Surface roughness measured by 'Debye ruler'. *Electrochimica Acta* **42,** 2853–2860 (1997).
48. Daikhin, L. I., Kornyshev, A. A. & Urbakh, M. Nonlinear Poisson–Boltzmann theory of a double layer at a rough metal/electrolyte interface: A new look at the capacitance data on solid electrodes. *J. Chem. Phys.* **108,** 1715 (1998).
49. Delgado, A. V., González-Caballero, F., Hunter, R. J., Koopal, L. K. & Lyklema, J. Measurement and Interpretation of Electrokinetic Phenomena (IUPAC Technical Report). *Pure Appl. Chem.* **77,** (2005).
50. Elimelech, M., Chen, W. H. & Waypa, J. J. Measuring the zeta (electrokinetic) potential of reverse osmosis membranes by a streaming potential analyzer. *Desalination* **95,** 269–286 (1994).
51. Rudziński, W. *et al.* Calorimetric studies of simple ion adsorption at oxide/electrolyte interface titration experiments and their theoretical analysis based on 2-pK charging mechanism and on the triple layer model. *Colloids Surf. Physicochem. Eng. Asp.* **137,** 57–68 (1998).
52. Young, T. An Essay on the Cohesion of Fluids. *Philos. Trans. R. Soc. Lond.* **95,** 65–87 (1805).
53. Laplace, P. S. *Théorie analytique des probabilités. Volume I. Introduction, Livre I, Volume I. Introduction, Livre I,*. (J. Gabay, 1995).
54. Wenzel, R. N. Resistance of solid surfaces to wetting by water. *Ind. Eng. Chem.* **28,** 988–994 (1936).
55. Cassie, A. B. D. & Baxter, S. Wettability of porous surfaces. *Trans. Faraday Soc.* **40,** 546–551 (1944).
56. Yang, C., Tartaglino, U. & Persson, B. N. J. Nanodroplets on rough hydrophilic and hydrophobic surfaces. *Eur. Phys. J. E* **25,** 139–152 (2008).
57. Podestà, A. *et al.* Cluster-Assembled Nanostructured Titanium Oxide Films with Tailored Wettability. *J. Phys. Chem. C* **113,** 18264–18269 (2009).
58. Semprebon, C. *et al.* Anisotropy of Water Droplets on Single Rectangular Posts. *Langmuir* **25,** 5619–5625 (2009).
59. Takeda, S., Fukawa, M., Hayashi, Y. & Matsumoto, K. Surface OH group governing adsorption properties of metal oxide films. *Thin Solid Films* **339,** 220–224 (1999).
60. Ostrovskaya, L., Podestà, A., Milani, P. & Ralchenko, V. Influence of surface morphology on the wettability of cluster-assembled carbon films. *EPL Europhys. Lett.* **63,** 401 (2003).
61. Dattilo, D., Armelao, L., Maggini, M., Fois, G. & Mistura, G. Wetting Behavior of Porous Silicon Surfaces Functionalized with a Fulleropyrrolidine. *Langmuir* **22,** 8764–8769 (2006).

62. Dattilo, D., Armelao, L., Fois, G., Mistura, G. & Maggini, M. Wetting Properties of Flat and Porous Silicon Surfaces Coated with a Spiropyran. *Langmuir* **23,** 12945–12950 (2007).
63. Zhou, X. b. & De Hosson, J. T. M. Influence of surface roughness on the wetting angle. *J. Mater. Res.* **10,** 1984–1992 (1995).
64. Palasantzas, G. & de Hosson, J. T. M. Wetting on rough surfaces. *Acta Mater.* **49,** 3533–3538 (2001).
65. Oliver, J. P., Huh, C. & Mason, S. G. An experimental study of some effects of solid surface roughness on wetting. *Colloids Surf.* **1,** 79–104 (1980).
66. Herminghaus, S. Roughness-induced non-wetting. *EPL Europhys. Lett.* **52,** 165 (2000).
67. Milani, P. *et al.* Cluster assembling of nanostructured carbon films. *Diam. Relat. Mater.* **10,** 240–247 (2001).

Part IV

Results

7. Morphological and structural properties

7.1. Sub-monolayer regime

Here I present the results of the characterization of the growth of ns-ZrO_x and ns-TiO_x cluster-assembled films in the sub-monolayer regime on silica substrates for different carries gas and cluster mass distributions as obtained by selecting different portions of the cluster beam. A complete characterization of the evolution of islands morphology with coverage has been performed only for zirconia clusters.

7.1.1. Preliminary framework

As it has been defined in Section 4.3.1, incident clusters (*primeval incident clusters*) are identified as the clusters analyzed in the first single shot, and I assume that their dimensions are not influenced by coalescence or juxtaposition phenomena. We have not a direct support of this strong assumption, however for very low coverages we can expect that the mean distance between deposited clusters is larger than the distance useful for aggregation processes in this cluster-substrate system. This hypothesis is supported for example for ns-ZrO_x (deposited by Argon) by other experiments, performed by TEM and XRD[1] (see also Section 5.2.1). This consideration suggests also that the ns-ZrO_x clusters deposited by Argon are crystalline at room temperature (cubic phase) and that a cluster coincides more or less with a crystalline grain. As a future outlook, it is important to verify and confirm this assumption also for the other systems analyzed (ns-TiO_x deposited with He and Ar as carrier gas and ns-ZrO_x deposited with He).

In Section 4.3.1, I have also defined *islands* as the strcutures on the substrate with z-dimension different from that of the first single shot; the term island is used regardless the structure is resulting from complete coalescence and juxtaposition in z-direction or if it is characterized by a spherical shape, semispherical or fractal-like. I decided not to perform a detailed analysis of the islands growth in x-y directions because the islands dimensions in x-y are affected by the convolution with the AFM tip, and a deconvolution process is poorly accurate for various reasons: the lack of a precise control on tip dimension and shape during the scanning of the sample and for the continuous evolution of the heterogeneous

shapes of the objects on the substrate which prevent me from choosing a model for the deconvolution.

Surface *coverage* is defined as the ratio between the area occupied by clusters on the surface and the scanned area. It is difficult to estimate an error associated to the coverage, because its value is affected by the convolution with the AFM tip. For this reason it is not reported in the figures. Anyway it can be considered about 30% for very low coverages and it decreases with increasing coverage.

Finally, height distributions are multi-modal because incident clusters are not mono-disperse in size. I have decided to study the evolution of the highest cluster/island height peak identified in the distribution.

7.1.2 Substrate characterization

I deposited clusters obtained from polished Si wafers at room temperature. The substrate were previously cleaned with acqua regia; later they have been cleaned in ethanol and dried with a nitrogen flux. The substrate morphology has been characterized before deposition; in Fig. 63 (a) it is shown a representative AFM topographical map of cleaned Si substrate and in Fig. 63 (b) the relative histogram of the height: RMS roughness of substrate is 0.22 ± 0.01 nm.

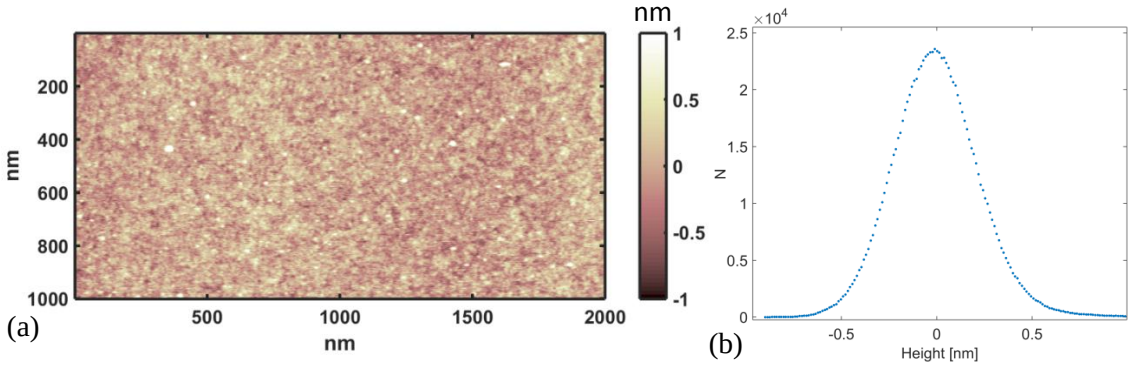

Fig. 63: (a) AFM topographical map of Si substrate and the corresponding height histogram (b) centered around 0 value.

7.1.3. Cluster size distribution

Ns-ZrO_x

The mean size of the incident clusters has been described by the distribution of particle heights of the objects identified in the AFM topographic maps, with the method explained in Section 4.3.1. In Fig. 64 the AFM images of ns-ZrO_x first single shot sample (very low coverage) are shown, reporting samples deposited with Helium (a-b) and with Argon (c-d), by using different regions of the beam from the centre to the periphery. It should be noted that what is imaged and characterized here is the fraction of the beam that passes through the aerodynamical lenses and the skimmer separating the source chamber from the deposition chamber, and effectively adheres onto the substrate; the largest particles likely do not survive these filtering processes, including the attachment to the substrate, and are therefore not imaged.

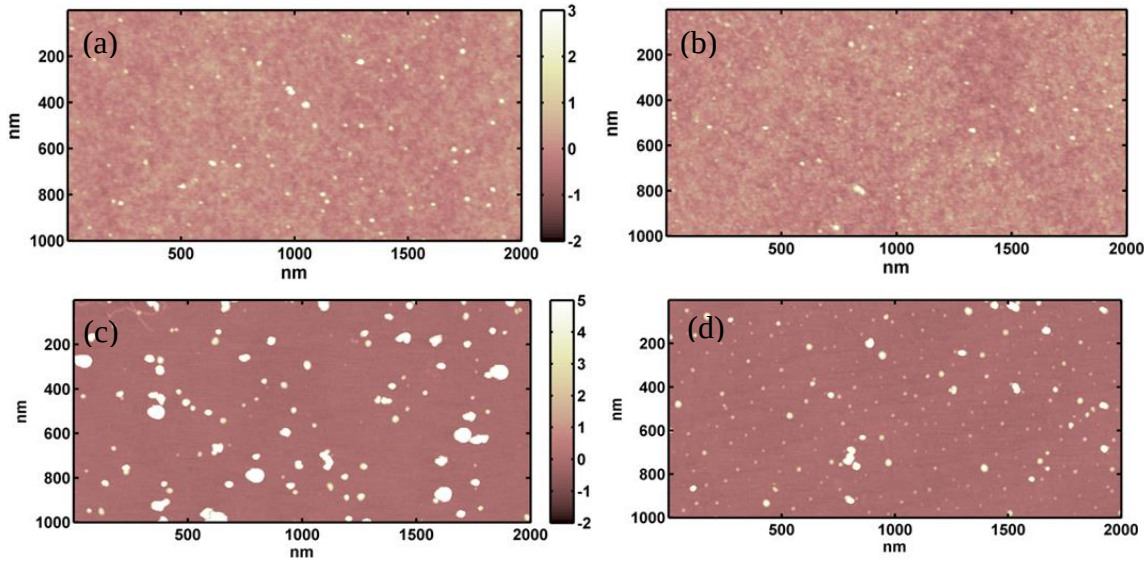

Fig. 64: AFM topographical maps of ns-ZrO_x sample with very low coverage; deposited with Helium (a-b) from the center to the periphery of the beam axis, or with Argon (c-d).

The normalized distributions of the heights of the objects analysed in the first single shot sample are reported in Fig. 65, in a semi-log scale. The distribution of cluster size is lognormal for systems which are characterized by aggregation processes[2]. The mean and geometrical standard deviation of the normal distributions are back-transformed into the median and standard deviation of log-normal distribution[3] and they are reported in the legends in Fig. 65.

For each system analysed, the size distributions (height distribution) is broad and multi-modal and affected by the carrier gas and position relative to the beam axis. The carrier gas strongly affects the size distribution: cluster height for He deposition is peaked at 2.5 ± 1 nm, while for Ar deposition is peaked at 5.3 ± 3.4 nm. This behaviour is expected

because of the well-known different sputtering yield of the two gases[4,5,6]. The inertial effects of clusters in the supersonic seeded beam, described in Section 1.3, determine the difference in clusters size in the different regions of the beam for both the systems: the larger clusters are in the center of the beam and the smaller ones in the periphery region.

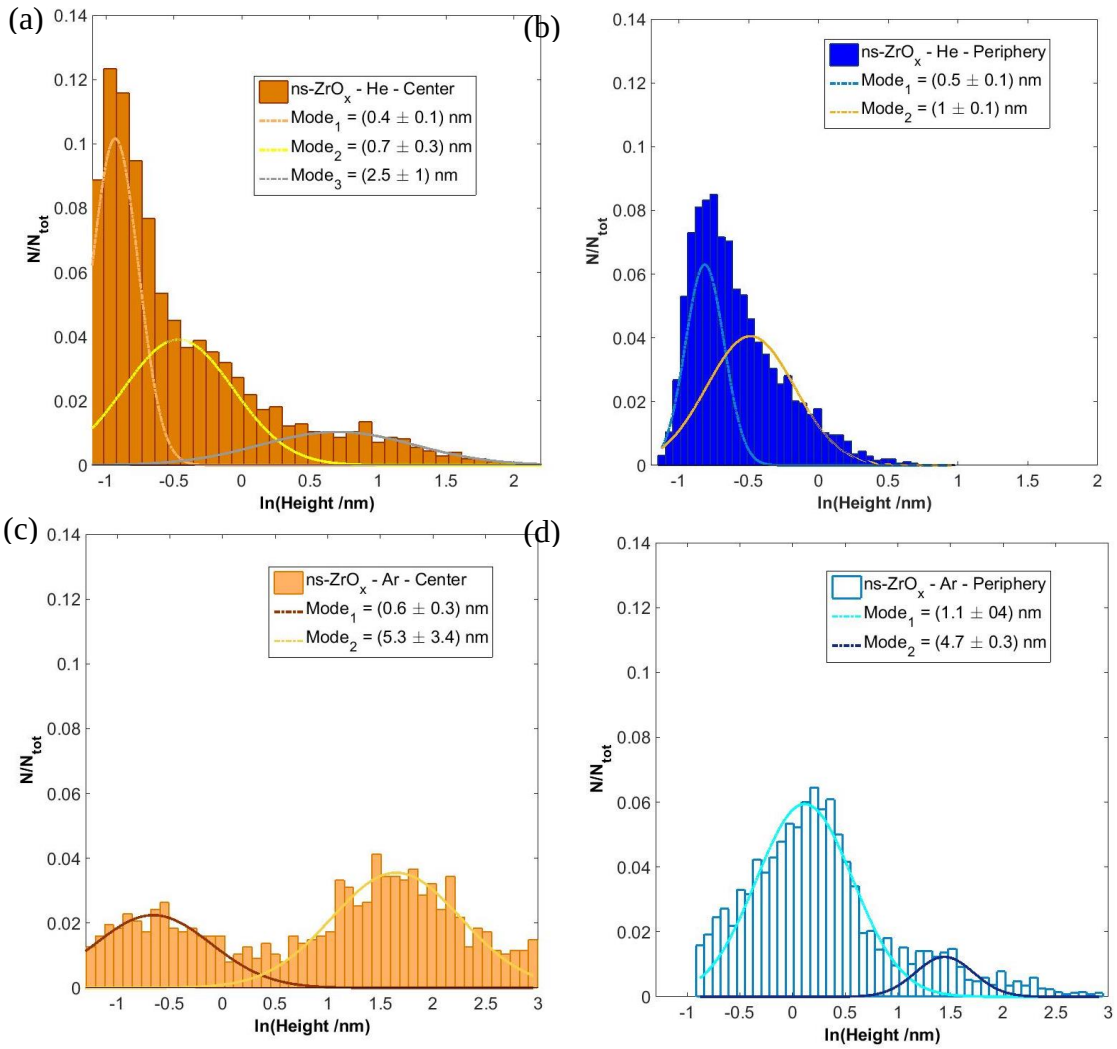

Fig. 65: height distributions of ns-ZrO_x sample calculated by the AFM images as the ones reported in Fig. 64, with superimposed multi Gaussian fit.

From TEM and XRD analysis[1] the cubic phase of zirconia clusters deposited at room temperature has been observed, in sub-stoichiometric conditions. The number of atoms in the incident ZrO_x clusters range from 500 to 22000, with the exception of the smaller ones. In fact in all the distribution plots also very small clusters are present on the surface. Their structure is probably amorphous.

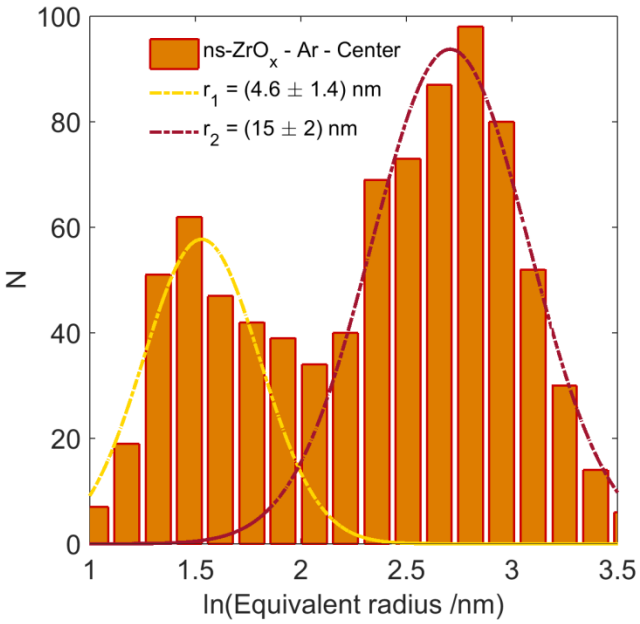

Fig. 66: equivalent radius distribution of clusters in semi-log scale and multi Gaussian fit.

In Fig. 66 I report in semi-log scale an example of the equivalent radius distribution obtained by the AFM images, in particular of ns-ZrO_x clusters deposited by Argon. It has been calculated by the projected area of the objects analyzed, assuming a cluster spherical shape. Fig. 66 allows the comparison of vertical (heights) with lateral dimensions of the clusters, as they have been calculated by the analysis of the AFM maps. From the back-transformed values reported in the legend of Fig. 66 it is evident that lateral dimensions appear larger that the vertical one, and this can be surely due to the effects of the convolution with the AFM tip during the acquisition of data. Assuming a tip radius of 6 nm and a spherical object shape, the deconvolved Gaussian peaks of the lateral dimensions are 0.9 nm and 9.4 nm. They are always larger that the heights, but we have to take into consideration that the real dimension and shape of the AFM tip and the shape of clusters observed are unknown.

Ns-TiO_x

TiO_x clusters show a rather wide size distribution depending again from the carrier gas used during deposition. Fig. 67 shows representative AFM images of ns-TiO_2 clusters deposited using Helium and Argon, intercepting the center and the periphery of the beam, accordingly. The corresponding distributions of particles heights are shown in Fig. 68 in semi-log scale.

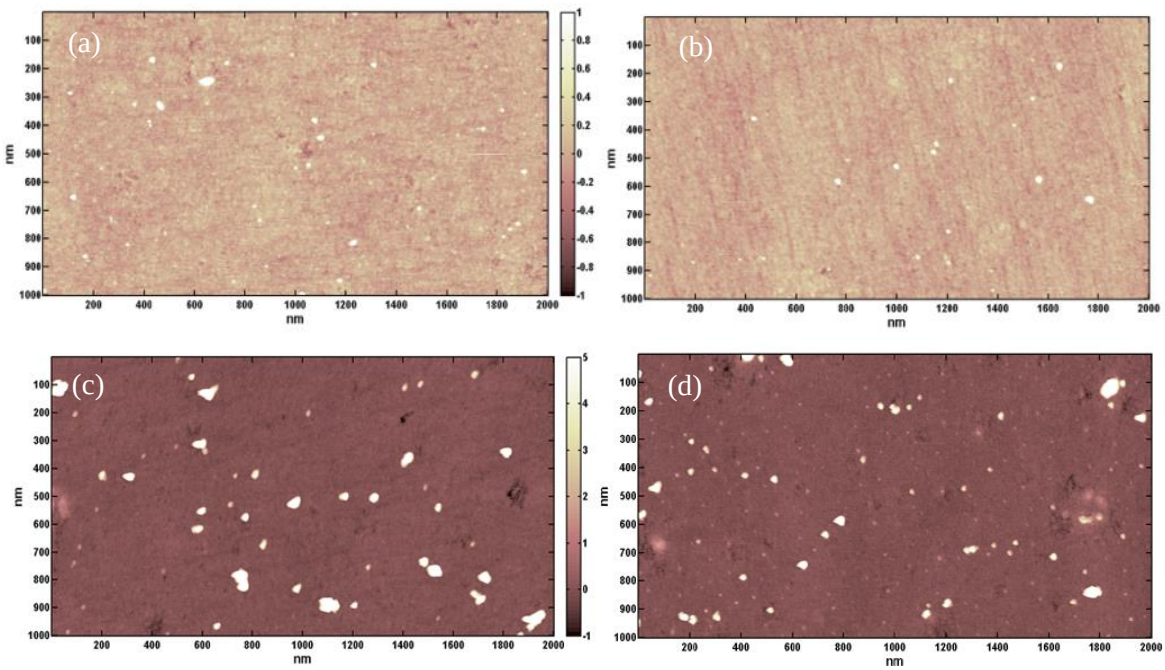

Fig. 67: Representative AFM topographic images of ns-TiO_2 clusters deposited using Helium (a-b) and Argon (c-d) on Si substrate, in the center and periphery of the beam.

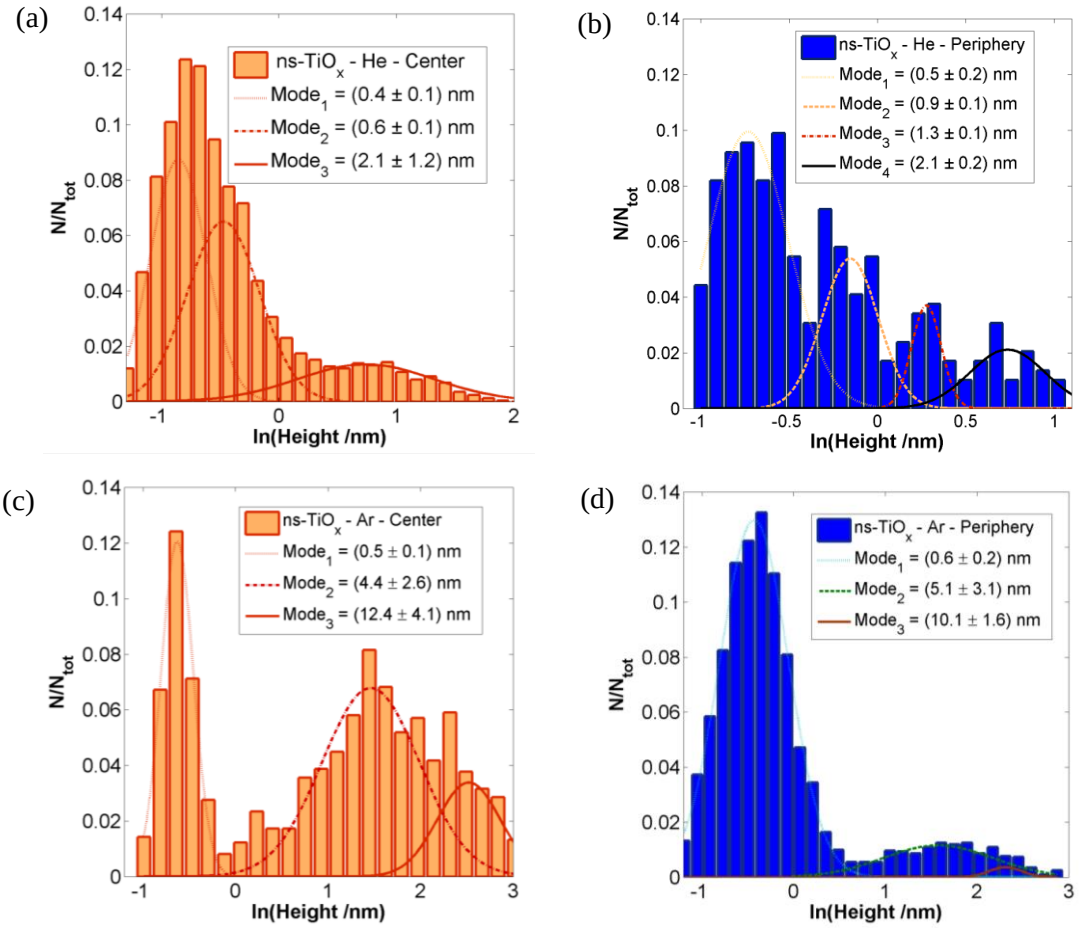

Fig. 68: the distributions of particles heights of Fig. 67, in semilog scale with multi Gaussian fit.

The size distributions of TiO_2 nanoparticles produced using Ar and He from the beam center are mainly bimodal. As for the ZrO_x system, the main relevant difference between Ar and He deposition is the median size of particles belonging to the major mode: the diameter is about 4.5 nm for Ar, and it is about 2.1 nm for He. As mentioned before for ns-ZrO_x depositions, this remarkable difference in particle diameter can be attributed to the different sputtering yield of the two gases. Selecting the carrier gas therefore allows the shift by a significant amount of the median particles diameter. Inertial effects of clusters in the supersonic beam determine the concentration of larger particles along the beam axis, as proved by the depletion of the large-diameter mode in the case of Ar; in the case of He, depletion is less important, probably because particles in the major mode are already relatively small. The central portion of the cluster beam, the more intense, provides the greatest contribution to thin film growth; therefore Fig. 68 (a, c) represent a quantitative characterization of the size and relative abundance of building blocks used to produce our ns-TiO_2 films.

7.1.4. Evolution of morphology with coverage

The study of the evolution of the morphology with coverage in sub-monolayer regime has been performed in details only for ZrO_x particles and not for TiO_x. Main results are shown below.

Height vs Coverage

In the height histograms shown above for the first single shot deposition (Fig. 65 and 68), it is noticeable the multi-modal distribution of particles heights, which represents here the diameter of the particles. This feature remains after subsequent shots during the beginning of aggregation phenomena, also in z-direction. I characterized the evolution of the highest peak of the cluster/island height distribution (and not of the most populated one) in order to pay specific attention to these growth events. In Fig. 69 the evolution of the islands z-diameter (or height) with surface coverage is shown for Helium and Argon deposition, according to the position with respect to the beam axis.

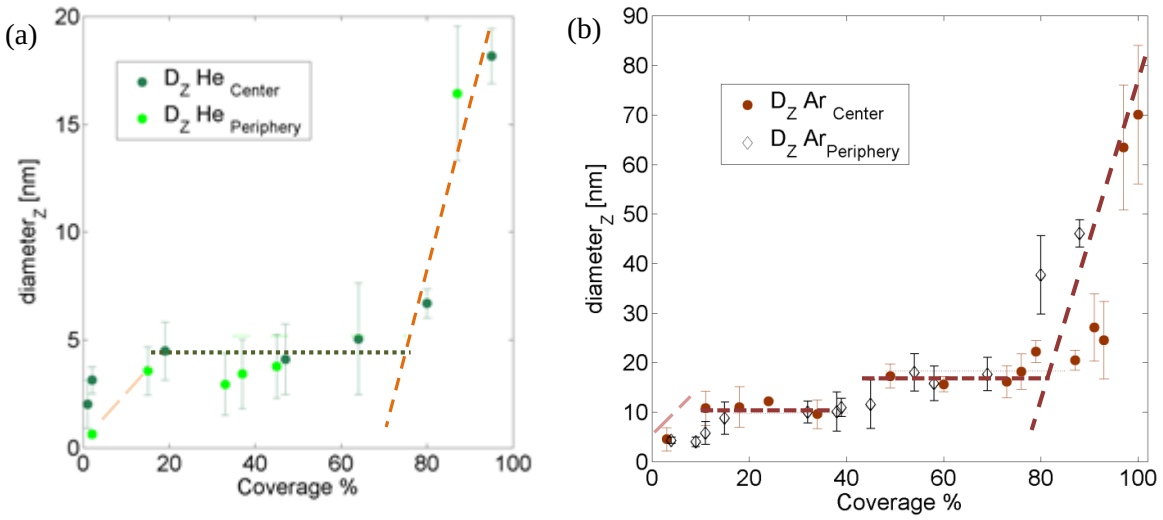

Fig. 69: Evolution of diameter (z-direction) of ns-ZrO_x islands on the substrate as a function of surface coverage, depending on the carrier gas used in the deposition (Helium – a, Argon – b) and the region of the film.

In all the systems analyzed, three are the characteristic regimes which can be identified in Fig. 69, according to the coverage range:

- 0 - 10 %: for very low coverage the coalescence and fast nucleation processes are promoted by the higher diffusivity of the smaller primeval incident cluster[7,8] and by their short time needed to coalesce[7] (see Section 2.2.2), driven by the minimization of the surface energy (Section 2.2.2)[9,10];
- 10 - 70 %: for intermediate coverage range the islands growth in z-direction in He system seems to be frozen, while for Ar system it seems to proceed stepwise around coverage of 50%. Fig. 69 in this range suggests that the islands growth (for He-system) proceeds for x-y juxtaposition or for nucleation of new islands on the surface. In the next Section I will discuss these possibilities;
- 70 – 100%: from coverage around 70%, the fast increase in z dimension of islands suggests that a percolation threshold is reached on the surface and that surface diffusion is hinibited because of the presence of pre-deposited clusters (aggregated in islands) on the surface. This is the starting point of ballistic deposition (Section 2.3.3) and takes place at the characteristic coverage of 70%.

$N_{islands}$ vs Coverage

By looking at the surface morphologies at 50% coverage (reported in Fig. 70), it is noticeable an asymmetry between Helium (a-b) and Argon (c-d) deposition: the number of nucleation sites of relatively small islands seems to be higher for Helium deposition instead of the Argon one, where islands shape suggests a juxtaposition growth process. In order to deeply analyze the evolution of surfaces with coverage range between 10 and 70 %, I decided to quantify evolution of the number of free primeval incident clusters and of the islands (defined in Section 7.1.1) on the surface (Fig. 71).

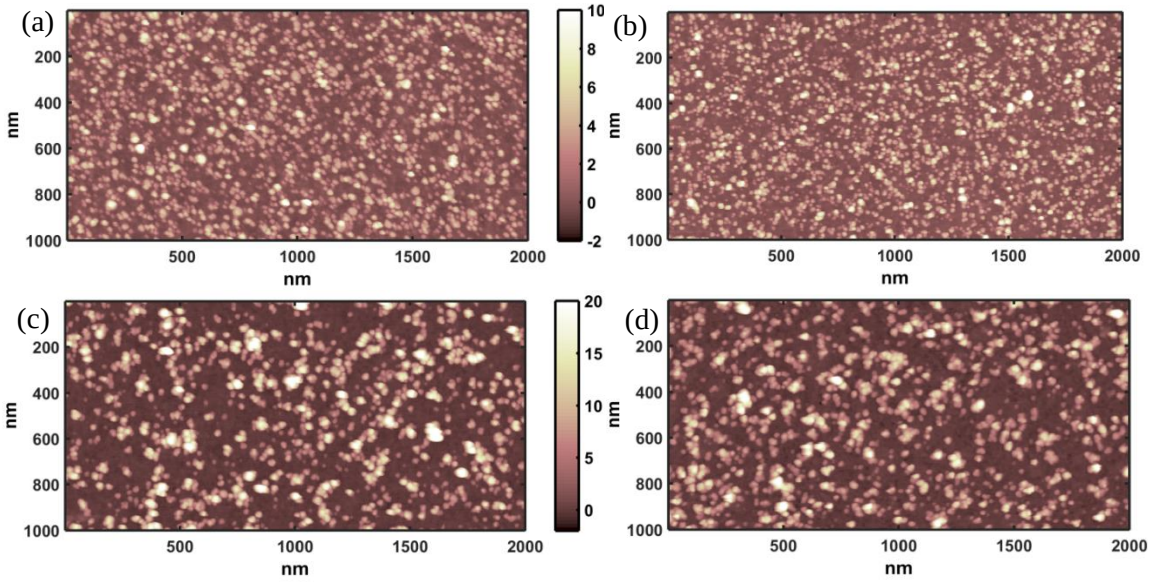

Fig. 70: AFM topographical maps of Helium (a-b) and Argon (c-d) deposition of ns-ZrO_x clusters for 50% of coverage, in the center of the beam (a-c) and in the periphery (b-d) of the beam.

The qualitative evolution of island density on the surface with coverage is similar to the one illustrated in Section 3.2.1 and in Ref [11]. For very low coverage the primeval incident cluster density rapidly grows leading to a rapid increase of island density N_s for nucleation events by cluster-cluster encounter on the surface. This goes on, until the islands occupy a small fraction of the surface, roughly 1-10%[8], depending on the incident cluster dimensions. For larger coverages, a competition appears between nucleation events and island growth processes, leading to a slower increase of island density. N_s saturates for coverage around 30-50% [8,11,12], when all the incident clusters are eaten by previously formed islands, before they can meet another cluster and form a new island: nucleation becomes negligible. When the coverage is about 30-50%, the linear dimension of the island

becomes of the order of their separation distance and coalescence between islands (static coalescence) starts, which leads to a decrease of the island density[11].

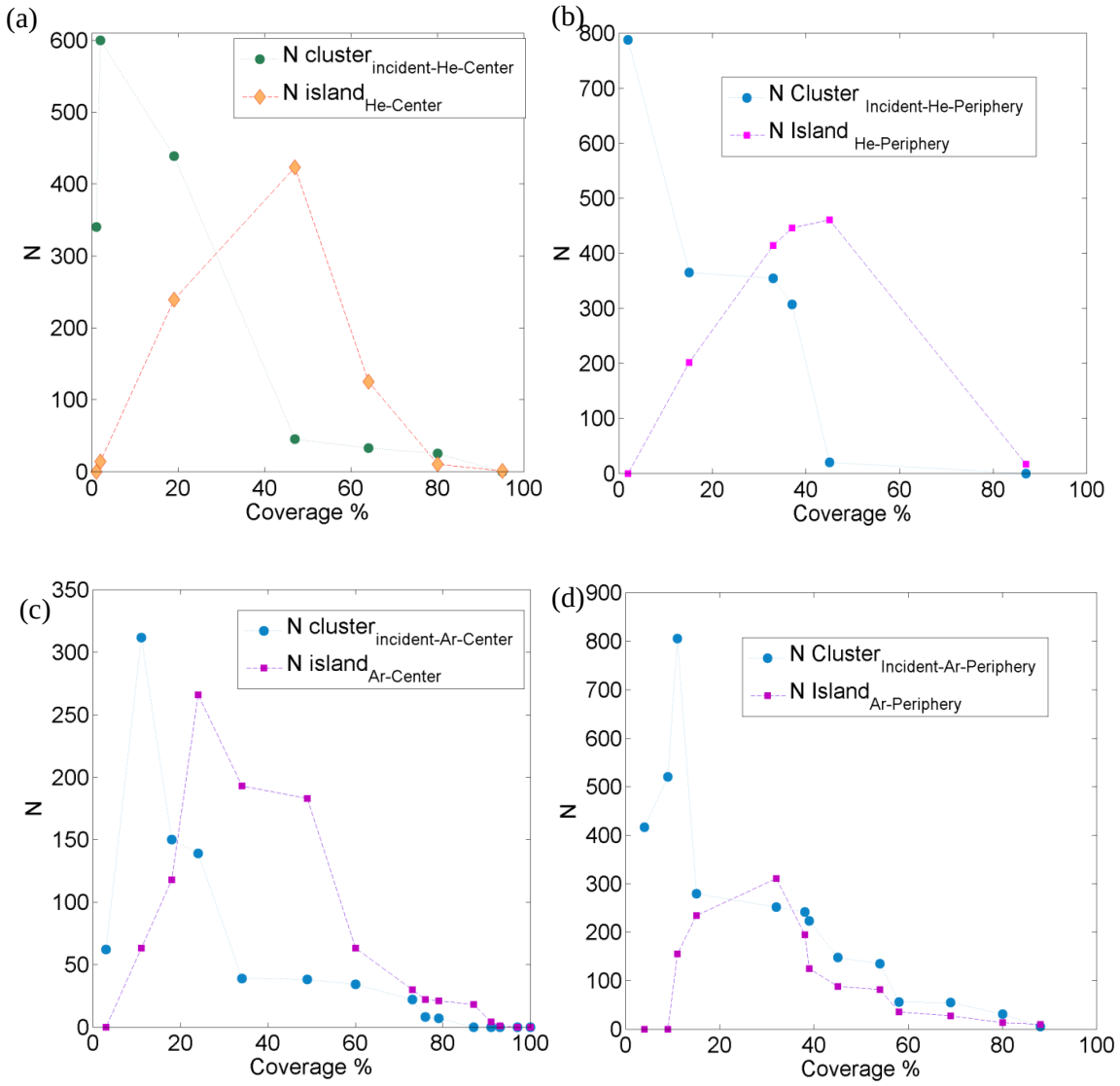

Fig. 71: Evolution of the primeval incident cluster and island densities as a function of the surface coverage, for Helium (a-b) and Argon (c-d) deposition, in the center (a-c) and periphery (b-d) of the beam.

By comparing the two systems (different carrier gases) for the same value of surface coverage, it is possible to appreciate an higher island density (or higher density of nucleation sites) for Helium deposition than for Argon. The smaller dimensions of He primeval incident clusters provide a larger free surface region for new nucleation events, favored also by the high surface diffusivity of the smaller amorphous He-ZrO_x clusters. For these small clusters, coalescence is preferred to juxtaposition, and so the occupied area of the new island is smaller than the one occupied by island formed by a juxtaposition

process[8]. The faster nucleation events of He primeval incident clusters, compared to Argon system, is also proved by the lower coverage needed for the saturation of He-free primeval incident clusters on the surface (~1%) than for Ar (~10%).

The saturation of island density (N_{sat}) is reached around 20-30 % of coverage for Ar; this value is predicted for a growth where only smaller incident clusters can move on the surface and cluster-cluster interactions are prevalently characterized by juxtaposition processes[11],[8]. Otherwise, N_{sat} is reached for higher coverage (40-50%) for He system. This behavior can be explained by the possibility that also islands (and not only primeval incident clusters) can move on the surface, by forbidding stationary nucleation sites (which are present in Ar system) for juxtaposition growth. Furthermore, I have just explained that for small He primeval incident cluster nucleation events by coalescence is preferred to juxtaposition processes. He-cluster arrive on the substrate after supersonic expansion with a higher impact velocity[6,13] and the lower deposition rate of Helium forced us to deposit a single shot for longer time than Ar sample, where the substrate intercept the beam with different angles of incidence in different times. All these conditions facilitate a larger diffusivity of He clusters on the surface[14] and so a higher nucleation events rate.

I have now more elements to produce a general picture of the growth mechanism for the two systems. In Helium-system, the islands growth in z-direction stops very early with coverage, but it is always favored instead of juxtaposition and it induces nucleation events also at high coverage. In Argon-system, few nucleation sites (composed by the larger incident clusters) attract the other smaller and mobile incident clusters and form islands for juxtaposition events. In Argon-system, the step growth in z-direction is probably facilitated by the arrival of new incident cluster on pre-deposited large cluster or island, which is trapped. In fact, larger clusters mean also a lower fractal dimension[15] and so an open structure of cluster which facilitate the capture.

Area-Volume vs Coverage

Fig. 72 shows the qualitative evolution of projected area and volume (referred to the highest peak of the area and volume distributions) of islands with coverage, for He and Ar systems. I refer to a qualitative evaluation of the trend and not to a quantitative one, because the estimation of area and volume of the objects identified in the AFM maps is always affected by the effects of the convolution with the AFM tip. Anyway, the estimation of the qualitative trend is important to confirm the considerations I have previously done about

islands growth in the intermediate coverage range (10% - 70%) and for this reason I have chosen to show them below. The maximum coverage studied is 70%, also because for higher coverage value objects area and volume on the surface increase of different order of magnitude, because of the interconnected morphology created on the surface. This observation further confirms that 70% coverage is the threshold for the starting point of ballistic deposition regime.

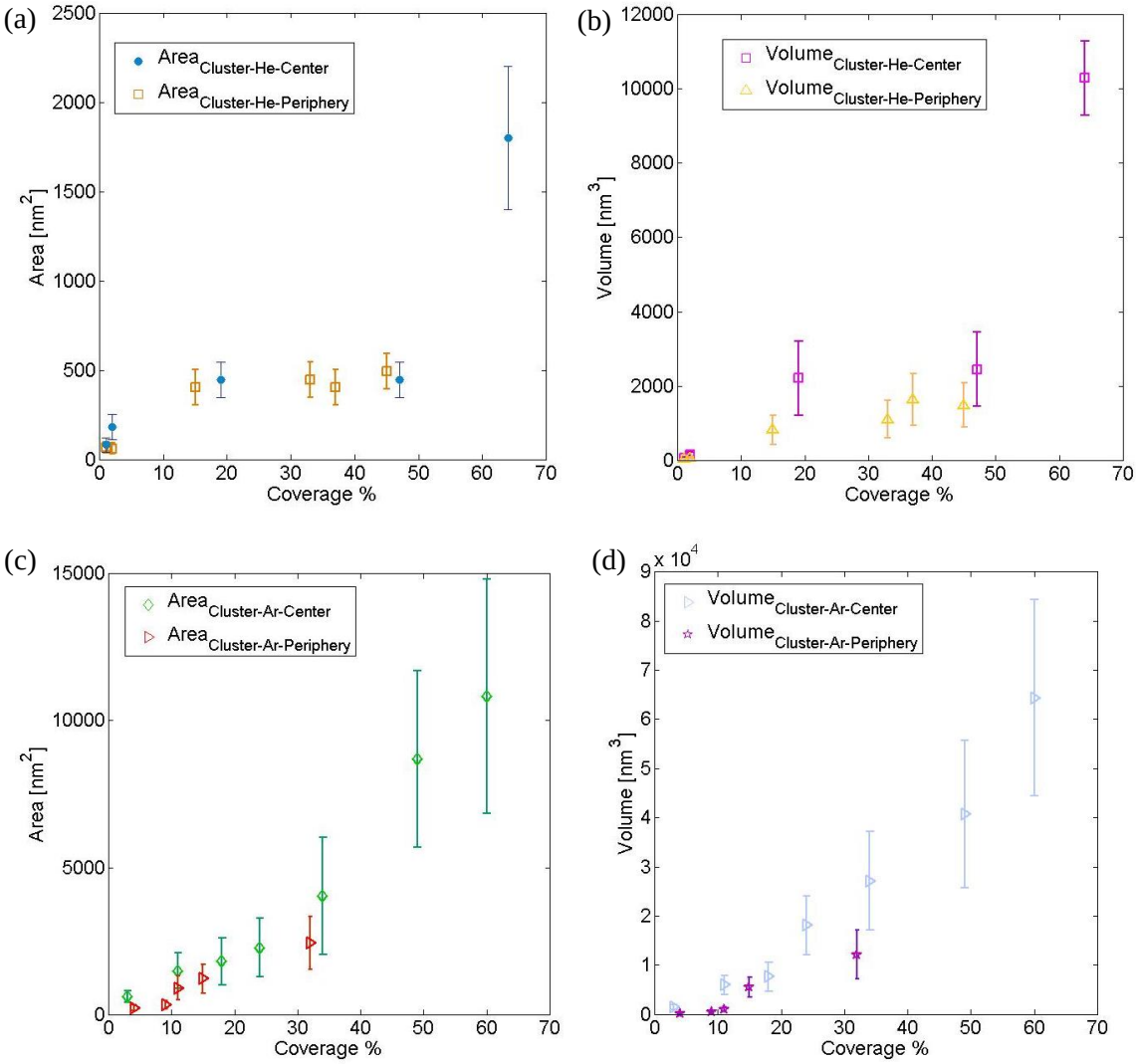

Fig. 72: Evolution of the highest peak of the projected area (a-c) and volume (b-d) of the distribution calculated by the AFM topographical maps versus coverage for Helium and Argon systems.

In Argon-systems (Fig. 72 c-d), area and volume grow quite linearly with coverage, and this evolution agrees with a juxtaposition growth mode. In Helium system (Fig. 72 a-b), for intermediate coverage values, area and volume are quite constant with coverage. Also this trend confirms the frozen island growth process and the grow of coverage mainly due to new nucleation events.

Mean Cluster size vs Coverage

In Ref [16] P. Jensen and coworkers have showed how the mean size of the cluster distribution can increase exponentially with coverage if clusters can move on the surface and coalescence occurs even at the early stage of growth. The mean size is defined as $\langle s \rangle = \sum s N_s / N_S$, where N_s is the number of clusters containing s particles. This exponential increase is very peculiar since usually, in growth models[17-19] power laws are found. Fig. 73 shows the linear increase of the mean cluster size with coverage in semilog scale, confirming and exponential growth.

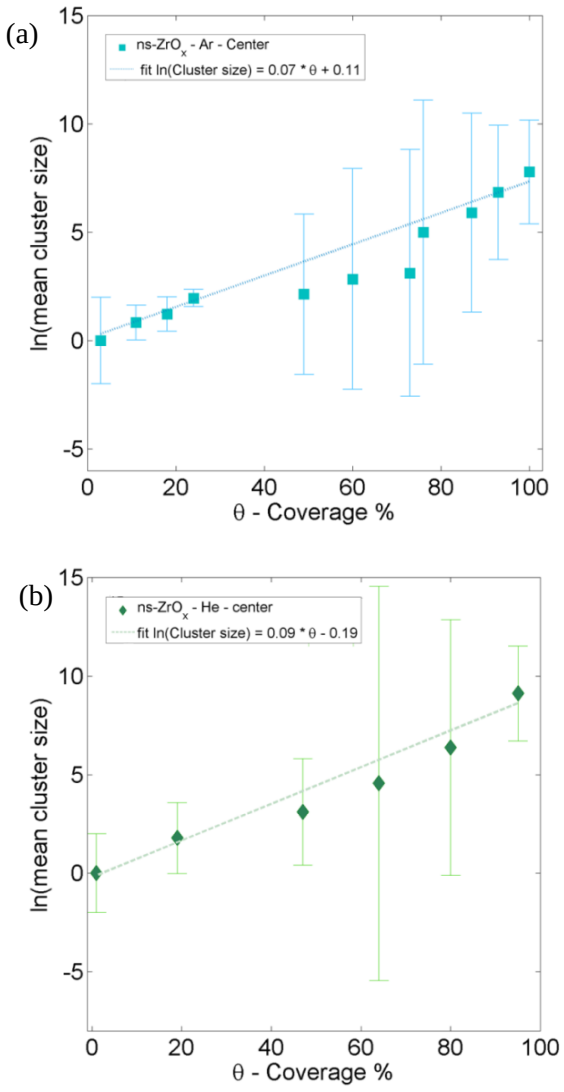

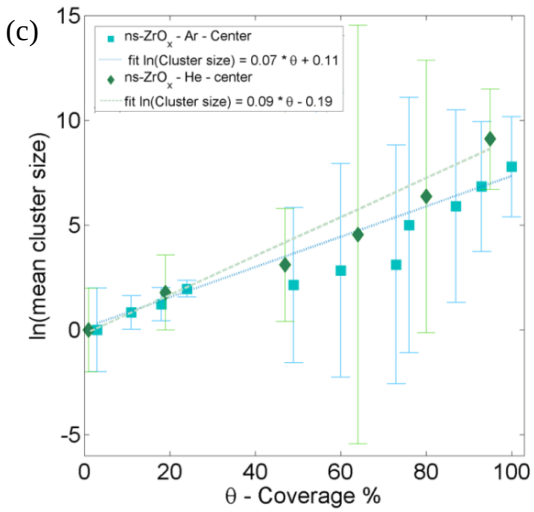

Fig. 73: Mean cluster size as a function of coverage for Argon-system (a), Helium system (b) and comparison between the two (c); superimposed and reported in the legend the linear fit in semi-log scale.

Fig. 73 confirms the exponential increase in the mean cluster size with coverage for our systems, which suggests continuous diffusion of the smaller zirconia cluster on the surface and coalescence processes with larger clusters and islands for both the systems.

7.1.5. Evolution of rms-roughness: from sub-monolayer to thin film

In order to correlate the sub-monolayer growth phenomena with thin film properties, I have characterized the RMS roughness (Rq) of the sample in the sub-monolayer regime. In Fig. 74 the trend of roughness with coverage is shown.

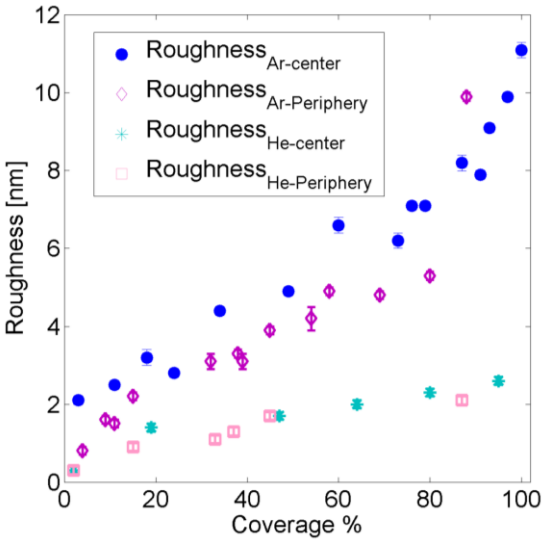

Fig. 74: Evolution of surface roughness with coverage in sub-monolayer regime.

The evolution of roughness with coverage exhibits a nearly linear trends for all the systems, but it increases faster in Argon-system. The slow increase of roughness with coverage for Helium-system is due to the smaller incident cluster dimension and islands formed on the surface (as shown before) and also to the different growth in z-direction, consisting in continuous nucleation events which induce to recover the surface before growing in other direction. This growth dynamic remind the layer growth mode of thin film, shown in Section 2.1.2.

Fig. 75 (a) shows the increase in surface roughness depending on the number of particles deposited on the surface, and it offers the opportunity to link sub-monolayer regime with thin film regime (up to 50 nm thin film). In Fig. 75 (b) the same data in log-log scale are shown.

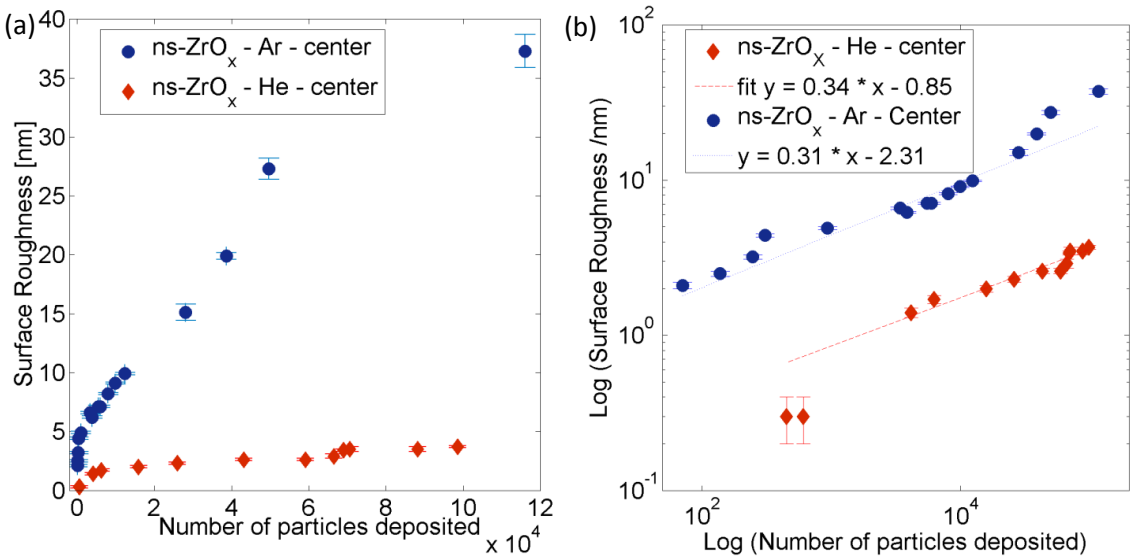

Fig. 75: (a) evolution of surface roughness with number of particle deposited, (b) in log-log scale with a linear fit.

Fig. 75 (b) shows clearly that the evolution of roughness with coverage, with the exception of an offset in z-direciton, is the same: the growth exponent is 0.34 for Helium and 0.31 for Argon. The deposition rate is not constant and for this reason I can not identify this growth exponent with the one defined in Section 2.3, but if we consider the mean deposition rate constant for different shots we can conclude that this growth exponent is peculiar of a ballistic deposition growth.

It is remarkable the continuity of the trend with the number of particles deposited, regardless of the growth regime. This result reveals the intrinsic character of ballistic deposition also for sub-monolayer growth.

7.2. Beyond the monolayer regime: thin films

Clusters are randomly assembled to constitute a porous structure (Fig. 76) with density of the film being roughly half of the corresponding bulk phase (2.5–2.7 g/cm^3 against 3.9–4.3 g/cm^3 for bulk TiO_2, as obtained from optical methods[20]). The nanostructure is characterized by ns-TiO_x nanocrystalline regions (prevalently anatase[21]) embedded in an amorphous matrix, or by entirely cubic phase[1] ns-ZrO_x clusters.

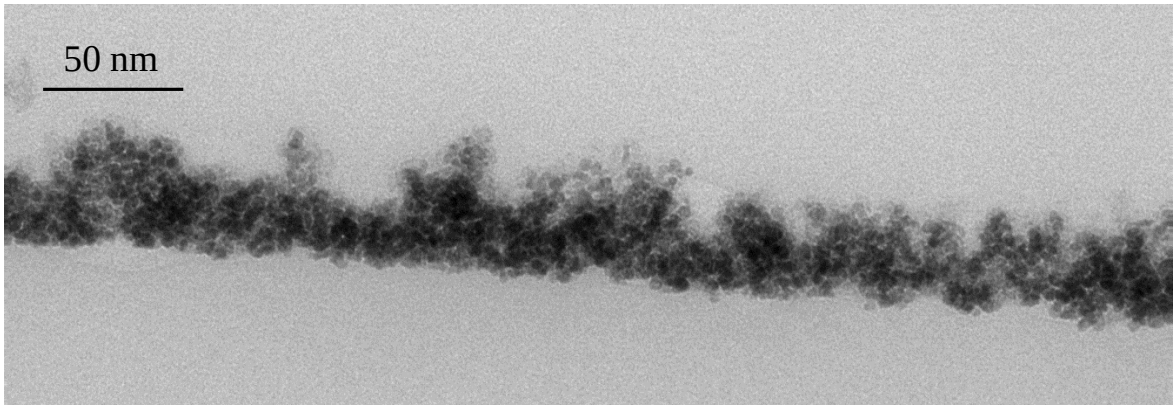

Fig. 76: TEM image of ns-ZrO_x porous thin film.

In this chapter I will compare the morphological properties calculated on thin film in order to identify, principally by scaling laws, the theoretical model which better describes our film growth. Clearly visible is the pattern of nanometer-sized grains, pores, with high aspect-ratio. Overall, the films are characterized by high specific area and porosity at the nano and sub-nanometer scale, extending in the bulk of the film.

7.2.1. Ballistic deposition

Ns-ZrO_x

Fig. 77 (a,b) shows representative topographic maps (top-view) of ns-ZrO_x films with similar thickness (about 30 nm, like the film shown in Figure 76) deposited using He and Ar as carrier gas, with rms roughness Rq of 8 and 21 nm, accordingly. The Argon thin film is in sub-monolayer regime but its roughness is already higher in value that the Helium thin film. The bigger dimensions of Argon-cluster instead of Helium one (yet dilated by the AFM tip convolution) is visible also by a visualization comparison of the AFM images. This difference, which has been quantitatively characterized as shown in the previous sections, can be explained in terms of the marked differences in the cluster size distributions

obtained using He and Ar. Fig. 77 (a,b) also clearly show the granular, nano-porous nature of low-energy cluster-assembled materials, and the remarkable gain in specific area due to the use of small nanometer-sized building blocks.

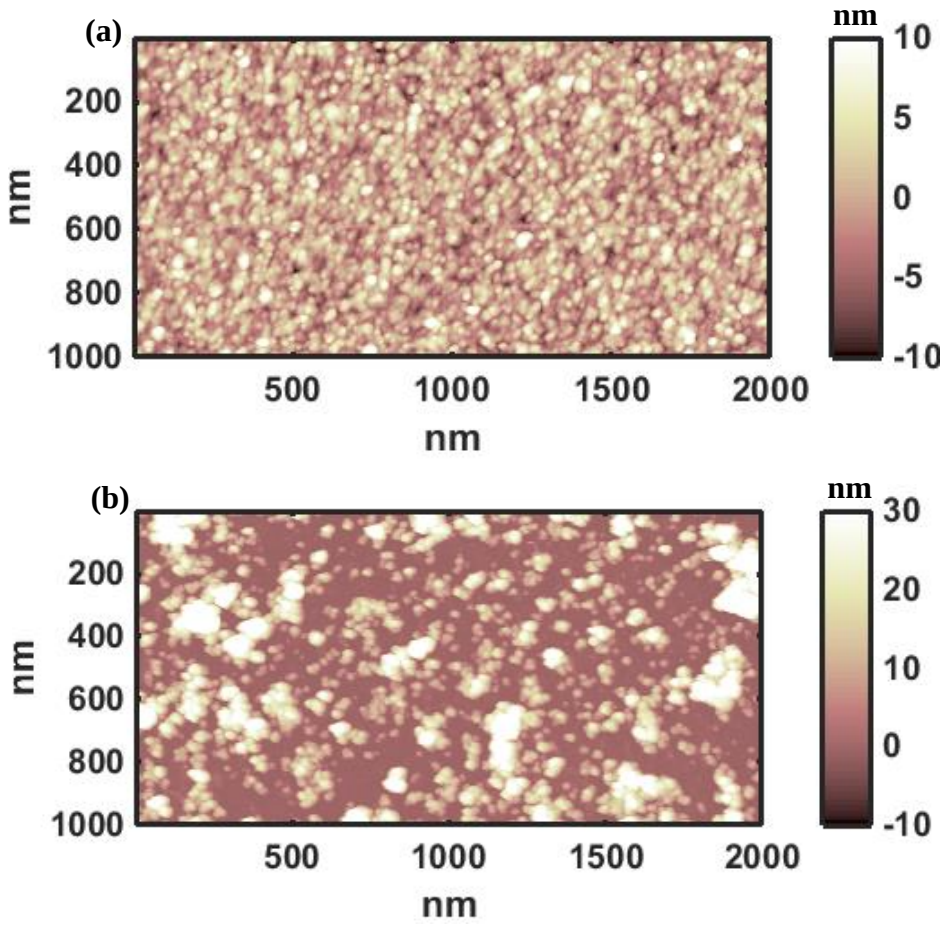

Fig. 77: Representative topographic maps (top-view) of ns-ZrO_x films with similar thickness (about 30 nm) deposited using He (a) and Ar (b) as carrier gas. Argon deposited film is in sub-monolayer regime.

For both the system I have analyzed the evolution of the main morphological properties with thickness (which I assume proportional to deposition time, i.e. constant deposition rate and constant density) in order to study the interfacial properties by scaling laws (section 2.3). According to AFM data, the growth exponent of cluster-assembled ns-ZrO_x films is $\beta = 0.37 \pm 0.05$ for Ar, and $\beta = 0.32 \pm 0.08$ for He. The scaling of the surface RMS roughness is therefore independent on the carrier gas (although the absolute value of Rq, at a given deposition time, can be dramatically different, as from Fig. 77 a,b and, quantitatively, from Fig. 78). Concerning the value of the growth exponent β, it is compatible with a ballistic deposition model (for which β spans from 0.3 to 0.33 in 2

dimensions, see section 2.3.3), where incoming particles land on the growing interface, stick, and do not diffuse significantly.

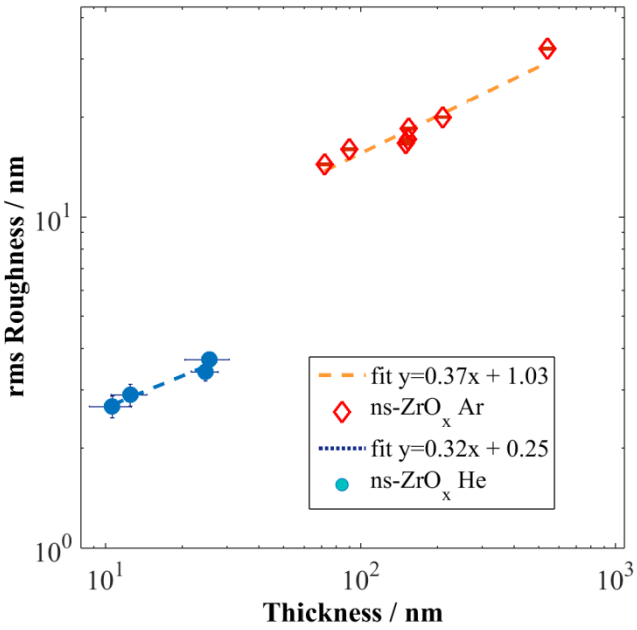

Fig. 78: Linear regression of the experimental curve $Rq \sim h^{\beta}$.

On the other side, the exponent z (or better the quantity 1/z) can be directly characterized by a linear regression in loglog scale of the experimental curve $\xi \sim h^{1/z}$ (Fig. 79), which describe the evolution of the lateral width of the surface.

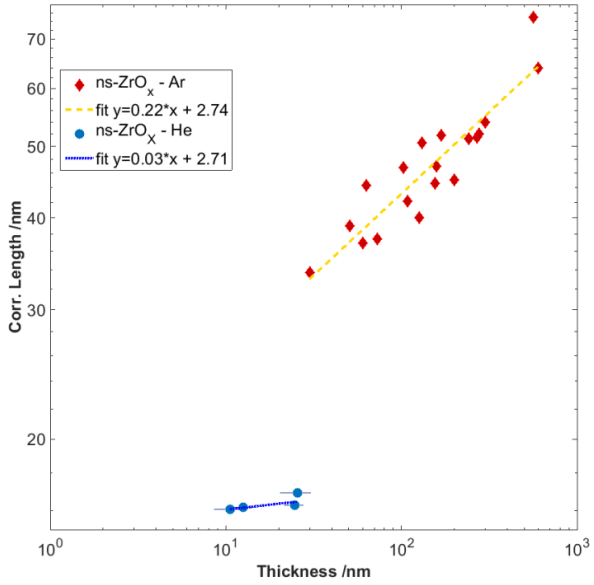

Fig.79: evolution of the lateral width of the surface $\xi \sim h^{1/z}$.

The roughness exponent α can be calculated as α=β/(1/z) (see section 2.3). I obtained the following results: 1/z = 0.22 ± 0.02 (z = 4.54 ± 0.11) and α = 1.68 in the case of Ar; 1/z = 0.03 ± 0.05 (z = 33.3 ± 0.30) and α = 10.6 in the case of He. The exponents 1/z and α in the case of He are strongly unusual, but I have analyzed few samples and they are faraway from a film-like regime.

Specific area is a critical parameter for interfacial phenomena, representing the gain in the area potentially available for surface reactions and interactions. As the rms roughness Rq and the correlation length ξ, also the specific area A_{spec} is an increasing function of film thickness, and its growth is governed by simple power laws. The scaling of the surface specific area excess Δr = r-1 with film thickness, $\Delta r \sim h^{\delta}$, is shown in Fig. 80. I found δ = 0.31 ± 0.01 for Ar, and δ = 0.13 ± 0.04 for He. In the case of Ar as carrier gas, the specific area excess grows faster, and films deposited using Ar have the highest specific area values.

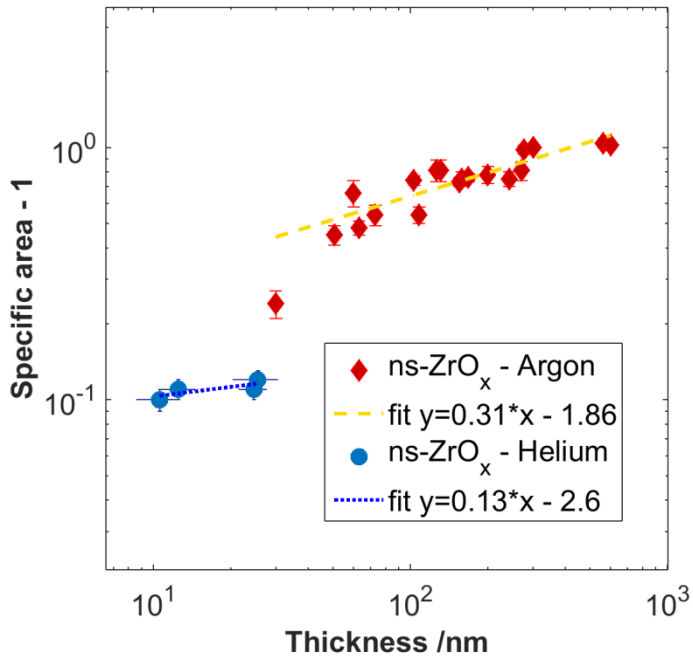

Fig. 80: The scaling of the surface specific area excess Δr = r-1 with film thickness ($\Delta r \sim w^{\delta}$) depending on the carrier gas used during deposition.

Specific area is closely related to the local surface slope, which is expected to follow a similar trend (while the *mesoscopic* average slope and specific area parameters, evaluated on a scale ξ, are not expected to change much, because Rq and ξ scaling exponents are similar).

Ns-TiO_x

Fig. 81 (a,b) shows representative topographic maps (top-view) of ns-TiO_x films with similar thickness (about 100 nm) deposited using He and Ar as carrier gas, with rms roughness Rq of 8 and 21 nm, accordingly. As for ZrO_x samples, despite the thickness is the same, a marked difference in surface corrugation is observed, as well as a difference in the average size of the surface grains, which represent either the precursor clusters in the beam (yet dilated by the AFM tip convolution), or their aggregation/ coalescence at the surface upon deposition. This difference, which has been quantitatively characterized as shown in the previous sections, can be explained in terms of the marked differences in the cluster size distributions obtained using He and Ar.

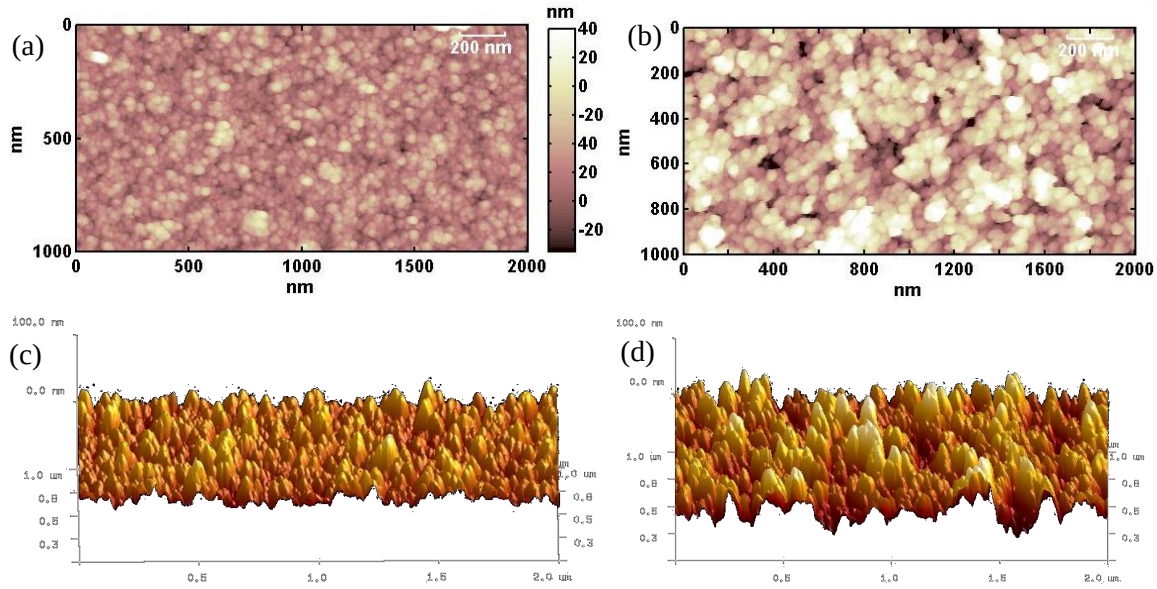

Fig. 81: Representative topographic maps (top-view) of ns-TiO_2 films with similar thickness (about 100 nm) deposited using He (a) and Ar (b) as carrier gas, with rms roughness w of 8 and 21 nm. 3D views of the surface of ns-TiO_2 films deposited using Ar, with roughness of 10 (c) and 22nm (d) are shown.

Fig. 81 (a,b) also clearly show the granular, nano-porous nature of low-energy cluster-assembled materials, and the remarkable gain in specific area due to the use of small nanometer-sized building blocks. To further highlight these morphological properties, three-dimensional views of the surface of ns-TiO_2 films deposited using Ar, with roughness of 10 and 22 nm are shown in Fig. 81 (c,d).

A linear regression of the experimental curve $Rq \sim h^{\beta}$ on a loglog scale is shown in Fig. 82. According to our data, the growth exponent of cluster-assembled ns-TiO_2 films is

β= 0.38 ± 0.04, for Ar, and β= 0.39 ± 0.02 for He. The scaling of the surface rms roughness is therefore independent on the carrier gas (although the absolute value of Rq, at a given deposition time, can be dramatically different, as from Fig. 81 a,b and, quantitatively, from Fig. 82).

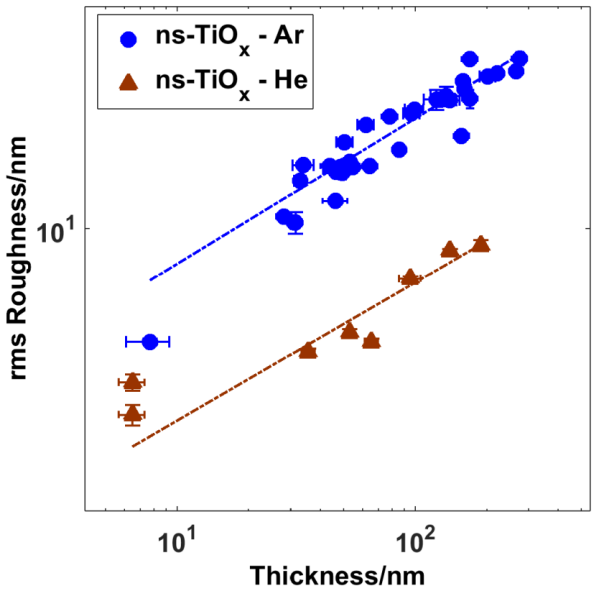

Fig 82: Linear regression of the experimental curve $w \sim h^{\beta}$; curve is plotted in loglog scale.

The exponent z (or better the quantity 1/z) can be directly characterized by a linear regression in loglog scale of the experimental curve $\xi \sim h^{1/z}$ (Fig. 83), which describe the evolution of the lateral width of the surface. Then, the roughness exponent α can be calculated as α=β/(1/z) (see section 2.3).

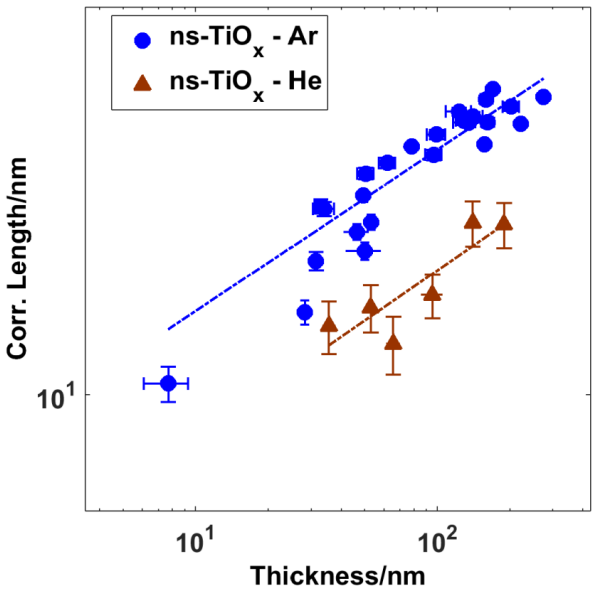

Fig. 83: evolution of the lateral width of the surface $\xi \sim h^{1/z}$; curve is plotted in loglog scale.

I obtained the following results: $1/z = 0.43 \pm 0.02$ ($z = 2.33 \pm 0.11$) and $\alpha = 0.88 \pm 0.06$ in the case of Ar; $1/z = 0.39 \pm 0.05$ ($z = 2.56 \pm 0.30$) and $\alpha = 1.00 \pm 0.14$ in the case of He.

Concerning the value of the growth exponent β, it is compatible with a ballistic deposition model (see Section 2.3.3). The ballistic deposition regime typical of the low-energy cluster-assembling from the gas phase, thanks to the absence of significant surface diffusion, allows growing films with high specific area and local aspect ratio.

The scaling of the surface specific area excess $\Delta r = r-1$ with film thickness, $\Delta r \sim w^{\delta}$, is shown in Fig. 84. We have found $\delta = 0.27 \pm 0.01$ for Ar, and $\delta = 0.45 \pm 0.04$ for He. In the case of He as carrier gas, the specific area excess grows faster, although in the accessible thickness range, for a given thickness, films deposited using Ar have the highest specific area values. This behavior could be understood in terms of the smaller average particle size with respect to Ar, leading to a more compact interface, with smaller sub-nanometer pores. Specific area is closely related to the local surface slope, as mentioned before for ns-ZrOx thin films.

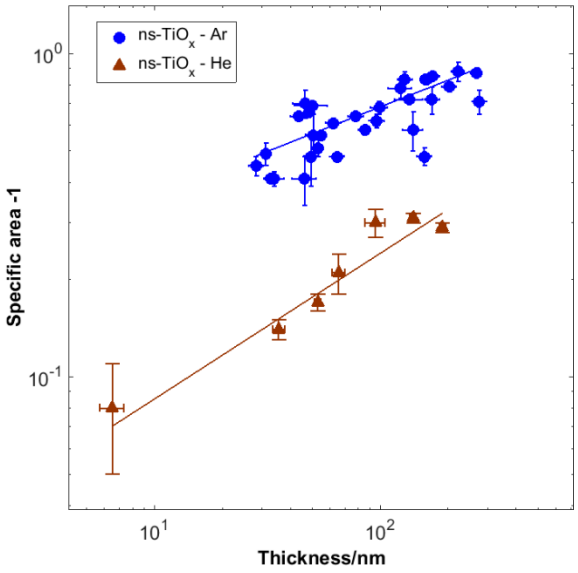

Fig. 84: The scaling of the surface specific area excess $\Delta r = r-1$ with film thickness ($\Delta r \sim w^{\delta}$) depending on the carrier gas used during deposition.

7.3. Effect of annealing temperature on morphology of thin films

Ns-ZrO$_x$

Evolution of grain size with annealing temperature

I have calculated the values of the grain equivalent radius in thin films, above the threshold for the onset of ballistic deposition regime, in order to study the correlation between observed granularity and chemico-physical phenomena occurring under thermal annealing. Grains have been identified and analyzed according to what reported in Seccion 4.3.3. In Fig. 85 (A) they are reported the dimensions of the equivalent grains radius as a function of annealing temperatures, depending on the surface roughness. We have shown the error bars of the grain dimensions referred to only one sample for sake of clarity; they correspond more or less to the same value for all the samples. It is an indicator of the dispersion of the grain dimension around the mean value (which corresponds to the median of the log-normal distribution of equivalent radius).

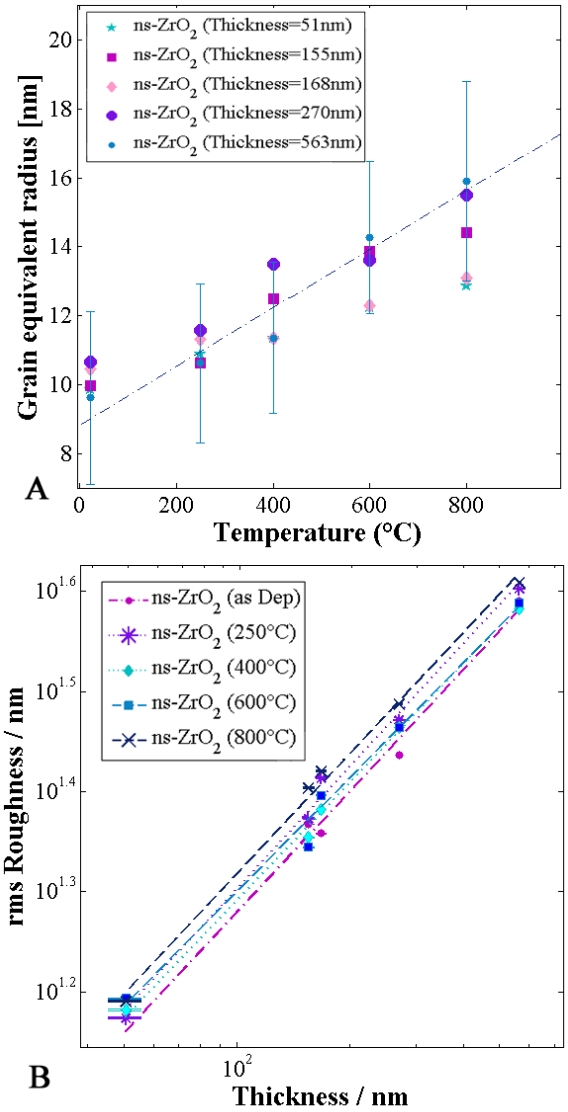

Fig. 85: (A) Evolution of the grain sizes with the annealing temperatures, depending on the roughness of the nanostructured zirconia surface. (B) log-log plot of the roughness versus thickness

of the as deposited ZrOx samples and of the annealed samples up to 250°C, 400°C, 600°C and 800°C.

Annealing at 250°C causes a little growth of nanoparticles, probably due to the complete crystallization of the smaller clusters from the amorphous-to-cubic phase[1]. Thermal annealing at 400°C and 600°C induce another phase transition, from cubic to monoclinic phase[1], which determine another slow growth of the clusters size. From the XRD analysis[1] it has been shown the linear increasing transition from cubic phase to monocline one in air in this range of temperature and the growth of crystalline grains correlated to the phase transition. During the annealing the cubic nano-crystals coarsen and when their size reaches a critical value they transform to stable monoclinic phase[1,24,25]. This behavior has been described by the critical-nuclear-size model[26-28]. According to this model the monoclinic crystallites cannot grow until the nucleus size of this phase reaches a critical value; this requires the agglomeration of fine-grained cubic particles into larger ones. The growth of cubic nano-crystallites beyond the critical size is energetically not favorable since cubic phase has a higher total energy compared to monoclinic one[29,30]. With the annealing at 800° C there's a further increase in cluster dimensions. In XRD analysis[1] the growth of single zirconia crystalline domains in air from 600°C to 800°C for the monocline phase is shown to be around 100%. From this granulometry studies, we can conclude that also in cluster-assembled thin films the cluster growth is principally induced by phase transition (in particular from cubic to monoclinic phase) and not for coalescence between clusters driven by thermal annealing.

With the increase of the annealing temperature begins also a restructuration of surface in all the 3D directions, which determines a very small increase of the surface roughness (as shown in Fig. 85 B), due to the increased cluster dimensions[31], and also the reorganization in x-y directions which influence the changes in A_{spec} and correlation length ξ values.

I have to notice that the determination of the radius, with the procedure shown in this work, is not an accurate quantitative characterization process; in fact it is affected by the effect of the convolution of the tip with the surface during the image acquisition process and can also be partially influenced by the analysis process, in particular during the individualization of the best grain mask (see Section 4.3.3). The level of criticality in the analysis explains also the large error associated to the median value of the radius distribution.

Scaling of morphological parameters of the annealed thin films

In the previous Section I have already pointed out the small adjustments in all the three dimensions of the morphological properties at the interface of the annealed cluster-assembled thin films. Anyway the granular, nano-porous matrix of low-energy cluster-assembled materials with high specific area and porosity at the nano and sub-nanometer scale remains also after thermal annealing treatments. The surface morphology of the high temperature annealed thin film keeps memory of the nanometers-size building blocks organization and deposition conditions.

In Fig. 85 (B) the small increasing of roughness values with annealing temperature is shown for each thickness for all the five samples studied. The linear fit of the log-log plot of roughness versus thickness show comparable values of β for all the annealing temperature analyzed, which varies from 0.38 to 0.41 (as reported in Table III), but remains basically constant within the error.

	As Dep.	250° C	400° C	600° C	800° C
β	0.37 ± 0.01	0.41 ± 0.06	0.39 ± 0.08	0.38 ± 0.06	0.40 ± 0.06

Table III: β exponents of ns-ZrOx sample with different post-deposition treatments.

The evolution of the nanostructure of the films is influenced by the structure of the precursor clusters even after a quite severe annealing. It keeps memory of the deposition process (ballistic deposition) even after high thermal annealing processes.

It is possible to appreciate this statement visually in Fig. 86, where the topographic maps of the sample 150 nm thick after different thermal treatments (as indicated by the labels) and two representative profiles are shown, and also in Fig. 87, where I have composed a 2μm x 1μm image with small sections of the images of the this sample annealed up to five different temperatures, as indicated from the labels in the Fig.86.

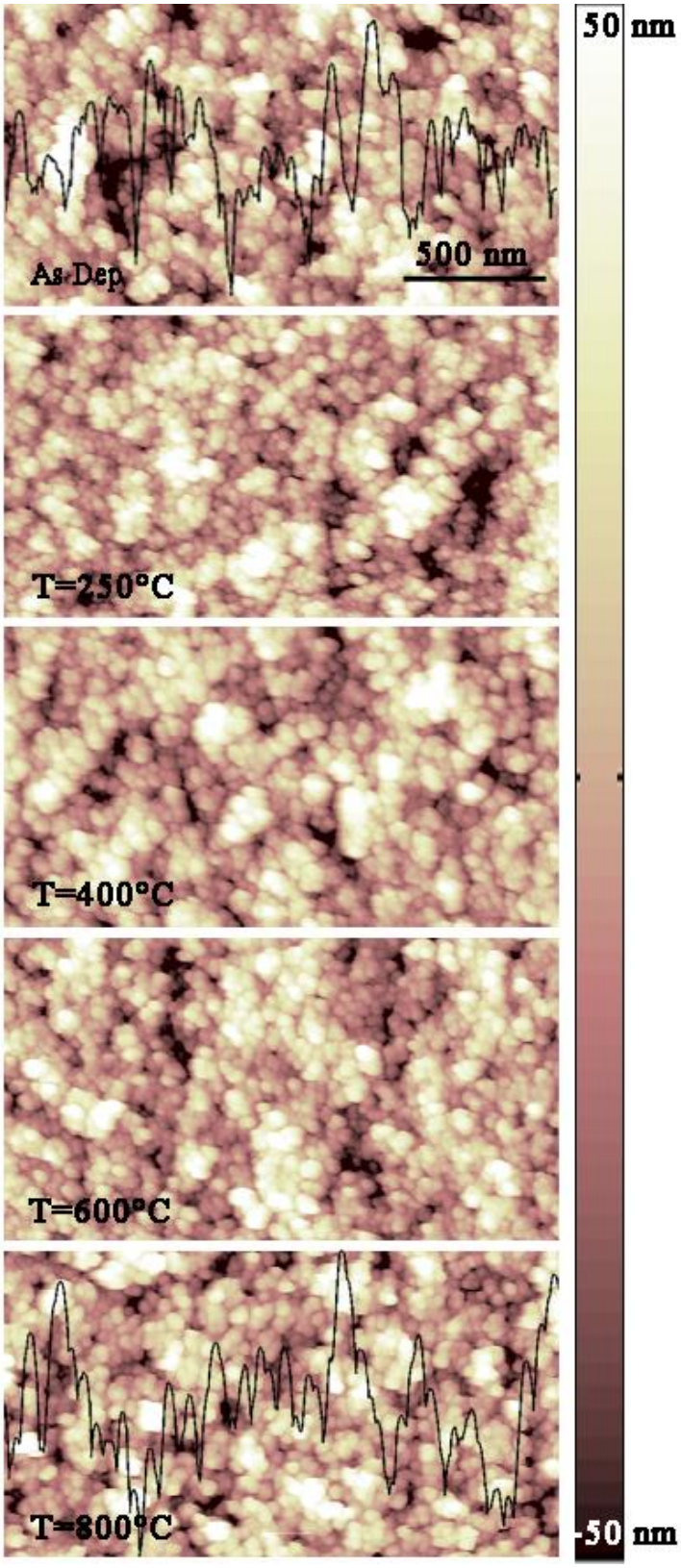

Fig. 86: ns-ZrO_2 surface topographic maps showing the surface morphology evolution depending on the thermal annealing processes, from the as deposited sample to the annealed up to 800° C.

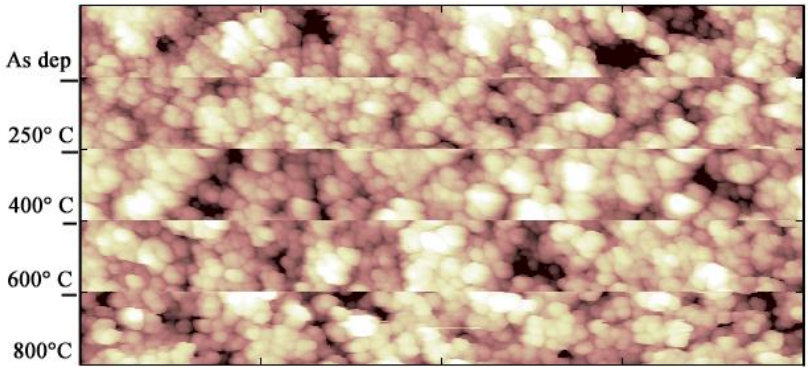

Fig. 87: topographic image built up with images acquired from the 150 nm thick sample annealed at diffrent temperatures.

Ns-TiO_x

In this section I report a very short study I have performed on AFM images acquired different years ago (2008), in order to compare ns-ZrO_x morphology evolution with thermal annealing with ns-TiO_x one. Titania deposition has been performed with Helium as carrier gas and the sample was characterized by a thickness of 100 nm. The sample was successively kept in an oven for three hours at different annealing temperature (from 200 °C to 1000 °C), in an Ar/O_2 80/20 atmosphere.

In Fig. 88 representative AFM maps of the sample annealed at different temperature are shown and in table IV are reported the main morphological properties of the surface.

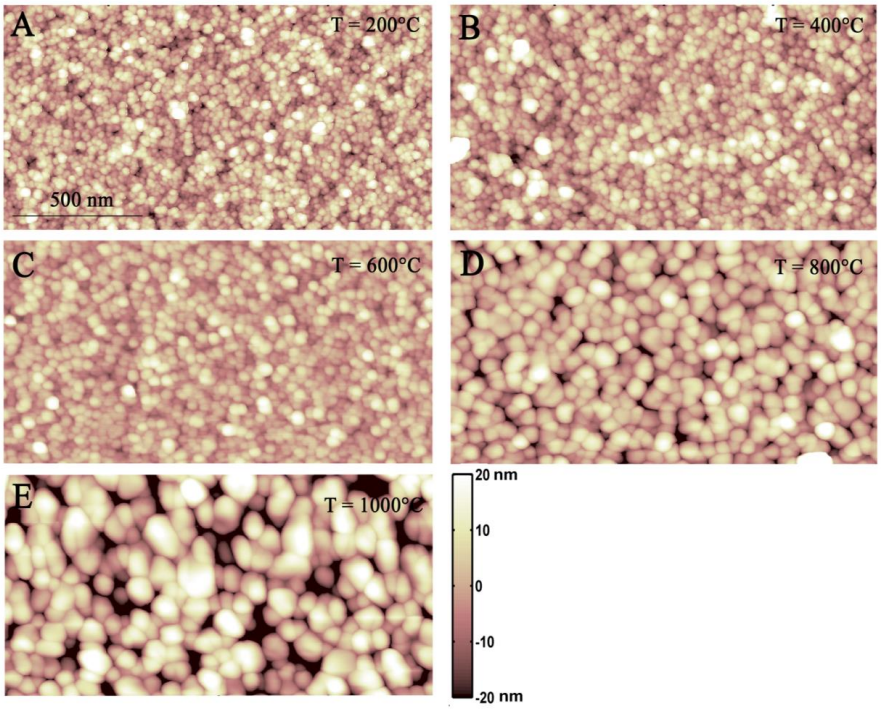

Fig. 88: ns-TiO_x AFM topographic maps with different thermal annealing treatments: 200°C (A),

400°C (B), 600°C (C), 800°C (D) e 1000°C (E).

Temperature (°C)	Rq [nm]	Cluster radius [nm]
200	7,3 ± 0,1	10.8 ± 1.5
400	6,9 ± 0,5	11.9 ± 1.4
600	5,5 ± 0,1	12.2 ± 1.5
800	8,4 ± 0,6	21.1 ± 1.4
1000	11,4 ± 0,2	30.1 ± 1.3

Table IV: roughness and cluster radius of ns-TiOx sample, with different post-deposition treatments.

The evolution of roughness with annealing temperature is similar to the trend of ns-ZrO_x sample: it remains quite constant until the cluster radius grows of 300%. The growth of cluster size is probably associated to the phase transformation from anatase to rutile (see section 5.1.1), but we have to confirm this hypothesis by structural analysis performed on Helium-deposited sasmple.

7.4. Memory effect

In Section 3.1.2 I have mentioned the peculiar feature of the morphological properties of cluster-assembled films associated to LECBD: they are determined by the original free clusters structure. This is called 'memory effect'. Three are the main results shown in this Chapter which are useful to underline and define memory effect phenomena of metal oxide nanostructured samples deposited by SCBD:

1. Precursor cluster dimensions affect the growth dynamics in sub-monolayer regime (Section 7.1): the diffusion on the surface and nucleation events are favored for smaller clusters, which form islands on the surface by both coalescence and juxtaposition processes; larger clusters act as static nucleation sites where juxtaposition growth-mode is promoted.

2. Growth dynamics in sub-monolayer regime determines different morphological properties of the cluster-assembled thin film (Section 7.2). The morphological properties of samples deposited with different primeval cluster sizes (by using Ar or He as carrier gas) are influenced by the dimension of clusters in a non banal way.

By a geometrical point of view, we can image that, for the same thickness film value, roughness is lower for film produced by small clusters while it is larger when bigger clusters are used during deposition. AFM experiments show also that the dynamics of growth of the film in sub-monolayer regime influences the final film roughness, in particular by the roughness value reach at coverage 70% when the ballistic deposition takes place.

3. The evolution of the nanostructured morphology of the films is influenced by the dimension and the structure of the precursor clusters even after a quite severe annealing; it has been demonstrated in Section 7.3. We have observed that the anatase ns-TiOx and cubic ns-ZrOx nanocrystallites grow up to a critical size where their further growth is not energetically favourable, so they transform to rutile and monoclinic respectively. This shows that size-dependent effects in grain growth kinetics affect the morphology evolution of nanostructured films. The system retains a memory of the initial nanostructure even after the annealing, showing well-crystallized nanograins with dimensions and packing depending upon the initial precursor clusters.

References

1. Lenardi, C., Sogne, E., Borghi, F., Podestà, A. & Paolo, M. Effects of Temperature and Oxygen Vacancies on Nanocrystallite Phase and Size in Metastable Cluster Assembled ZrO2 films. (to be published).
2. Granqvist, C. G. & Buhrman, R. A. Statistical model for coalescence of islands in discontinuous films. *Appl. Phys. Lett.* **27,** 693 (1975).
3. Limpert, E., Stahel, Werner A. & Abbt, M. Log-normal Distributions across the Sciences: Keys and Clues. *BioScience* **51,** 341–352 (2001).
4. Kubart, T., Nyberg, T. & Berg, S. Modelling of low energy ion sputtering from oxide surfaces. *J. Phys. Appl. Phys.* **43,** 205204 (2010).
5. Yamamura, Y. & Tawara, H. Energy Dependence of Ion-induced Sputtering Yields from Monatomic Solids at Normal Incidence. *At. Data Nucl. Data Tables* **62,** 149–253 (1996).
6. Huang, C. *et al.* Supersonic jet deposition of silver nanoparticle aerosols: Correlations of impact conditions and film morphologies. *J. Appl. Phys.* **101,** 064902 (2007).
7. Yoon, B. *et al.* Morphology control of the supported islands grown from soft-landed clusters. *Surf. Sci.* **443,** 76–88 (1999).
8. Jensen, P. Growth of nanostructures by cluster deposition: Experiments and simple models. *Rev. Mod. Phys.* **71,** 1695–1735 (1999).
9. Navrotsky, A. Thermochemistry of Nanomaterials. *Rev. Mineral. Geochem.* **44,** 73–103 (2001).
10. Benning, L. G. & Waychunas, G. A. in *Kinetics of Water-Rock Interaction* (eds. Brantley, S. L., Kubicki, J. D. & White, A. F.) 259–333 (Springer New York, 2008). at <http://link.springer.com/chapter/10.1007/978-0-387-73563-4_7>
11. Bardotti, L. *et al.* Diffusion and aggregation of large antimony and gold clusters deposited on graphite. *Surf. Sci.* **367,** 276–292 (1996).
12. Amar, null, Family, null & Lam, null. Dynamic scaling of the island-size distribution and percolation in a model of submonolayer molecular-beam epitaxy. *Phys. Rev. B Condens. Matter* **50,** 8781–8797 (1994).
13. Melinon, P. *et al.* Low-energy cluster beam deposition : do you need it ? *J. Phys. I* **3,** 1585–1603 (1993).
14. Francis, G. M., Goldby, I. M., Kuipers, L., von Issendorff, B. & Palmer, R. E. Deposition and growth of noble metal clusters on graphite. *J. Chem. Soc. Dalton Trans.* 665 (1996). doi:10.1039/dt9960000665
15. T Mazza, M. D. Accessing the fractal dimension of free clusters in supersonic beams. *New J. Phys.* **13,** 023009 (2011).

16. Jensen, P., Barabási, A.-L., Larralde, H., Havlin, S. & Stanley, H. E. Deposition, diffusion, and aggregation of atoms on surfaces: A model for nanostructure growth. *Phys. Rev. B* **50,** 15316–15329 (1994).
17. Tang, L.-H. Island formation in submonolayer epitaxy. *J. Phys. I* **3,** 935–950 (1993).
18. Bartelt, M. C. & Evans, J. W. Scaling analysis of diffusion-mediated island growth in surface adsorption processes. *Phys. Rev. B* **46,** 12675–12687 (1992).
19. Vicsek, T. *Fractal growth phenomena*. (World Scientific, 1992).
20. Barborini, E. *et al.* Nanostructured TiO2 Films with 2 eV Optical Gap. *Adv. Mater.* **17,** 1842–1846 (2005).
21. Carbone, R. *et al.* Biocompatibility of cluster-assembled nanostructured TiO2 with primary and cancer cells. *Biomaterials* **27,** 3221–3229 (2006).
22. Barabási, A.-L. *Fractal concepts in surface growth*. (Press Syndicate of the University of Cambridge, 1995).
23. *Dynamics of fractal surfaces*. (World Scientific, 1991).
24. S. Schlabach, D. V. S. Zirconia and Titania Nanoparticles Studied by Electric Hyperfine Interactions, XRD, and TEM. *J. Alloys Compd.* **434-435,** 590–593 (2007).
25. Garvie, R. C. The Occurrence of Metastable Tetragonal Zirconia as a Crystallite Size Effect. *J. Phys. Chem.* **69,** 1238–1243 (1965).
26. Borg, R. J. & Dienes, G. J. *The Physical Chemistry of Solids*. (Academic Press, 1992).
27. Kumar, K.-N. P., Keizer, K., Burggraaf, A. J., Okubo, T. & Nagamoto, H. Textural evolution and phase transformation in titania membranes: Part 2.?Supported membranes. *J. Mater. Chem.* **3,** 1151 (1993).
28. Kumar, K.-N. P. Growth of rutile crystallites during the initial stage of anatase-to-rutile transformation in pure titania and in titania-alumina nanocomposites. *Scr. Metall. Mater.* **32,** 873–877 (1995).
29. Kresse, G. & Furthmüller, J. Efficient iterative schemes for ab initio total-energy calculations using a plane-wave basis set. *Phys. Rev. B* **54,** 11169–11186 (1996).
30. Christensen, A. & Carter, E. A. First-principles study of the surfaces of zirconia. *Phys. Rev. B* **58,** 8050–8064 (1998).
31. Namavar, F. *et al.* Thermal stability of nanostructurally stabilized zirconium oxide. *Nanotechnology* **18,** 415702 (2007).

8. Interfacial functional properties affected by surface morphology

8.1. Double layer interaction

8.1.1. IsoElectric Point of rough interface

Ns-TiO_x

Here below, my work " Nanoscale roughness and morphology affects the IsoElectric Point of titania surfaces"[4] is reported.

OPEN ACCESS Freely available online

PLOS ONE

Nanoscale Roughness and Morphology Affect the IsoElectric Point of Titania Surfaces

Francesca Borghi[1], Varun Vyas[1,2¤], Alessandro Podestà[1]*, Paolo Milani[1]

1 Interdisciplinary Centre for Nanostructured Materials and Interfaces (C.I.Ma.I.Na.) and Dept. of Physics, Università degli Studi di Milano, Milano, Italy, **2** European School of Molecular Medicine (SEMM), IFOM-IEO Campus, Milano, Italy

Abstract

We report on the systematic investigation of the role of surface nanoscale roughness and morphology on the charging behaviour of nanostructured titania (TiO_2) surfaces in aqueous solutions. IsoElectric Points (IEPs) of surfaces have been characterized by direct measurement of the electrostatic double layer interactions between titania surfaces and the micrometer-sized spherical silica probe of an atomic force microscope in NaCl aqueous electrolyte. The use of a colloidal probe provides well-defined interaction geometry and allows effectively probing the overall effect of nanoscale morphology. By using supersonic cluster beam deposition to fabricate nanostructured titania films, we achieved a quantitative control over the surface morphological parameters. We performed a systematical exploration of the electrical double layer properties in different interaction regimes characterized by different ratios of characteristic nanometric lengths of the system: the surface rms roughness R_q, the correlation length ξ and the Debye length λ_D. We observed a remarkable reduction by several pH units of IEP on rough nanostructured surfaces, with respect to flat crystalline rutile TiO_2. In order to explain the observed behavior of IEP, we consider the roughness-induced self-overlap of the electrical double layers as a potential source of deviation from the trend expected for flat surfaces.

Citation: Borghi F, Vyas V, Podestà A, Milani P (2013) Nanoscale Roughness and Morphology Affect the IsoElectric Point of Titania Surfaces. PLoS ONE 8(7): e68655. doi:10.1371/journal.pone.0068655

Editor: Richard G. Haverkamp, Massey University, New Zealand

Received May 22, 2013; **Accepted** May 30, 2013; **Published** July 16, 2013

Funding: The authors have no support or funding to report.

Competing Interests: The authors have declared that no competing interests exist.

* E-mail: alessandro.podesta@mi.infn.it

¤ Current address: Institute of Material Sciences, University of Connecticut, Storrs, Connecticut, United States of America

Introduction

Electrostatic interactions taking place at the interface of transition metal oxides (TMO) with water play a fundamental role in determining the behavior of systems and devices strategic for applications in biomedicine, catalysis, energy production/conversion, environmental remediation [1,2,3]. Biophysical phenomena such as the formation of bilayer membranes [4,5,6] or the adsorption and reorganization of proteins and cells at interfaces [7,8] depend upon the charging state of TMO surfaces in aqueous medium [8,9,10,11,12].

The charge of TMO surfaces in aqueous medium is mainly determined by two phenomena: protonation/de-protonation of surface hydroxyls [13,14,15], and adsorption of electrolyte ions onto the surface [16]. Two spatially defined regions of electric charge thus develop: a first compact layer of charge (Stern layer), closer to the solid surface and a few atomic sizes thick, including truly surface charges (originating in the amphoteric dissociation of surface groups) and surface-bound charges (adsorbed ions from the solution); a second diffuse layer of hydrated ions of both signs extends toward the bulk of the solution [17,18,19]. An electrostatic potential, solution of the Poisson-Boltzmann equation, exponentially decaying away from the surface, is associated to the overall charge distribution [19,20,21].

An important parameter to describe these electrostatic phenomena is the IsoElectric Point (IEP), which corresponds to the pH value at which the net charge of the compact layer is zero [22]. At IEP, also the ζ potential of the surface, which is responsible of the electrophoretic properties of particles in solutions [1,22,23], is zero, provided we identify the ζ potential with the potential at the boundary between the compact and the diffuse layers [22]. The Point of Zero Charge (PZC) corresponds to the pH required to have zero net surface charge. For an oxide surface without specific adsorption of ions (different from H^+ or OH^-) the IEP coincides with the PZC and, in particular, the ζ potential is negative for pH above the IEP, and positive below it [24,25].

When two interacting surfaces approach to a distance comparable or smaller than the typical screening length of the electrolytic solution (the Debye length, determined by the ionic strength of the solution), the overlap of the charged layers determines complex regulation phenomena [17] that are difficult to describe theoretically. In particular, when regulation phenomena occur, none of the following conditions, the constant surface charge or the constant surface potential, hold; these quantities become a function of the separation distance between the two interacting surfaces, or equivalently of the degree of overlap of the corresponding double layers. This brings the solution of the electrostatic problem far from the boundaries of the simplified linearized theory, which strictly holds only at low surface potential, large distances, and low ionic strength [19,20,21].

While significant insights have been obtained on the properties of the electric double layers formed between flat smooth surfaces [11,16,17,21], the case of rough surfaces still represents a severe challenge, hampering analytical, yet approximate, solutions of the

double layer equations to be reliably obtained. Several authors have speculated that surface roughness may be responsible for discrepancies observed between experimental data and the predictions of the linearized DLVO theory; for example, a geometrical implication of surface corrugation is that the "average plane of charges", which produces the electrostatic double layer interaction, is shifted backwards with respect to the point of first contact between the surface and an incoming probe [26,27,28, 29,30,31]. Despite the paramount importance of the explicit consideration of surface corrugation for the description of double layer electrostatic phenomena in real systems, and the significant theoretical efforts made to model electrostatic interactions at rough interfaces, the practical implementation of such models is still a land of pioneering studies, relying on approximated representations of rough morphology and/or on suitable approximation of the Poisson-Boltzmann equations. The interaction energy between mildly corrugated planes exhibiting periodic undulations (in the weak roughness regime, i.e. amplitude small compared to wavelength) has been calculated by means of Derjaguin approximation [32] by Tsao [33] and by Suresh et al. [34]. The surface element integration (SEI) technique allowed overcoming the limitations of the Derjaguin approximation when calculating the interaction energy between curves surfaces, modeled as a collection of convex and concave regions (spherical or sinusoidal bumps or depressions) with arbitrarily large curvatures (yet within the limits of the linearized PB equations) [35,36,37,38,39]. In these works an effort is made to relate the simplified topological model of surface roughness to statistical parameters that can be measured by an atomic force microscope (AFM), such as root-mean-square and other roughness parameters, specific area, etc.; moreover, it is recognized that the ratio of characteristic lengths of the system (Debye length, surface roughness, asperity separation…) influences the relative strength of different contributions to the interaction energy (van der Waals, electrostatic, Lewis acid-base acidity…). Duval et al. have explicitly included in their calculation of interfacial electrostatic interactions the charging mechanisms of the surfaces, developing a theoretical/numerical framework to account for local morphological (though calculations are implemented only for LEGO-like corrugated interfaces) as well as chemical heterogeneities of the surfaces. Their model takes into account the fine structure of the electrostatic double layer and boundary conditions beyond the limits of the linearized PB equations, allowing therefore to account for spatially-resolved charge regulation mechanisms and surface roughness effects [40]. Daikhin et al. have considered a statistical representation of surface morphology (in terms of height distributions) rather than on simplified geometrical constructions [41,42,43]; yet, their focus is limited to the calculation of some measurable electrochemical observables, typically the double layer capacitance. None of the works discussed so far present explicit calculations of the interaction force between rough surfaces in electrolyte solutions, and for this reason a direct application of theories for the analysis of experimental data acquired at complex rough interfaces is not straightforward.

Since most of the relevant biophysical phenomena cited above take place at the nanoscale, the characterization of charging mechanisms of nanostructured surfaces in electrolytic solutions and of the influence of the surface nanostructure is a necessary step towards the fundamental understanding and the effective exploitation of the role of nanostructured surfaces in tailoring and determining the functionality of the TMO interface with bio-objects [7,8,9].

A major problem hampering to reach a systematic and theoretically well-established description at the nanoscopic scale of interface charging is the lack of systematic experimental studies on double layer interactions at nanorough interfaces: in particular this is a consequence of the difficulty of preparing and characterizing, at the nanoscale, interfaces with controlled morphology, roughness, average slope, specific area, etc. Electrokinetic and electrophoretic measurements, potentiometric and calorimetric titration methods have been employed to characterize IEP and PZC of oxide particles in suspension [9,23,44,45,46], unfortunately these methods cannot provide quantitative local (i.e. at sub-micrometer scale) information of surface properties, and the application of these standard macroscopic techniques to surfaces in the form of thin films supported on solid substrates is problematic.

Here we report on the systematic and quantitative characterization of the role of nanoscale morphology on the charging behaviour of one of the most popular transition metal oxide surfaces: nanostructured titania. We have characterized IEP of nanostructured titania surfaces by direct measurement of the electrostatic double layer interaction in NaCl aqueous electrolyte using an atomic force microscope equipped with custom-made colloidal probes [47]. AFM is the technique of choice for sensing weak electrostatic forces (down to a few picoNewton) in solution, and has widely been employed to characterize double layer interactions (see, among many others references, Refs [25,29,48,49]); in those situations where surface roughness effects can be neglected, values of diffuse layer potentials measured by AFM and electrokinetic techniques have been found to be in good agreement [26,31,50,51].

Titania nanostructured films have been produced by supersonic cluster beam deposition (SCBD), a bottom-up approach providing a quantitative control over morphological nanoscale properties such as root-mean-square roughness, specific interfacial area, average surface slope [52 56]. Cluster-assembled titania surfaces has been recently demonstrated as a very reach playground to study the influence of nanostructure on proteins and cells [56,57,58,59].

In this manuscript we present experimental evidence of a marked dependence of the IEP of ns-TiO_2 surfaces on surface morphology, and we discuss our results on the basis of existing knowledge of the influence of surface morphology on double layer interactions; in the last part of the paper we consider the possibility that roughness-induced self-overlap of local diffuse layers acts as a potential source of deviation from the trend expected for flat surfaces.

Materials and Methods

Synthesis of Nanostructured Thin Films by PMCS and Reference Substrates

A Supersonic Cluster Beam Deposition (SCBD) apparatus equipped with a Pulsed Micro-plasma Cluster Source (PMCS) has been used to deposit nanostructured titania (ns-TiO_2) films by assembling clusters produced in gas phase [52,53,54,60,61]. The PMCS operation principle is based on the ablation of a target rod by a helium or argon plasma jet, ignited by a pulsed electric discharge; the ablated species thermalize with helium or argon and condense to form clusters [60,61]. The mixture of clusters and inert gas is then extracted into the vacuum through a nozzle to form a seeded supersonic beam [54,62], which is collected on a set of round borosilicate glass coverslips (diameter 15 mm, thickness 0.13 0.17 mm) intercepting the beam in a deposition chamber. The clusters kinetic energy is low enough to avoid fragmentation and hence a nanostructured film is grown, leading to a highly porous, high-specific area material [55,56].

We deposited nine different ns-TiO_2 batches (samples SMP1 9 in Table 1, where the corresponding morphological parameters measured by AFM are also reported). In particular, ns-TiO_2 samples are characterized by thickness in the range 5 200 nm, rms roughness (R_q) ranging from 5 to 26 nm and specific area A_{spec} from 1.2 to 1.8 (Table 1). Film roughness, specific area and the other chemico-physical parameters can be varied in a broad range by simply changing the thickness of the deposited films, without changing their surface chemistry [55]. Immediately prior to AFM characterization (morphological and electrostatic) ns-TiO_2 films have been thermally annealed for 2 hours at 250°C in ambient air, in order to remove organic contaminants and to recover the hydroxilated and hydrophilic surfaces.

The following substrates have been used as references to compare with the ns-TiO_2 film behavior: flat single-crystal <100> rutile TiO_2 (Sigma Aldrich), flat polycrystalline rutile TiO_2 and borosilicate glass coverslip (SLI Supplies). All the reference substrates were exposed to UV radiation for five minutes and then cleaned with ethanol and distilled water in order to remove contaminants from the surfaces. Borosilicate glass coverslips were used to realize a symmetrical system for DLVO measurements in order to characterize the net surface charge of the AFM probe at different pH (data presented in file Text S1, section 2.1, and Figs. S7,S8); to this purpose, in order to obtain surface properties comparable to those of the borosilicate glass colloidal probes, which undergo a thermal annealing above 750°C during production, borosilicate glass substrates were annealed at 600°C before characterization (it was not possible to anneal glass coverslips at higher temperature due to their tendency to bend significantly).

Characterization of ns-TiO_2 films Morphology

The surface morphology of ns-TiO_2 films was characterized in air using a Multimode AFM equipped with a Nanoscope IV controller (BRUKER). The AFM was operated in Tapping Mode, using rigid silicon cantilevers mounting single crystal silicon tips with nominal radius 5 10 nm and resonance frequency in the range 250 350 kHz. Several 2 μm×1 μm images were acquired on each sample with scan rate of 1 Hz and 2048×512 points. The images were flattened by line-by-line subtraction of first and second order polynomials in order to remove artifacts due to sample tilt and scanner bow. From flattened AFM images root-mean-square surface roughness R_q was calculated as the standard deviation of surface heights; specific area was calculated as the ratio of surface area to the projected area (more details on the calculation of morphological parameters are provided in file Methods S1, section 1, and Fig. S1). The film thickness was calculated by AFM, acquiring images across a sharp step produced masking the coverslip before the deposition.

Characterization of Electrostatic Interactions by AFM

We have used a Bioscope Catalyst AFM (Bruker) to measure the electrostatic interactions between a colloidal probe and sample surfaces in electrolyte solutions with different ionic strength and pH. To this purpose force-distance curves (shortly force curves) were acquired by recording cantilever deflection versus piezoelectric translator displacement at the liquid/solid interface [49,63,64]; ramp size was typically 1 μm (2048 points) with a scan rate of 1 Hz. Samples were placed at the bottom of a petri dish filled by the electrolyte. The raw deflection signal from the detector in Volts was converted into a displacement in nm units multiplying by the deflection sensitivity factor (the inverse of the slope of the contact region of the force curve, acquired on a hard glass surface) [49], and then converted into force units in nN multiplying by the cantilever vertical force constant, calculated by thermal noise method [65]. The tip-sample distance D is calculated summing the cantilever deflection to the piezo displacement [63,64]. The long ramp size allows fitting and subtracting effectively an oscillating trend from force curves due to laser interference effects.

Force curves were acquired in aqueous solution (distilled Millipore water) with controlled ionic strength and pH, in the range 3 7 pH units at 20°C (see file Methods S1, section 3, and Figs. S4,S5, for details). We have used a monovalent (1:1) electrolyte (NaCl) and a strong acid or base (HCl or NaOH) to change respectively the ionic strength and the pH of the solution [66,67]. NaCl electrolyte is an appropriate choice, because for low concentration ([NaCl] ≤0.1 M) it is inert for SiO_2 [68] and TiO_2 [69,70,71,72] surfaces; it affects the value of the Ionic Strength but it does not change the value of the surface IEP. Setting the concentration of NaCl in pure water to 1 mM (corresponding to $\lambda_D \approx 9.6$ nm) during experiments on ns-TiO_2 films allowed detecting weak electrostatic interactions with good signal-to-noise ratio for the reliable evaluation of surface charge parameters (this is critical in particular in the proximity of IEP, where net surface charge densities tends to zero); at the same time 1 mM concentration is high enough to prevent modification of the ionic strength of the solution at the lowest pH values. For each sample 100 force curves were typically acquired in six different locations (separated by 100 μm) in order to accurately characterize the Debye length and the charge densities of the surfaces (errors on Debye lengths and charge densities were calculated as described in file Methods S1, section 3.2).

Table 1. Morphological parametrs of ns-TiO_2 samples measured by AFM.

Ns-TiO_2 sample	Thickness (nm)	Roughness R_q (nm)	Specific Area A_{spec}	Correlation length ξ (nm)	Slope $2R_q/\xi$
SMP 1	7.7+1.6	4.9+0.1	1.19+0.01	16.2	0.605
SMP 2	31.4+1.2	10.4+0.7	1.21+0.1	42.0	0.495
SMP 3	33.9+3.4	14.9+0.2	1.41+0.02	37.1	0.803
SMP 4	50.5+3.9	17.2+0.1	1.56+0.09	41.0	0.839
SMP 5	62.0+4.8	19.2+0.4	1.61+0.02	43.3	0.886
SMP 6	96.5+7.6	20.6+0.1	1.62+0.03	42.7	0.965
SMP 7	99.1+8.7	21.1+0.5	1.68+0.03	47.2	0.894
SMP 8	123.0+14.6	22.5+1.4	1.78+0.05	49.9	0.902
SMP 9	202.0+15.4	26.0+0.2	1.79+0.03	44.2	1.176

doi:10.1371/journal.pone.0068655.t001

Colloidal probes provide a significantly enhanced signal-to-noise ratio compared to standard AFM tips and allow sensing the overall effects of nanoscale morphology, while a standard AFM tip with nanometer-sized apex would be sensitive to finer nanoscale fluctuations [29]. Moreover, colloidal probes determine a well-defined interaction geometry, allowing the use of simplified models to analyze data [21,29,48], where the radius of the probe can be set as a fixed and accurately calibrated parameter. We produced colloidal probes made of borosilicate glass following a novel protocol described in details in Ref. [47]. The probe size and its geometry are characterized by reverse AFM imaging of the probe on a MikroMasch TGT01 spiked grating (details are provided in file Methods S1, section 2, and Figs. S2,S3).

Electrostatic and van der Waals forces in aqueous solution usually occur together and are considered additive in the Derjaguin-Landau-Verwey-Overbeek (DLVO) theory. In particular the interaction between a sphere and a flat surface is approximated by the following equations, valid for $D>\lambda_D$ [21,48,63,64,73,74]:

$$F_{DLVO}^{cc}=\frac{2\pi R\lambda_D}{\varepsilon\varepsilon_0}\left[2\sigma_S\sigma_T e^{-\frac{D}{\lambda_D}}+\left(\sigma_S^2+\sigma_T^2\right)e^{-\frac{2D}{\lambda_D}}\right]-\frac{AR}{6D^2} \quad (1)$$

$$F_{DLVO}^{cp}=\frac{2\pi R\lambda_D}{\varepsilon\varepsilon_0}\left[2\psi_S\psi_T e^{-\frac{D}{\lambda_D}}-\left(\psi_S^2+\psi_T^2\right)e^{-\frac{2D}{\lambda_D}}\right]-\frac{AR}{6D^2} \quad (2)$$

Here the superscripts *cc* and *cp* indicate constant-charge and constant-potential boundary conditions for the electrostatic contributions (first terms in Eqs. 1, 2, while the second terms represent the van der Waals force); the constant charge and constant potential conditions are typically well satisfied on insulating and conductive (metallic) surfaces, accordingly. R and σ_T (ψ_T) are the radius and surface charge density (surface potential) of the sphere (the AFM probe), and σ_S (ψ_S) is the surface charge density (surface potential) of the smooth (idealized) sample surface; ε is the dielectric constant of the medium (the aqueous electrolyte, we assume $\varepsilon = 78.54$), ε_0 is the vacuum permittivity, λ_D is the Debye length, i.e. the screening length of the electrolyte:

$$\lambda_D=\sqrt{\frac{\varepsilon\varepsilon_0 k_B T}{2e^2 I}} \quad (3)$$

where k_B is the Boltzmann constant, T is the absolute temperature, e is the electric charge of the electron and I the ionic strength of the solution: $I=1/2\sum_i z_i^2 c_i$, c_i and z_i being the concentration (number of particles per unit volume) and valence of the i-th ionic species. The higher is the ionic strength, the more effective is the screening of electric fields in the solution. For 1:1 NaCl electrolyte with bulk concentration c = [NaCl], Eq. 3 simplifies to:

$$\lambda_D=0.3/\sqrt{[NaCl]}\ \text{nm} \quad (4)$$

where the concentration of the salt is given in mol/l.

The Van der Waals force in Eqs. 1,2 depends on the Hamaker constant A of the surface/medium/probe system [73]. We have assumed for our experimental setup $A=0.8\ 10^{-20}$ J for borosilicate glass coverslip [29,49,75,76,77] and $A=0.7\ 10^{-20}$ J for ns-TiO_2 [78] (both against a borosilicate glass probe).

Potentials and surface charge densities in Eqs. 1,2 are related by the Grahame equation, which for a 1:1 electrolyte is [19]:

$$\sigma=\sqrt{8\varepsilon\varepsilon_0 k_B T c}\ sinh(e\psi/2k_B T) \quad (5)$$

It should be noted that AFM tip senses the diffuse part of the electrostatic double layer [28,79], therefore surface charge densities σ_S and σ_T in Eqs. 1,2 must be identified with the surface charge density σ_d of the diffuse layer, i.e. with the charge in the diffused layer projected on the outer Helmholtz plane; this charge density is equal in magnitude to the total charge density of the Stern layer: $\sigma_d=-(\sigma_0+\sigma_i)$, where σ_0 is the density of truly surface charges and σ_i is the density of charges by ions from the electrolyte adsorbed (complexated) at the inner Helmholtz plane [17]. On amphifunctional surfaces, i.e. on surfaces where an electronic surface charging mechanism is present (as for example on bare, or partially oxidized, metallic surfaces), the previous equation must be changed in: $\sigma_d=-(\sigma_0+\sigma_i+\sigma_e)$, where σ_e is the electronic surface charge density of the solid surface [11,16]. Our ns-TiO_2 however have a marked insulating character [80] and we will neglect in the following the σ_e term. Under the assumption that the ions bind only to oppositely charged sites (energetically the most favourable option) it turns out that σ_d represents a net surface charge density, being determined by the density of naked surface charges M-O^- and M-OH_2^+ only, i.e. by those charges that are not neutralized by specifically absorbed electrolyte ions [22,46,79] (file Text S1, section 1). At IEP $\sigma_d=0$ while at PZC $\sigma_0=0$. AFM measurements can be used therefore to characterize IEP, not directly PZC, unless ion adsorption is negligible or symmetrical (indifferent electrolyte), in which case PZC = IEP.

The first terms of Eqs. 1,2 represent upper and lower limits for the general case of double layer interactions when charge regulation phenomena occur. We have tested the applicability of these simplified models to our systems, and concluded that the constant charge model is more appropriate to describe the experimental force data: the constant potential curves, built using potentials derived from charge densities according to Eq. 5 (in the limit of large distances, both *cc* and *cp* curves must overlap), systematically failed to reproduce the experimental data (details are provided in file Methods S1, section 3.1, and Fig. S6). Notice that while this suggests that the overlap of probe and sample double layers dos not lead to important regulation mechanisms, it does not imply that regulation phenomena are absent also *within* the double layer of corrugated ns-TiO_2 surfaces, as it is discussed later. For relatively large distances Eq. 1 simplifies to:

$$F_{DLVO}^{cc}=\frac{4\pi R\lambda_D}{\varepsilon\varepsilon_0}\sigma_S\sigma_T e^{-\frac{D}{\lambda_D}}-\frac{AR}{6D^2} \quad (6)$$

Fitting average force curves with Eq. 6 provides the value of the charge densities product $\sigma_S\sigma_T$ and of the Debye length λ_D, the tip radius R being known from probe calibration (details in file Methods S1, section 2, and Figs. S2,S3). In order to decouple from the fitted charge density product $\sigma_S\sigma_T$ the unknown contribution of the AFM borosilicate glass probe, we have characterized the net surface charge density of the borosilicate glass probe as a function of pH by recording force curve in aqueous electrolyte against a borosilicate glass smooth substrate, in order to realize a symmetrical system where $\sigma_S \approx \sigma_T$ and therefore $\sigma_T \approx \sqrt{\sigma_S\sigma_T}$

(file Text S1, section 2.1, Fig. S8). This allowed in turn determining the absolute net surface charge density of flat crystalline TiO_2 and ns-TiO_2 surfaces.

Charge density products, rather than absolute charge densities, have been used to extrapolate pH_{IEP} values, being this process based on the nullification of the prefactor of Eq. 6. To this purpose, all IEP values were extracted from $\sigma_S\sigma_T$ vs pH curves by interpolation between the closest experimental data with opposite sign, as shown in file Text S1, section 2 (data reported in Figs. S7B,S9right-S19right). In order to identify precisely the neighborhood of IEP on different surfaces, a few measurements at lower ionic strength ($[NaCl]<10^{-3}$ mM) were typically performed, which reduces the electrostatic screening and increases the signal-to-noise ratio; these tests allowed identifying the pH values at which charge reversal takes place (Figs. S14right-S19right in file Text S1, section 2.3). The determination of the pH_{IEP} value is rather insensitive to the choice of the fitting model, being based on the nullification of surface charge product $\sigma_S\sigma_T$, rather than on the precise characterization of its magnitude in the neighborhood of the IEP. Overall, our setup is characterized by a sensitivity of about 2% in the determination of pH_{IEP}.

As part of the calibration of our experimental setup, in addition to determining the net surface charge density and IEP of the AFM probe, we have characterized the IEP of flat reference samples (Table 2; see file Text S1, section 2.2, Figs. S9,S10, for details). Our experimental apparatus has proved to be accurately calibrated: the measured pH_{IEP} values for borosilicate glass (silica-boron oxide mixture, annealed above 600°C), rutile single-crystal <100> and polycrystalline TiO_2 turned out to be in good agreement with the values reported in literature [9,72,83]. Robustness of the approach for the determination of pH_{IEP} is witnessed also by the very good reproducibility of determination of IEP of the colloidal probe, despite the many different (chemically and morphologically) interfaces against which the probe has been used.

Results

Surface Morphology of ns-TiO_2 Films

Fig. 1 shows representative AFM topographic maps of the ns-TiO_2 samples (both top- and 3-dimensional views), as well as single topographic profiles. The morphology of ns-TiO_2 films deposited by SCBD consists of a fine raster of nanometer-sized grains, with high specific-area, and porosity at the nano and sub-nanoscale depending on the film thickness [53,54,55,56], with grains diameter ranging from few nm up to 50 nm. Morphological parameters calculated from AFM topographies are reported in Table 1. The surface sections of Fig. 1 show nanometric pores of diverse depths and widths; an higher thickness means an increased geometrical accessibility of the pore, an increased local electric field strength around the sharpest asperities of the profile and a modification in the local surface charge distribution due to the overlapping, in the bottom and sides of the pore, of the diffuse double layers.

Table 2. IEP of colloidal AFM probe and reference flat substrates.

Sample	pH_{IEP}
Borosilicate glass (colloidal probe annealed at 780°C)	3.20±0.05
Borosilicate glass (coverslip annealed at 600°C)	2.82±0.05
TiO_2 flat, polycrystalline rutile	6.28±0.05
TiO_2 flat, single-crystal <100> rutile	3.47±0.05

doi:10.1371/journal.pone.0068655.t002

Electrical Double Layer Properties of Rough ns-TiO_2 Surfaces

Fig. 2A shows average force curves for ns-TiO_2 films with roughness in the range 5 26 nm (SMP1 9, Table 1) at pH = 5.4 and [NaCl] = 1 mM (the ionic strength was kept constant through all the experiments, when not otherwise stated). At this pH all ns-TiO_2 surfaces are significantly charged. Fitting the curves shown in Fig. 2A by Eq. 6, we obtained the values of charge density and Debye length of all samples.

Fig. 2B shows the dependence on R_q of the net surface charge density σ_S of ns-TiO_2. The net surface charge density measured on the single-crystal rutile <100> TiO_2 surface, at the same pH, is also shown in Fig. 2B (empty square); this value represents a reference because the IEP of single-crystal <100> rutile is similar to those of rougher ns-TiO_2 surfaces (see below). In Fig. 2C we report the measured Debye lengths as a function of surface roughness of ns-TiO_2 films.

The trend of the charge density σ_S of ns-TiO_2, which increases as R_q increases up to a maximum value (for $R_q \approx 17$ nm), then drops to values that are significantly lower than those of reference crystalline surface smaller values, is qualitatively and quantitatively counter-intuitive. Considering that the specific area of ns-TiO_2 samples increases (almost linearly - see Table 1) with R_q, we would expect on rougher surfaces a proportionally higher charge density with respect to the smooth rutile single-crystal <100> surface.

One would also expect that λ_D does not depend on surface roughness, being a property of the bulk electrolyte, determined only by the ionic strength of the solution according to Eqs. 3,4. λ_D is constant to a value $\lambda_D \approx 10$ nm close to the one predicted by Eq. 4 for [NaCl] = 1 mM only for $R_q<20$ nm, while on rougher samples λ_D grows beyond 15 nm.

These experimental observations provide an indication that Eq. 6, which describes double layer interactions at smooth surfaces, may not provide an accurate description of charging and ionic re-distribution processes at rough surfaces. We have been therefore prompted by our data to consider the peculiar role of surface nano-morphology in electrostatic interactions between a micro-sphere and a rough surface, in the presence of an aqueous electrolyte.

Based on our observations and on previous reports [26,27,28,29,30,31] we have modified Eq. 6 in order to describe more accurately the probe-surface interaction force. Eq. 6 represents the approximated DLVO force in the case of a spherical colloidal micro-probe interacting with a smooth flat surface, such as for example the two crystalline reference rutile surfaces considered in this study. The situation when rough surfaces are involved, as in the case of ns-TiO_2 samples, is schematically represented in Fig. 3. A smooth object (the probe) is contacting the highest asperities of the surface of the nanostructured films; this is because the AFM probe is definitely too large to penetrate inside the surface nano-pores. The origin of distance axis in force curves corresponds to the point of first contact of the AFM tip with these protruding asperities, highlighted by the topmost red dash-dotted line in Fig. 3. Approximately, the separation between the actual contact line and the mid surface plane, represented by the lower dash-dotted line, is equal to R_q, the rms surface roughness. If we consider the mid-plane as an effective locus where all the electric surface charge is evenly distributed, it turns out that the distance axis for the double layer term in Eq. 6 must be shifted by $+R_q$ in order to recover an effective description of double layer

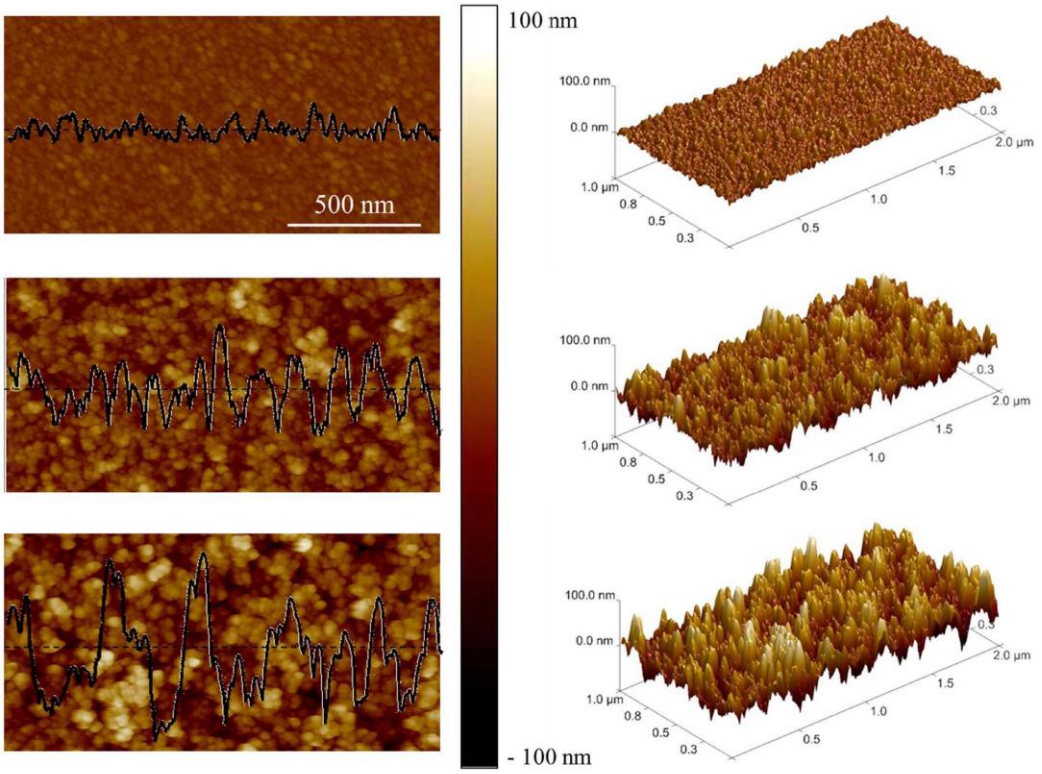

Figure 1. Top and 3-dimensional views of AFM topographic maps of ns-TiO_2 films. Thickness of ns-TiO_2 films is (A, D) 8 nm; (B, E) 50 nm; (C, F) 200 nm. Representative topographic profiles are superimposed to top-view maps.
doi:10.1371/journal.pone.0068655.g001

interactions between a smooth and a rough surface. In other words, the average plane of charge in the case of corrugated surfaces is displaced backwards by R_q (or by the sum of the R_q of the two surfaces, in the case both are corrugated) with respect to the plane of first contact, located at the tops of surface asperities. We notice that while the shift of the distance axis does not change the value of IEP, determined by the zeroing of the product $\sigma_S\sigma_T$ in Eq. 6, it allows to evaluate more accurately the magnitude of such product. This is clear if we consider explicitly the effect of the shift of the distance axis on Eq. 6. If D is the apparent distance calculated from the point of first contact, the electrostatic force F_{EL} at a distance $D+R_q$ from the mid plane is:

$$F_{EL}=\frac{4\pi R\lambda_D}{\varepsilon\varepsilon_0}\sigma_S\sigma_T e^{-\frac{D+R_q}{\lambda_D}}=\frac{4\pi R\lambda_D}{\varepsilon\varepsilon_0}\left(\sigma_S\sigma_T e^{-\frac{R_q}{\lambda_D}}\right)e^{-\frac{D}{\lambda_D}} \quad (7)$$

which can be written as a function of the apparent distance D as:

$$F_{EL}^{app}=\frac{4\pi R\lambda_D}{\varepsilon\varepsilon_0}\overline{\sigma_S\sigma_T}e^{-\frac{D}{\lambda_D}} \quad (8)$$

where

$$\overline{\sigma_S\sigma_T}=\sigma_S\sigma_T e^{-\frac{R_q}{\lambda_D}} \quad (9)$$

is an apparent charge density product (σ_S reported in Fig. 2B is therefore an apparent charge density). Eqs. 7,8 show that when the distance axis is not shifted by R_q, the surface charge parameter extracted from the fit of Eq. 6 is exponentially underestimated by a factor depending on the ratio R_q/λ_D. Eq. 7 also predicts that the shift of the distance axis does not affect the Debye length.

The shift of the distance axis allows treating the rough surface as an effective smooth plane where the total surface charge is evenly distributed on the mid plane, which is approximately located a distance R_q away from the surface peaks protruding towards the bulk of the electrolyte. A similar strategy has been adopted by the authors of Ref. [28], who pointed out that the potential at the outer Helmholtz plane of a rough gold surface (approximated by the ζ potential) can be rescaled by shifting the distance axis by an amount comparable to rms surface roughness; the authors applied to the electrostatic potential a correction similar to our Eq. 7. Similarly, Ducker et al. applied the same correction to extract the value of the surface potential of silica surfaces [29].

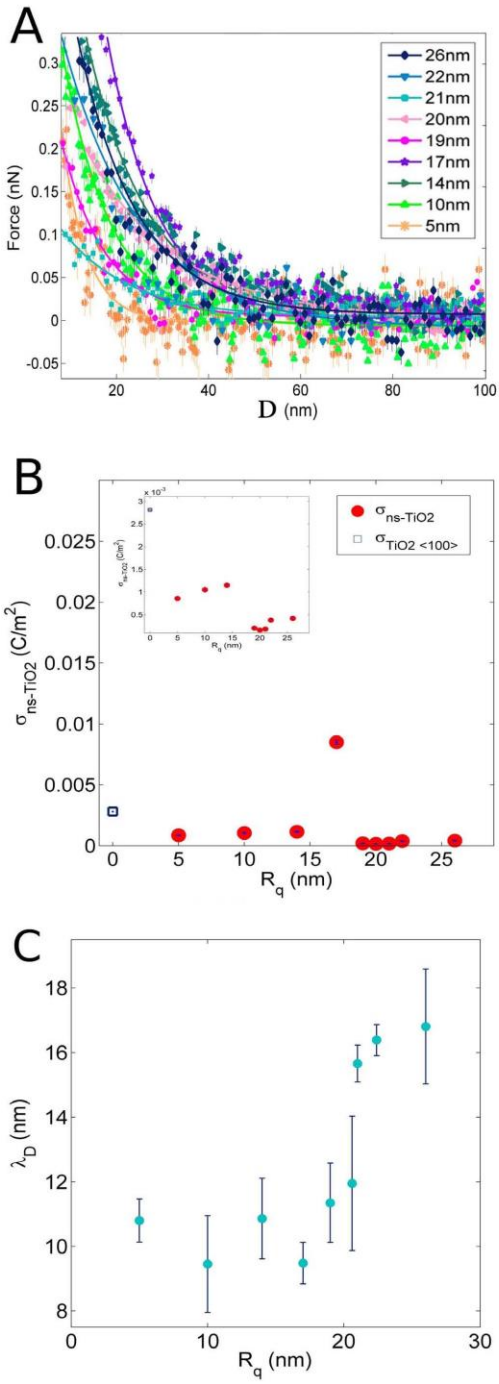

Figure 2. Double layer force-distance curves at ns-TiO_2 surfaces. (A) Average force curves at pH~5.4 and [NaCl] = 1 mM between the colloidal borosilicate glass probe and ns-TiO_2 films with different roughness. (B) The net surface charge density σ_S of ns-TiO_2 versus roughness R_q, extracted from the best fit of average force curves by Eq. 6. For comparison, the net surface charge density of the reference <100> rutile TiO_2 surface is also shown. (C) Debye lengths λ_D as a function of the surface roughness R_q of ns-TiO_2 films extracted from the best fit of force curves by Eq. 6.
doi:10.1371/journal.pone.0068655.g002

Fig. 4A shows the same force curves of Fig. 2A with corrected distance axes (all the distance axes of force curves shown from here on, and used to extract double layer parameters, have been shifted by R_q). Fig. 4B shows the corrected net surface charge densities σ_S at pH 5.4 as a function of surface roughness. In Fig. 4B a clearer trend of the relative surface charge density vs R_q is observed, with respect to Fig. 2B. σ_S increases as R_q increases: the increase is moderate for R_q<20 nm; for R_q>20 nm the increase is dramatic, and σ_S of nanostructured samples is definitely much higher than that of smooth crystalline ones. The influence of surface roughness and specific area on charge density can be further appreciated in Fig. 5, showing the combined effect of pH and surface roughness ($R_q \geq 20$ nm) on the net surface charge density σ_S. As expected, σ_S increases almost linearly as $|pH\text{-}pH_{IEP}|$ increases, due to the larger fraction of ionized surface groups. All samples (including SMP5, used for normalization) have similar IEP (pH_{IEP}~3.2, see later), i.e. at a given pH they should all be similarly charged. This is not the case, being evident that nanoscale morphology boosts the surface charge density in fact more than proportionally with respect to the increase in specific area.

Table 3 reports the value of IEP measured on different ns-TiO_2 surfaces. Fig. 6 shows the trend of IEP vs R_q of ns-TiO_2 films. The observed shift of pH_{IEP} is monotonic and seems to be only limited by the probed pH range: the loss of resolution in the measurement of pH_{IEP} values on samples SMP5–8 is due to the fact that at these pH the AFM probe is almost neutral, therefore the force measured

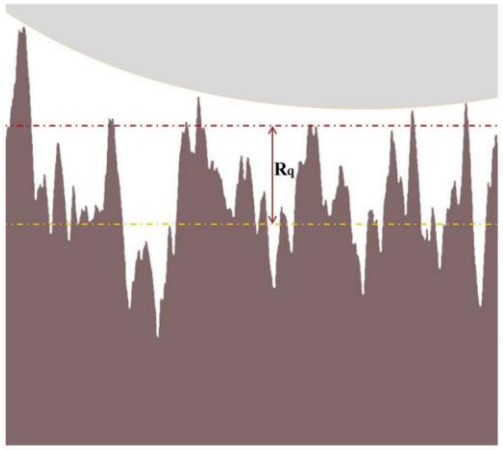

Figure 3. Schematic representation of the interaction geometry of a colloidal probe with a nano-rough surface. Red upper line: plane of first-contact, defined by the protruding asperities; orange bottom line: mid-plane, or average plane of charges. The distance between the two planes is approximately equal to R_q.
doi:10.1371/journal.pone.0068655.g003

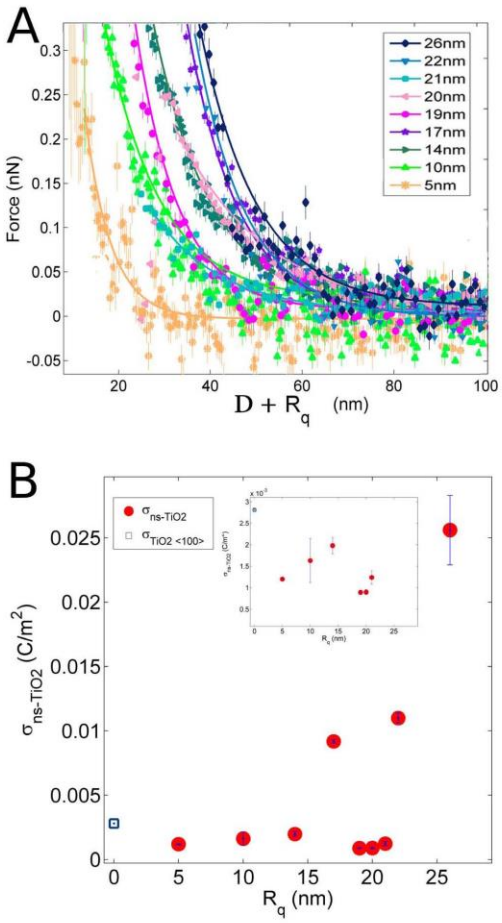

Figure 4. Double layer force-distance curves at ns-TiO_2 surfaces with corrected distance axis. (A) Average force curves at pH~5.4 and [NaCl] = 1 mM between the colloidal borosilicate glass probe and ns-TiO_2 films with different roughness with corrected distance axis (i.e. positively shifted by R_q, see main text for details). (B) The net surface charge density σ_S of ns-TiO_2 versus R_q, extracted from the best fit of force curves by Eq. 6 after correction of distance axes. For comparison, the net charge density of the reference <100> rutile TiO2 is also shown.
doi:10.1371/journal.pone.0068655.g004

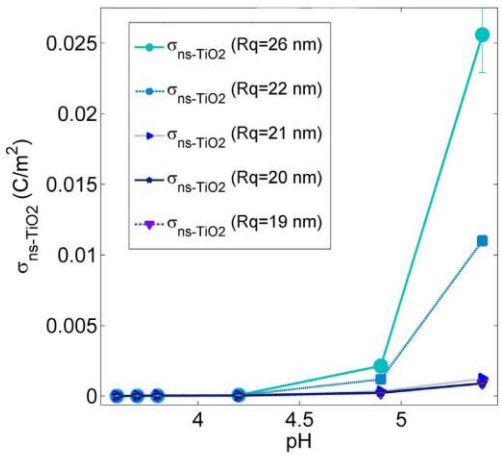

Figure 5. The net surface charge density σ_S of ns-TiO_2 films. Evolution of the net surface charge density σ_S with pH for ns-TiO_2 films with increasing roughness ($R_q \geq 20$ nm; all films have similar IEP, see Table 3 and Figure 6).
doi:10.1371/journal.pone.0068655.g005

was very weak and the signal to noise ratio very low. The average force curves of each ns-TiO_2 sample at different pH, as well as the $\sigma_S\sigma_T$ vs pH curves, are reported in file Text S1, section 2.3, Figs. S11-S19. The difference between the pH_{IEP}s of ns-TiO_2 samples with lowest and highest surface roughness ($R_q = 5$ nm and $R_q = 26$ nm, accordingly) is remarkably more than two pH units and in particular the lower is the roughness of the ns-TiO_2 surface, the higher is the pH_{IEP} value, with a monotonic trend towards the pH_{IEP} of polycrystalline rutile TiO_2 ($pH_{IEP/polyTiO2} = 6.28 \pm 0.05$) and anatase TiO_2 ($pH_{IEP} = 6.1$–6.3 [72]). This is consistent with the fact that the structure of ns-TiO_2 films is an amorphous matrix embedding rutile and anatase nano-crystallites [81,82], and that all the crystalline planes are likely randomly exposed. As R_q increases, pH_{IEP} monotonically decreases, reaching a value of 3.09 pH units. This value is close to that of flat single-crystal rutile <100>, which among different rutile crystallographic planes is the one exhibiting the lowest pH_{IEP} [83].

Discussion

Charging of Metal Oxide Surfaces in Aqueous Electrolytes

The starting point in the discussion of experimental results is the consideration of the standard picture of surface charging of metal oxides in electrolytic solutions, which is generally attributed to the amphoteric character of surface hydroxyl groups [9,10,11, 16,22,84]. Charging of the solid surface can be formally regarded as either a two-step protonation of surface M-O^- groups, or equivalently as the interaction of surface hydroxyl M-OH with OH^- and H^+ ions. In addition to association/dissociation of surface hydroxyls, also adsorption of anions A^- and cations C^+ from solution to charged surface sites may take place. Details about the charging processes of oxide surfaces can be found in file Text S1, section 1.

At the point of zero charge (PZC), the net electric charge at the solid/liquid interface is zero (the number of positively charged sites is equal to the number of negatively charged sites). This condition is achieved at a pH equal to [24,45]:

$$pH_{PZC} = 1/2(pK_1 + pK_2) - 1/2\log[(1 + K_+ a_+)(1 + K_- a_-)] \quad (10)$$

where $pK_i = -\log_{10}(K_i)$ (i = 1,2,+,−), $K_{1/2}$, $K_{+/-}$ being the equilibrium constants for the association/dissociation reactions of the active species), and $a_{+/-}$ are the activity of cations and anions, accordingly (for 1:1 salt, like NaCl, $a_+ = a_- \equiv a$).

At the Isoelectric Point (IEP), the net charge of the compact layer (i.e., also including the adsorption of anions and cations of

Table 3. IEP of ns-TiO_2 samples.

Sample	pH_{IEP}
SMP1 (R_q = 5 nm)	5.20±0.05
SMP2 (R_q = 10 nm)	4.30±0.05
SMP3 (R_q = 14 nm)	4.10±0.10
SMP4 (R_q = 17 nm)	3.70±0.04
SMP5 (R_q = 19 nm)	3.20±0.05
SMP6 (R_q = 20 nm)	3.20±0.05
SMP7 (R_q = 21 nm)	3.20±0.05
SMP8 (R_q = 22 nm)	3.20±0.05
SMP9 (R_q = 26 nm)	3.09±0.04

doi:10.1371/journal.pone.0068655.t003

the electrolyte) is zero. An expression for pH_{IEP}, similar to Eq. 10, has been obtained under the hypothesis that the slip plane coincides with the outer Helmholtz plane, i.e. the ζ potential is equal to ψ_d, the potential at the beginning of the diffuse layer [24]:

$$pH_{IEP} = 1/2(pK_1 + pK_2) - 1/2\left[(0.431e^2N_s/k_BC_1RT)a(K_- - K_+)\right]/\left[2 + (K_1/K_2)^{1/2} + a(K_- + K_+)\right] \quad (11)$$

In Eq. 11, N_S is the total number of surface sites, k_B is the Boltzmann constant, R is the universal gas constant, T is the absolute temperature, a is the bulk activity of NaCl, and C_1 is the capacity of the layer of ion pair localization, typically in the range 10–100 $\mu F/cm^2$. We have already stressed that IEP rather than PZC is characterized by AFM, because the AFM probe is sensitive to the overall charge of the compact Stern layer, or equivalently to the overall charge of the diffuse layer projected at the outer Helmholtz plane, which is equal and opposite, thanks to the electro-neutrality condition.

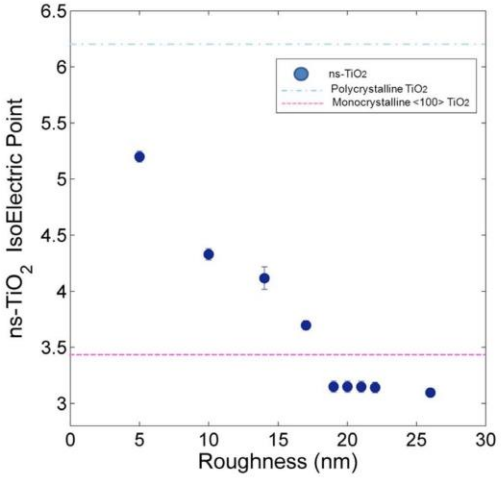

Figure 6. pH_{IEP} of ns-TiO_2 samples with different rms roughness R_q. For comparison, pH_{IEP} of flat single-crystal <100> and polycrystalline rutile TiO_2 samples are shown.
doi:10.1371/journal.pone.0068655.g006

In order to get insights on how the evolving nanoscale surface morphology influences the IEP, we inquire the hidden role of morphological parameters in Eq. 10,11. We consider different possibilities, discussing them on the basis of our knowledge of charging mechanisms and of the physico-chemical properties of cluster-assembled titania.

Typically for smooth, flat surfaces in 1:1 aqueous electrolytes at low ionic strength, in the neighbourhood of the IEP/PZC (low surface potentials), one or more of the following conditions, leading to the equality $pH_{PZC} = pH_{IEP}$, are met:

i) Negligible ionic strength ($a \approx 0$);
ii) Negligible adsorption ($K_{+/-} \approx 0$);
iii) Symmetric adsorption ($K_+ = K_-$).

According to Eqs 10,11, when conditions i)-iii) are met and $pH_{PZC} \approx pH_{IEP}$, changes of IEP can be due only to changes of pKs. When on the other hand conditions i)-iii) are not satisfied, also the activities $a_{+/-}$, as well as the equilibrium constants $K_{+/-}$, of electrolyte ions may couple to morphology and induce shift in the IEP. The picture is very complex because the failure of one or more of conditions i)-iii) can be itself determined by the evolving surface morphology. Equilibrium constants Ks depend on the atomistic properties of the surface, i.e. the density of active sites and the atomic neighbourhood of the active species (i.e. which atoms are bound to them, and by which kind of bond), and on the local electrostatic potential (i.e. on the local structure of the electrical double layer); ionic activities depend as well on the local electrostatic potential [46,85,86]. Clues to understand the morphology-driven variance of pH_{IEP} and pH_{PZC} of nanostructured oxide surfaces must be sought therefore in the morphology-induced modification of local surface chemistry and/or in the morphology-induced modification of the double layer structure. In the first case, the evolving morphology determines a change of IEP by directly modifying the local atomic environment of the active species (density of active sites, coordination, bonding); in the second case, the impact of the evolving morphology is more subtle and indirect, effectuating through the modification of the structure of the electrical double layer, i.e. through the modification of the electrostatic potential.

We will consider in the following firstly the possibility that morphology can change the local chemical environment of the active charge-determining surface species, and secondly the effect on electrical double layer. Before continuing, an important preliminary observation about the role of surface morphology must be done. IEP depends on the density of surface active sites rather than on their absolute number, i.e. IEP is an intensive surface property; this rules out the possibility that the observed shift of IEP on ns-titania towards more acidic pH is due to the increase of specific area on rough samples, i.e. to the capability of the surface to accommodate more (negative) charge due to the increased area, which would require more H^+ ions (lower pH) to achieve charge neutrality.

Influence of Nanoscale Morphology on Local Chemical Environment

Several site-binding models [85,86] have been developed and proved to be effective in predicting the charging behaviour of oxide surfaces, and in particular the values of equilibrium constants and pKs, pH_{PZC} and pH_{IEP} values through Eqs.

10,11. According to these models, equilibrium constants depend on the atomic-scale environment and on the electronic properties of the surface sites (coordination, bond length, valence), as well as by the density of active sites, and on the electrostatic environment. Differences among IEP of different crystal faces of the same material can be readily accounted for by surface complexation models: individual surface planes of metal oxides, even in the absence of defects, typically possess several non-equivalent, differently coordinated oxygen atoms (singly, doubly, or triply coordinated), characterized by different activity coefficients.

A clear example of how surface structure affects PZC/IEP is the difference of pH_{IEP} of different faces of rutile, recently determined by direct measurement of double layer forces by AFM [83]. A strong correlation of IEP with the density of cationic surface sites was demonstrated, the more acidic (with lowest pH_{IEP} in the range 3.2 3.7) being the <100> surface of rutile. Polycrystalline surfaces of both rutile and anatase forms of TiO_2 possess the same PZC ($pH_{IEP} \approx 6$), resulting from the weighted average of the PZC of the single crystal faces.

Previous spectroscopic studies of electronic structure of ns-TiO_2 films produced using SCBD showed that Ti^{3+} point defect states, related to oxygen vacancies and structural defects, are natively present in the material and relatively abundant; annealing at 250°C in presence of oxygen is effective in reducing the concentration of such defects [59,87]. Ns-TiO_2 films are mainly amorphous in nature, although both rutile and anatase nanocrystals are embedded in the amorphous matrix of the film [81,82]. There is evidence that the growth under sub-stoichiometric conditions in the cluster source favours the formation of rutile particles (typically for sizes below 5 nm). The differences in stoichiometry and crystalline phases of ns-TiO_2 films with respect to crystalline surfaces can account for static differences of PZC/IEP, but they could hardly account for the observed evolution of IEP with surface morphology. No evidence of any dependence of electronic and crystalline structure of ns-TiO_2 films on thickness and roughness has emerged from the mentioned previous spectroscopic studies.

Similarly to stoichiometry and crystalline phase, also the presence of chemical surface heterogeneities (including hydrophilic/hydrophobic nanoscale patches), partially penetrating the nanoporous matrix of the material, could in principle determine a change of IEP with respect to the pristine material; theoretical evidence has been recently provided of the direct influence of such surface chemical heterogeneities on electrostatic/electrokinetic interfacial properties [88,89]. However, the effects of such chemically different nanoscale domains on IEP should not evolve with rms roughness, but rather stay constant, as all subpopulations are equally amplified as the specific area increases.

A contribution from the $pK_{+/-}$ of the electrolyte ions could be expected from Eqs. 10,11, whenever the conditions i)-iii) are not satisfied. According to these equations preferential adsorption of anions leads to a decrease of IEP and increase of PZC (opposite trends are expected in the case of preferential adsorption of cations). On flat smooth interfaces, however, a slight predominance of one of the $K_{+/-}$ with respect to the other determines only small shifts of IEP/PZC by fractions of a pH unit, typically within the experimental errors, which are not comparable to the shift we have observed on nanostructured titania (more than 3 pH units, see Table 3). For example, in the case of TiO_2, K_{Cl^-} is reported to be slightly larger than K_{Na^+}, but the maximum shift towards smaller values of pH_{IEP} for variation of NaCl concentration over decades (from 10^{-3} M to 10^{-1} M) is only 0.8 pH units [24]. For this reason NaCl is generally considered as inert electrolyte towards smooth TiO_2 for low concentration ([NaCl] $\leq$0.1 M) [69,70,71,72] (we verified this assumption by measuring double layer interactions on flat surfaces in the presence of ions at different concentrations, data not shown). We exclude therefore that small changes of the $pK_{+/-}$ for NaCl, due to different stoichiometry and crystalline phases of ns-TiO_2 with respect to crystalline TiO_2, can account for the observed marked shift of the IEP.

Influence of Nanoscale Morphology on the Structure of the Electrical Double Layer

Ruled-out the direct influence of evolving surface morphology in changing the overall surface chemistry and therefore the pKs and the IEP of the system, we consider the possible effect of evolving morphology on the evolution of the structure of the electrical double layer, in particular on the electrostatic potential within the compact charge layer, which acts directly on pKs and activities; this could have potentially a very strong impact on the charging mechanisms of rough surfaces.

On rough surfaces, the double layer can be influenced by surface morphology, in particular by topological effects related to the local curvature, as well as to shadowing effects of surface charge and regulation mechanisms triggered by strong double layer overlap [17]. Standard DLVO theory developed for smooth surfaces and based on linearized Poisson-Boltzmann equations fails accounting for these topological effects. Although an approximate picture of the interfacial properties can be obtained by introducing the average plane of charge, i.e. by shifting the distance axis by R_q towards larger distances, fine effects on double layer potential as well as counter-ion distribution related to surface morphology are not accounted for by this simple strategy. The anomalous behaviour of the Debye length shown in Fig. 2C can be an indication of this. Previous works have indeed suggested that surface morphology can affect the Debye length; on one hand, a surface-potential dependent Debye length, intended as an effective diffuse layer thickness, has been predicted for rough surfaces when non-linear Poisson-Boltzmann equations are considered [43]; on the other hand it has been recognized that on rough surface the electrostatic interaction has essentially three-dimensional components, therefore the extension of the electric field depends on surface morphology [40].

Recent works that have explicitly addressed the problem of solving the Poisson-Boltzmann equations in the case of rough (non-porous) surfaces [40,41,42,43] report that the properties of the double layer at a rough solid/liquid interface are mainly governed by the relative importance of ratios of the characteristic lengths of the electrode/electrolyte interface: λ_D/ξ and $2R_q/\xi$, where ξ is the lateral correlation length of the surface, i.e. the average peak to valley distance (see file Methods S1, section 1, and Fig. S1, for details) and $2R_q/\xi$ represents the average slope of the surface.

Roughness-induced Self-interaction of the Electrical Double Layer

Based on these works and on reports on charge regulation phenomena [1,17], we consider the idea of self-interaction of the double layer at nano-rough surfaces, i.e. the overlap of portions of the double layer pertaining to neighboring regions of the same surface; this effect is truly related to the corrugation of the surface, and in particular to the presence of contiguous regions with opposite slopes. A simplified case, that of two LEGO-like protrusions on a flat surface, has been previously addressed by numerical methods by Duval et al. [40]. Whenever double layers interact, either belonging to the AFM probe and the surface, or to

adjacent surface regions, charge regulation phenomena occur, which, in the limit of strong overlap, may lead to severe distortions of the electrostatic potential and to the failure of the assumptions underlying the application of the linearized Poisson-Boltzmann equations.

By invoking a simplified geometrical model of the rough interface we suggest that the role of surface morphology is to enhance the self-overlap of double layer of neighboring surface regions. Figs. 7A,B show schematic representations of an average surface "pore". The pore is built by considering that, on average, peaks and valley across the surface are separated by a distance ξ ((the correlation length)), and that about 70% of surface heights lies within a distance of $\pm R_q$ from the mid-plane, so that we may assume $2R_q$ as the average peak-to-valley separation. This picture is consistent with the fact that for gaussian surfaces the average surface slope is $2R_q/\xi$ In Fig. 7A the geometrical features of the average pore are highlighted. Assuming that the double layer stems perpendicularly from the surface up to a distance λ_D from it (this cut-off is of course arbitrary, but does not influence the general conclusions of this reasoning), it turns out that because of the finite slope, double layers of adjacent walls overlap to some extent, the overlapping volume (an area in our 2-dimensional representation) being that of the quadrilateral enclosed by the dotted line in Fig. 7A. Qualitatively, the larger are λ_D and surface slope, the stronger is the self-overlap of the double layer. The degree of morphology-induced self-overlapping of double layer on rough surfaces can be characterized by the fraction γ of the double layer volume in each pore where overlap occurs. In our 2-dimensional representation γ is the ratio of the area Σ of the quadrilateral to the total area Σ_0 occupied by the double layer, i.e. $\gamma = \Sigma/\Sigma_0$. It turns out (details on calculations in file Text S1, section 3, and Fig. S20) that for $2R_q/\xi \leq 1$:

$$\gamma = \frac{(\lambda_D/\xi)(2R_q/\xi)}{2\sqrt{1+(2R_q/\xi)^2}-(\lambda_D/\xi)(2R_q/\xi)} \qquad (12)$$

A similar formula holds for $2R_q/\xi > 1$ (Eq. S9 in file Text S1, section 3, and Fig. S21).

Eqs. 12 and S9 clearly show that the self-overlap of the double layer on nano-rough surfaces depends only on the ratios λ_D/ξ and $2R_q/\xi$ of the characteristic electrostatic and morphological lengths (a similar scaling has been found by Daikhin et al. for the double layer capacitance [41,42,43]). In general, the degree of overlap inside each pore increases when the two ratios λ_D/ξ and $2R_q/\xi$ increase. This can be also seen in Figs. 7A,B: upon increase of the slope at constant R_q, the overlap increases significantly. Eqs. 12,S9 also predict that for suitable combination of λ_D and ξ ((relatively large λ_D and small ξ)) nearly complete overlap ($\gamma \approx 1$) inside a pore can be reached. This condition is easily achieved on rough nanostructured surfaces, where pores of lateral half-width ξ and vertical width $2R_q$ are decorated by smaller and smaller pores, whose local width and slope are typically higher than the mesoscopic quantities ξ and $2R_q/\xi$ A schematic representation of the structure and sub-structure of the real pore of a nanostructured surface is shown in Fig. 7C (see also the topographic profiles shown in Fig. 1A,B,C), from which it is possible to infer that on rough nanostructured surfaces, the morphology-induced self-overlap of the electrical double layer can be dramatic. Overall, the roughness-induced self-overlap of the electric double layer brings the system far from the conditions when linearized PB equations hold, namely weak potentials and low ionic concentration, turning the interface into a strongly regulated one [17].

We think that regulation processes enhanced by double layer self-overlap can determine strong local gradient of surface potential and ionic concentration, leading to an increase of the net interfacial charge density $\sigma_d = -(\sigma_0+\sigma_i)$ (what is measured by AFM). Redistribution of ions within the rough interface can be far from uniform, with a compression of the inner part of the diffuse layer inside the steepest and narrowest sub-pores, compensated by a depletion of the outer part, witnessed by an increase of λ_D on rougher ns-TiO_2 samples (Fig. 2C).

Concerning the marked roughness-induced shift of IEP towards lower values, we can speculate mechanisms triggered by strong changes of the electrostatic potential due to double layer self-overlap and regulation effects. One such mechanism is the direct impact of the intense surface potential on the pKs, and therefore on the IEP [90], through Eq. 11; another mechanism is the rupture of the symmetry of cationic and anionic activities leading to a modification of the adsorption of electrolyte ions [16]. In the case of TiO_2, where a weak predominance of adsorption of anions with respect to cations has been reported [24], an enhancement of adsorption of Cl^- anions would induce a downward shift of the IEP, according to Eq. 11.

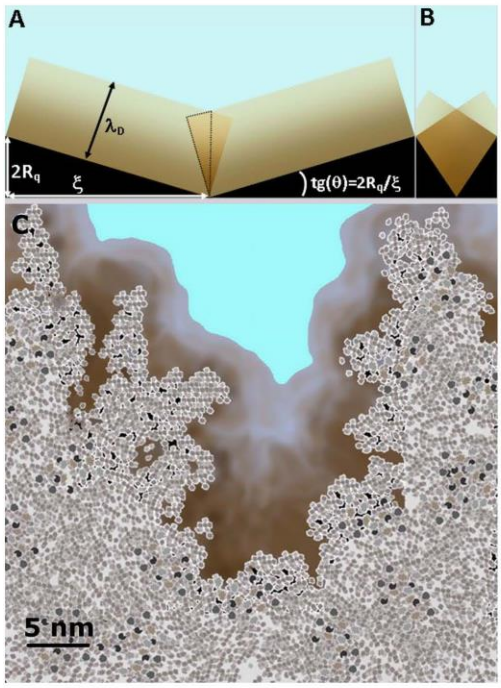

Figure 7. Schematic representation of the self-overlap of electrical double layers at corrugated interfaces. A simplified double layer extending to a distance λ_D into the bulk of the electrolyte is shown. Surface pores are characterized by half-width ξ, height $2R_q$, and slope $2R_q/\xi$. (A,B) Two pores with same height $2R_q$, same double layer depth λ_D, but markedly different slope. (C) A "real" surface pore of a cluster-assembled nanostructured surface in aqueous electrolyte: pore structure is statistically scale-invariant, replicating itself at small scales.
doi:10.1371/journal.pone.0068655.g007

The picture is further complicated by the fact that the investigated materials are porous in nature, being the result of random assembling of nanoparticles. The solid/liquid interface extends therefore inside the bulk material, inside nanopores, where extreme charge regulation effects may take place; the tail of the bulk double layer structure [91] can interfere with the outer double layer.

Conclusions

This work represents a systematic effort aiming at mitigating the lack of experimental quantitative data on the effects of surface nanoscale morphology on the properties of electric double layers. The experimental approach we have adopted turned out to be very effective for the study of morphological effects on nanoscale interfacial electrostatic interaction. On one side, the use of SCBD technique for the synthesis of nanostructured titania films allowed to carry out a systematic investigation of the effects of nano-roughness on double layer properties thanks to the possibility of a fine control of morphological parameters; on the other side, operating an atomic force microscope in force-spectroscopy mode equipped with micrometer colloidal probes turned out to be effective in characterizing charging phenomena of nanostructured metal oxide thin film surfaces, a task which can hardly be accomplished by means of standard electrokinetic techniques, as well as by means of standard nanometer-sized AFM tips.

The most remarkable and novel result of our study is the observation of the shift of the IEP of cluster-assembled nanostructured titania by more than three pH units towards more acidic character with respect to reference crystalline surfaces, as the surface roughness increased from about 5 to 26 nm, values comparable to the Debye length of the electrolyte $\lambda_D = 9.6$ nm. We have related the observed trend of IEP to the increasing importance of nanoscale morphology-induced self-overlap of the local diffuse layers, leading to strong charge regulation effects, local enhancement of surface potential and ionic concentration, and overall deviation from the trends expected for the linearized Poisson-Boltzmann theory. We propose a simple geometrical model for the self-overlap of the double layer, which highlights the importance of the ratios of characteristic lengths of the system (surface roughness R_q, correlation length ξ, and Debye length λ_D). Furthermore this model suggests that the competition of these lengths controls the properties of the double layer. In nanostructured interfaces all relevant morphological lengths are comparable to the electrostatic lengths λ_D of the electrolytes; in particular, as λ_D typically varies from a few angstroms to a few tens of nm, there will always be some surface structures of comparable size, in between the scale of single nanopores and that of mesoscopic structures of depth $\sim R_q$ and width $\sim\xi$.

The charging behavior of nanostructured surfaces may have important consequences for adsorption processes, as in the case of cell or protein-surface interactions. An incoming species, at a given distance from the surface (i.e. from the protruding asperities) of the order of one or two Debye lengths, will feel a reduced electric field compared to the case of interaction with a smooth surface, despite the fact that the surface is able to accommodate a greater amount of electric charge; this latter fact can be expected to play a role once the incoming species has approached to a distance comparable or smaller than the pore size, when the augmented local charge density and the dispersion forces will be felt directly and drive the final part of the adsorption process. The observed shift of the IEP on rough nanostructured titania films could potentially determine adsorption figures of proteins that markedly differ from those reported on smooth surfaces.

Supporting Information

Methods S1 Characterization of surface morphology by Atomic Force Microscopy; characterization of colloidal probe radius; details on force curves and curve fitting procedures; applicability of the constant charge model for DLVO force; bibliography.
(PDF)

Text S1 Charging of surfaces in liquid electrolytes; determination of charge density products and IEPs of reference systems; self-overlap of electrostatic double-layers: a simplified picture; bibliography.
(PDF)

Acknowledgments

We thank C. Piazzoni and C. Lenardi for the deposition of ns-TiO_2 films.

Author Contributions

Conceived and designed the experiments: AP PM. Performed the experiments: FB VV. Analyzed the data: FB AP. Contributed reagents/materials/analysis tools: AP PM. Wrote the paper: AP FB PM.

References

1. Lyklema JJ, de Keizer A, Bijsterbosch BH, Fleer GJ, Cohen Stuart MA, editors (1995) Fundamentals of Interface and Colloid Science: Solid-Liquid Interfaces, Volume 2, Academic Press, ISBN: 978-0-12-460524-4.
2. Leonard KC, Suyama WE, Anderson MA (2012) Evaluating the Electrochemical Capacitance of Surface-Charged Nanoparticle Oxide Coatings. Langmuir 28: 6476 6484. DOI: 10.1021/la204173w.
3. Khin MM, Nair AS, Babu VJ, Murugan R, Ramakrishna S (2012) A review on nanomaterials for environmental remediation. Energy Environ. Sci. 5: 8075 8109. DOI: 10.1039/C2EE21818F.
4. Cremer PS, Boxer SG (1999) Formation and Spreading of Lipid Bilayers on Planar Glass Supports. J. Phys. Chem. B 103: 2554 2559. DOI: 10.1021/jp983996x.
5. Oleson TA, Sahai N (2008) Oxide-Dependent Adsorption of a Model Membrane Phospholipid, Dipalmitoylphosphatidylcholine: Bulk Adsorption Isotherms. Langmuir 24: 4865 4873. DOI: 10.1021/la703599g.
6. Oleson TA, Sahai N, Wesolowski DJ, Dura JA, Majkrzak CF, Giuffre AJ (2012) Neutron reflectivity study of substrate surface chemistry effects on supported phospholipid bilayer formation on source sapphire. J Colloid Interface Sci. 370: 192 200. DOI: 10.1016/j.jcis.2011.12.031.
7. Vogler EA (1998) Structure and reactivity of water at biomaterial surfaces. Advanced Colloid Interface Science 74: 69 117. DOI: 10.1016/S0001-8686(97)00040-7.
8. Wilson CJ, Clegg RE, Leavesley DI, Pearcy MJ (2005) Mediation of Biomaterial - Cell Interactions by Adsorbed Proteins: A Review. Tissue Eng. 1: 1 18. DOI: 10.1089/ten.2005.11.1.
9. Parks GA (1965) The isoelectric points of solid oxides, solid hydroxides, and aqueous hydroxo complex systems. Chemical Reviews 65: 177 198. DOI: 10.1021/cr60234a002.
10. Brown GE, Henrich VE, Casey WH, Clark DL, Eggleston C, et al. (1999) Metal oxide surfaces and their interactions with aqueous solutions and microbial organisms. Chem. Rev. 99: 77 174. DOI: 10.1021/cr980011z.
11. Duval JFL, Lyklema J, Kleijn JM, van Leeuwen HP (2001) Amphifunctionally Electrified Interfaces: Coupling of Electronic and Ionic Surface-Charging Processes. Langmuir 17: 7573 7581. DOI: 10.1021/la010833i.
12. Bonnell DA, Garra J (2008) Scanning probe microscopy of oxide surfaces: atomic structure and properties. Rep. Prog. Phys. 71: 044501. DOI:10.1088/0034-4885/71/4/044501.
13. Morimoto T, Nagao M, Tokuda F (1969) The Relation between the Amounts of Chemisorbed and Physisorbed Water on Metal Oxides. J. Phys. Chem. 73: 243 248. DOI: 10.1021/j100721a039.
14. Schaub R, Thostrup P, Lopez N, Lægsgaardet E (2001) Oxygen vacancies as active sites for water dissociation on rutile TiO_2 (110). Phys Rev Lett 87: 266104. DOI: 10.1103/PhysRevLett.87.266104.
15. Brookes IM, Muryn CA, Thornton G (2001) Imaging water dissociation on TiO_2 (110). Phys Rev Lett 87, 266103. DOI: 10.1103/PhysRevLett.87.266103.

16. Duval JFL, Kleijn JM, Lyklema J, van Leeuwen HP (2002) Double layers at amphifunctionally electrified interfaces in the presence of electrolytes containing specifically adsorbing ions. Journal of Electroanalytical Chemistry. 532: 337 352. DOI: 10.1016/S0022-0728(02)00718-0.
17. Lyklema J, Duval JFL (2005) Hetero-interaction between Gouy-Stern double layers: Charge and potential regulation. Advances in Colloid and Interface Science 114 115: 27 45. DOI: 10.1016/j.cis.2004.05.002.
18. Oldham KB (2008) A Gouy-Chapman-Stern model of the double layer at a (metal)/(ionic liquid) interface. J Electroanalytical Chemistry 613: 131 138. DOI:10.1016/j.jelechem.2007.10.017.
19. Grahame DC (1947) The electrical double layer and the theory of electrocapillarity. Chem Rev. 41: 441 501.
20. Debye P, Hückel E (1923) De la theorie des electrolytes. Physikalische Zeitschrift 24: 185 206.
21. Parsegian VA, Gingell D (1972) On the electrostatic interaction across a salt solution between two bodies bearing unequal charges. Biophysical Journal 12: 1192 1204. DOI:10.1016/S0006-3495(72)86155-1.
22. Kallay N, Preocanin T, Kovacevic D, Lützenkirchen J, Chibowski E (2010) Electrostatic Potentials at Solid/Liquid Interfaces. Croat. Chem. Acta 83: 357 370.
23. Delgado AV, González-Caballero F, Hunter RJ, Koopal LK, Lyklema J (2005) Measurement and interpretation of electrokinetic phenomena. Pure Appl. Chem. 77: 1753 1805. DOI: 10.1351/pac200577101753.
24. Bogdanova NF, Ermakova LE, Sidorova MP (2010) Electrosurface Characteristics of Titanium Dioxide in Solutions of Simple Electrolytes: II. Calculation of Electrical Double Layer Parameters of TiO_2 from Adsorption and Electrokinetic Measurements. Colloid Journal 72: 749 755. DOI: 10.1134/S1061933X 10060049.
25. Lin X, Creuzet F, Arribart H (1993) Atomic Force Microscopy for Local Characterization of Surface Acid-Base Properties. J. Phys. Chem. 97: 7272 7276. DOI: 10.1021/j100130a025.
26. Johnson SB, Drummond CJ, Scales PJ, Nishimura S (1995) Electrical double layer properties of hexadecyltrimethylammonium. Colloids and A 103: 195 206. DOI: 10.1016/0927-7757(95)03257-E.
27. Johnson SB, Drummond CJ, Scales PJ, Nishimura S (1995) Comparison of Techniques for Measuring the Electrical Double Layer Properties of Surfaces in Aqueous Solution: Hexadecyltrimethylammonium Bromide Self-Assembly Structures as a Model System. Langmuir 11: 2367 2375. DOI: 10.1021/la00007a009.
28. Barten D, Kleijn JM, Duval J, Leeuwen HPV, Lyklema J, Cohen Stuart MA (2003) Double Layer of a Gold Electrode Probed by AFM Force Measurements. Langmuir 19: 1133 1139. DOI: 10.1021/la0117092.
29. Ducker WA, Senden TJ, Pashley RM (1992) Measurement of forces in liquids using a force microscope. Langmuir 8: 1831 1836. DOI: 10.1021/la00043a024.
30. Drummond CJ, Senden TJ (1994) Examination of the geometry of long-range tip-sample interaction in atomic force microscopy. Colloids and Surfaces A 87: 217 234. DOI: 10.1016/0927-7757(94)80070-7.
31. Considine RF, Drummond CJ (2001) Surface Roughness and Surface Force Measurement: A Comparison of Electrostatic Potentials Derived from Atomic Force Microscopy and Electrophoretic Mobility Measurements. Langmuir 17: 7777 7783. DOI: 10.1021/la0017227.
32. White LR (1983) On the Derjaguin approximation for the interaction of macrobodies. J. Colloid Interface Sci. 95: 286 288. DOI:10.1016/0021-9797(83)90103-0.
33. Tsao H-K (1999) The Electrostatic Interactions between Two Corrugated Charged Planes. J. Colloid Interface Sci. 216: 370 378. DOI: 10.1006/jcis.1999.6328.
34. Suresh L, Walts JY (1996) Effect of Surface Roughness on the Interaction Energy between a Colloidal Sphere and a Flat Plate. J COLLOID INTERF SCI 183: 199 213. DOI: 10.1006/jcis.1996.0535.
35. Bhattacharjee S, Ko CH, Elimelech M (1998) DLVO interaction between rough surfaces. Langmuir 14: 3365 3375. DOI: 10.1021/la971360b.
36. Hoek EMV, Bhattacharjee S, Elimelech M (2003) Effect of membrane surface roughness on colloid-membrane DLVO interaction. Langmuir 19: 4836 4847. DOI: 10.1021/la027083c.
37. Hoek EMV, Agarwal GK (2006) Extended DLVO interactions between spherical particles and rough surfaces. Journal of Colloid and Interface science 298: 50 58. DOI: 10.1016/j.jcis.2005.12.031.
38. Huang X, Bhattacharjee S, Hoek EMV (2010) Is Surface Roughness a "Scapegoat" or a Primary Factor When Defining Particle-Substrate Interactions? Langmuir 26: 2528 2537. DOI: 10.1021/la9028113.
39. Martines E, Csaderova L, Morgan H, Curtis ASG, Riehle MO (2008) DLVO interaction energy between a sphere and a nano-patterned plate. Colloids and Surfaces A 318: 45 52. DOI: 10.1016/j.colsurfa.2007.11.035.
40. Duval JFL, Leermakers FAM, van Leeuwen HP (2004) Electrostatic Interactions between Double Layers: Influence of Surface Roughness, Regulation, and Chemical Heterogeneities. Langmuir 20: 5052 5065. DOI: 10.1021/la030404f.
41. Daikhin LI, Kornyshev AA, Urbakh M (1996) Double-layer capacitance on a rough metal surface. Physical Review E 53: 6192 6199. DOI: 10.1103/PhysRevE.53.6192.
42. Daikhin LI, Kornyshev AA, Urbakh M (1997) Double layer capacitance on a rough metal surface: surface roughness measured by "Debye ruler". Electrochimica Acta 42: 2853 2860. DOI: 10.1016/S0013-4686(97)00106-0.
43. Daikhin LI, Kornyshev AA, Urbakh M (1998) Nonlinear Poisson-Boltzmann theory of a double layer at a rough metal/electrolyte interface: A new look at the capacitance data on solid electrodes. J. Chem. Phys 108: 1715 1723. DOI: 10.1063/1.475543.
44. Elimelech E, Chen WH, Waypa JJ (1994) Measuring the zeta (electrokinetic) potential of reverse osmosis membranes by a streaming potential analyser. Desalination 95: 269 286. DOI: 10.1016/0011-9164(94)00064-6.
45. Rudzifiski W, Charmas R, Piasecki W, Cases JM, Francois M, et al. (1998) Calorimetric studies of simple ion adsorption at oxide/electrolyte interface. Titration experiments and their theoretical analysis based on 2-pK charging mechanism and on the triple layer model. Colloids and Surfaces A: Physicochemical and Engineering Aspects 137: 57 68. DOI: 10.1016/S0927-7757(97)00369-5.
46. Preocanin T, Kallay N (2006) Point of zero charge and surface charge density of TiO_2 in aqueous electrolyte solution as obtained by potentiometric mass titration. Croatica Chemical Acta 79: 95 106.
47. Indrieri M, Podestà A, Bongiorno G, Marchesi D, Milani P (2011) Adhesive-free colloidal probes for nanoscale force measurements: production and characterization. Rev Sci Instrum 82: 023708 10. DOI: 10.1063/1.3553499.
48. Butt H (1991) Measuring electrostatic, van der Waals, and hydratation forces in electrolyte solutions with an atomic force microscope. Biophys J 60: 1438 1444. DOI: 10.1016/S0006-3495(91)82180-4.
49. Butt H, Jaschke M, Ducker W (1995) Measuring surface forces in aqueous electrolyte solution with the atomic force microscope. Biochemistry and Bioengeniring 38: 191 201. DOI: 10.1016/0302-4598(95)01800-T.
50. Hartley PG, Larson I, Scales PJ (1997) Electrokinetic and Direct Force Measurements between Silica and Mica Surfaces in Dilute Electrolyte Solutions. Langmuir 13: 2207 2214. DOI: 10.1021/la960997c.
51. Larson I, Drummond CJ, Chan DYC, Grieser G (2002) Direct force measurements between titanium dioxide surfaces. J. Am. Chem. Soc. 115: 11885 11890. DOI: 10.1021/ja00078a029.
52. Barborini E, Kholmanov IN, Conti AM, Piseri P, Vinati S, et al. (2003) Supersonic cluster beam deposition of nanostructured titania. Eur Phys J 24: 277 282. DOI: 10.1140/epjd/e2003-00189-2.
53. Kholmanov IN, Barborini E, Vinati S, Piseri P, Podestà A, et al. (2003) The influence of the precursor clusters on the structural and morphological evolution of nanostructured TiO_2 under thermal annealing. Nanotechnology 14: 1168 1173. DOI: 10.1088/0957-4484/14/11/002.
54. Wegner K, Piseri P, Tafreshi V, Milani P (2006) Cluster beam deposition: a tool for nanoscale science and technology. J Phys D: Appl Phys 39: R439-R459. DOI: 10.1088/0022-3727/39/22/R02.
55. Podestà A, Bongiorno G, Scopelliti PE, Bovio S, Milani P, et al. (2009) Cluster assembled nanostructured titanium oxide films with tailored wettability. J Phys Chem C 113: 18264 18269. DOI: 10.1021/jp905930r.
56. Scopelliti PE, Borgonovo A, Indrieri M, Giorgetti L, Bongiorno G, et al. (2010) The Effect of Surface Nanometre-Scale Morphology on Protein Adsorption. PLoS ONE 5: e11862. DOI: 10.1371/journal.pone.0011862.
57. Carbone R, Marangi I, Zanardi A, Giorgetti L, Chierici E, et al. (2006) Biocompatibility of cluster-assembled nanostructured TiO_2 with primary and cancer cells. Biomaterials 27: 3221 3229. DOI: 10.1016/j.biomaterials.2006.01.056.
58. Carbone R, Giorgetti L, Zanardi A, Marangi I, Chierici E, et al. (2007) Retroviral microarray-based platform on nanostructured TiO_2 for functional genomics and drug discovery. Biomaterials 28: 2244 2253. DOI: 10.1016/j.biomaterials.2006.12.026.
59. Giorgetti L, Bongiorno G, Podestà A, Berlanda G, Scopelliti PE, et al. (2008) Adsorption and stability of streptavidin on cluster-assembled nanostructured TiOx films. Langmuir 24: 11637 11644. DOI: 10.1021/la801910p.
60. Barborini E, Piseri P, Milani P (1999) A pulsed microplasma source of high intensity supersonic carbon cluster beams. J Phys D: Appl Phys 32: L105 L109. DOI:10.1088/0022-3727/32/21/102.
61. Tafreshi HV, Piseri P, Benedek G, Milani P (2006) The role of gas dynamics in operation conditions of a pulsed microplasma cluster source for nanostructured thin films deposition. J Nanosci Nanotechnol 6: 1140 1149. DOI: 10.1166/jnn.2006.139.
62. Piseri P, Podestà A, Barborini E, Milani P (2001) Production and Characterization of Highly Intense and Collimated Cluster Beams by Inertial Focusing in Supersonic Expansions. Review of Scientific Instruments 72: 2261 2267. DOI: 10.1063/1.1361082.
63. Cappella B, Dietler G (1999) Force-distance curves by atomic force microscopy. Surface Science Reports 34: 1 104. DOI: 10.1016/S0167-5729(99)00003-5.
64. Butt HJ, Cappella B, Kappl M (2005) Force measurements with the atomic force microscope: Technique, interpretation and applications. Surface Science Reports 59: 1 152. DOI: 10.1016/j.surfrep.2005.08.003.
65. Butt H, Jaschke M (1995) Calculation of thermal noise in atomic force microscopy. Nanotechnology 6: 1 7. DOI: 10.1088/0957-4484/6/1/001.
66. Lide DR (1997) Handbook of Chemistry and Physics, 78th edition, CRC Press.
67. Dean JA (1992) Lange's handbook of Chemistry, 15th edition, McGraw-Hill.
68. Franks GV (2002) Zeta potential and Yield Stresses of silica suspensions on concentrated monovalent electrolytes: isoelectric point shift and additional attraction. J Colloid Interface Sci 249: 44 51. DOI: 10.1006/jcis.2002.8250.
69. Kosmulski M, Dukhin AS, Priester T, Rosenholm JB (2003) Multilaboratory study of the shifts in the IEP of anatase at high ionic strengths. J Colloid Interface Sci 263: 152155. DOI: 10.1016/S0021-9797(03)00328-X.

70. Kosmulski M, Rosenholm JB (2004) High Ionic Strength electrokinetics. Advances in Colloid and Interface Science 112: 93 107. DOI: 10.1016/j.cis.2004.09.005.
71. Suttiponparnit K, Jiang J, Sahu M, Suvachittanont S, Charinpanitkul T, et al. (2011) The role of particle surface area, primary particle size, and crystal phase on TiO_2 nanoparticle dispersion properties. Nanoscale Research Letters 6: 1 8. DOI: 10.1007%2Fs11671-010-9772-1.
72. Kosmulski M (2011) The pH-dependent surface charging and points of zero charge. Journal of Colloidal and Interfac. Science 353: 1 15. DOI: 10.1016/j.jcis.2010.08.023.
73. Leckband D, Israelachvili J (2001) Intermolecular forces in biology. Quarterly Reviews of Biophysics 34: 105 267. DOI: 10.1017/S0033583501003687.
74. Butt H-J (1992) Electrostatic interaction in scanning probe microscopy when imaging in electrolyte solutions. Nanotechnology 3: 60 68. DOI:10.1088/0957-4484/3/2/003.
75. Senden TJ, Drummond CJ (1995) Surface chemistry and tip-sample interactions in atomic force microscopy. Colloids and Surfaces A: Physicochemical and Engineering Aspects 94: 29 51. DOI: 10.1016/0927-7757(94)02954-Q.
76. Lokar WJ, Ducker WA (2004) Proximal Adsorption at Glass Surfaces: Ionic Strength, pH, Chain Length Effects. Langmuir 20: 378 388. DOI: 10.1021/la035288v.
77. Sokolov I, Onga QK, Shodieva H, Chechikc N, James D, et al. (2006) AFM study of forces between silica, silicon nitride and polyurethane pads. Journal of Colloid and Interface Science 300: 475 481. DOI: 10.1016/j.jcis.2006.04.023.
78. Bergström L (1997) Hamaker constants of inorganic materials. Adv. in Colloid and Interface Science 70: 125 169. DOI: 10.1016/S0001-8686(97)00003-1.
79. Raiteri R, Martinoia S, Grattarola M (1996) pH-dependent charge density at the insulator-electrolyte interface probed by a scanning force microscope. Biosensors and Bioelectronics 11: 1009 1017. DOI: 10.1016/0956-5663(96)87660-3.
80. Ciro Chiappini (2006) Electrical transport measurements on nanostructured Titanium Dioxide thin films. Master Thesis, Università degli Studi di Milano.
81. T Caruso, Lenardi C, Mazza T, Policicchio A, Bongiorno G et al. (2007) Photoemission investigations on nanostructured TiO_2 grown by cluster assembling. Surface Science 601: 2688 2691. DOI : 10.1016/j.susc.2006.12.025.
82. Mazza T, Barborini E, Kholmanov IN, Piseri P, Bongiorno G et al. (2005) Libraries of cluster-assembled titania films for chemical sensing. Appl Phys Lett 87: 103108-1-103108-3. DOI: 10.1063/1.2035874.
83. Bullard JW, Cima MJ (2006) Orientation dependence of the Isoelectric Point of TiO_2 (Rutile) surfaces. Langmuir 22: 10264 10271. DOI: 10.1021/la061900h.
84. Hsua JP, Huanga S-W, Tseng S (2004) Effect of ionic sizes on the stability ratio of a dispersion of particles with a charge-regulated surface. J Colloid Interface Sci 272: 352 357. DOI: 10.1016/j.jcis.2003.10.007.
85. Hiemstra T, Riemsdijk WH (1996) A Surface Structural Approach to Ion Adsorption: The Charge Distribution (CD) Model. J Colloid Interface Sci 179: 488 508. DOI: 10.1006/jcis.1996.0242.
86. Hiemstra T, Venema P, Van Riemsdijk WH (1996) Intrinsic proton affinity of reactive surface groups of metal (Hydr)oxides: the bond valence principle. J Colloid Interface Sci 184: 680 692. DOI: 10.1006/jcis.1996.0666.
87. Caruso T, Lenardi C, Agostino RG, Amati M, Bongiorno G, et al. (2008) Electronic structure of cluster assembled nanostructured TiO_2 by resonant photoemission at the Ti $L_{2,3}$ edge. J Chem Phys 128: 094704 8. DOI:10.1063/1.2832321.
88. Langlet J, Gaboriaud F, Gantzer C, Duval JFL (2008) Impact of Chemical and Structural Anisotropy on the Electrophoretic Mobility of Spherical Soft Multilayer Particles: The Case of Bacteriophage MS2. Biophysical Journal 94: 3293 3312. DOI: 10.1529/biophysj.107.115477.
89. Duval JFL, Merlin J, Narayana PAL (2011) Electrostatic interactions between diffuse soft multi-layered (bio)particles: beyond Debye-Hückel approximation and Deryagin formulation. Phys. Chem. Chem. Phys. 13: 1037 1053. DOI: 10.1039/C004243A.
90. Kallay N, Preocanin T, Žÿalac S (2004) Standard States and Activity Coefficients of Interfacial Species. Langmuir 20: 2986 2988.DOI: 10.1021/la036185f.
91. Yang KL, Yiacoumi S, Tsouris C (2002) Monte Carlo simulations of electrical double-layer formation in nanopores. J Chem Phys 117: 8499 8507. DOI: 10.1063/1.1511726.

Ns-ZrO_x

A precise characterization of the double layer interactions and a deep study of the evolution of IsoElectric Point of ns-ZrOx thin films with different surface roughness is still a work in progress. Anyway a preliminary study on ns-ZrO_x IEP has been accomplished and the main results are shown.

Morphological characterization

The morphological properties of three different ns-ZrO_x thin films have been characterized by the analysis of topographical AFM maps. Representative AFM images of two samples (0.4 nm rough and 23.1 nm rough samples) are shown in Fig. 89 and the corresponding morphological properties are reported in Table V.

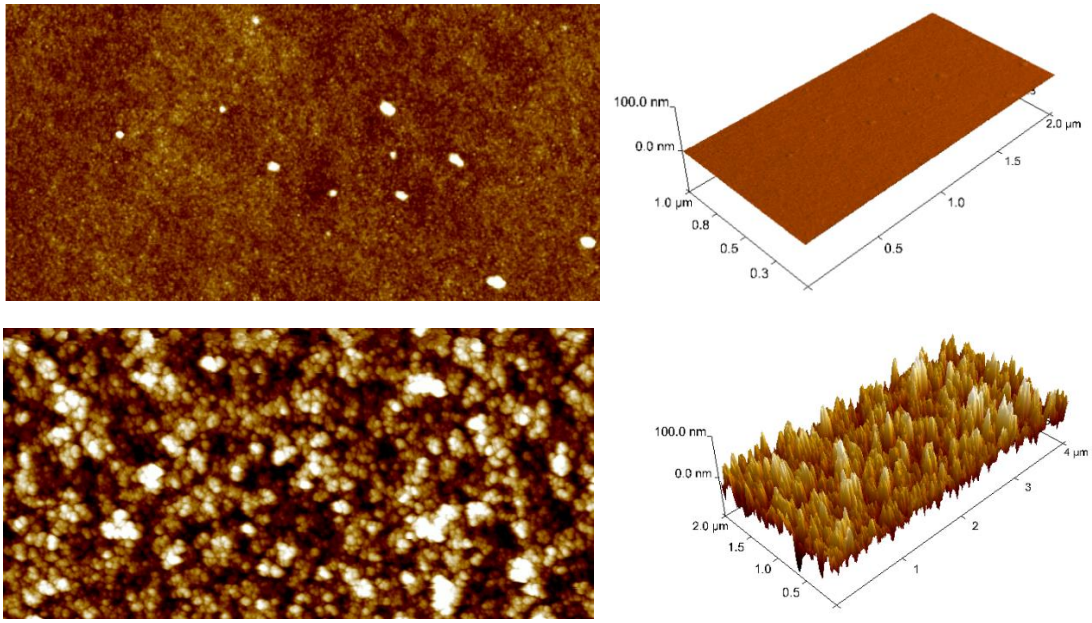

Fig. 89: (a-c) Representative AFM topographical maps (2000x1000x5nm^3 and 4000x2000x100nm^3) of flat and rough ns-ZrO_x samples; (b-d) 3D view of the AFM images, with z-scale of 100 nm for both the images.

Ns-ZrO_2	Thickness [nm]	Roughness [nm]	Specific Area
1	---	0.36 ± 0.01	1.008 ± 0.001
2	63 ± 8	15.3 ± 0.1	1.49 ± 0.01
3	213 ± 16	23.1 ± 0.4	1.57 ± 0.04

Table V: morphological properties of cluster assembled ns-ZrO_x thin films.

The morphological properties of ns-ZrOx films confirm the trend of morphology evolution presented in Section 7.2.1. The phase of these nanostructures films is cubic at room temperature (see Section 5.2.1).

Double layer interactions

As it has been shown before for ns-TiO_x, also IEP value of ns-ZrO_x decreases with increasing surface roughness (see Table VI). Also for zirconia samples, concerning the marked roughness-induced shift of IEP towards lower values, we can speculate mechanisms triggered by strong changes of the electrostatic potential due to double layer self-overlap and regulation effects at the nano-porous surface of the material (see Section before).

Roughness [nm]	IEP
0.36 ± 0.01	4.3 ± 0.5
15.3 ± 0.1	4.3 ± 0.5
23.1 ± 0.4	3.8 ± 0.5

Table VI: IsoElectric Point of ns-ZrO_x sample, depending on surface roughness.

In Fig. 90 the evolution of λ_D with surface roughness is shown. λ_D is constant to a value λ_D <10 nm close to the one predicted by Eq. 25 for [NaCl]=1 mM only for flat surface, while on rougher samples λ_D grows beyond 11 nm. These experimental observations provide an indication that Eq. 22, which describes double layer interactions at smooth surfaces, may not provide an accurate description of charging and ionic redistribution processes at rough surfaces.

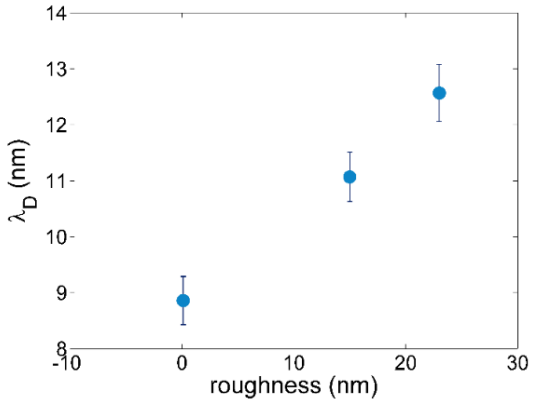

Fig. 90: Debye lengths λ_D as a function of the surface roughness Rq of ns-ZrO_2 films extracted from

the best fit of force curves by Eq. 25.

The shift of the distance axis allows treating the rough surface as an effective smooth plane where the total surface charge is evenly distributed on the mid plane, which is approximately located a distance Rq away from the surface peaks protruding towards the bulk of the electrolyte. Fig. 91 shows the corrected surface charge densities σ^*_S (all the distance axes of force curves used to extract double layer parameters, have been shifted by Rq), normalized with respect to the surface charge densities of the flat ns-ZrO_x sample at pH 5.4, as a function of surface roughness.

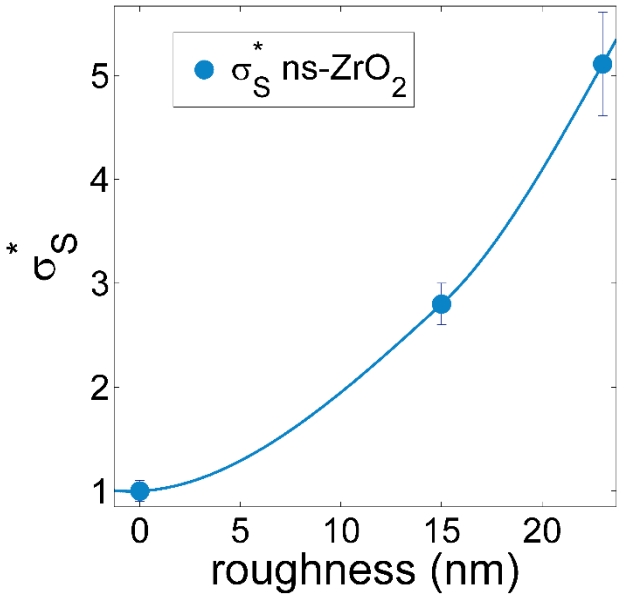

Fig. 91: The net surface charge density σ^*_S of ns-ZrO_2, normalized with respect to the surface charge densities of the flat ns-ZrO_x sample at pH 5.4, versus Rq, extracted from the best fit of force curves by Eq. 22 after correction of distance axes.

The evolution of the Debye length and of the surface charge density with ns-ZrO_x surface roughness confirm the experimental results with ns-TiOx, presented in the Section before. This consideration is of great relevance, because it means that peculiar double layer interactions observed for these nanostructured film is independent on the metal oxide material used but they are only determined by the surface morphology.

8.1.2. Surface charge density depending on thermal annealing

In order to quantify a possible difference in surface charge density of thin films depending on the thermal annealing treatments, I have performed force spectroscopy measurements

in 1mM NaCl solution (neutral pH, before and after thermal treatment) with AFM, in order to calculate the value of surface charge density by the analysis of DLVO interaction.

In Ref.[1] and [2] the sub-stoichiometric character of nanostructured ZrO_x and TiO_x at room temperature was reported. The samples become more stoichiometric after thermal annealing. Furthermore, by performing thermal annealing treatments also the phase of ns-ZrOx and ns-TiOx changes and in particular the monoclinic[1] and rutile[3] phase respectively becomes prevalent.

I have used all the precautions for the analysis of a rough interface, explained in Section 8.1.1. The colloidal AFM tip radius is 8200 ± 100 nm, and force constant of the cantilever is 0.14 ± 0.01 N/m.

Ns-ZrO_x

I have left two ns-ZrO_x samples with different surface roughness (Rq ~ 15 and 25 nm) in an oven for two hours at 600° C. Later, I have acquired force-curves with AFM and analysed the data by DLVO model modified for a rough interface, as explained in Section 8.1.1. In table VII the absolute values of surface charge density of ns-ZrO_x surfaces depending on the roughness and the thermal annealing treatments of the surface are reported.

$\lvert\sigma_S\rvert$ (C/m^2)	**As dep**	**Annealed**
Rq=15 nm	0.0041 ± 0.0001	0.0044 ± 0.0001
Rq=25 nm	0.017 ± 0.001	0.036 ± 0.001

Table VII: Absolute values of the surface charge density depending on the roughness and thermal annealing treatments of the ns-ZrO_x surfaces.

The absolute value of the surface charge density increases with roughness (as shown in the Section before) and with the thermal annealing of the surface (the surfaces are negatively charged). In particular a marked increase of the surface charge density induced by thermal treatments is observed on the rougher sample.

The main mechanisms implied in the charging of metal oxide surfaces in aqueous electrolytes are shown in section 6.1.2. and they imply interaction of surface hydroxyls M-OH with OH^- and H^+ ions and also adsorption of anions A^- and cations C^+ from solution to charged surface sites.

The improved surface charge density of ns-ZrOx films upon annealing at moderate temperatures can be explained in terms of removal of physisorbed organic contaminants and of the recovering of OH^- groups bonded to undercoordinated Zr atoms.

This results is also of great relevance for the interpretation of the protein adsorption experiments shown in Section 9.1.2.

Ns-TiO_x

In table VIII the absolute values of surface charge density of ns-TiO_x surfaces depending on the roughness and the thermal treatments of the surface. The experimental set-up is the same of the previous Section.

$\lvert\sigma_S\rvert$ (C/m^2)	**As dep**	**Annealed**
Rq=15 nm	0.0023 ± 0.0001	0.0024 ± 0.0001
Rq=25 nm	0.0078 ± 0.0005	0.0084 ± 0.0005

Table VIII: Absolute value of the surface charge density depending on the roughness and thermal treatment of the ns-TiO_x surfaces.

The increase in surface charge density with roughness[4] is confirmed.

The minimal difference in surface charge density values depending on annealing treatments, compared to the experimental results of ZrO_x, is explained by the slight sub-stoichiometry of the ns-TiO_x as deposited (the value of x in ns-TiO_x is less but very close to 2 [2]).

By a comparison of the ns-ZrO_x and ns-TiOx surface charge densities, for as deposited samples with the same roughness, we can conclude that the higher (negative) ns-ZrO_x surface charge density is probably due to a higher surface OH^- group density, due to the greater sub-stoichiometry of the zirconia surface[1] and the electronegativity of metal elements directly bound to the oxygen atoms[5]. As a future outlook I have to confirm this hypothesis.

8.2. Wettability of nanostructured materials

Ns-TiO_x

The results about ns-TiO_x wettability depending on roughness and annealing temperature are reported in Section 6.2.1 as in Ref. [2]. Here I report only the Fig. 92 which shows the main results about wettability in order to simplify the comparison with ns-ZrO_x results.

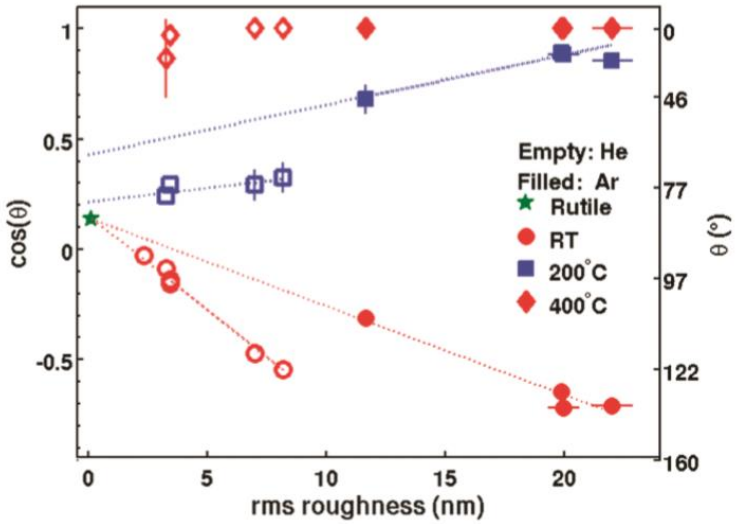

Fig. 92: Contact angles and corresponding cos(θ) values measured on ns-TiO_x films produced in different deposition and post-deposition conditions as a function of root-mean-square roughness. The contact angle measured on a single-crystal rutile TiO_2 sample at room temperature is also shown as reference. The dotted lines are a linear fit of data. Error bars, when not visible, are smaller than the data markers[2].

Ns-ZrO_x

Contact angles of water have been measured with a homemade apparatus consisting of a syringe pump, a video camera, and motorized sample and camera stages, all of them controlled via a PC. Small drops (volume ~0.5 mL) of Milli-Q water were produced with the syringe pump and gently deposited on the surface (Fig. 93 (a)). For each image, the overall drop profile was fitted with an elliptic curve (Fig. 93 (b)) and the error related to the fitting procedure was typically less than ±1° [6]. To obtain statistically sound results, at least five drops for each sample were typically analysed. The representative contact angle θ was then taken as the mean of these different determinations and the corresponding standard deviation was around ±2°, unless otherwise stated.

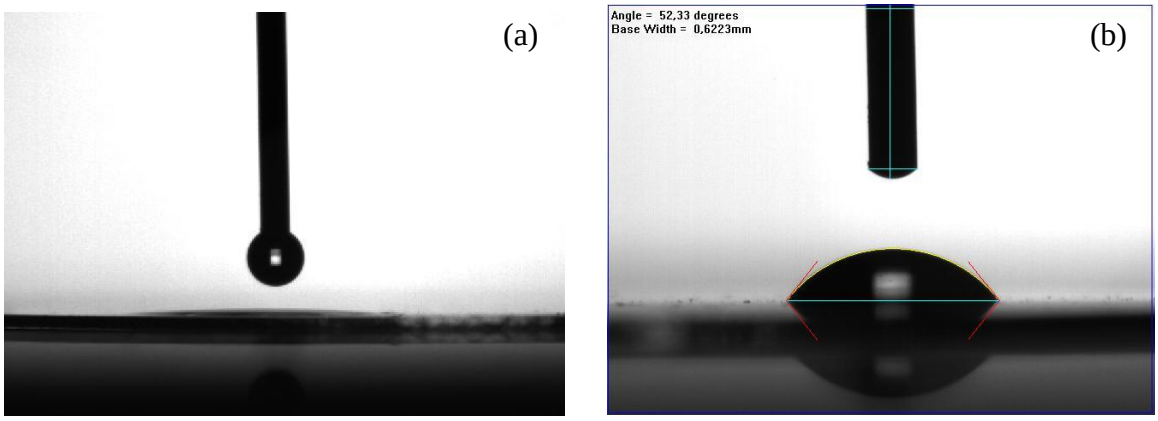

Fig. 93: (a) Camera image of the syringe pump and droplet that is going to be deposited on the surface; (b) drop profile with the elliptic curve fitted for the contact angle valuation.

Fig. 94 shows the contact angle θ measured on ns-ZrO_x films with different root-mean-square roughness, which underwent different thermal treatments.

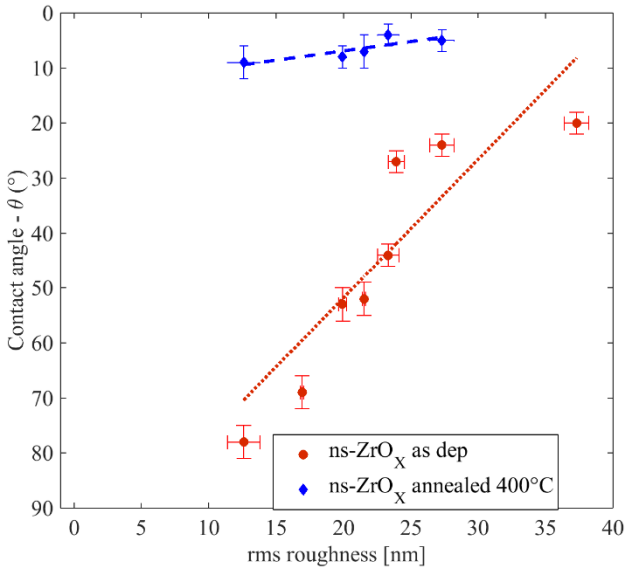

Fig. 94: Contact angles measured on ns-ZrO_x films with different post deposition conditions as a function of root-mean-square roughness. The dotted lines are a linear fit of data.

Data show that post-deposition thermal annealing improves the overall wetting character of ns-ZrOx films: while as-deposited films are hydrophilic, annealing at 400 °C makes them super-hydrophilic (as for ns-TiOx films, see Section 6.2.1).

Anyway, the wettability behaviour of ns-ZrOx films as-deposited is in contrast with TiO_x data[2] (hydrophobic in as-deposited conditions). This is probably due to the different surface charge density of the as-deposited samples, underlined also in Section 8.1.2., which

can explain the improved wettability of ns-ZrOx films with the increased recovering of OH groups bonded to undercoordinated Zr atoms[5].

Morphology has an important impact also on the wetting behaviour of ns-ZrOx. Controlling surface roughness in the range 10-40 nm allows tuning the contact angle from 70° to 20° in the hydrophilic regime. Notice that a residual dependence on Rq is observed also after annealing, in the superhydrophilic samples.

The measured cos(θ) values for the samples as-deposited and annealed at 400 °C scale linearly to a good approximation with the surface roughness. The dotted lines in Fig. 94 represent linear fits to the data. The trend observed for the as-deposited samples is compatible with the Wenzel equation (Eq. 37), predicting a positive slope for the cos(θ) vs. specific area curve, i.e., the enhancement of the intrinsic hydrophilic character of the surface, if we consider the sample with lower roughness as the reference flat sample.

Anyway, as a future outlook, we have to measure the value of the wettability for flat ZrOx sample.

I have decided to report this wettability results because is also of great relevance for the interpretation of the protein adsorption experiments shown in Section 9.1.2.

References

1. Lenardi, C., Sogne, E., Borghi, F., Podestà, A. & Paolo, M. Effects of Temperature and Oxygen Vacancies on Nanocrystallite Phase and Size in Metastable Cluster Assembled ZrO2 films. (to be published).
2. Podestà, A. *et al.* Cluster-Assembled Nanostructured Titanium Oxide Films with Tailored Wettability. *J. Phys. Chem. C* **113,** 18264–18269 (2009).
3. Kholmanov, I. N. *et al.* The influence of the precursor clusters on the structural and morphological evolution of nanostructured TiO_2 under thermal annealing. *Nanotechnology* **14,** 1168–1173 (2003).
4. Borghi, F., Vyas, V., Podestà, A. & Milani, P. Nanoscale Roughness and Morphology Affect the IsoElectric Point of Titania Surfaces. *PLoS ONE* **8,** e68655 (2013).
5. Takeda, S., Fukawa, M., Hayashi, Y. & Matsumoto, K. Surface OH group governing adsorption properties of metal oxide films. *Thin Solid Films* **339,** 220–224 (1999).
6. Semprebon, C. *et al.* Anisotropy of Water Droplets on Single Rectangular Posts. *Langmuir* **25,** 5619–5625 (2009).

9. Biological relevance of engineered nanostructured surfaces

According to the most recent studies on biomaterials[1-3], cells can actively 'sense' and adapt to the surface where they adhere and activate specific intracellular signals that influence cell survival and behavior.

In vivo, cell attachment is the consequence of the binding with specific cell adhesion proteins in the ECM, and it is intrinsically influenced, besides by receptor–ligand specific interactions, by the physical and mechanical signals arising from the topography of the external environment[4-6]. In vitro, on the other hand, cells set up a complex network of interactions both with the artificial surface and with the secreted and serum ECM proteins. The possibility of optimizing cell-substrate interactions can open up new perspectives in the design of biomimetic supports[7,8]. The topography of the ECMs is characterized by features over different length scales ranging from the nano to the mesoscale and it regulates the cellular behavior in a way that it is still far from a complete understanding[9-11]. The coexistence of ECM features at different length scales is probably one of the key factors, however it is not clear if there is a hierarchical organization of different structures and to what extent the various length scales can influence cellular response[12,13]. In Ref [14] they have shown that the thin films, deposited by SBCD, are characterized at the nanoscale, by a granularity and porosity mimicking those of recently observed ECM structures. They thus propose this new material as an optimal substrate for different applications in cell-based assays, biosensors or microfabricated medical devices.

In order to discover and understand the possibilities of these cluster-assembled films as biomaterials with physical properties which are comprehensible for biological systems, I have begun a series of studies which concerns the interaction between biological entities (proteins and cells) with nanostructured films. In this Chapter the main results are shown.

9.1. Proteins adsorption

9.1.1. The role of morphology on protein adsorption

Ns-TiO_x

In Ref[15] it is experimentally shown that the increase of nanoscale roughness (from 15 nm to 30 nm) of ns-TiO_x thin film induces a decrease of protein binding affinity (≤90%) and a relevant increase in adsorbed proteins (≥500%) beyond the corresponding increase of specific area. They demonstrated that these effects are caused by protein nucleation on the surface, which is promoted by surface nanoscale pores. Of relevance for a broad class of surface-active nanoparticles, from biological enzymes to solid-state nano-catalysts, it has been observed during experiments on the adsorption of the enzyme trypsin on ns-TiO_2, that the aggregation of the protein inside nanopores perturbs its relative catalytic activity in a roughness-dependent manner. In particular, the specific activity per mass of adsorbed enzyme decreased linearly with roughness, reflecting the reciprocal increase of steric hindrance of active sites with the ns-TiOx roughness[16].

First of all I have confirmed the trend of Langmuir Isotherms with surface roughness with ns-TiO_x sample, and later I have performed the same measurements with Ns-ZrO_x.

In Fig. 95 the adsorption BSA isotherms on nanostructured titania are shown, depending on surface roughness.

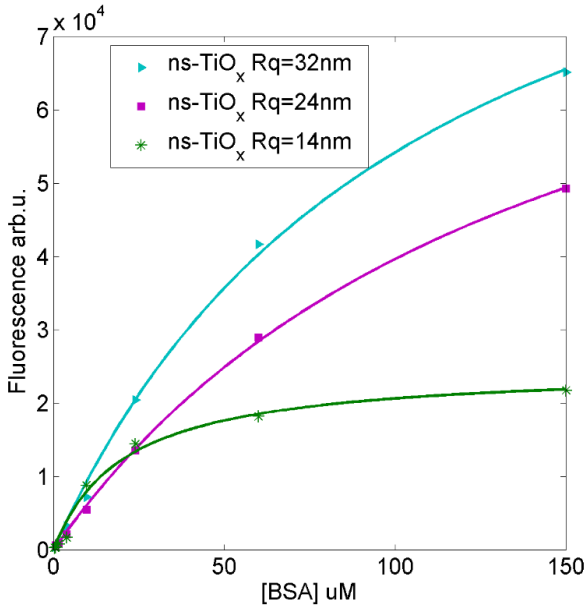

Fig 95: Adsorbed BSA as function of protein concentration (adsorption isotherms) for 3 ns-TiOx samples with different surface roughness.

Ns-TiO_x samples were annealed at 250°C in an oven for two hours; after annealing films are hydrophilic[17]. In table IX are reported the values of the saturation uptakes and the equilibrium dissociation constants, defined in Section 4.4.1, and related to the Langmuir isotherms of Fig. 95.

Ns-TiOx/BSA	**S.U. (a.u.)**	**K_D [µM]**
Rq= 14 nm	24899 ± 200	21 ± 5
Rq= 25 nm	97487 ± 200	80 ± 25
Rq= 32 nm	112820 ± 500	107 ± 35

Table IX: Adsorption saturation uptake and K_D as a function of the surface roughness for BSA.

The increasing trends of SU and of K_D with roughness confirm the one reported in Ref.[15]. The larger values of K_D (compared to the one of Ref.[15]) could be due to difference in surface wettability which alters the value of the SU and also the one of K_D[18], defined in Section 4.4.1 as the concentration for which the isotherm reaches its half maximum.

Ns-ZrO_x

Here below the protein adsorption isotherms of BSA (a) and fibrinogen (b) on ns-ZrOx samples (as deposited) are shown in Fig. 96 and the corresponding SU and K_D values are reported in table X and table XI.

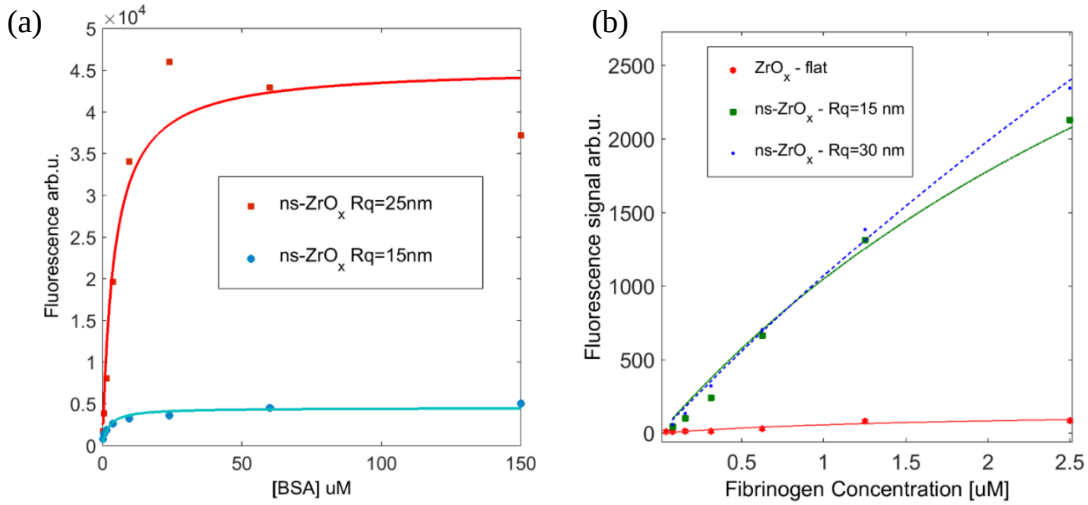

Fig. 96: (a) Adsorbed BSA and (b) fibrinogen as function of protein concentration (adsorption isotherms) for 2 ns-ZrO_x samples with different surface roughness.

Ns-ZrOx/BSA	**S.U. (a.u.)**	**K_D [µM]**
Rq= 15 nm	4512 ± 50	2.3 ± 0.5
Rq= 25 nm	45350 ± 200	4.3 ± 0.5

Table X: Adsorption saturation uptake and K_D as a function of ns-ZrOx surface roughness for BSA.

Ns-ZrOx/FIB	**S.U. (a.u.)**	**K_D [µM]**
flat	157 ± 10	1.8 ± 0.5
Rq= 15 nm	5975 ± 100	4.8 ± 0.5
Rq= 25 nm	13979 ± 200	12.5 ± 2

Table XI: Adsorption saturation uptake and K_D as a function of ns-ZrOx surface roughness for Fibrinogen.

For both proteins, the trends of SU and K_D with surface roughness is similar to the one of TiO_x: their values increase with the increasing of surface roughness and of the other morphological properties, like aspect-ratio of pores[15]. Ns-ZrOx samples are used as-deposited, without annealing treatments. In the previous Section we have seen that as-deposited ns-ZrOx samples are hydrophilic, and this is an important property for the improvement of protein adsorption on surfaces[19]. This hydrophilic behavior for as-deposited samples is an advantage of zirconia (instead of titania) which can be used immediately after deposition, without other thermal treatments.

9.1.2. Surface charge density and wettability

Ns-ZrO_x

In order to study protein adsorption for a fixed roughness, depending on the surface charge density and wettability, I have performed Fibrinogen adsorption experiments on ns-ZrOx sample as-deposited and annealed at 600 °C, for two different roughness values (Rq=15 and 25 nm). Fibrinogen adsorption isotherms on ns-ZrOx samples are shown in Fig. 97, while in Table XII the corresponding SU and K_D values are reported.

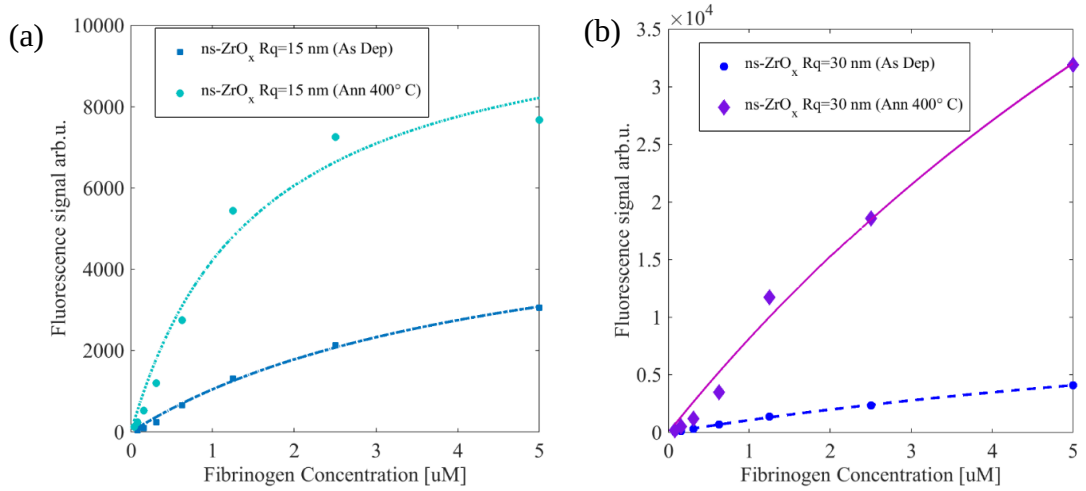

Fig 97: Adsorbed fibrinogen as function of protein concentration (adsorption isotherms) for

different post-deposition conditions and for two different surface roughness (a Rq=15 nm, b Rq=25nm).

Ns-ZrOx/FIB	**S.U. (a.u.)**	**K_D [µM]**
Rq= 15 nm (as dep)	5975 ± 100	4.8 ± 0.5
Rq= 15 nm (ann)	10765 ± 200	10 ± 2
Rq= 25 nm (as dep)	13979 ± 200	12.5 ± 2
Rq= 25 nm (ann)	120240 ± 200	14.3 ± 2

Table XII: Adsorption saturation uptake and K_D as a function of ns-ZrOx surface roughness for Fibrinogen, for different post-deposition conditions.

The reason why samples annealed (400 °C) are more suitable for protein adsorption are twofold:

- Annealing procedures increase the wettability behaviour of cluster-assembled thin film, as it is demonstrated by the results of the previous Sections 8.2 and in Ref.[17]; samples become superhydriphilic, and this implies the possibility for protein to penetrate inside the porous matrix and increase the adsorption.
- The increase in surface charge density of the annealed samples (Section 8.1.2) reinforce the local electrostatic interactions between proteins and surface which can enhance protein adsorption.

An increase in proteins adsorption with thermal annealing of the surface is also reported in Ref[18], for the adsorption of streptavidin on cluster-assembled nanostructured TiOx films.

9.2 Influence of surface morphology on cell adhesion

The world surrounding a cell is characterised by topographic features with nanoscopic dimensions. Cells[20-23], and in particular neuronal cells [24-26], are capable of sensing, in a surprisingly precise manner, differences in the mechanical characteristics and the nanotopography of the environment they interact with, mainly via integrin-mediated adhesion sites[21-23,27]. In consequence the information obtained by the cells can have a strong impact on cellular mechanics and eventually the cell's behaviour and fate.

In collaboration with other physicists and biologists of my group, we have recently observed the effect of biophysical signals from nanostructured zirconia surface to cell (PC12 cell line) adhesion and differentiation, in particular we have highlighted the role of

nanotopography. I have decided to report only a short abstract of the main results below, hopefully a detailed paper will be soon accepted and it will be accessible online.

Ns-ZrOx

Thanks to mechanotransductive components cells are competent to perceive biophysical signals of their microenvironment and to convert them into biochemical responses. These signals comprise the microenvironmental nanotopograpy and in fact cells can sense surface differences on a nanoscopic level. This provides the rationale to modulate cellular activities by nanotechnological engineering of biomaterial topography, but the underlying molecular mechanisms are only partially understood. In this work we produced, by supersonic cluster beam deposition of zirconia nanoparticles, nanostructured films with controllable roughness. Specific nanotopographical features of these films triggered neuritogenesis in PC12 cells by the induction of mechanotransductive events proceeding from the cell/nanostructure interface to the nucleus. A broad methodological approach unravelled how the surface nanoscale information is converted into this biological response. The cellular interaction with an appropriate surface topography, i.e. integrin clustering-restrictive features, enforces a nanoscopic architecture of the adhesion regions that affects the focal adhesion dynamics and cytoskeletal organisation. Consequentially, the general cellular biomechanical properties are modulated which furthermore impacts on the nuclear architecture/tension, transcription factors relevant for neuronal differentiation (i.e. CREB), and the protein expression profile. The proteomic profile reflects also congruently the executed adhesion complex-related and biomechanical processes. Altogether, this mechanotransductive signal integration eventually promotes and realises the nanostructure-induced neuronal differentiation.

References

1. McMurray, R. J., Dalby, M. J. & Tsimbouri, P. M. Using biomaterials to study stem cell mechanotransduction, growth and differentiation. *J. Tissue Eng. Regen. Med.* **9,** 528–539 (2015).
2. Costa, P., Almeida, F. V. M. & Connelly, J. T. Biophysical signals controlling cell fate decisions: how do stem cells really feel? *Int. J. Biochem. Cell Biol.* **44,** 2233–2237 (2012).
3. Govey, P. M., Loiselle, A. E. & Donahue, H. J. Biophysical regulation of stem cell differentiation. *Curr. Osteoporos. Rep.* **11,** 83–91 (2013).
4. Lutolf, M. P. & Hubbell, J. A. Synthetic biomaterials as instructive extracellular microenvironments for morphogenesis in tissue engineering. *Nat. Biotechnol.* **23,** 47–55 (2005).
5. Kleinman, H. K., Philp, D. & Hoffman, M. P. Role of the extracellular matrix in morphogenesis. *Curr. Opin. Biotechnol.* **14,** 526–532 (2003).
6. O'Brien, L. E., Zegers, M. M. P. & Mostov, K. E. Building epithelial architecture: insights from three-dimensional culture models. *Nat. Rev. Mol. Cell Biol.* **3,** 531–537 (2002).
7. Shin, H., Jo, S. & Mikos, A. G. Biomimetic materials for tissue engineering. *Biomaterials* **24,** 4353–4364 (2003).
8. Hubbell, J. A. Materials as morphogenetic guides in tissue engineering. *Curr. Opin. Biotechnol.* **14,** 551–558 (2003).
9. Flemming, R. G., Murphy, C. J., Abrams, G. A., Goodman, S. L. & Nealey, P. F. Effects of synthetic micro- and nano-structured surfaces on cell behavior. *Biomaterials* **20,** 573–588 (1999).
10. Stevens, M. M. & George, J. H. Exploring and Engineering the Cell Surface Interface. *Science* **310,** 1135–1138 (2005).
11. Curtis, A. Tutorial on the biology of nanotopography. *IEEE Trans. Nanobioscience* **3,** 293–295 (2004).
12. Tan, J. & Saltzman, W. M. Biomaterials with hierarchically defined micro- and nanoscale structure. *Biomaterials* **25,** 3593–3601 (2004).
13. Yim, E. K. F. & Leong, K. W. Significance of synthetic nanostructures in dictating cellular response. *Nanomedicine Nanotechnol. Biol. Med.* **1,** 10–21 (2005).
14. Carbone, R. *et al.* Biocompatibility of cluster-assembled nanostructured TiO2 with primary and cancer cells. *Biomaterials* **27,** 3221–3229 (2006).
15. Scopelliti, P. E. *et al.* The Effect of Surface Nanometre-Scale Morphology on Protein Adsorption. *PLoS ONE* **5,** e11862 (2010).

16. Gailite, L. *et al.* Nanoscale Roughness Affects the Activity of Enzymes Adsorbed on Cluster-Assembled Titania Films. *Langmuir* **30,** 5973–5981 (2014).
17. Podestà, A. *et al.* Cluster-Assembled Nanostructured Titanium Oxide Films with Tailored Wettability. *J. Phys. Chem. C* **113,** 18264–18269 (2009).
18. Giorgetti, L. *et al.* Adsorption and stability of streptavidin on cluster-assembled nanostructured TiOx films. *Langmuir ACS J. Surf. Colloids* **24,** 11637–11644 (2008).
19. Vogler, E. A. Protein adsorption in three dimensions. *Biomaterials* **33,** 1201–1237 (2012).
20. McNamara, L. E. *et al.* Investigation of the limits of nanoscale filopodial interactions. *J. Tissue Eng.* **5,** 2041731414536177 (2014).
21. Geiger, B., Spatz, J. P. & Bershadsky, A. D. Environmental sensing through focal adhesions. *Nat. Rev. Mol. Cell Biol.* **10,** 21–33 (2009).
22. Albuschies, J. & Vogel, V. The role of filopodia in the recognition of nanotopographies. *Sci. Rep.* **3,** (2013).
23. Dalby, M. J., Gadegaard, N. & Oreffo, R. O. C. Harnessing nanotopography and integrin-matrix interactions to influence stem cell fate. *Nat. Mater.* **13,** 558–569 (2014).
24. Brunetti, V. *et al.* Neurons sense nanoscale roughness with nanometer sensitivity. *Proc. Natl. Acad. Sci.* **107,** 6264–6269 (2010).
25. Moore, S. W. & Sheetz, M. P. Biophysics of substrate interaction: influence on neural motility, differentiation, and repair. *Dev. Neurobiol.* **71,** 1090–1101 (2011).
26. Chua, J. S. *et al.* Extending neurites sense the depth of the underlying topography during neuronal differentiation and contact guidance. *Biomaterials* **35,** 7750–7761 (2014).
27. Humphries, J. D., Paul, N. R., Humphries, M. J. & Morgan, M. R. Emerging properties of adhesion complexes: what are they and what do they do? *Trends Cell Biol.* (2015). doi:10.1016/j.tcb.2015.02.008

10. Conclusions and outlooks

One of the main scientific problems I have tackled in this PhD work is how the nanometer-scale morphology of different transition metal oxides systems (nanostructured TiOx and ZrOx), deposited by SCBD, evolves from sub-monolayer to thin film regime, depending on the incident cluster size. I have also studied the influence of the surface morphology of cluster-assembled films on the main functional properties of the interface, like surface charge density, IsoElectric Point and wettability. Finally, I have performed a qualitative characterization of the effects of these structural and functional properties on proteins adsorption and neuronal cells adhesion and differentiation mechanisms.
The principle results of my PhD work can be summarized as follows:

I have characterized, by atomic force microscopy, the evolution of the main morphological properties of thin film growth in sub-monolayer regime. By AFM investigation of ns-ZrOx and ns-TiOx samples it has been possible to highlight the mechanisms of diffusion of the smaller clusters, coalescence and juxtaposition phenomena which control the islands growth in sub-monolayer regime. I have identified 70% surface coverage as the turning-point between a first growth regime, where diffusion of particles plays an important role in determining islands formation, and the ballistic deposition regime, where diffusion is strongly disadvantaged and that characterized the morphology evolution in the thin film regime.

For these transition metal oxides systems, I have highlighted different results associated to memory effect phenomena. In particular, I can assert that the growth dynamic in sub-monolayer regime depends on the precursor cluster dimensions and that this growth dynamic determines different morphological properties of the thin film, even if the thin film growth beyond sub-monolayer occurs in ballistic deposition regime, irrespective of the incident cluster size. Successively I have also shown how the nanostructured morphology typical of ballistic deposition, composed by a highly porous matrix with high surface area, is preserved also after thermal annealing treatments thanks to the dimension and structure of the incident clusters.

An experimental quantitative characterization of the effects of surface nanoscale morphology on the properties of electric double layers has been performed. The experimental approach I have adopted turned out to be very effective for the study of morphological effects on nanoscale interfacial electrostatic interaction. On one side, the use of SCBD technique for the synthesis of nanostructured films allowed to carry out a systematic investigation of the effects of nano-roughness on double layer properties thanks to the possibility of a fine control of morphological parameters; on the other side, operating an atomic force microscope in force-spectroscopy mode equipped with micrometer colloidal probes turned out to be effective in characterizing charging phenomena of nanostructured metal oxide thin film surfaces.

I have proposed a simple geometrical model for the self-overlap of the double layer, which highlights the importance of the ratios of characteristic lengths of the system (surface roughness R_q, correlation length ξ, and Debye length λ_D). Furthermore this model suggests that the competition of these lengths controls the properties of the double layer. In nanostructured interfaces all relevant morphological lengths are comparable to the electrostatic lengths λ_D of the electrolytes; in particular, as λ_D typically varies from a few angstroms to a few tens of nm, there will always be some surface structures of comparable size, in between the scale of single nanopores and that of mesoscopic structures of depth $\sim R_q$ and width $\sim\xi$.

Surface charge density and wettability of different nanostructured transition metal oxide materials have been studied depending on thermal annealing treatments. Surface morphology has a fundamental role in determining the functional properties of cluster-assembled films, which show properties of great relevance even without post-deposition functionalization processes: the increase in surface roughness determines a huge increase in surface charge density and in the wettability behavior of the thin film. The annealing treatment further enhances the functional properties of the nanostructured surface.

A qualitative characterization of the influence of the morphological and functional properties on proteins adsorption has been proposed. I confirmed results concerning the influence of surface nanoscale morphology on protein adsorption and the

relevant role of surface pores as preferential sites for proteins nucleation phenomena. I have shown the influence of surface charge density and wettability in proteins adsorption processes, for different proteins types.

The results I achieved have important implications for the development of new applications of nanomaterials and for the understanding of basic mechanism at nano-bio interfaces.

One of the main future objectives to approach is the development of reliable procedures for the production of platforms with independently controlled morphological and functional properties. These platforms can be ideal templates for the investigation of molecular mechanisms of biocompatibility.

Appendix

11. Au-Polydimethylsiloxane (PDMS) nanocomposites

Here below, the works "Patterning of gold–polydimethylsiloxane (Au–PDMS) nanocomposites by supersonic cluster beam implantation" and "Stretchable nanocomposite electrodes with tunable mechanical properties by supersonic cluster beam implantation in elastomers" are reported in Section 11.1 and 11.2.

IOP Publishing Journal of Physics D: Applied Physics
J. Phys. D: Appl. Phys. 47 (2014) 015301 (10pp) doi:10.1088/0022-3727/47/1/015301

Patterning of gold–polydimethylsiloxane (Au–PDMS) nanocomposites by supersonic cluster beam implantation

C Ghisleri[1,2], F Borghi[1], L Ravagnan[2], A Podestà[1], C Melis[3], L Colombo[3] and P Milani[1,2]

[1] CIMAINA and Dipartimento di Fisica, Università degli Studi di Milano, via Celoria 16, 20133 Milano, Italy
[2] WISE srl, Piazza Duse 2, 20122 Milano, Italy
[3] Dipartimento di Fisica, Università di Cagliari, Cittadella Universitaria, 09042 Monserrato (Ca), Italy

E-mail: pmilani@mi.infn.it

Received 19 August 2013, revised 10 October 2013
Accepted for publication 24 October 2013
Published 3 December 2013

Abstract
Patterned gold–polydimethylsiloxane (Au–PDMS) nanocomposites were fabricated by supersonic cluster beam implantation (SCBI) of neutral gold nanoparticles in PDMS through stencil masks. The influence of nanoparticle dose on the surface roughness and morphology of the micropatterned regions of the nanocomposite was characterized. Nanoparticle implantation causes the swelling of PDMS without affecting substantially the lateral resolution of the patterns. In order to have an insight on the mechanism and the influence of nanoparticle implantation on the polymeric matrix, large-scale molecular dynamics simulations of the implantation process have been performed. The simulations show that even a single cluster impact on PDMS substrate strongly affects the polymer local temperature and density. Our results show that SCBI is a promising methodology for the efficient fabrication of nanocomposite microstructures on polymers with interesting morphological, structural and functional properties.

Keywords: nanocomposites, nanoparticles, stretchable polymers, micropatterning, AFM

(Some figures may appear in colour only in the online journal)

1. Introduction

Stretchable functional materials are enabling ingredients for the fabrication of wearable electronics [1], smart prosthetics [2, 3] and soft robotics [4–6]. These applications require the integration of electronic, optical and actuation capabilities on soft, conformable and biocompatible polymeric substrates [7, 8]. In particular, the fabrication of stretchable patterned microelectrodes is necessary for actuation [6, 9], electrical stimulation and recording in neuroprosthetics [10–12].

Poly(dimethylsiloxane) (PDMS) is a very popular playground for the proof-of-principle of soft devices since it couples biocompatibility with mechanical properties and machinability suitable for the production of dielectric elastomeric actuators [13]. Incorporation of metal nanoparticles in PDMS thin films using reduction of chemical precursors by superficial penetration or direct incorporation of preformed clusters have been used for the fabrication of lab-on-chip and optical devices ([14] and references therein). Particular efforts are also currently being concentrated on the fabrication of stretchable metallic circuits and microelectrodes integrated on PDMS [9, 15, 16].

A straightforward approach to the metallization (e.g. with Au, Ag, Pt, Pd) of PDMS is metal vapour deposition (MVD) [17], however, the use of MVD is hampered by the weak adhesion of the metallic layer on the elastomer and the subsequent delamination of the conducting layers even at very low deformations [11, 18, 19]. The use of adhesion layers such as Cr or Ti, or the treatment of the PDMS surface by oxygen plasma improve the performances, however the resilience is not adequate for a large number of applications [18, 20].

An alternative to MVD is ion implantation where noble metal ions are implanted with energies in the range of keV atom^{-1}, thus forming a conductive layer just below the polymeric substrate surface [21]; the diffusion of implanted ions gives also rise to the formation of nanoparticles

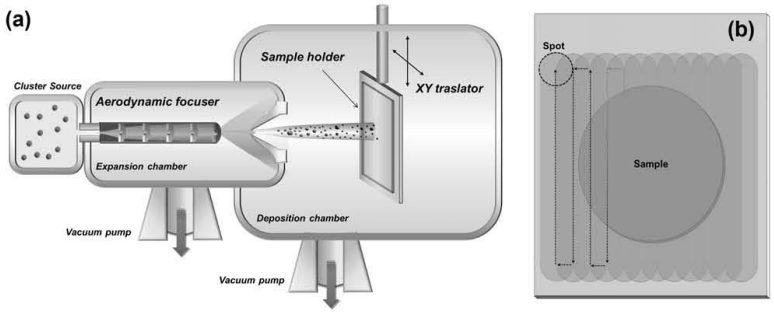

Figure 1. (*a*) The SCBI apparatus. The mix of gas and clusters produced in a cluster source attached to the expansion chamber is accelerated by a difference of pressure between the source and the expansion chamber and collimated by the aerodynamic focuser. Then the nanoparticles enter the deposition chamber and they are implanted in the polymeric substrate held on a movable sample holder allowing the deposition on large areas though a *rastering* technique. (*b*) Scheme of the rastering process: by moving repeatedly the sample holder vertically and horizontally with respect to the cluster beam, it is possible to uniformly implant large samples.

via Ostwald-ripening phenomena [22, 23]. Stretchable electrodes fabricated by ion implantation show adhesion and electrical conductivity degradation rates upon cyclical stretching that are significantly better than evaporated electrodes, however a substantial modification of the polymeric matrix due to radiation-induced disruption of chemical bonds, carbonization, bond reorganization and cross-linking is observed [24–26]. The use of ions also results in the build-up of electrical charges within the polymer substrate in the initial stages of the implantation process: this can perturb the trajectories of the incoming ions, thus lowering the lateral resolution of patterning performed using shadow masks. For this reason, shadow masks can be used only for structures larger than 100 μm; in general, micropatterning with high lateral resolution is obtained with ion implantation through photolithography steps or lift-off processes [21].

Recently we demonstrated that neutral metallic nanoparticles produced in the gas phase and aerodynamically accelerated in a supersonic expansion can be implanted in a polymeric substrate to form a conductive nanocomposite with superior resilience and interesting structural and functional properties [27, 28]. This approach is called supersonic cluster beam implantation (SCBI) and it is based on the use of a highly collimated supersonic beam carrying metallic clusters with a kinetic energy of about 0.5 eV atom^{-1}. Even if the kinetic energy is significantly lower than in ion implantation, neutral clusters are able to penetrate up to tens of nanometres into the polymeric target forming a conducting nanocomposite and avoiding electrical charging and carbonization [27, 28].

Supersonic cluster beams can be efficiently used for the production of micrometre-scale patterns through stencil masks [29, 30]. In particular, SCBI can produce micropatterns and microelectrodes on thin flexible polymeric substrates, such as SU8 using lift-off techniques [31]. Preliminary results showed also that electrically conducting regions can be patterned on PDMS with SCBI using stencil masks [27]. High-resolution patterning achievable with SCBI is a considerable advantage for soft devices microfabrication compared to chemical methods for functional nanocomposite production.

Here we present a characterization of 2D micropatterned regions of Au–PDMS nanocomposite integrated on PDMS by gold nanoparticle implantation through stencil masks. We have focused our attention on the evolution of surface roughness and morphology of Au–PDMS patterned nanocomposites and how this affects the lateral resolution attainable with SCBI. In order to have an insight into the influence of nanoparticle implantation on the polymeric matrix, we performed numerical simulations of the implantation process.

2. Experimental section

2.1. Supersonic cluster beam implantation

The supersonic cluster beam used for the implantation was produced by a pulsed microplasma cluster source (PMCS), as described in detail in [27, 32, 33]. Briefly, a PMCS consists in a ceramic body with a cavity where a metallic target (Au in the present case) is sputtered by a localized electrical discharge ignited during the pulsed injection of an inert carrier gas (He or Ar) at high pressure (40 bar). The sputtered metal atoms from the target thermalize with the carrier gas and aggregate in the cavity forming metal clusters. The carrier gas–cluster mixture expands out of the PMCS through a nozzle into a low pressure (10^{-6} mbar) expansion chamber (figure 1(*a*)). The supersonic expansion originating from the high pressure difference between the PMCS and the expansion chamber results in highly collimated supersonic beam: a divergence lower than 1° is obtained by using aerodynamic focusing nozzles [27, 33].

The central part of the cluster beam enters a second vacuum chamber (deposition chamber, at a pressure of about 10^{-5} mbar) through a skimmer, and it impinges on the polymeric substrate, supported by a motorized substrate holder. During implantation, the holder displaces the substrate in the two directions orthogonal to the cluster beam axis, allowing implantation on an arbitrarily wide area with a high homogeneity [31]. A typical scheme of this raster process is sketched in figure 1(*b*).

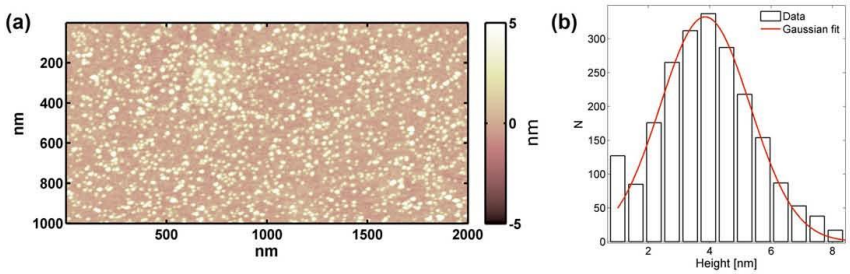

Figure 2. (*a*) AFM topography map (2 μm $\times$ 1 μm) of gold nanoparticles on silicon substrate; (*b*) Au nanoparticles size distribution obtained from the AFM map.

The size distribution of the nanoparticles used for implantation has been determined with atomic force microscopy (AFM) [34], by imaging a sub-monolayer sample obtained on a silicon substrate exposed to the nanoparticle beam for 3 s at a deposition rate of 0.02 nm s^{-1}. Figure 2(*a*) shows a representative topography of a 1 μm $\times$ 2 μm area of gold nanoparticles deposited on Si. The diameter of the nanoparticles (D_z) has been determined as the height of the objects. The distribution of heights (diameters) of nanoparticles, calculated from the analysis of ten topographic images, and the corresponding Gaussian fit are shown in figure 2(*b*). A mean value $D_z = 3.9 \pm 1.4$ nm (mean$\pm$standard deviation) was obtained.

Supersonic expansion accelerates the clusters to a mean velocity of approximately 1000 m s^{-1}, meaning that the metal clusters are accelerated towards the polymeric substrate with a kinetic energy E_k of roughly 0.5 eV atom^{-1} [35]. This energy is about four orders of magnitude less than the typical kinetic energies for ion beam implantation in polymers [9, 20]. Considering the atomic deposition rate N_{atm} (number of atoms reaching surface unit area per second), one can calculate the surface power density for the cluster implantation: $P_{surf} = N_{atm} \cdot E_k$. This power density is of the order of some μW cm^{-2} in the case of SCBI, thus not producing a significant increase of the substrate temperature above room temperature (RT). This should be compared with the power density for ion beams which is typically of the order of tenths of watts [21].

While for atom or nanoparticle deposition on a hard substrate one can define the thickness of the deposited material, in the case of nanoparticle implantation in polymers this quantity is not well defined. During implantation we placed a rigid substrate (generally a half-masked silicon or glass) on the sample holder together with the polymeric substrate to be implanted so that both intercept the same section of nanoparticles beam. Since the amount of deposited or implanted nanoparticles on the two substrates is the same, we can define the *equivalent thickness* t_{eq} of nanoparticles implanted in the nanocomposite as the thickness of the film produced by the same amount of nanoparticles deposited on the hard substrate.

2.2. Elastomeric substrates

PDMS substrates used in this work were produced with a Sylgard 184 Elastomer Kit (Dow Corning) by mixing for about 15 min the base and the curing agent in a 10 : 1 ratio. The mix was degased for 30 min in low vacuum in a desiccator and casted in a 10 cm diameter Petri dish up to a thickness of roughly 1 mm. After the polymerization at 100 °C for 1 h in an oven in ambient air, the PDMS was cut into pieces of the desired dimensions.

2.3. Patterning of the Au–PDMS nanocomposites

We used stencil masks for the nanocomposite patterning with micrometric resolution by exploiting the high collimation typical of supersonic beams. Three transmission electron microscopy (TEM) grids B, C and D (respectively, G2760N, G2786N, G220-8 from Agar Scientific) and a small piece of steel mesh (pattern E) were placed in front of the bare PDMS substrate at a distance of roughly 500 μm from the surface (figure 3(*a*)). The nickel grids have hexagonal, square and round holes with micrometric sizes of 30 μm, 7.5 μm and 36.5 μm, respectively, while the steel mesh consists in 4 μm $\times$ 90 μm and 60 μm spaced triangular apertures (see insets of figure 3(*b*)). Next to the masks a uniform region (area A in figure 3(*a*), size of 5 mm $\times$ 5 mm) was homogeneously implanted as a reference. Implantation through the masks was performed for 45 min at a rate of about 0.02 nm s^{-1}, reaching an equivalent thickness of 59 nm.

2.4. Implantation of nanoparticles with a radial density gradient

We characterized the effect of the dose of implanted nanoparticles on the surface morphology of PDMS by producing samples with a nanoparticles density gradient (figure 4). By moving the substrate during implantation only in the vertical direction (as schematically shown in figure 4(*a*)) we obtained a homogeneous nanocomposite in the direction parallel to the raster, with a gradient in the dose of nanoparticles implanted in the direction perpendicular to the raster. The deposition scheme of the sample with density gradient is shown in figure 4(*a*): a glass slide is half covered by a 13 mm wide and 76 mm long PDMS film, an aluminum foil mask partially shadows the PDMS film and the bare glass substrate. This configuration allows producing in one step a sample where implanted regions can be compared with pristine PDMS and cluster-assembled film on glass for

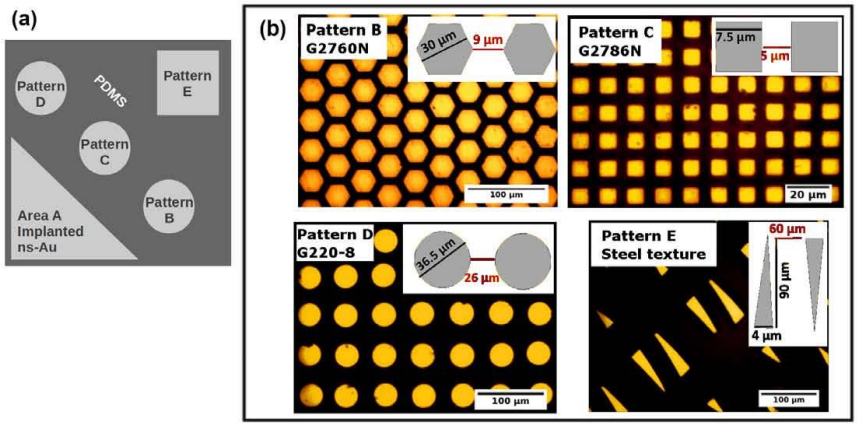

Figure 3. (*a*) Scheme of the sample prepared for the morphological characterization. Three TEM grids (patterns B, C, D) and a steel texture (pattern E) were used as stencil masks. The area A in the bottom left corner of the sample serves as reference for a non-patterned nanocomposite. (*b*) The four patterns in detail: the pictures represent the patterned PDMS observed with an optical microscope (50× magnification for pattern C, 20× magnification for the others), the insets in the top right corner in each picture represent the detailed scheme of the respective pattern.

the exact determination of the equivalent thickness gradient. The substrate underwent a SCBI process for 27 min with a deposition rate of 0.06 nm s^{-1}, reaching a maximum equivalent thickness (in the central position of the gradient) of 100 nm (figure 4(*b*)). The equivalent thickness of gold nanoparticles implanted in the PDMS follows a symmetric bell-shape trend in the horizontal direction, as reported in figure 4(*c*).

2.5. AFM characterization

The surface morphology of the nanocomposites was investigated using a Bioscope Catalyst/Nanoscope V AFM (Bruker Instruments). The AFM was operated in tapping mode in air, using rigid cantilevers with resonance frequency 250–350 kHz, equipped with single crystal silicon tips with nominal radius 5–10 nm. In the case of the sample produced with the radial density gradient, several 2 μm × 1 μm (2048 × 512 points) topographic maps were acquired on each of 12 different regions distributed along the gradient of the deposition and separated by about 100 μm from each other. The images were flattened by line-by-line subtraction of first- and second-order polynomials in order to remove artefacts due to sample tilt and scanner bow. AFM topographies are plotted using a colour scale spanning a finite vertical height range (dark to bright). On each flattened AFM image the RMS roughness R_q was calculated as the standard deviation of surface heights; R_q values have been averaged and standard deviation of the mean has been calculated as associated error.

2.6. TEM characterization

TEM was used for the evaluation of the clusters penetration depth d_{nc} in PDMS. Small PDMS substrates (approximately 5 mm long, 2 mm wide and 1 mm thick) were implanted with different increasing doses in order to evaluate the evolution of the implantation process and nanoparticle organization in the matrix. We used implantation times of 3 s, 30 min and 120 min at a rate of about 0.02 nm s^{-1}, reaching an equivalent sub-monolayer on a rigid substrate and equivalent thicknesses of 40 nm and 140 nm, respectively. Ultra-thin slices (with a thickness of about 100 nm) of nanocomposite were cut with a cryo-ultramicrotome at −160 °C and laid down on TEM grids covered with a layer of carbon-coated Formvar. Images were acquired with a Philips CM10 (80 kV) microscope.

2.7. Wettability characterization

The wettability of the nanocomposite surface was analysed by contact angle measurements with First Ten Angstroms FTA200. A milli-Q water droplet (volume: 3 × 10^{-6} l) was deposited on the surface of area A of the patterned nanocomposite sample and the contact angle value obtained by averaging 150 measures from as many droplet images acquired by a CCD camera immediately after the deposition.

2.8. Modelling

We performed large-scale molecular dynamics simulations of the implantation process based on state-of-the-art force fields [36]. While technical details of the present simulations have been published elsewhere [37], here we remark on their most important features. First of all, in order to keep the present simulations on the relevant experimental length scale we made use of very large-scale simulation cells containing as many as ∼4.6 million atoms. This system size corresponds to 25.6 × 25.6 × 85.35 nm^3: indeed, a very large simulation cell (demanding a very intense computer effort), is necessary if the full process of surface impact, the propagation into the substrate and the stopping of the Au clusters must be reproduced. Such large systems have been aged for as many

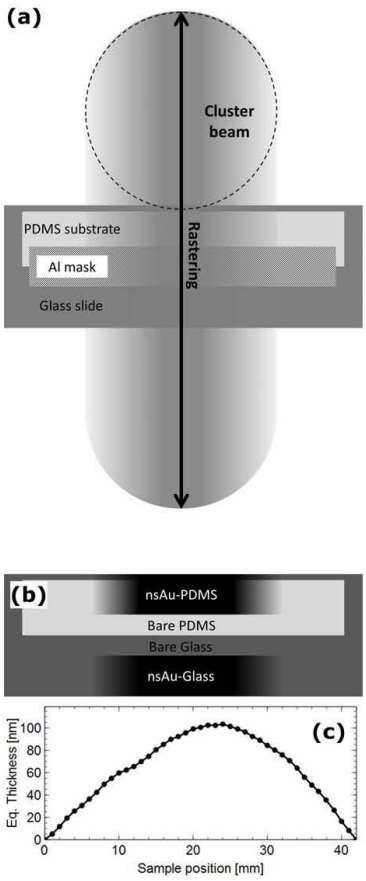

Figure 4. (*a*) Scheme of the sample prepared for the morphological characterization of the nanocomposite as a function of the equivalent thickness. The rastering in the vertical direction allows obtaining a gradient of nanoparticle dose implanted in the PDMS substrate. (*b*) Scheme of the sample after the implantation process: the deposition on glass serves as reference of a cluster-assembled film on a rigid substrate. (*c*) Equivalent thickness as a function of the horizontal position of the analysed sample.

as 180 ps. Such a relatively long simulation time was indeed necessary in order to allow the system to fully stabilize after the cluster impact.

Furthermore, special care was taken to model the interactions between the implanted Au clusters and the target substrate, as well as the possible presence of molecular linkers into the PDMS film. Accurate benchmark calculations have been executed on well-known physical properties of pristine PDMS (such as density and radial distribution function), confirming the quantitative reliability of the present computational set-up. Finally, the simulated protocol of implantation was chosen so as to mimic as close as possible the actual SCBI process; in particular, we implanted Au clusters with radius of 3 nm with energies of 0.5, 1.0 and 2.0 eV atom^{-1}.

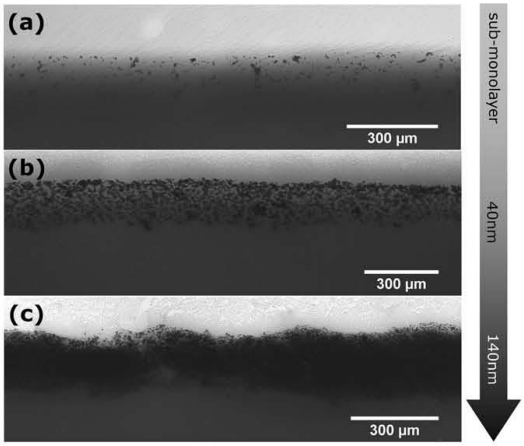

Figure 5. TEM images of thin slices (about 100 nm thickness) of the PDMS implanted for 3 s (*a*), with an equivalent thickness of 40 nm (*b*) and 140 nm (*c*) of gold nanoparticles. The penetration depth of the nanoparticles is approximately 180 nm in each case.

3. Results and discussions

3.1. Cluster implantation depth

The implantation of gold nanoparticles for different t_{eq} has been characterized by TEM imaging of ultra-thin slices of nanocomposite cut by cryo-ultramicrotomy. Figure 5(*a*) shows the nanoparticles embedded in the polymer resulting from a supersonic beam exposure of the substrate of 3 s, the implantation depth is roughly of 180 nm. A slight increase of nanoparticles density towards the PDMS surface is visible: this can be explained in terms of the limited dynamic range of the CCD camera overexposing the polymer–vacuum interface. By increasing the dose of implanted nanoparticles to equivalent thicknesses of 40 nm (figure 5(*b*)) and 140 nm (figure 5(*c*)), an increase of the volume filling factor (defined as the ratio between the total volume of the nanoparticles and the volume of the polymer in which they are implanted) is observed without any significant change in the cluster implantation depth. These observations indicate that implantation depth does not depend on the dose of implanted nanoparticles. A further increasing of the dose results in the surfacing of the clusters on top of the polymeric substrate and in the formation of a cluster-assembled metallic layer on the PDMS surface [27].

3.2. Patterning and swelling

Different nanocomposite patterns were produced and analysed, as described in the experimental section: here we report the results relative to hexagonal-shaped patterns; similar results have been obtained for the other patterns. Figure 6(*a*) shows the AFM characterization of the pattern, figures 6(*b*) and (*c*) show an individual hexagon with a surface presenting fractures. The equivalent thickness of implanted nanoparticles is $t_{eq} = 59 \pm 3$ nm, while the measured height of Au/PDMS hexagon is larger, being 100 ± 6 nm; this suggests that PDMS

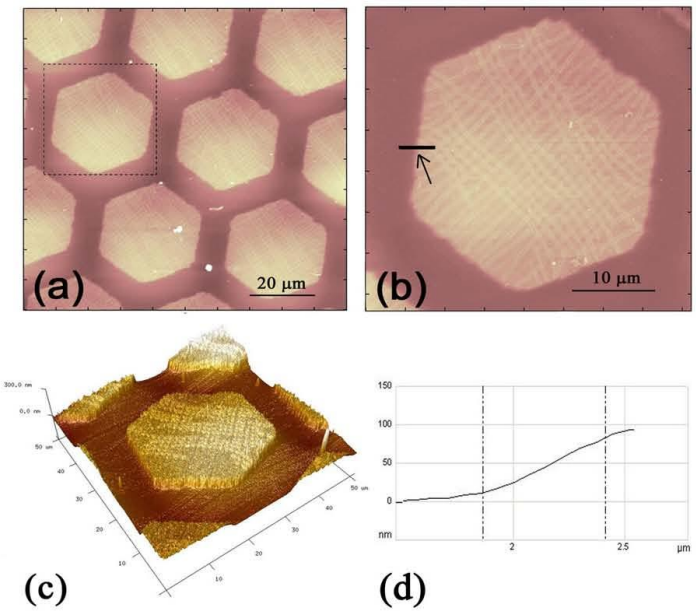

Figure 6. (*a*) AFM morphological map of the hexagonal patterns; (*b*) single hexagonal pattern, *z* scale ranges from −100 to 300 nm; (*c*) 3D map of the same pattern; (*d*) topographic profile across the boundary between bare PDMS and Au-nc/PDMS indicated by the arrow in (*b*).

undergoes swelling upon cluster implantation. Swelling in PDMS is reported as a consequence of solvent exposure [38]; far less studied is the effect of nanoparticle embedding on the reorganization of polymeric chains in silicones, although the formation of voids in polymers embedding inorganic particles has been reported [39]. In our case swelling could degrade the lateral resolution obtainable with patterning through stencil masks. To check this aspect we performed an AFM analysis of the boundary between bare PDMS and Au/PDMS hexagonal pattern (as indicated by the arrow in figure 6(*b*)). The effective lateral resolution of the pattern ranges from 0.5 to 1 μm showing that good lateral resolution can be obtained by SCBI in spite of the swelling phenomenon (figure 6(*d*)).

In order to clarify the relationship of the implanted nanoparticle dose with the PDMS swelling, we systematically analysed the evolution of the step between the bare PDMS substrate and the Au/PDMS nanocomposite in the sample with a nanoparticle density gradient (see section 2.4). The equivalent implantation thickness and the height of the swollen region of Au/PDMS nanocomposite with respect to the bare PDMS substrate were calculated from the histogram of the heights of AFM images acquired across sharp steps at the ns-Au/glass or Au-nc/PDMS boundaries, accordingly, produced by masking (figure 4(*b*)). The mean thickness/height was extracted as the distance between the peaks of the height distribution of the topographic maps; the errors associated with the average quantities were calculated summing in quadrature a statistical error (the standard deviation of the mean of step values calculated from different images), and a systematic error (7%), due to the non-linearity of the AFM piezo. The step height is always larger than the corresponding t_{eq}: the relation

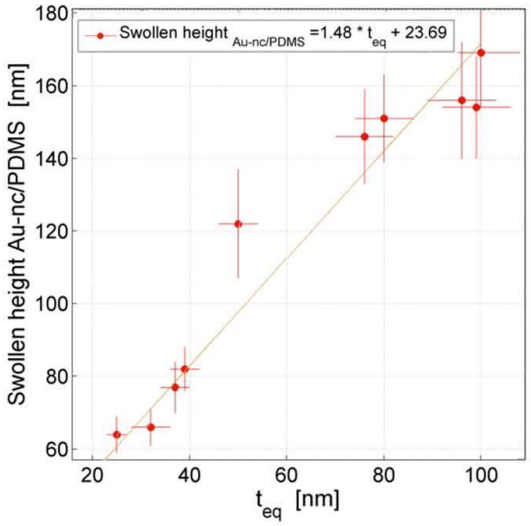

Figure 7. Thickness of the swollen gold nanoparticles PDMS nanocomposite versus the equivalent thickness of implanted clusters. The linear equation fit of the data is also shown.

between t_{eq} and the swelling height is to a good approximation linear as reported in figure 7. The swelling of PDMS grows with t_{eq} and even with $t_{eq} = 100$ nm it increases for more than a rigid offset without saturation in the investigated interval.

A possible origin of the observed swelling is the modification of the links between polymer chains caused by

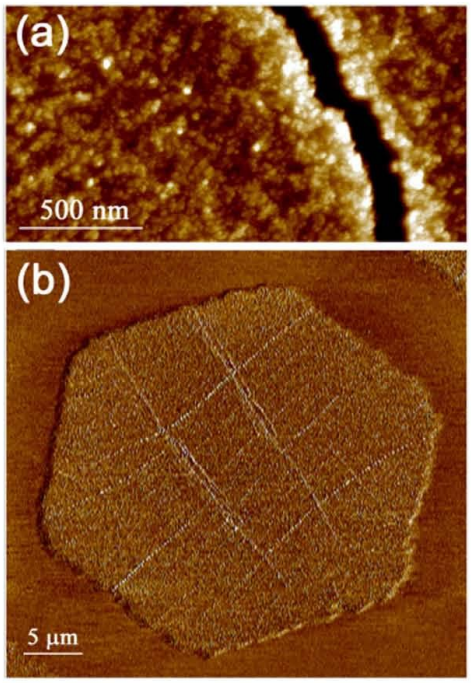

Figure 8. (*a*) AFM topographic map of the Au-nc/PDMS, with a detail of a crack on the surface. (*b*) Phase map of the hexagonal pattern.

nanoparticle impact during implantation: in order to check the presence of partial break up and reorganization of links at the polymer surface, we measured the wettability of implanted and pristine PDMS. For each of the two surfaces three series of data were acquired by depositing droplets in different points, in order to test the homogeneity of the sample. A contact angle of $(113 \pm 3)^\circ$ was measured on the bare PDMS, while the PDMS implanted with an equivalent thickness of 59 nm of gold nanoparticles (area A in figure 3) is characterized by a contact angle of $(112 \pm 3)^\circ$. These measurements suggest that gold cluster implantation does not significantly affect the microscopic structure of the PDMS surface.

Numerical simulations (see below) confirm that chains breakage is not occurring, whereas a local heating upon implantation is produced; this might be the origin of a local decrease of polymer density.

3.3. Surface morphology

Figure 6(*b*) and the 3D map in figure 6(*c*) show the presence of scratches on the surface. In figure 8(*a*) a detail of one of these surface defects, which appears like a fracture with elevated rims, is shown. The depth of the fracture as measured from the AFM image is 25 nm, although due to the limited penetration of the AFM tip inside the high aspect ratio defect this value must be taken as a lower limit for the actual fracture depth. We analysed the Au/PDMS roughness in 12 different positions along the gradient of deposited material, characterized by equivalent thickness t_{eq} ranging from 20 to 100 nm. Figure 9 reports the evolution of surface morphology upon the increase of the implantation dose from a pristine PDMS surface to three Au-nc/PDMS samples characterized by increasing equivalent thicknesses ($t_{eq} \approx 20$ nm, 40 nm and 100 nm, respectively). Nanoparticles implantation in PDMS produces an increasing corrugation as t_{eq} increases, with the appearance of craters and fractures which grow deeper and larger as the Au cluster loading on PDMS increases. The RMS roughness R_q of Au/PDMS nanocomposite evolves with t_{eq}: the quantitative analysis of the evolution of R_q with t_{eq} is reported in log–log scale in figure 10. For comparison purposes, we report in figure 11 the AFM topography of a Au/PDMS nanocomposite and that of a nanostructured film obtained by deposited gold cluster on a silicon substrate (ns-Au/Si) with the same equivalent thickness $t_{eq} \approx 20$ nm.

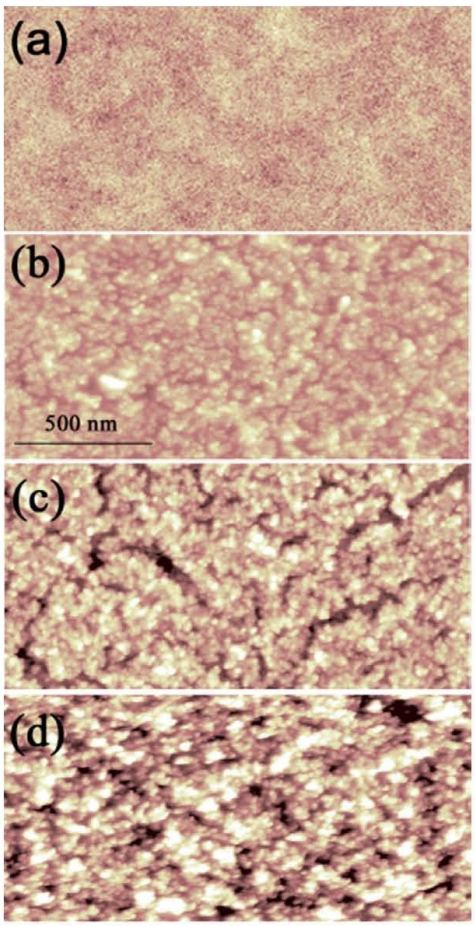

Figure 9. AFM topographical maps of PDMS (*a*), and three different samples of Au-nc/PDMS with equivalent thicknesses ~20 nm (*b*), 40 nm (*c*) and 100 nm (*d*); *z* scale ranges from −20 to 20 nm.

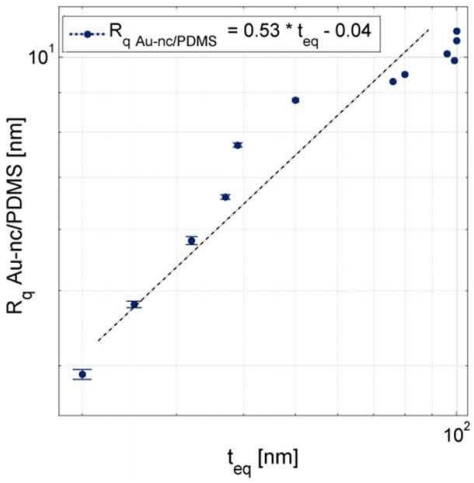

Figure 10. Log–log plot of the roughness of the swollen gold nanoparticles PDMS nanocomposite versus the equivalent thickness.

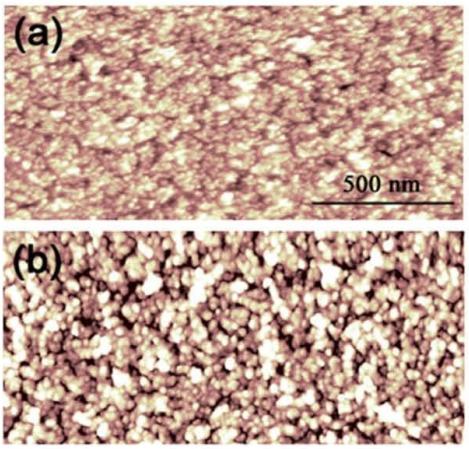

Figure 11. AFM topographical maps of Au-nc/PDMS (a) and ns-Au/Si (b). z scale ranges from −10 to 10 nm.

Table 1. RMS roughness R_q of the bare PDMS in different locations of the patterned sample (see figure 3).

Sample	Roughness R_q (nm)
Isolated PDMS	0.56 ± 0.01
Pattern B	0.98 ± 0.01
Pattern C	1.18 ± 0.01
Pattern D	0.78 ± 0.03
Pattern E	0.84 ± 0.01

Despite the similar thickness, roughness is markedly different: R_q of ns-Au/Si $= 6.8 \pm 0.1$ nm, while R_q Au-nc/PDMS $= 3.9 \pm 0.1$ nm.

The implantation of gold clusters in PDMS induces a change of morphology also in the PDMS regions close to the implanted area, as reported in table 1. The increase in PDMS roughness could be due to the horizontal swelling of the PDMS with implanted Au clusters or to the diffusion of Au clusters in the PDMS polymeric substrate, even though in AFM phase maps (figure 8(b)), a clear contrast between the bare PDMS and the Au-nc/PDMS nanocomposite is not visible.

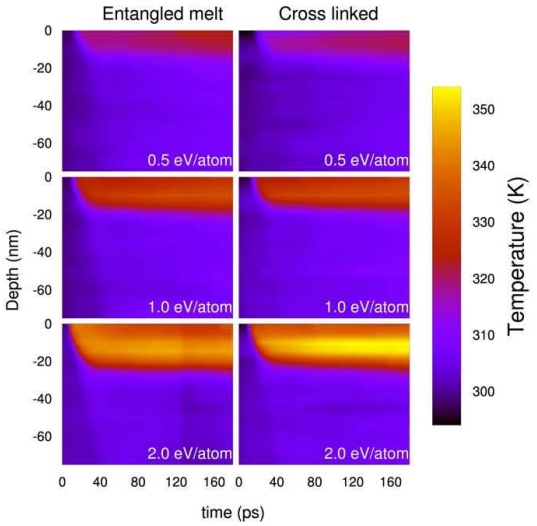

Figure 12. Temperature field (versus time and depth) of the EM- (left) and CL- (right) PDMS for the implantation energies of 0.5 eV atom^{-1} (top), 1.0 eV atom^{-1} (middle) and 2.0 eV atom^{-1} (bottom).

3.4. Numerical simulation of cluster implantation

Neutral metallic cluster implantation in polymers has been discovered only very recently [26, 27] and no detailed physical models of this phenomenon are available. Computer experiments are currently underway to gain deeper understanding of the microscopic mechanisms and the influence of the structural and mechanical properties of the polymeric matrix on the implantation. Recent simulations [36] provided evidence that for both entangled-melt (EM) and cross-linked (CL) PDMS the Au cluster penetration depth linearly depends on the implantation energy, having an angular coefficient of 7 nm eV^{-1} or 6 nm eV^{-1}, respectively. These results were explained in terms of the so-called *clearing the way effect* [40] which also predicts an inverse dependence of the same depth on the substrate cohesive energy.

In order to better characterize the implantation effect, we investigated the temperature field (wave) generated (propagating) inside the PDMS substrate upon cluster impact. In particular, we calculated the time-dependent temperature profile of the substrate during the implantation as a function of the penetration depth from the PDMS surface. Results are shown in figure 12 for the EM- (left) and CL- (right) substrates, corresponding to implantation energies of 0.5 (top), 1.0 (middle) and 2.0 (bottom) eV atom^{-1}. For both EM- and CL-PDMS we observe a sudden temperature increase ΔT_{PDMS} in the surface region: $\Delta T_{\mathrm{PDMS}} \sim 20$, 30 and

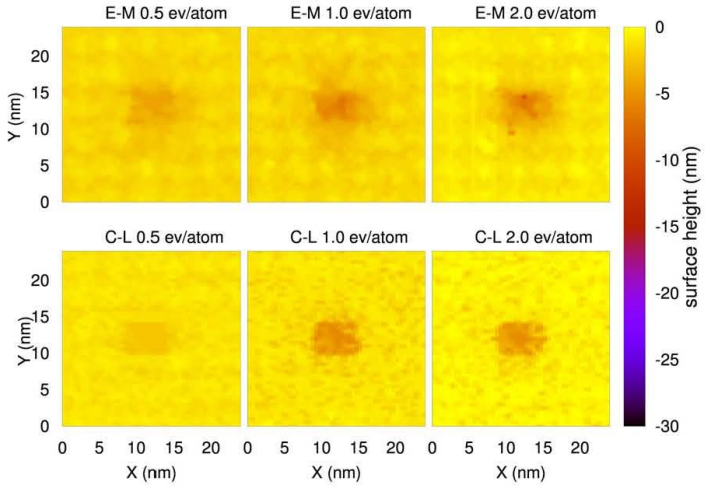

Figure 13. EM- (top) and CL- (bottom) PDMS surface height map for the implantation energies of 0.5 eV atom^{-1} (left), 1.0 eV atom^{-1} (centre) and 2.0 eV atom^{-1} (right).

50 K for increasing implantation energy. The corresponding temperature wave generated upon the impact is dissipated within the bulk substrate. After 180 ps we identify two main temperature spots in the PDMS substrate, namely: a *hot* region (H) at $T \sim 320$–350 K (figure 12, red–yellow shaded area) close to the surface and a *cold* region (figure 12, blue shaded area) at $T \sim 300$–310 K deeper into the substrate. We remark that the overall temperature increase is always larger for the cross-linked substrate, as a consequence of the different stiffness: the deformation upon the impact is larger in the case of the EM-PDMS substrate, thus resulting in a comparatively reduced increase of temperature.

The extension of the H region depends also on the implantation energy: by increasing its value from 0.5 to 2.0 eV atom^{-1}, we observe an increase of the H region depth from ∼10 nm up to ∼25 nm. Therefore, another effect of a single cluster impact is to increase the PDMS surface temperature up to 50 K, thus generating a decrease of the substrate density as large as ∼5%. This feature is in good agreement with the experimental finding of [41] that predicts a PDMS density decrease of ∼5% by increasing the temperature from 300 to 350 K. Therefore, the next impinging clusters will penetrate easily on a lower density PDMS substrate, further enhancing the effect of the local polymer density. This density decrease could explain the PDMS swelling experimentally observed upon the implantation.

We have extensively investigated the effect of a single cluster impact on the PDMS surface morphology by performing a theoretical analysis of the surface roughness. By analogy with the experimental AFM investigations reported above, we analysed the PDMS surface and internal nanopores by means of a spherical Au probe of radius 1.0 nm placed on top of the substrate. The probe interacts with the substrate via a 9-6 Lennard-Jones potential having the ε and σ parameters taken from the COMPASS force field. We spotted the PDMS surface by a square grid of points with 0.5 nm spacing; at each point of the grid we placed the probe and, by gently moving it up and down, we determined probe height corresponding to the minimum energy of the probe–substrate system. The envelope of such heights provided the simulated surface topography map, as shown in figure 13. The map, which has been suitably smoothed by means of a spline procedure, represents the surface height with respect to a conventional zero set at the maximum atom vertical position in the PDMS film.

In all cases we notice the presence of a crater created on the surface by the impinging Au cluster. The lateral dimensions of the crater (as large as ∼6 nm) are almost unchanged by increasing the implantation energy, while the crater depth strongly depends on it. In fact, for EM-(CL-)PDMS, we measure crater depths of ∼6 (3) nm, ∼8 (6) nm and ∼10 (7) nm for implantation energies of 0.5 eV atom^{-1}, 1.0 eV atom^{-1} and 2.0 eV atom^{-1}, respectively. The overall root-mean-square roughness (R_q) of EM-(CL-) PDMS increases with the implantation energy: $R_q = 1.1 \pm 0.1$ (0.9±1) nm, 1.8±0.1 (1.7±0.1) nm and 2.5±0.1 (2.3±0.1) nm for implantation energies of 0.5 eV atom^{-1}, 1.0 eV atom^{-1} and 2.0 eV atom^{-1}, respectively.

Shallower craters and an overall smaller roughness have been observed in the case of CL-PDMS. These results are consistent with the reduced cluster penetration depth observed for CL-PDMS [37]. This is due to the fact that in EM-PDMS the polymer chains are bonded only via dispersion and electrostatic interactions, while in the CL-PDMS the chains are partially covalently linked via the cross-linker molecule. Since the cluster penetration inside the PDMS matrix involves the breaking of the inter-chains bonds, we conclude that during the penetration inside the EM-PDMS substrate, the cluster experiences a weaker friction with respect to CL-PDMS.

4. Conclusions

We demonstrated the micrometric 2D patterning of Au–PDMS nanocomposite by supersonic cluster beam implantation through stencil masks on PDMS. The evolution of surface morphology and swelling of the patterned substrate can be quantitatively correlated to the dose of implanted nanoparticles. The PDMS swelling upon implantation does not substantially affect the lateral resolution of the pattern.

Atomistic simulations provide information on the PDMS microstructural evolution upon cluster implantation: the results show that even a single cluster impact on the PDMS substrate remarkably changes the polymer local temperature and density. Moreover, we observe the presence of craters created on the polymer surface having lateral dimensions comparable to the cluster radius and depths strongly dependent on the implantation energy.

Our results suggest that SCBI is a promising methodology for the efficient and easy fabrication of nanocomposite microstructures on polymers with interesting morphological, structural and functional properties.

Acknowledgments

The authors acknowledge Regione Lombardia and Regione Sardegna for their financial support to the project 'ELDABI - Elettronica Deformabile per Applicazioni Biomediche' (project n. 26599138). We also acknowledge computational support by CINECA (Bologna, Italy) under project ISCRA-UCIP, Maura Francolini, Elisa Sogne and Fondazione Filarete for support in TEM and Contact Angle measurements

References

[1] Pang C, Lee C and Su K-Y 2013 *J. Appl. Polym. Sci.* **130** 1429
[2] Moon J-H, Baek D H, Choi Y Y, Lee K H, Kim H C and Lee S-H 2010 *J. Micromech. Microeng.* **20** 025032
[3] Baek J-Y, An J-H, Choi J-M, Park K-S and Lee S-H 2008 *Sensors Actuators* A **143** 423
[4] Nawroth J C, Lee H, Feinberg A W, Ripplinger C M, McCain M L, Grosberg A, Dabiri J O and Parker K K 2012 *Nature Biotechnol.* **30** 792
[5] Buselli E, Smith A, Grover L, Levi A, Allman R, Menciassi A, Mattoli V and Beccai L 2011 *Microelectron. Eng.* **88** 1676
[6] Kovacs G, Lochmatter P and Wissler M 2007 *Smart Mater. Struct.* **16** S306
[7] Ma Z 2011 *Science* **333** 830
[8] Rogers J A, Someya T and Huang Y 2010 *Science* **327** 1603
[9] Rosset S and Shea H R 2013 *Appl. Phys.* A **110** 281
[10] Cyganowski A, Minev I R, Vachicouras N, Musick K and Lacour S P 2012 *IEEE Sensors 2012 Conf. (28–31 October)* paper 1974
[11] Graudejus O, Morrison B, Goletiani C, Yu Z and Wagner S 2012 *Adv. Funct. Mater.* **22** 640
[12] Lacour S P, Benmerah S, Tarte E, FitzGerald J, Serra J, McMahon S, Fawcett J, Graudejus O, Yu Z and Morrison B III 2010 *Med. Biol. Eng. Comput.* **48** 945
[13] Molberg M, Leterrier Y, Plummer C J G, Walder C, Löwe C, Opris D M, Nüesch F A, Bauer S and Månson J-A E 2009 *J. Appl. Phys.* **106** 054112
[14] Berry K R Jr, Russell A G, Blake P A and Roper D K 2012 *Nanotechnology* **23** 375703
[15] Zhang Y, Xu S, Fu H, Lee J, Su J, Hwang K-C, Rogers J A and Huang Y 2013 *Soft Matter* **9** 8062
[16] Adrega T and Lacour S P 2010 *J. Micromech. Microeng.* **20** 055025
[17] Graz I M, Cotton D P J and Lacour S P 2009 *Appl. Phys. Lett.* **94** 071902
[18] Douville N J, Li Z, Takayama S and Thouless M D 2011 *Soft Matter* **7** 6493
[19] Tuinea-Bobe C L, Lemoine P, Manzoor M U, Tweedie M, D'Sa R A, Gehin C and Wallace E 2011 *J. Micromech. Microeng.* **21** 115010
[20] Akogwu O, Kwabi D, Munhutu A, Tong T and Soboyejo W O 2010 *J. Appl. Phys.* **108** 123509
[21] Rosset S, Niklaus M, Dubois P and Shea H 2009 *Adv. Funct. Mater.* **19** 470
[22] Popok V N 2012 *Rev. Adv. Mater. Sci.* **30** 1
[23] Bechelany M, Maeder X, Riesterer J, Hankache J, Lerose D, Christiansen S, Michler J and Philippe L 2010 *Cryst. Growth Des.* **10** 587
[24] Jagielski J, Piatkowska A, Aubert P, Thomé L, Turos A and Abdul Kader A 2006 *Surf. Technol.* **200** 6355
[25] Abdul-Kader A M, Turos A, Grambole D, Jagielski J, Piatkowska A, Madi N K and Al-Maadeed M 2005 *Nucl. Instrum. Methods* B **240** 152
[26] Clough R L 2001 *Nucl. Instrum. Methods* B **185** 8
[27] Corbelli G, Ghisleri C, Marelli M, Milani P and Ravagnan L 2011 *Adv. Mater.* **23** 4504
[28] Ravagnan L, Divitini G, Rebasti S, Marelli M, Piseri P and Milani P 2009 *J. Phys. D: Appl. Phys.* **42** 082002
[29] Barborini E, Piseri P, Podestà A and Milani P 2000 *Appl. Phys. Lett.* **77** 1059
[30] Barborini E *et al* 2008 *J. Micromech. Microeng.* **18** 055015
[31] Marelli M, Divitini G, Collini C, Ravagnan L, Corbelli G, Ghisleri C, Gianfelice A, Lenardi C, Milani P and Lorenzelli L 2011 *J. Micromech. Microeng.* **21** 045013
[32] Barborini E, Piseri P and Milani P 1999 *J. Phys. D: Appl. Phys.* **32** L105
[33] Wegner K, Piseri P, Tafreshi H V and Milani P 2006 *J. Phys. D: Appl. Phys.* **39** R439
[34] Keller D 1991 *Surf. Sci.* **253** 353
[35] Milani P and Iannotta S 1999 *Cluster Beam Synthesis of Nanostructured Materials* (Berlin: Springer)
[36] Sun H 1998 *J. Phys. Chem.* B **102** 7338
[37] Cardia R, Melis C and Colombo L 2013 *J. Appl. Phys.* **113** 224307
[38] Lee J N, Park C and Whitesides G M 2003 *Anal. Chem.* **75** 6544
[39] Shirazi Y, Ghadimi A and Mohammadi T 2012 *J. Appl. Polym. Sci.* **124** 2871
[40] Yamamura Y and Muramoto T 1992 *Phys. Rev. Lett.* **69** 1463
[41] Shih H and Flory P J 1972 *Macromolecules* **56** 758

11.2. Nano-mechanical properties of Au-PDMS nanocomposites

APPLIED PHYSICS LETTERS **106**, 121902 (2015)

Stretchable nanocomposite electrodes with tunable mechanical properties by supersonic cluster beam implantation in elastomers

F. Borghi,[1] C. Melis,[2] C. Ghisleri,[3] A. Podestà,[1] L. Ravagnan,[3] L. Colombo,[2] and P. Milani[1,a)]
[1]*CIMAINA and Dipartimento di Fisica, Università degli Studi di Milano, via Celoria 16, 20133 Milano, Italy*
[2]*Dipartimento di Fisica, Università di Cagliari, Cittadella Universitaria, I-09042 Monserrato (Ca), Italy*
[3]*WISE srl, Piazza Duse 2, 20122 Milano, Italy*

(Received 23 February 2015; accepted 17 March 2015; published online 25 March 2015)

We demonstrate the fabrication of gold-polydimethylsiloxane nanocomposite electrodes, by supersonic cluster beam implantation, with tunable Young's modulus depending solely on the amount of metal clusters implanted in the elastomeric matrix. We show both experimentally and by atomistic simulations that the mechanical properties of the nanocomposite can be maintained close to that of the bare elastomer for significant metal volume concentrations. Moreover, the elastic properties of the nanocomposite, as experimentally characterized by nanoindentation and modeled with molecular dynamics simulations, are also well described by the Guth-Gold classical model for nanoparticle-filled rubbers, which depends on the presence, concentration, and aspect ratio of metal nanoparticles, and not on the physical and chemical modification of the polymeric matrix due to the embedding process. The elastic properties of the nanocomposite can therefore be determined and engineered *a priori*, by controlling only the nanoparticle concentration. © *2015 AIP Publishing LLC.* [http://dx.doi.org/10.1063/1.4916350]

Dielectric elastomer actuators (DEAs) are attracting a rapidly increasing interest as lightweight and inexpensive electromechanical transducers for the fabrication of soft robots,[1,2] smart actuators,[3] haptic interfaces, and energy harvesting systems.[4,5] DEAs are based on an elastomer sandwiched between two electrodes: this configuration results in a deformation (in plane or out of plane) under compression when the two electrodes are electrically polarized using voltages of several kV.[2,4]

In view of a widespread utilization of DEAs and of their integration in microdevices, one of the major challenges is the (micro)fabrication of compliant and well-adherent electrodes able to sustain a very large number of deformations (millions of cycles) while remaining electrically conductive. Their mechanical properties must be, as much as possible, similar to those of the elastomeric material in order not to alter the stiffness and deformation characteristics of the actuator.[4] Electrodes made by metal thin films deposited by sputtering or evaporation show poor adhesion, deterioration, and delamination after few deformation cycles.[6,7] Moreover, the Young's modulus of a metal film is several orders of magnitude higher than that of dielectric elastomers (50–100 GPa compared to 0.2–1 MPa), causing a very low actuation strain.[4]

Low-energy implantation of metallic ions in elastomers has been used for the fabrication of thin polymer-metal nanocomposite layers acting as electrodes in DEAs.[8,9] The nanocomposite layer is formed by metallic clusters, resulting from the aggregation of atomic species subsequent to ion implantation, embedded in the elastomeric matrix. This technique assures a good adhesion to the bare elastomer and a high degree of compliance.[8,9]

Recently, we showed that neutral metal clusters, accelerated in a supersonic expansion, can be implanted in elastomers to form an electrically conductive nanocomposite.[10,11] This process, called supersonic cluster beam implantation (SCBI), avoids both sample heating and charging and it is fully compatible with stencil mask micropatterning and lift-off technology.[11,12] Stretchable electrodes obtained by Au nanoparticles (NPs) implantation in polydimethylsiloxane (PDMS) are able to withstand more than 1×10^6 of uniaxial stretching cycles (at 40% strain) preserving finite and reproducible electrical resistance.[10]

Here, we demonstrate the fabrication of electrodes based on Au/PDMS nanocomposite with a Young's modulus depending solely on the amount of metal clusters implanted in the elastomeric matrix. We show both experimentally and by numerical simulations that the mechanical properties of the nanocomposite can be maintained close to that of the bare elastomer for significant metal volume concentrations. The elastic properties of the Au-PDMS nanocomposites are experimentally characterized by nanoindentation and modeled with molecular dynamics (MD) simulations and the Guth-Gold classical model.[13–15]

We fabricated Au-PDMS electrodes by implanting different quantities of neutral Au nanoparticles with a size distribution reported in Fig. 1(a) (as obtained by transmission electron microscopy (TEM) images. We used a deposition apparatus equipped with a Pulsed Microplasma Cluster Source (PMCS), as described in Ref. 10. Briefly, a PMCS consists a ceramic body with a cavity in which a solid Au target (purity 99.9%) is vaporized by a localized electrical discharge ignited during the injection of a pulse of inert gas (He or Ar) at high pressure (40 bars). The metal atoms, sputtered from the target, aggregate in the source cavity to form metal clusters; the mixture of clusters and inert gas expands subsequently through a nozzle forming a supersonic beam

a)Author to whom correspondence should be addressed. Electronic mail: pmilani@mi.infn.it.

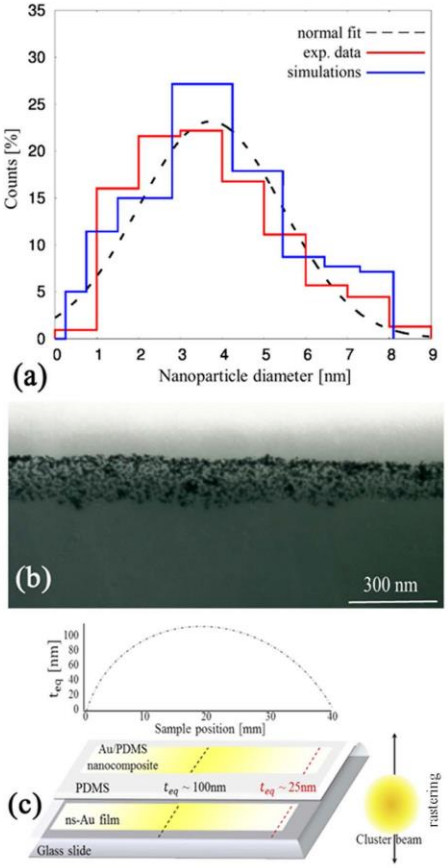

FIG. 1. (a) Experimental (red) and simulated (blue) Au cluster diameter distribution. The mean value of the normal distribution is 3.7 ± 1.7 nm. (b) TEM image of a thin section of the PDMS implanted with an equivalent thickness of 30 nm. The penetration depth of the nanoparticles is approximately 180 nm. (c) Schematic representation of a typical sample. A symmetric gradient of Au NPs on the clean glass surface is used to measure the equivalent thickness t_{eq} of implanted Au (which ranges from 100 nm in the center to 25 nm at the border). The same gradient of Au NPs implanted on a uniform PDMS film, covering the upper half of the glass slide, is used to characterize the Young's modulus for different equivalent thicknesses. A portion of PDMS is left unimplanted as reference in the nanomechanical analysis.

into an expansion chamber kept at 10^{-6} mbars. Electrically neutral nanoparticles exiting the PMCS are aerodynamically accelerated in a highly collimated beam with divergence lower than 1° and with a kinetic energy typically of 0.5 eV/atom.[16] The central part of the supersonic cluster beam enters, through a skimmer, a second vacuum chamber (deposition chamber) where the beam is intercepted by the PDMS substrate. The implanted Au nanoparticles volume fraction (Au volume concentration) is defined as the ratio between the total volume of the metal nanoparticles (the metal filler) and the volume of polymer in which the nanoparticles are implanted. Considering a homogeneously filled nanocomposite, this corresponds to the ratio between the equivalent thickness of the implanted nanoparticles and the thickness of the nanocomposite layer.[10] The thickness of the nanocomposite layer (nanoparticle implantation depth) can be obtained by TEM characterization (Fig. 1(b)). The equivalent thickness t_{eq} of nanoparticles implanted into the PDMS is obtained by measuring, by Atomic Force Microscopy (Bioscope Catalyst AFM, Bruker), the thickness of the Au cluster-assembled film deposited on a bare glass substrate region next to the PDMS film (Fig. 1(c)).

In order to systematically characterize the role of the nanoparticle volume fraction on the nanocomposite mechanical properties, we produced samples with a nanoparticle density gradient, as schematically shown in Fig. 1(c). This is obtained by rastering the PDMS substrate against the supersonic cluster beam only along one axis in order to obtain a homogeneous nanocomposite in the direction parallel to the raster, with a gradient in the amount of implanted nanoparticles along the orthogonal axis. The same nanoparticle gradient is deposited on the glass substrate to allow the direct measurement of the equivalent thickness. PDMS and glass substrates underwent an implantation and deposition process, respectively, for 27 min with a deposition rate of 0.06 nm s^{-1}, reaching $t_{eq} = 100$ nm in the center of the sample.

PDMS substrates were produced with a Sylgard 184 Elastomer Kit by mixing the base and the curing agent in a 10:1 ratio for about 15 min.

The evolution of the Young's modulus of Au-PDMS nanocomposites when t_{eq} is varying has been characterized by recording force vs indentation curves[17,18] with an AFM equipped with custom-made micro-probes consisting of spherical silica microparticles attached to tipless cantilevers[19] with force constant $k = 2.9$ N/m. The AFM probe is periodically pushed against the nanocomposite surface and the elastic indentation of the material is measured as a function of the total applied force (Fig. 2). The use of spherical probes with a diameter of 2 μm allows well-defined contact geometry (sphere on flat) and the use of analytical contact

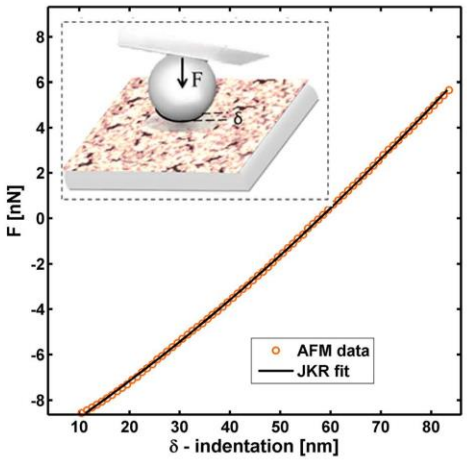

FIG. 2. A representative force-indentation curve acquired on the Au-implanted PDMS sample, with the modified JKR fit superimposed to the experimental data. In the inset, a schematic representation of the AFM indentation test is shown.

mechanics models for data fitting; moreover, large spherical probes provide an averaged and stable mechanical readout, representative of the mesoscopic properties of the nanocomposite material.[19,20]

Twelve different regions of the Au-PDMS nanocomposite sample have been tested: 100 force curves have been typically acquired in three different positions (separated by 10 μm) of each region. For large, adhesive contacts and soft surfaces, the Johnson-Kendall-Roberts (JKR) model is appropriate to describe indentation;[21,22] we have used a modified JKR equation to fit data, which takes into account also a constant capillary adhesive force due to the presence of a water meniscus (measurements have been carried out in ambient conditions, at relative humidity of 35%) (Fig. 2). The Poisson coefficient has been set to 0.5, as typical for polymers.[17,23] From force-indentation curves, the effective Young's modulus of the composite structure formed by the thick PDMS substrate and the thin nanocomposite Au-PDMS layer is extracted.[9] The values of the effective Young's modulus have been normalized by the value of the modulus of the unimplanted PDMS, in order to better evaluate the Au concentration-dependent variations and compare to numerical simulation data (the same normalization has been applied to in silico data).

The characterization of the nanocomposite Young's modulus via AFM indentation necessarily implies the use of mesoscopic models aimed at the description of the tip-sample interactions. The transferability of our findings to a macroscopic "bulk" scale is not straightforward; on the other hand, the typical dimensions of our nanocomposite electrodes do not allow the standard elasticity characterization approach for bulk samples based on traction-elongation cycles.[24] Hence, we decided to complement the experimental investigation by all-atom calculations aimed at predicting the dependence of the Young's modulus upon Au content by simulated traction-elongation cycles on nanocomposite samples.

Computer-generated nanocomposite samples have been obtained by simulating multiple implantations of Au clusters into the PDMS substrate. The implantation process strictly followed the procedure described in Refs. 11 and 25, although in the present case more than one clusters were implanted, with the size distribution obtained by TEM images reported in Fig. 1(a). Overall five different Au-PDMS nanocomposite samples were generated with Au volume concentration ranging between 8% and 29%. The corresponding number of particles in our simulation cells ranged between 350 000 and 450 000. An increasing number of Au nanoparticles were sequentially implanted on the PDMS substrate. For computational convenience in computer-generating the samples, the implantation was emulated by setting an impact energy of 2 eV/atom and a deposition rate of 50 ps^{-1}. Such a rate, although higher than in typical SCBI experiments, was nevertheless small enough to allow the full relaxation of the PDMS substrate upon each implantation event. Therefore, like in real SCBI experiments, the next cluster impacted on a fully relaxed substrate. Interatomic interactions have been modeled as reported in Refs. 11 and 25.

Once the nanocomposite samples at different Au nanoparticle concentrations were generated, we estimated the corresponding Young's modulus by simulating traction-elongation cycles. In detail, each cubic simulation cell with edge L_0 (containing an Au-PDMS sample with given Au content) was gently (strain rate = 1.75 ns^{-1}) elongated at constant room temperature for 0.8 ns, by imposing volume conservation.[26] During the traction cycle, intermediate configurations have been saved every 0.2 ns, providing four different strained samples (with same Au content). Their final extension L is defined as: $L = \lambda L_0$, where $\lambda = 1.1$, 1.2, 1.3, and 1.4. At this stage, each strained sample was carefully relaxed at room temperature by a constant-volume annealing as long as 2.5 ns, driving the corresponding atomic structure at its minimum-energy configuration, where the tensile stress σ_T was eventually calculated (such a stress value was calculated using the standard virial expression for the atomic-scale stress tensor).[27]

A typical stress-strain plot from MD simulations is shown in Fig. 3 for an Au-PDMS composite containing 8% of metallic clusters, providing evidence of the stress-strain dependence formulated in terms of the deformation parameters $\lambda^2 - 1/\lambda$.

This dependence, which is as well found in all systems here investigated, stands for the robustness of the present results since it is in agreement with the prediction of elementary viscoelasticity theory,[26] where it is proved that

$$\sigma_T = G(\lambda^2 - 1/\lambda). \quad (1)$$

In this framework, G is the elastic modulus of the elastomer, which is related to the corresponding Young's modulus through a very simple relation: $E = 3G$. The calculation of the stress-strain curve through MD simulations of a traction-elongation cycle directly offers a prediction on the Young's modulus of Au-PDMS composites.

Fig. 4 shows the normalized Young's modulus measured in silico and the normalized effective Young's modulus measured by AFM as a function of Au volume concentration. The modulus is basically constant (slightly decreasing in the case of experimental values) for concentration ρ below ~20%; above this threshold, we observe an exponential increase of E up to 5 times E_0 for $\rho \sim 30\%$. The agreement between the experimentally determined effective modulus and the numerically determined modulus is remarkable. Both experimental and numerical data can be fitted by an analytical function in the form $1 + \exp(-A(B - x))$ (the blue and red curves in Fig. 4), with A = 0.3, 0.2 and B = 23.1, 24.3 for the experimental and numerical data, accordingly.

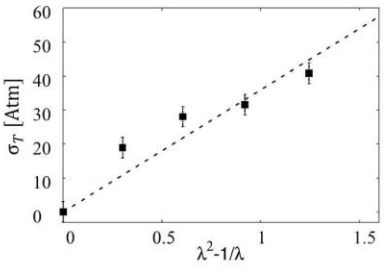

FIG. 3. σ_T vs. $\lambda^2 - 1/\lambda$ for an Au-PDMS nanocomposite having Au volume concentration $\rho = 8\%$. The black line represents the linear fit obtained according to equation $\sigma_T = G(\lambda^2 - 1/\lambda)$.

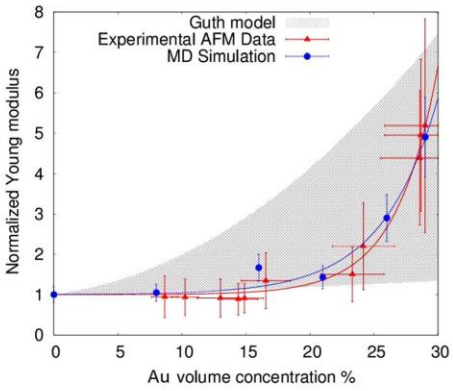

FIG. 4. Normalized E/E_0 vs. Au volume concentration ρ calculated from dynamic mechanical simulations (blue dots) and nano-indentation AFM experiments (red triangles). The shaded region represents the prediction of the Guth-Gold model for different nanoparticles aspect ratios ($\alpha = 1$ for the lower bound, $\alpha = 6$ for the upper bound), calculated as $E/E_0 = 1 + 0.67(\alpha\rho) + 1.62(\alpha\rho)^2$. The blue and red fitting curves are obtained by considering an analytical fitting function $1 + \exp(-A(B - x))$.

In the case of pristine PDMS, we estimated through the above traction-elongation MD protocol a Young's modulus $E_0 = 6.4 \pm 0.8$ MPa. This value is about 3 times larger than those measured in nanoindentation AFM experiments. This discrepancy is likely due to a different distribution of the length of the polymer chains: while in MD simulations this distribution is by construction unimodal (corresponding to a typical length of 40 monomers per chain), the corresponding distribution of real PDMS samples is not known in detail. We also remark that it has been shown[28] that the Young's modulus in pristine PDMS can vary over 2 orders of magnitudes by increasing the chain length from 1 to 1000. In order to reconcile simulations to experiments, the calculated/measured values of E in Au-PDMS composites have been renormalized to the corresponding value in pristine PDMS. This procedure, while straightforward, is very effective in separating the role of the implanted Au nanoclusters on the elastic properties of pristine PDMS (which is indeed the main target of this investigation) from the possible effects due to a different distribution of polymer chains.

It is remarkable that the agreement between the presented experimental/simulated results and the theoretical expectations of the classical Guth-Gold model[13–15] has been proposed to describe the effect of a filler on the elastic properties of a continuous rubber matrix, as indicated by the shadowed area in Fig. 4. The Guth-Gold model has been proposed to predict the modification of the normalized Young's modulus E/E_0 of a rubber-like polymer filled with metal nanoparticles with a specific aspect ratio α and at a given volume fraction ρ, according to the following equation:[15]

$$E/E_0 = 1 + 0.67(\alpha\rho) + 1.62(\alpha\rho)^2. \quad (2)$$

The shadowed region in Fig. 4 corresponds to the area spanned by the Guth-Gold curves obtained for different nanoparticle aspect ratios α ranging from 1 (lower bound, spherical particles) to 6 (upper bound, elongated particles).

The agreement is remarkable since the characterization approaches of the Young's modulus are based on very different assumptions, approximations, and length scales. The Guth-Gold model assumes that the modification of the nanocomposite elasticity only depends on the presence, concentration, and aspect ratio of the metal nanoparticles and not on the physical and chemical modification of the polymeric matrix due to the embedding process. This supports the assumption[10,11] that SCBI is not causing bond breaking events along the polymer chain, without modification of the underlying chemistry. Rather, only a microstructure evolution of the polymeric host is observed upon cluster incorporation. This, however, strongly affects the elastic properties of the polymeric matrix, as stated in Ref. 29. The comparison among different approaches reported in Fig. 4 actually indicates that SCBI is effectively a cold implantation technique, not damaging the chemical composition and structure of the polymeric chains and thus maintaining the mechanical properties of the polymeric substrate unaltered. Another interesting observation is that AFM indentation results shift toward a higher particles aspect ratio for increasing concentration of nanoparticles; this suggests that nanoparticles coalesce to form irregular larger aggregates towards the onset of a percolative structure, as already observed by electrical characterization of the nanocomposites.[10]

In conclusion, we have demonstrated both experimentally and theoretically the production of Au-PDMS nanocomposites with a Young's modulus depending solely on the amount of nanoparticle embedded in the elastomer. The elastic properties of the nanocomposite can be determined and engineered *a priori*, by controlling only one parameter thus allowing the preparation of DEAs electrodes with suitable mechanical properties.

A very important point is that the results of AFM indentation tests of the nanocomposite can be modeled and reproduced both by atomic-scale MD simulations and by the macroscopic Guth-Gold model: this shows that the assumptions of our approach are robust and they can be used to predict and design the functional and structural properties on a novel class of nanocomposites obtained by SCBI and used for stretchable electronics and optics.[30]

This work has been supported by project "ELDABI - Elettronica Deformabile per Applicazioni Biomediche" (Project No. 26599138). We thank R. Simonetta for support in nanoindentation experiments.

[1]S. Bauer, S. Bauer-Gogonea, I. Graz, M. Kaltenbrunner, C. Keplinger, and R. Schwödiauer, Adv. Mater. **26**, 149 (2014).
[2]I. A. Anderson, T. A. Gisby, T. G. McKay, B. M. O'Brien, and E. P. Calius, J. Appl. Phys. **112**, 041101 (2012).
[3]A. P. Gerratt, B. Balakrisnan, I. Penskiy, and S. Bergbreiter, Smart Mater. Struct. **23**, 055004 (2014).
[4]S. Rosset and H. R. Shea, Appl. Phys. A **110**, 281 (2013).
[5]G. Kang, K. S. Kim, and S. Kim, Rev. Sci. Instrum. **82**, 046101 (2011).
[6]O. Graudejus, B. Morrison, C. Goletiani, Z. Yu, and S. Wagner, Adv. Funct. Mater. **22**, 640 (2012).
[7]C. L. Tuinea-Bobe, P. Lemoine, M. U. Manzoor, M. Tweedie, R. A. D'Sa, C. Gehin, and E. Wallace, J. Micromech. Microeng. **21**, 115010 (2011).
[8]S. Rosset, M. Niklaus, P. Dubois, and H. R. Shea, Adv. Funct. Mater. **19**, 470 (2009).
[9]M. Niklaus and H. R. Shea, Acta Mater. **59**, 830–840 (2011).

[10]G. Corbelli, C. Ghisleri, M. Marelli, P. Milani, and L. Ravagnan, Adv. Mater. **23**, 4504 (2011).
[11]C. Ghisleri, F. Borghi, L. Ravagnan, A. Podestà, C. Melis, L. Colombo, and P. Milani, J. Phys. D: Appl. Phys. **47**, 015301 (2014).
[12]M. Marelli, G. Divitini, C. Collini, L. Ravagnan, G. Corbelli, C. Ghisleri, A. Gianfelice, C. Lenardi, P. Milani, and L. Lorenzelli, J. Micromech. Microeng. **21**, 045013 (2011).
[13]E. Guth and O. Gold, Phys. Rev. **53**, 322 (1938).
[14]E. Guth, J. Appl. Phys. **16**, 20 (1945).
[15]Y. P. Wu, Q. X. Jia, D. S. Yu, and L. Q. Zhang, Polym. Test. **23**, 903 (2004).
[16]P. Piseri, H. V. Tafreshi, and P. Milani, Curr. Opin. Solid State Mater. Sci. **8**, 195 (2004).
[17]E. K. Dimitriadis, F. Horkay, J. Maresca, B. Kachar, and R. S. Chadwick, Biophys. J. **82**, 2798 (2002).
[18]H. J. Butt, B. Cappella, and M. Kappl, Surf. Sci. Rep. **59**, 1 (2005).
[19]M. Indrieri, A. Podestà, G. Bongiorno, D. Marchesi, and P. Milani, Rev. Sci. Instrum. **82**, 023708 (2011).
[20]L. Puricelli, M. Galluzzi, C. Schulte, A. Podestà, and P. Milani, "Nanomechanical and topographical imaging of living cells by Atomic Force Microscopy with colloidal probes," Rev. Sci. Instrum. (in press).
[21]K. L. Johnson, K. Kendall, and A. D. Roberts, Proc. R. Soc. London, Ser. A **324**, 301 (1971).
[22]D. Tabor, J. Colloid Interface Sci. **58**, 2 (1977).
[23]J. E. Mark, *Polymer Data Handbook* (Oxford University Press, New York, 1999).
[24]S. Lampman, *Characterization and Failure Analysis of Plastics* (ASM International Editor, 2003).
[25]R. Cardia, C. Melis, and L. Colombo, J. Appl. Phys. **113**, 224307 (2013).
[26]M. Rubistein and R. H. Colby, *Polymer Physics* (Oxford University Press, 2003).
[27]S. Giordano, A. Mattoni, and L. Colombo, Rev. Comput. Chem. **27**, 1 (2011).
[28]D. R. Heine, G. S. Grest, C. D. Lorenz, M. Tsige, and M. J. Stevens, Macromolecules **37**, 3857 (2004).
[29]P. J. Flory, Polym. J. **17**, 1 (1985).
[30]C. Ghisleri, M. A. C. Potenza, L. Ravagnan, A. Bellacicca, and P. Milani, Appl. Phys. Lett. **104**, 061910 (2014).

List of Publications

Refereed publications

- A.V.Singh, M. Ferri, M. Tamplenizza,F. Borghi, G. Divitini, C. Ducati, C. Lenardi, C. Piazzoni, M. Merlini, A. Podestà, P. Milani, Bottom-up engineering of the surface roughness of nanostructured cubic zirconia to control cell adhesion. Nanotechnology 23, 475101 (2012).
- A.V. Singh, M. Galluzzi, F. Borghi, M. Indrieri, V. Vyas, A. Podestà, W.N. Gade. Interaction of Bacterial Cells with Cluster-Assembled Nanostructured Titania Surfaces: An Atomic Force Microscopy Study. Journal of Nanoscience and Nanotechnology 13, 77 (2013).
- C.Ghisleri, F. Borghi, L. Ravagnan, A. Podestà, C. Melis, L. Colombo, P. Milani, Patterning of gold-polydimethylsiloxane (Au-PDMS) nanocomposites by supersonic cluster beam implantation. J. Phys. D: Appl. Phys. 47, 015301 (2014).
- F. Borghi, V. Vyas, A. Podestà, P. Milani, Nanoscale Roughness and Morphology Affect the IsoElectric Point of Titania Surfaces. PLoS ONE 8, e68655 (2013).
- F. Borghi, C.Ghisleri, L. Ravagnan, A. Podestà, C. Melis, L. Colombo, P. Milani, Stretchable nanocomposite electrodes with tunable mechanical properties by supersonic cluster beam implantation in elastomers. APL 106, 121902 (2015).

Publications in preparation

- Podestà, F. Borghi, M. Indrieri, S. Bovio, P. Milani, Engineering the surface morphology and the interfacial functionalities of nanostructured titanium oxide thin films exploiting cluster-assembling from the gas phase.
- Schulte, S. Rodighiero, M. A. Cappelluti, L. Puricelli, F. Borghi et al, Nanoscale information of nanorough zirconia surfaces orchestrates mechanotransductive events that promote neuronal differentiation.
- F. Borghi, E. Sogne, C. Lenardi, A. Podestà, P. Milani, Cluster-assembled cubic ZrO_2 films with tunable and stable nanoscale morphology and high surface area against thermal annealing.

- F. Borghi, C. Piazzoni, A. Podestà, P. Milani, Evolution of surface morphology of nanostructured zirconia islands deposited by low-energy cluster beam deposition.
- C. Lenardi, E. Sogne, F. Borghi, A. Podestà, P. Milani, Effects of Temperature and Oxygen Vacancies on Nanocrystallite Phase and Size in Metastable Cluster Assembled ZrO_2 films.

Poster presented in conferences and workshops

- 1ST Workshop of condensed matter Highlights, Milano, 2013-09-25 'Nanoscale roughness and morphology affect the IsoElectric Point of titania surfaces' F. Borghi,V. Vyas, A. Podestà, P. Milani.
- Linz winter workshop, Linz, 2012-02-03 'Investigation of adhesion mechanisms of proteins on nanostructured surfaces by a combined local approach based on Atomic Force Microscopy', F. Borghi, V. Vyas, A. Podestà, P. Milani.
- 2013 MRS Spring Meeting & Exhibit, San Francisco, 2013-01-04 'High-resolution stiffness patterns on stretchable polymers', C. Ghisleri, R. Simonetta, F. Borghi, L. Colombo, A. Podestà, P. Milani.
- Training school AFM 2013 in biology, Genova, 2013-16-09 'Investigation of adhesion mechanisms of proteins on nanostructured surfaces by a combined local approach based on Atomic Force Microscopy', F. Borghi, V. Vyas, A. Podestà, P. Milani.
- CSI Workshop 2014, Gazzada Schianno, 2014-02-06/2014-04-06 'Evolution of surface morphology of nanostructured zirconia islands deposited by low-energy cluster beam deposition' F. Borghi, C. Piazzoni, A. Podestà, P. Milani.

Acknowledgments

Anzitutto grazie ad Alessandro Podestà per i preziosi insegnamenti di questi anni, a partire dalla tesi magistrale. Grazie in particolare per la pazienza e la tenacia con cui hai voluto condividere con me la tua esperienza e professionalità.
Grazie Paolo Milani per la fiducia che mi hai sempre dato, per l'attenzione con cui mi hai sostenuta e per il tempo che mi hai dedicato.
Ringrazio di cuore tutti i ragazzi che mi hanno accompagnata in questi anni di lavoro nel box AFM: Marco Indrieri, Simone Bovio, Massimiliano Galluzzi, Luca Puricelli, Alice Meroni e tutti i tesisti che hanno avuto la fortuna di incontrarci. Un grazie particolare al dolcissimo Luca che è venuto a trovarmi in ospedale (a Busto Arsizio!) dopo la mia prima gravidanza.
Grazie a Cristian (senza h) Ghisleri e Elisa Sogne per aver condiviso con me risate e momenti bui: chi trova un amico trova un tesoro (*Bibbia*, Siracide 6, 14).
Grazie a tutti gli altri professori del CIMaINa, post-doc, dottorandi, tesisti e studenti di laboratorio che ho incontrato. Davvero senza ognuno di voi non mi sentirei così a casa entrando in laboratorio e non potrei ripensare con così tanta simpatia a questi anni. Grazie a Sabrina e a Giulia: che segretarie!
Ringrazio tutti i miei amici, perché avete continuato a desiderare l'amicizia con me anche quando la condivisione del tempo non era più la stessa. Grazie perché non vi curate della mia distrazione.
Ringrazio i miei genitori e le mie sorelle perché mi volete molto bene. Inoltre, grazie nonni per il servizio gratuito reso!
Grazie Daniele, Pietro e "la creatura": fate parte di me e non posso più pensare a niente di quello che vivo, neanche al lavoro, senza avervi negli occhi e nel cuore.